

**Optical sampling and metrology using a
soliton-effect compression pulse source**

Gregor John McDonald

**Thesis submitted for the degree of
Doctor of Philosophy**

**Department of Electronic and Electrical Engineering
University College London**



2009

*"I certify that all material in this dissertation **which is not my own work** has been identified with appropriate acknowledgement and referencing and I also certify that no material is included for which a degree has previously been conferred upon me."*

.....

Author contact details

Gregor McDonald, QinetiQ, PA225, St Andrews
Road, Malvern, Worcestershire, WR14 3PS

gmcDonald@qinetiq.com Tel: 01684 895525

Supervisor and team members

UCL Supervisor: Professor Alwyn Seeds, Head of Photonics Group,
Department of Electronic and Electrical
Engineering, University College London
Torrington Place, London, WC1E 7JE

QinetiQ supervisor: Dr Andy Lewin, QinetiQ Fellow and Senior
Research Scientist, QinetiQ, PA221, St Andrews
Road, Malvern, Worcestershire, WR14 3PS
alewin@qinetiq.com Tel: 01684 895080

QinetiQ metrology team: Dr Andy Lewin
Dr David Orchard

QinetiQ ADC team: Professor Meirion Lewis
Dr Mike Kane
Jean-Donan Olliero

Acknowledgements and gratitude

Gregor McDonald would like to thank all of the above for their helpful advice throughout this work.

In particular, Gregor would like to thank Professor Alwyn Seeds for identifying the potential of the soliton-effect compression source for use in optical sampling, and for providing much needed insight throughout the work and for his many valuable suggestions which, without fail, led to system improvements.

Gregor has found Dr Andy Lewin to be an inspirational colleague, and owes a debt of gratitude to Andy for coupling the potential of the soliton-effect compression source with his 20+ years experience in the field of high-precision measurement systems to create the SIPOD metrology system. Gregor has never before met someone with Andy's terrier-like approach to problem solving.

In addition Gregor would like to thank Dr David Orchard, an exhausting colleague to work with due to his constant generation of ideas, tests and questions which Gregor simply cannot keep up with! Thank you also to Dr Ed Burr (UCL), Peter Sample (a former consultant to QinetiQ) and Dr Ed Chidley (QinetiQ). Gregor would also like to thank the QinetiQ QUEST team for the frequent use of their E5500 phase noise measurement system, and in particular Dr Paul Rice for his advice and support with this equipment. Thank you also Drs Martyn Fice and Cyril Renaud of UCL for their excellent advice and proof reading of the pulse source SPIE paper in September 2006.

This work was partly funded by the Emerging Underpinning Technology Domain of the United Kingdom Ministry of Defence Corporate Research Programme. Permission has been granted by D Def Sy for the public release of all relevant information in this thesis.

Sections of this work were performed under European Space Agency contract number 20874/07/NL/IA, project title "Alternative Concepts for Optical Metrology". Gregor would like to thank the customer Zoran Sodnik for his hugely enthusiastic support and advice throughout this programme.

Abstract

A low jitter optical pulse source for applications including optical sampling and optical metrology was modelled and then experimentally implemented using photonic components. Dispersion and non-linear fibre effects were utilised to compress a periodic optical waveform to generate pulses of the order of 10 picoseconds duration, via *soliton-effect compression*. Attractive features of this pulse source include electronically tuneable repetition rates greater than 1.5 GHz, ultra-short pulse duration (10-15 ps), and low timing jitter as measured by both harmonic analysis and single-sideband (SSB) phase noise measurements. The experimental implementation of the modelled compression scheme is discussed, including the successful removal of stimulated Brillouin scattering (SBS) through linewidth broadening by injection dithering or phase modulation. Timing jitter analysis identifies many unwanted artefacts generated by the SBS suppression methods, hence an experimental arrangement is devised (and was subsequently patented) which ensures that there are no phase modulation spikes present on the SSB phase noise spectrum over the offset range of interest for optical sampling applications, 10Hz-Nyquist. It is believed that this is the first detailed timing jitter study of a soliton-effect compression scheme. The soliton-effect compression pulses are then used to perform what is believed to be the first demonstration of optical sampling using this type of pulse source.

The pulse source was also optimised for use in a novel optical metrology (range finding) system, which is being developed and patented under European Space Agency funding as an enabling technology for formation flying satellite missions. This new approach to optical metrology, known as Scanning Interferometric Pulse Overlap Detection (SIPOD), is based on scanning the optical pulse repetition rate to find the specific frequencies which allow the return pulses from the outlying satellite, i.e. the measurement arm, to overlap exactly with a reference pulse set on the hub satellite. By superimposing a low frequency phase modulation onto the optical pulse train, it is possible to detect the pulse overlap condition using conventional heterodyne detection. By rapidly scanning the pulse repetition rate to find two frequencies which provide the overlapping pulse condition, high precision optical pulses can be used to provide high resolution unambiguous range information, using only relatively simple electronic

detection circuitry. SIPOD's maximum longitudinal range measurement is limited only by the coherence length of the laser, which can be many tens of kilometres. Range measurements have been made to better than 10 microns resolution over extended duration trial periods, at measurement update rates of up to 470 Hz. This system is currently scheduled to fly on ESA's PROBA-3 mission in 2012 to measure the inter-satellite spacing for a two satellite coronagraph instrument.

In summary, this thesis is believed to present three novel areas of research: the first detailed jitter characterisation of a soliton-effect compression source, the first optical sampling using such a compression source, and a novel optical metrology range finding system, known as SIPOD, which utilises the tuneable repetition rate and highly stable nature of the compression source pulses.

Table of Contents

1	The requirement for highly stable picosecond optical pulses	
1.1	Introduction	14
1.2	Development of a soliton-effect compression pulse source	14
1.3	Thesis overview	16
2	Optical sampling and photonic analogue to digital conversion	
2.1	Introduction	22
2.2	Analogue to digital conversion applications	23
2.3	ADC performance measurements	24
2.3.1	Timing jitter	25
2.4	Overview of all-electronic ADC approaches	27
2.4.1	Interleaving ADCs	28
2.4.2	Summary of state-of-the-art commercial all-electronic ADC performance	29
2.5	Conclusion on all-electronic ADC technology	31
2.6	Benefits of optical domain sampling	31
2.7	Entirely optical analogue to digital conversion, including quantisation	32
2.8	Opto-electronic analogue to digital conversion	33
2.9	Time-interleaved photonic ADCs	35
2.10	Frequency-interleaved photonic ADCs	36
2.11	Time-stretched photonic ADCs	38
2.12	All optical detection and quantisation	39
2.13	Photonic ADC resolution limitations	40
	<i>References for Chapter 2</i>	40
3	Optical metrology implemented using tuneable optical pulses	
3.1	Introduction to formation flying satellite requirements for optical metrology	44
3.2	Optical metrology approaches – the basic concepts	47
3.3	Scanning Interferometer Pulse Overlap Detection (SIPOD)	49
3.4	SIPOD system architecture	51
	<i>References for Chapter 3</i>	54
4	Soliton and soliton-effect pulse compression	
4.1	Introduction to theory	55
4.2	Practical implementation of a soliton compression scheme	58
4.2.1	Pulsed lasers	59

4.2.2	Beat frequency from two laser sources	59
4.2.3	Periodic waveform generated using a modulator	60
4.3	Survey of published pulse compression schemes	62
4.4	Pulse compression jitter implications	68
4.5	Conclusion on published pulse compression schemes	68
	<i>References for Chapter 4</i>	69

5 Modelling pulse compression through fibre

5.1	The split-step Fourier algorithm	72
5.2	Model implementation	74
5.3	Model accuracy	78
5.3.1	Global relative error	79
5.3.2	Fibre step size through SMF-28	79
5.3.3	Number of points per pulse window through the SMF-28	82
5.3.4	FFT windowing	83
5.3.5	Verifying the model with a soliton input	84
5.4	Evaluating viable pulse repetition rates and launch powers	86
5.5	Modelling compression through standard telecommunications fibre (SMF-28)	90
5.6	Specific SMF-28 input power and repetition rate example	92
5.7	Dispersion decreasing fibre (DDF) model implementation	94
5.8	DDF model runs	97
5.8.1	DDF step size accuracy	98
5.8.2	DDF number of points per time-slot	99
5.8.3	Example of high quality DDF output pulse	100
5.9	DDF performance summary	101
5.10	Conclusions from pulse modelling	102
	<i>References for Chapter 5</i>	103

6 Experimental pulse source implementation

6.1	Generic experimental arrangement	104
6.2	Removing EDFA amplified spontaneous emission	106
6.3	Stimulated Brillouin scattering (SBS)	106
6.4	Final arrangement for experimentally generating short ultra-stable pulses	115
6.5	Pulse tuneability	119
6.6	Autocorrelation measurements	119
6.7	Higher order pulses	120
6.8	Comparison with modelling	120
6.9	Summary of pulse compression implementation	124
	<i>References for Chapter 6</i>	124

7	Pulse timing jitter performance (SMF-28 compression fibre)	
7.1	Timing jitter measurement options	126
7.2	Single-sideband phase noise measurements	127
7.3	Overcoming stimulated Brillouin scattering using injection dithering	129
7.4	Overcoming stimulated Brillouin scattering using phase modulation	130
7.5	Fibre Bragg grating effect on SSB phase noise	132
7.6	Analysis of SSB phase noise timing jitter measurements	133
7.7	Microwave source jitter observations	134
7.8	Optical pulse jitter observations	134
7.9	General comments on SSB phase noise timing jitters measured	135
7.10	SSB phase noise jitter measurements summary	136
7.11	Timing jitter measurements using spectral analysis	137
7.12	Analyser method “sanity check”	142
7.13	Comparison of compressed pulse performance with a gain switched laser	143
7.14	Implementing the pulse compression scheme into an ADC system	147
7.15	Summary of compression pulse timing jitter performance	149
	<i>References for Chapter 7</i>	152
8	Optical metrology system design	
8.1	Introduction to SIPOD	153
8.2	Target/preliminary specifications for SIPOD system	154
8.3	Top level system architecture	155
8.4	Initial optical range finding using repetition rate tuneability	156
8.5	Component specifications/requirements	160
8.6	System error analysis	162
8.7	SIPOD error analysis summary	177
8.8	Summary of uncertainty levels in frequency scan measurements	178
8.9	SIPOD sub-system modules	179
8.9.1	Frequency reference unit (with up-converter)	179
8.9.2	Laser pulse generation sub-system	181
8.9.3	Interferometer head (including collimator)	184
8.9.4	Frequency sweep and overlap detection	186
8.9.5	Signal generation instrumentation	187
8.9.6	Control system and software	188
8.10	SIPOD system size, weight and power summary	190
8.11	Projected specifications for the SIPOD demonstrator and final systems	191
8.12	SIPOD design summary	192
	<i>References for Chapter 8</i>	193

9	Optical metrology experimental implementation	
9.1	Experimental implementation of SIPOD	194
9.2	Conclusions on experimental de-risking implementation	209
	<i>References for Chapter 9</i>	209
10	Build and testing of an optimised SIPOD demonstrator	
10.1	Introduction to system design and build	210
10.2	Key SIPOD component tests	211
10.3	Experimental arrangement for performing range measurements	219
10.4	SIPOD range detection algorithms	222
10.5	SIPOD operational testing	223
10.5.1	Static range measurement performance	223
10.5.2	Range calibration	225
10.5.3	Long translation stage scans at extended ranges	227
10.5.4	Dynamic range measurement - constant velocity drift	229
10.5.5	Lateral alignment sensitivity	231
10.5.6	Temperature sensitivity	232
10.5.7	Measurement of an oscillatory target	234
10.5.8	Sensitivity at reduced signal strength	236
10.6	Conclusions of SIPOD range finding performance testing	238
11.	Design of an optimised SIPOD compression fibre	
11.1	Introduction to fibre modelling	239
11.2	Modelling commercially available highly non-linear compression fibres	243
11.3	Modelling custom manufactured fibres	249
11.4	Summary of highly non-linear fibre modelling	253
11.5	Experimentally verifying model with Fibercore's reduced core fibres	256
11.6	SBS implications of smaller core fibres	262
11.7	Summary of compression fibre modelling and experimental de-risking	265
	<i>References for Chapter 11</i>	265
12.	Experimental characterisation of a bespoke compression fibre	
12.1	Fibre specifications on delivery	266
12.2	Experimental pulse compression performance	266
12.3	Range finding performance using the bespoke compression fibre	269
12.4	SBS implications for bespoke compression fibre	269

12.5	Polarisation maintaining performance	270
12.6	Predicted pulse width performance from future improved draw iterations	273
12.7	Conclusions on experimental performance of custom compression fibre	275
12.8	Future compression fibre development	276
	<i>References for Chapter 12</i>	276
13.	Conclusions on compression source and applications	
13.1	Introduction	277
13.2	Summary and conclusions of the compression source development	277
12.1	Future work	280
12.3	Summary	284
 Appendices		
A	Options for ultra-short, ultra-stable optical pulse generation	285
A.1	Gain switched lasers	286
A.2	Q-switched lasers	289
A.3	Mode-locking	293
A.3.1	Diode laser mode-locking	296
A.3.2	Mode-locked fibre lasers	299
A.3.3	Mode-locked waveguide lasers	304
A.4	Conclusions on options for low jitter, high repetition rate pulse sources	304
A.5	Comparison with state-of-the-art crystal oscillators	308
	<i>References for Appendix A</i>	308
B	Jitter measurement techniques	313
B.1	Introduction	313
B.2	Phase noise approach to jitter measurement	314
B.3	Measuring jitter from the power spectrum	317
B.4	Summary of jitter measurement approaches	319
	<i>References for Appendix B</i>	320
C	Sampling issues	321
D	Timing Jitter and number of bits resolution	321
E	Electric field generated by modulator biased at null	322
F	Relating dispersion parameter D to group velocity dispersion β_2	325
G	Publications arising from the work presented in this thesis	327

Acronym list

ADC	analogue to digital converter
ASE	amplified spontaneous emission
AWG	arrayed waveguide grating
CAD	computer aided design
CDPF	comb-like dispersion profiled fibre
CNR	carrier to noise ratio
CW	continuous wave
DAC	digital to analogue converter
DDF	dispersion decreasing fibre
DDS	direct digital synthesis
DFB	distributed feedback laser
DIF	dispersion increasing fibre
DSF	dispersion shifted fibre
EDFA	erbium doped fibre amplifier
EDFL	erbium doped fibre laser
EAM	electro-absorption modulator
EO	electro-optic
ESA	European Space Agency
FBG	fibre Bragg grating
FFT	fast Fourier transform
FP	Fabry Perot
FPGA	field programmable gate array
FWHM	full-width half-maximum
GVD	group velocity dispersion
HPOM	high precision optical metrology
LO	local oscillator
LSB	least significant bit
LUT	look up table
MZ	Mach Zehnder
OFDR	optical frequency domain reflectometry
PROBA	project for onboard autonomy
PER	polarisation extinction ratio
PM	polarisation maintaining
QCSE	quantum confined Stark effect
RIHP	relative integrated harmonic power
RMS	root mean square
S-SEED	symmetric self-electro-optic effect device

SAW	surface acoustic wave
SFDR	spurious free dynamic range
SIPOD	scanning interferometric pulse overlap detection
SMF	single mode fibre
SNR	signal to noise ratio
SPM	self phase modulation
SBS	stimulated Brillouin scattering
SRS	stimulated Raman scattering
SSB	single sideband
STF	standard telecommunications fibre
WDM	wavelength division multiplexing
β	mode propagation constant, i.e. β_2 is typically given in ps^2/km
D	dispersion parameter (typical units of $\text{ps}/\text{nm}/\text{km}$)
γ	nonlinear coefficient (typical units of $\text{W}\cdot\text{km}^{-1}$)
α	fibre attenuation coefficient (typical units of dB/km)

1. The requirement for highly stable picosecond optical pulses

1.1 Introduction

A diverse range of applications within ultra-fast physics research have been made possible due to the availability of highly accurate optical pulses with durations shorter than a few tens of picoseconds, including laser spectroscopy, electro-optic sampling and high-intensity physics. Ultra-short pulses have facilitated an equally wide range of industrial applications, including femtosecond material processing and micro-machining of components, medical treatments such as tomography, and optical fibre communications.

In terms of commercial success, short optical pulses have perhaps been most successfully implemented in the telecommunications sector, where multi-gigabit pulses facilitate the transmission of the high bandwidth binary signals which carry broadband data and digital television channels around the globe.

In telecommunications systems the pulse fidelity requirements are not as stringent as in some applications due to the use of a detection regime with the lowest possible amplitude resolution requirements, i.e. binary. Large-scale system implementation drives the industry to use low cost laser solutions which can be mass produced, meaning that telecommunications pulsed laser sources often trade pulse precision for cost benefits. Some loss of pulse performance can be offset by the fact that binary data transmission normally benefits from error checking protocols known as checksums; a typical Ethernet data frame for example comprises information data and a 32-bit checksum. This substantial error checking overhead means that telecommunications systems can accommodate the fact that some pulses will experience significant amplitude or timing jitter, with the result that individual pulses are incorrectly received. These errors occur despite the detection circuitry consisting of a simple binary amplitude threshold, meaning that jitter has affected the pulse amplitude to such an extent that the pulse level has flipped in value across the 50% binary threshold, possibly because the timing jitter has been so significant that the pulse has migrated by many tens of picoseconds into a neighbouring pulse time-slot.

1. The requirement for highly stable picosecond optical pulses

Many other applications exist however which demand substantially higher stability optical pulse trains than the telecommunications networks. Analogue to digital converters (ADCs) allow the conversion of real-world analogue signals into discrete binary form and are critical components in a wide range of processing systems, from audio equipment through to military radar, enabling subsequent analysis, manipulation and storage of digitised analogue information by today's powerful digital processing systems. ADCs implemented using photonic technologies benefit from many of the inherent properties of optics such as optical parallelism, interleaved architectures with no additional jitter penalties, very high input bandwidths (DC to >40 GHz) and the existence of very low jitter optical pulse sources. When optical sampling is used within a high bandwidth ADC system, the pulse detection system only has a single opportunity to sample a waveform which may contain temporal artefacts which vary notably over timescales of the order of the sampling pulse width; in addition, detection must be performed on this timescale to as high a resolution as possible, normally to 8-bits (256 discrete levels) or more. Therefore for high-end optical sampling applications, the optical pulse source must exhibit exceptionally low amplitude and timing jitter, typically sub-picosecond and less than one quantisation level respectively (i.e. 1 part in 256 for an 8-bit ADC). Additionally, for sampling high-bandwidth signals such as military radar, it is desirable to use very short sampling pulses of only several picoseconds duration, in order that the waveform does not change significantly during the sampling window.

Optical metrology (range finding) is another application which requires highly stable optical pulses. In its simplest form, longitudinal optical metrology can involve transmitting a pulse over the unknown distance to the target under measurement, and measuring the round-trip time taken for the pulse to return. In this case, it is essential that the exact time of the pulse generation and receipt can be measured with as little timing jitter as possible, to minimise range measurement errors. A more sophisticated approach involves averaging multiple time-of-flight readings for a train of optical pulses travelling the round trip length under measurement. Increasing levels of sophistication and complexity can be added to pulsed optical metrology systems to improve pulse stability and aid pulse detection, and therefore refine the range measurement. Pulse

1. The requirement for highly stable picosecond optical pulses

durations should be minimised to increase range resolution, since features such as the peak can be defined more accurately on short pulses.

1.2 Development of a soliton-effect compression pulse source

A QinetiQ photonic ADC programme was the principal motivation behind the development of a gigahertz repetition rate pulse source implemented using soliton-effect compression. This thesis describes what is believed to be the first detailed timing jitter characterisation of such a soliton-effect compression pulse source, a critical parameter for high-speed, high-accuracy optical sampling. The compression source was used to perform optical sampling in a photonic ADC arrangement, and this is believed to be the first implementation of a soliton-effect compression pulse source for this application.

A highly attractive feature of the soliton-effect compression pulse source is that the optical pulse repetition rate is set by the frequency output of an electronically controllable microwave source. This ability to very accurately and rapidly scan the pulse repetition rate led to the pulse source being optimised for use in a novel optical metrology system, which is being developed under European Space Agency funding as an enabling technology for formation flying satellite missions. A novel metrology technique was developed, based on scanning the optical pulse repetition rate to find the specific frequencies which allow the return pulses from the outlying satellite to overlap exactly with a reference pulse set on the hub satellite; this system is known as Scanning Interferometric Pulse Overlap and Detection (SIPOD). The pulse overlap condition corresponds to a detected peak in a heterodyne signal superimposed onto the optical carrier. In this way, high precision optical pulses can be used to provide unambiguous range information over many hundreds or thousands of metres, using only relatively simple heterodyne detection circuitry. The maximum range is limited only by the stability of the master microwave clock and the coherence length of the laser, which can be many kilometres for narrow linewidth fibre laser sources. Range measurements have been made to better than 30 microns resolution over extended duration trials. This technique has been filed as a patent.

The soliton-effect compression source was implemented using commercially available photonic components, the majority of which already exist in either military or space

1. The requirement for highly stable picosecond optical pulses

qualified versions. Initially, a periodic waveform is created by driving an optical modulator with a single frequency microwave source. This waveform is then optically amplified to the required power level and then propagated through appropriately selected optical fibre, such that non-linear fibre effects compress the waveform to generate pulses of the order of 10-15 picosecond duration, via soliton-effect compression. The first iteration of the pulse source used 25 km of Corning's SMF-28 fibre as the compression fibre. The pulse source was later upgraded with a 2.5 km, reduced core diameter fibre manufactured by Fibercore. Attractive features of this pulse source include electronically tuneable repetition rates greater than 1.5 GHz, ultra-short pulse duration (10-15 ps), and timing jitters limited by the electronic microwave source. The use of standard commercially available components makes the system relatively straight-forward to implement. In addition, the system is inherently robust to thermal effects unlike some low jitter pulse source alternatives, which often employ extended cavities and pulse seeding techniques to achieve lower timing jitter; a comprehensive review of alternative pulse source techniques is provided in Appendix A, which cites the Q-switched lasers, gain switched lasers and mode-locked lasers possessing the most stable reported performance. The best reported timing jitters for each laser type and variant is provided in a summary table (A.4), showing that the jitter performance of the soliton-effect compression source is comparable to the very best gain- and Q-switched lasers, and two orders of magnitude higher than the lowest published mode-locked laser timing jitter values (using single-sideband phase noise analysis over the same frequency offset ranges).

1.3 Thesis overview

Chapter 2 introduces the topic of analogue to digital conversion, explaining the limitations of all-electronic systems and the current unfulfilled top-end military and satellite requirements for high-resolution high-bandwidth ADC functionality. The benefits of photonic ADC systems are then explained, in particular the fact that optics can greatly reduce the sampling errors which arise when using all-electronic sampling circuits. When the analogue signal sampling is performed with an electro-optic modulator, the detected pulse energy of each output optical pulse has a direct correspondence to the analogue electrical signal level at the instant the pulse propagated through the modulator. A phase-encoded sampling scheme compares the ratio of both

1. The requirement for highly stable picosecond optical pulses

outputs from a dual-output modulator, thus linearising the modulator transfer function and largely suppressing any *amplitude jitter* present on the optical pulses, as discussed in Appendix B. Therefore, the optical pulse *timing jitter* becomes one of the important parameters governing the photonic ADC system performance, along with pulse duration. Appendix B also provides a description of the main approaches to measuring optical pulse timing jitter, namely harmonic analysis and single-sideband phase noise measurements.

A second, quite different application is then introduced in Chapter 3, which discusses optical metrology and the European Space Agency's requirement for highly accurate range finding for formation flying satellite missions. Particular focus is given to PROBA-3, a two-satellite test-bed mission which primarily aims to prove the feasibility of formation flying instrumentation systems. PROBA-3 will carry a scientific payload in the form of a coronagraph which, when positioned correctly by the optical metrology system, will exactly block the observation satellite's view of the sun to facilitate imaging of the coronosphere. The PROBA-3 mission is planned to last for two years with the launch date scheduled as 2012. At present the SIPOD system prototyped by QinetiQ has been short listed as the key optical metrology system for this mission, and it is currently undergoing rapid space ruggedisation in order to meet the launch date. Chapters 9 and 10 discuss two prototype iterations based on the soliton-effect compression source modelled and experimentally characterised in Chapters 5, 6 & 7 of this thesis.

A separate survey, detailed in Chapter 4, examines published methods for generating repetitive pulse trains of short pulse duration, based on soliton-effect compression. This identifies that the modulator biased-at-null approach has not been published before for low gigahertz rates, and that no detailed timing jitter analysis appears to have been performed on any experimental soliton-effect compression scheme before.

The pulse propagation is modelled in Chapter 5 using the split-step Fourier algorithm, which identifies generic pulse behaviour following propagation through various lengths of standard telecommunications fibre and, in Chapter 11, various specialist highly non-linear fibres. Viable regions of input powers, pulse repetition rates and corresponding fibre lengths are indicated in both chapters. Chapter 5 uses the relative global error

1. The requirement for highly stable picosecond optical pulses

approach, to verify that the model has been implemented using high enough precision. The model is shown to propagate mathematically perfect solitons indefinitely in an undistorted manner, as predicted by theory.

The experimental implementation of the modelled compression scheme is discussed in Chapter 6, detailing the successful removal of stimulated Brillouin scattering (SBS) through linewidth broadening by injection dithering or phase modulation. In Chapter 7, timing jitter analysis identifies many unwanted artefacts generated by the SBS suppression methods, hence an experimental arrangement is devised (which has subsequently been filed as a patent) which ensures that there are no phase modulation spikes present on the SSB phase noise spectrum over the offset range of interest for optical sampling applications, 10Hz-Nyquist. The improved performance of the QinetiQ photonic ADC is demonstrated when optical sampling is performed using the compression pulse source as opposed to a basic gain switched laser.

Following this first demonstration of a soliton-effect compression pulse source for optical sampling, the source was then used as a key enabling component in the SIPOD optical metrology system being developed for ESA. Chapter 8 is an architectural design review which provides the first detailed analysis of all potential system error and noise sources, focussing in particular on issues relating to the compression pulse source which is core to the technique.

Chapter 9 discusses the subsequent successful experimental implementation of a de-risking SIPOD prototype, where the proof-of-principle system experimentally demonstrates the European Space Agency requirement of 25-250 metres range and <30 microns accuracy, using sub-optimal components. Chapter 10 then describes the completed build and verification procedures for an optimised SIPOD breadboard system, including detailed analysis of its static and dynamic range measurement capabilities. The tests were devised to verify that the system achieves its design goals and to explore its limitations within the constraints of a laboratory environment. This chapter includes an analysis of the key pulse compression source components. The test procedures describe the principal system performance areas, including range resolution, absolute range accuracy, and ability to cope with range drift velocities.

1. The requirement for highly stable picosecond optical pulses

The final area of work undertaken is described Chapters 11 and 12, which completes the reporting on the development of the compression source by modelling both commercially available and speculative non-linear fibres. The aim of this work was to determine a compression arrangement which substantially reduces either the output pulse durations and/or the required fibre length in comparison to the pulses already demonstrated through 25 km of standard telecommunications fibre (Corning's SMF 28). The SIPOD application in particular requires the minimum possible system volume and weight for use on micro-satellite platforms. Modelling suggests at least two different manufacturers (Sumitomo and Furukawa) supply fibres which can generate <2 picosecond pulses after propagation through a length of fibre an order of magnitude shorter than the 25 km of SMF-28 implemented in the previous chapters. To verify the accuracy of the modelling, compressed pulses of the order of 10 picoseconds duration were experimentally demonstrated using 2.5 km of a reduced core diameter fibre from a third manufacturer, Fibercore, a company which has previously supplied ESA with radiation tolerant fibres for gyroscope applications. Fibercore also offer a broad range of polarisation maintaining fibres. Based on the modelling work and the experimental verification, a custom draw was subsequently specified, combining three desirable properties from Fibercore's existing fibre portfolio to create a new fibre; these parameters are polarisation maintaining, radiation tolerant composition, and reduced core diameter to achieve a higher non-linear coefficient to increase pulse compression per unit length. Chapter 12 describes the very high level of correlation between the modelled pulse compression performance and the experimental characterisation of a custom fibre specified by QinetiQ and manufactured by Fibercore; pulses as short as 10 picoseconds duration have been demonstrated using this bespoke compression fibre.

In summary, an optical pulse compression source based on soliton-effect compression was modelled and experimentally implemented after a survey of available pulsed laser options identified that this approach had not been implemented for low gigahertz repetition rates before. Additionally, detailed characterisation of the timing jitter of this approach does not appear to have been reported previously in the literature. The pulse source was then used to perform optical sampling for what is believed to be the first time, before being tailored for use in a novel approach to optical metrology. Due to the high resolution range finding performance of the SIPOD system, coupled with the attractive system parameters of low size, weight and power, SIPOD is due to fly on an

1. The requirement for highly stable picosecond optical pulses

ESA mission in 2012. Throughout this thesis, the emphasis of the discussions is on the engineering issues which were overcome to physically realise the optical pulse source, such as the optimal removal of stimulated Brillouin scattering. Where appropriate the underlying physical properties have been investigated and modelled. The design and engineering considerations of the SIPOD system, for which the pulse source with its tuneable and highly stable pulses is the key enabling component, forms another major section of the engineering analysis which is a common theme throughout this thesis. Again, where appropriate, analysis of the underlying physical mechanisms is included for completeness.

2. Optical sampling and photonic analogue to digital conversion

Analogue to digital conversion is a key component in enabling today's powerful binary processing systems to analyse, transmit and store real-world analogue signals. The idea of using photonic technologies has been considered for many decades as a method for improving the digital sampling of analogue electrical signals. This chapter introduces analogue to digital conversion (ADC), before reviewing the historical background of photonic ADC work and the various photonic approaches which have proved the most successful to date.

2.1 Introduction

Analogue to digital converters (ADCs) are a fundamental component of a range of sophisticated signal processing systems, facilitating the analysis and transmission of continuous time-signals through conversion to a discrete binary-coded format. ADCs are essential subsystems for a wide variety of applications including sonar, radar, instrumentation, consumer electronics, electronic warfare, medical applications, telecommunications systems and many others.

A wide range of technology options and architectures exist for implementation of the analogue to digital conversion function, including all-electronic and opto-electronic (photonic) approaches. Despite the different implementation techniques, the performance of each approach can be characterised by a relatively small number of parameters, depending on the intended application: sample rate, sample resolution (effective number of bits), signal-to-noise ratio (SNR), spurious-free dynamic range (SFDR) and power dissipation.

Extensive industry surveys have been undertaken at regular intervals to evaluate state-of-the-art ADCs, including both experimental and commercially available systems^[1]. These studies highlight the technological limitations of cutting-edge ADC technologies at each sampling frequency and explain how new architectures aim to overcome the current limits.

A review of some of the different ADC implementation techniques is provided as an introduction to the subject, with consideration given to the merits of various all-electronic and opto-electronic (photonic) techniques. The methods used to characterise the different ADC types are also introduced. The benefits of photonic systems, such as the ability to perform parallel operations, the potential to use interleaved architectures with no relative jitter and the fundamentally high bandwidth of optical components make photonic systems an attractive option for realising high-speed ADC systems. Perhaps the main benefit of using photonics in an ADC system is the ultra-low jitter performance of optical pulsed laser systems, which govern both the timing and amplitude accuracy of the optical sampling and hence the resolution of the ADC system as a whole. A comprehensive review of optical pulse source options and their performance is given in Appendix A, focussing in particular on their timing jitter properties. Appendix B describes two of the most common approaches for performing timing jitter analysis; single-sideband phase noise analysis and harmonic analysis.

2.2 Analogue to digital conversion applications

The analogue to digital converter is a key component of any system which senses the natural environment and displays, processes or stores the captured information through digital processing or representation. By far the preferred method of processing, storing and transmitting signals is through digital means, yet the vast majority of signals in the physical world are analogue, making the ADC critical to the success of an enormous range of systems, from commercial communications systems to consumer audio equipment, and military and space applications.

The Walden survey^[1] of ADC performance trends identified the different requirements of many varied ADC applications, with their associated resolution and sampling frequency requirements. A similar more generic representation of the various ADC applications is given in Shoop's "Photonic Analog-to-Digital Conversion"^[2], which is the basis for the generic Fig. 2.1. At the slowest sampling speeds, high-fidelity audio consumer products require up to 24 bits at 192 kHz sampling speeds (DVD-audio format), whereas at the other extreme of the ADC requirement span are ultra-wide bandwidth satellite communications which require many gigahertz sampling rates and can accommodate working with only a few bits resolution. Somewhere in the middle

are many military applications, for use in radar for example, which require both high resolution and ultra-wide bandwidth. Fig. 2.1 is a generic plot intended to demonstrate that there is a trade-off between sampling rate and resolution for the most demanding ADC applications.

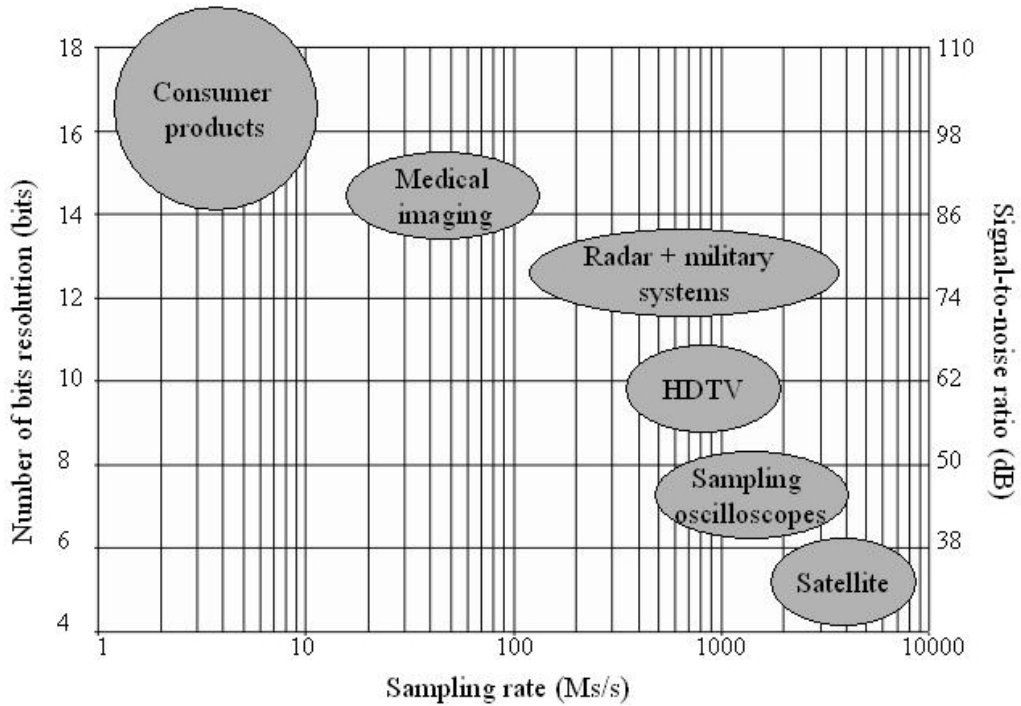


Fig. 2.1. ADC applications and corresponding sampling rate and resolution requirements (figure generated for this thesis from information in Ref [2]).

2.3 ADC Performance Measurements

As discussed, there is a wide range of ADC applications from low-resolution and slow-speed voltmeters, through high-resolution and moderate-speed entertainment systems, to high-performance satellite and military systems requiring high-speeds and as high an amplitude resolution as possible. This expansive set of applications means that ADCs have a range of distinctly different fields, markets and end-users, which has resulted in a similarly wide range of performance measures and terminology. It is important therefore to note that different ADC applications often define different measurement performance characteristics and that it is difficult to find parameters which have been universally agreed upon which cover all the different ADC end-user interests.

However, core to every ADC scenario is the requirement that the input signal can be adequately sampled to allow further digital analysis and manipulation. It is important for the user to ensure the correct choice of ADC in terms of the required conversion speed and resolution. Consequently, an ADC is typically characterised by its sampling rate, the highest input frequency that can be converted, and its resolution.

Various texts detail ADC performance measurements (including Ref. [2]), some of which can be measured quasi-statically, such as the number of bits of resolution and some sampling nonlinearities. Other performance measurements such as spurious-free dynamic range (SFDR) and two-tone intermodulation must be obtained dynamically. For high-speed ADCs, many performance measures are obtained through spectral analysis of the ADC output and these generally provide a much more accurate prediction of ADC performance than the quasi-static resolution of the ADC.

2.3.1 Timing Jitter

One parameter fundamental to the successful realisation of all ADCs is their sampling timing jitter performance, and it is this parameter which will now be discussed in more detail to explain the reasoning behind the development of the low jitter optical pulse source detailed later in this report.

At the basic level, the ADC takes an unknown input analogue waveform and samples it at discrete intervals to obtain the sampled output, Fig. 2.2. A more detailed description, including the analogous frequency domain implications, is given in Appendix C.

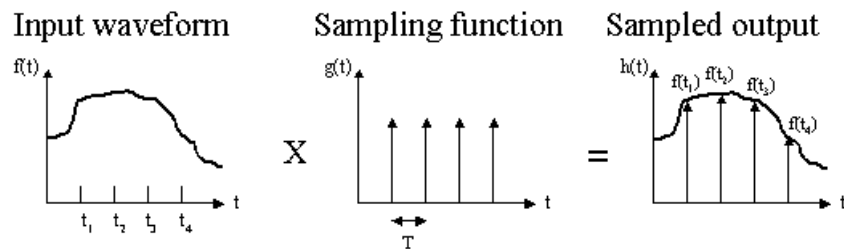


Fig 2.2. Generic ADC behaviour, sampling an analogue input at discrete time intervals.

2. Optical sampling and photonic analogue to digital conversion

The sampling aperture window is the period during which the unknown input analogue signal is averaged when the sampler is open. Ideally every single sampling aperture will be equally spaced in the time domain, but in real ADC systems timing jitter is introduced and samples are unavoidably taken with some timing error, such as Fig. 2.3. This can introduce large errors for rapidly slewing input signals, Fig. 2.4.

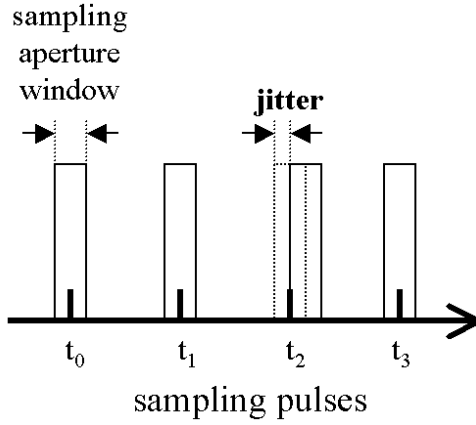


Fig. 2.3. Ideally the sampling pulses will be equally spaced in the time domain, however a real system this will experience some timing jitter such as the pulse at t_2 .

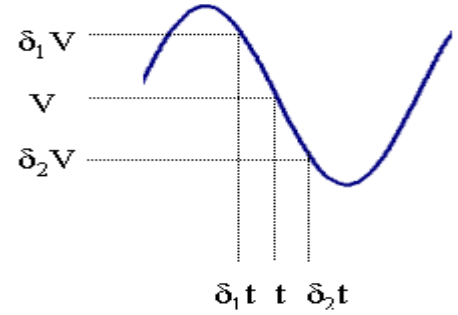


Fig. 2.4. A small timing jitter can result in large digitisation errors on rapidly slewing signals.

If the timing jitter is assumed to be uncorrelated then we can use the standard deviation, τ_{jitter} , to obtain to an upper bound for the effective number of bits, b_{eff} , of amplitude resolution obtained for a given level of sampling jitter (see Appendix D for derivation)

$$b_{\text{eff}} = \log_2 \left[\frac{1}{2\pi f_s \tau_{\text{jitter}}} \right] \quad (2.1)$$

where $f_s = 2f_x$ is the sampling frequency of the ADC operating at the Nyquist sampling frequency on the input signal frequency f_x , for the worst case sampling of a sinusoidal input signal.

Fig. 2.5 illustrates the maximum acceptable sampling pulse jitter values for a series of input sinusoidal frequencies if we wish to achieve a given number of bits resolution. To sample a 1 GHz signal at 8 bits requires a timing jitter of less than 600 fs, with 12 bits resolution at 1 GHz requiring less than 40 fs jitter. For higher input frequencies, timing

jitter becomes even more critical, with 4 GHz input signals digitised at 12 bits requiring less than 9 fs jitter.

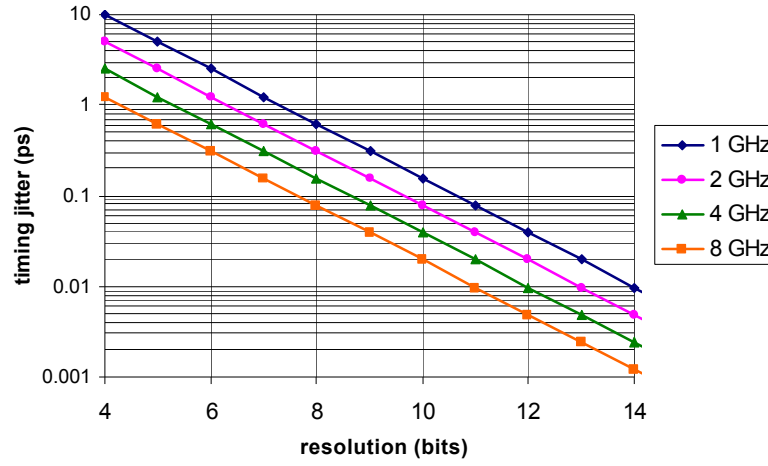


Fig. 2.5. Maximum timing jitter acceptable for capturing a given input sinusoidal waveform to the required bit resolution

The issue of sampling pulse stability is therefore of extreme importance to the overall performance of the ADC system, particularly for high resolution performance at high input bandwidths. Appendix A evaluates the different existing pulse source options for photonic ADCs and Chapters 5-7 discuss the development of a novel approach for low-jitter pulses based on soliton-effect compression. The following sections introduce all-electronic ADC and photonic ADC technologies to describe the motivation behind the soliton-effect pulse compression system development, and the reason for considering photonic implementations of ADC systems.

2.4 Overview of all-electronic ADC approaches

It is beyond the scope of this thesis to give detailed analysis of the implementation methods used by all-electronic ADC approaches. However all-electronic ADCs are introduced here both for completeness and to illustrate the high-speed limitations of all-electronic ADCs and hence the potential attraction of photonic ADC systems with their inherently low timing jitter coupled with high instantaneous bandwidths. Details of the main all-electronic ADC architectures can be found in many textbooks^[2]. Fig. 2.6 depicts various electronic ADC types and their relative resolution and bandwidth performances.

2. Optical sampling and photonic analogue to digital conversion

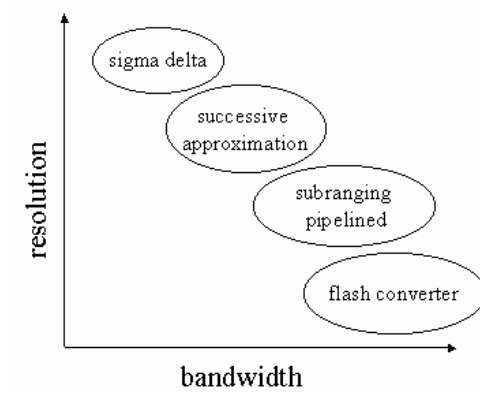


Fig. 2.6. Various all-electronic ADC architectures and their generic resolution vs. bandwidth performance

Walden's survey^[1] concluded that finite transistor speeds are one limiting factor for electronic ADCs, manifesting themselves as comparator ambiguities, or rather comparator inability to resolve the unknown input waveform voltage accurately enough in the given amount of time. The other major limiting factor is aperture uncertainty due to fluctuations in the timing clock and skew from the sampler itself if the switched capacitor's behaviour is influenced by the level of the signal being digitised.

2.4.1 Interleaving ADCs

To realise higher sampling speeds and overcome the finite speed of the integrated circuit technology of individual devices, multiple electronic ADCs can be time-interleaved to increase the converter's effective sample rate, Fig. 2.7. Now the limit on the ADC performance is no longer imposed by the finite speed of the integrated circuit technology but instead the greatest speed requirement is placed only on the sampling function which, in general, is superior in speed/bandwidth to the quantisation function.

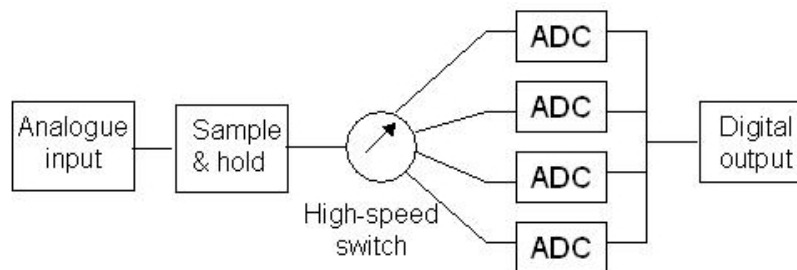


Fig. 2.7. Example architecture of interleaved electronic ADCs

2. Optical sampling and photonic analogue to digital conversion

Although time-interleaving relaxes the requirements on the comparator performance, it increases the sampling aperture uncertainty problem for integrated circuit systems, since multiple clocks must now be aligned with a fixed phase offset relative to each other. With a time-interleaved architecture, the repetition rate of each clock which triggers the sampling process is reduced by the number of channels, but the timing accuracy required of the overall interleaved clock signal remains unchanged. Also, the electrical clock signal must now be distributed to multiple channels and therefore over a larger area. Distribution of a high-speed electrical clock whilst maintaining low clock timing jitter and skew between the various clock signals becomes extremely difficult as the area of distribution increases.

In addition, time-interleaving related errors arise such as gain/offset mismatches and clock skew, all of which increase distortion in the final interleaved signal. The gain and offset mismatches are often due to mismatches in device size, a problem present in all circuit technologies. These errors can be minimised using calibration procedures in the time domain, careful circuit design and layout, a suitable selection of data converters, and digital post-processing, a complex process entailing extra design costs and lengthy calibration procedures.

It is by interleaving multiple ADCs that top end oscilloscopes achieve high bandwidths with relatively high resolution.

2.4.2 Summary of state-of-the-art commercial all-electronic ADC performance

The following figures are intended to provide a snapshot of some of the fastest state-of-the-art commercially available devices after a survey of the offerings from leading companies in the field such as Maxim, Analog Devices, Infineon, Texas Instruments, National Semiconductor, Atmel and Rockwell Scientific.

In terms of high sampling rates with moderate resolution (around 8 bits) of interest to the military, Rockwell Scientific's products represent some of the fastest available ADC chips, Table 2.1, operating at several GSamples/s with around 8-bit resolution.

2. Optical sampling and photonic analogue to digital conversion

Chip	Gs/s	Resolution (bits)	SFDR (dB)	Bandwidth (GHz)
RAD006	6	6	40	10
RAD008	3	8	55	10
RAD0010	1	10	60	6

Table 2.1. Selection of 3 of the fastest Rockwell Scientific all-electronic ADC chips.

Oscilloscope manufacturers Le Croy, Tektonix, Agilent and others regularly bring out new models in order to compete at the top-end of the market. The Agilent Infiniium, LeCroy WaveExpert and Tektronix DPO70000 families all currently operate at 40-50 GSamples/s with ~12-20 GHz bandwidth and up to 8 bits resolution for DC inputs. Silicon germanium is becoming the material of choice for implementing this fast circuitry. It should be noted that in order to achieve these figures, the Agilent oscilloscope for example involves interleaving 80 individual ADC devices and is therefore a bulky and power hungry system (20 kg and 800 Watts^[3]).

A more recently published survey intended to update Walden's electronic ADC survey with new photonic ADC developments was published by a group from the Aerospace Corporation in 2004^[4] (see Fig. 2.8 for a summary figure based on the data in this paper). It determined that five of the top six state-of-the-art electronic ADCs in 2004 lie below Walden's trend line slope of 1-bit per octave which was drawn in 1999, whereas all but one of the top six photonic ADC results are 2-3 bits above the trend line, despite the fact that the photonic results are research systems and not complete ADC systems^[5-12]. This illustrates the slow development in all-electronic ADC technology, which Walden predicted as being ~2.5 bits improvement every 8 years for a given sampling rate.

2. Optical sampling and photonic analogue to digital conversion

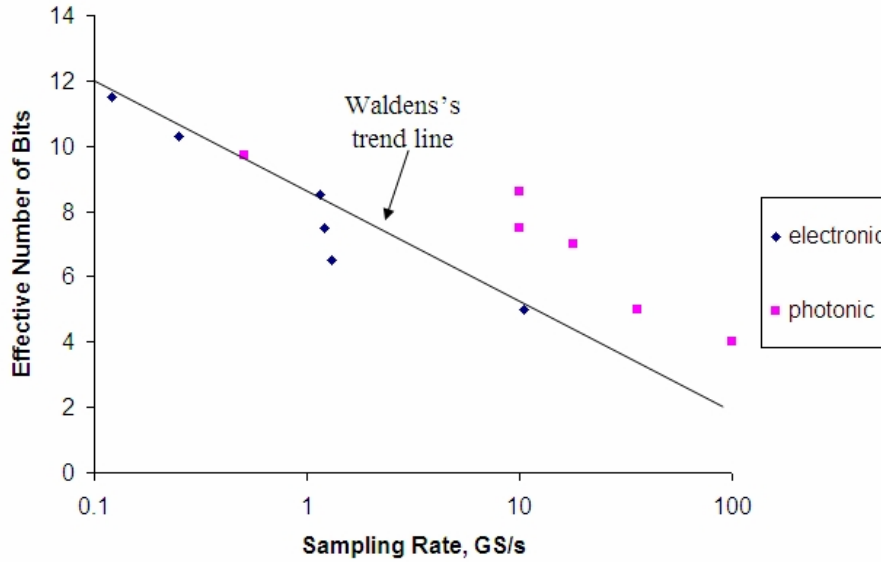


Fig. 2.8. Reproduction of a plot in an update^[4] to the Walden survey, plotting the top six photonic and top six all-electronic ADC implementations, referenced against Walden's trend line slope of 1-bit per octave

2.5 Conclusion on all-electronic ADC technology

By using multiple ADC devices in parallel (80 in Agilent's case), state-of-the-art oscilloscope manufacturers and others have managed to achieve sampling bandwidths of up to 12 GHz with resolutions around 8 bits, at the expense of making the system large, bulky and power hungry. However there still exists an unfulfilled requirement for both military and satellite ADC applications operating at many tens of GHz bandwidth with as many bits resolution as possible (ideally with at least 8 bits). Given the slow rate of all-electronic ADC improvement since the Walden survey in 1999, certainly no faster than the predicted 2.5 bits increase in resolution every 8 years, then it is by no means certain that all-electronic ADC technology will fulfil the requirements of high sampling rate ADC applications for many years to come.

2.6 Benefits of optical domain sampling

Photonic ADCs benefit from many of the inherent properties of optics such as optical parallelism, interleaved architectures (with no additional jitter penalty), very high input bandwidths (DC to >40 GHz) and the existence of very low jitter optical pulse sources. The main implementation options for photonic ADCs will now be reviewed, to explain how photonic ADC technology has been one of the main drivers of low jitter optical

2. Optical sampling and photonic analogue to digital conversion

pulse source development. The compression pulse source developed at QinetiQ and discussed later in this report was optimised to explore, for the first time, the suitability of a soliton compression source for performing the optical sampling front-end function within an ADC system.

One huge benefit of using the optical domain for performing the sampling process is that this approach allows for highly efficient manipulation of the broadband signals since they can be superimposed onto optical carriers. A 1 ps sampling pulse has a bandwidth of approximately 500 GHz bandwidth, whether in the optical or electrical domain. However, in the optical domain this signal is carried on an optical carrier with a centre frequency of the order of 100 THz, giving a fractional bandwidth of 0.005 in the optical regime as opposed to ~ 1 in the electrical domain. Due to this small bandwidth ratio in the optical domain, optical fibres and waveguides can minimise dispersion for short interconnects. Similarly, the availability of very broadband optical antireflection coatings means impedance matching problems are avoided.

Various analogue to digital conversion architectures have been implemented in the optical domain which utilise the availability of low jitter, short duration, high repetition rate optical pulse sources. Optics benefits from the existence of components such as modulators and arrayed waveguide gratings (AWGs) which can demultiplex these pulse trains, so that the sampling can be performed at high rates, while the detection and quantisation can be performed with much slower electronics.

2.7 Entirely optical analogue to digital conversion, including quantisation

There exists a range of photonic components which possess the required functionality to allow the realisation of entirely photonic analogue to digital conversion, including well known components such as Mach-Zehnder modulators, optical waveguide switches, acousto-optic devices, multiple quantum well modulators and smart pixel devices. Combinations of these and other components can allow construction of photonic systems capable of optical sampling^[13], optical switching and demultiplexing, and optical quantisation through optical bistabilities. In fully optical ADCs the quantisation can be performed using a bistable thresholding device, such as a symmetric self-electro-optic effect device (S-SEED) or potentially a photonic crystal based device^[14].

However, bistable S-SEED devices typically offer switching times of 10's of ps^[15,16], giving sampling rates of 10's of GHz but only at 1-bit resolution, which is simply not sufficient to meet the requirements of high-end users such as radar applications, even if oversampling and filtering are employed to boost the resolution at the expense of effective sampling speed.

An alternative all-optical approach to quantising the analogue input is to convert each sample of the input analogue waveform into a soliton, with the soliton order linearly representing the amplitude of each particular sample. Kitayama et al.^[17] optically sampled an analogue input signal with an optical pulse train, and propagated the subsequent amplitude modulated pulse train through appropriate fibre with the aim of generating a corresponding train of different order solitons. The higher order solitons are then collided with a pulse of different wavelength to count the number of solitons to provide the bit resolution. They demonstrated 3-bit resolution at modest sampling rates of 25 MHz, but predict that sampling rates of up to 100 GSamples/s are possible.

2.8 Opto-electronic analogue to digital conversion

However, rather than performing the analogue to digital conversion process entirely optically, arguably the most successful photonic implementations to date have utilised photonics to achieve step improvements in the performance of all-electronic ADCs, by using photonics as an extremely high bandwidth, high accuracy front-end sampler as input to one or more electronic ADCs.

The concept of utilising photonic and opto-electronic technologies to increase the sampling performance of electrical signals has been considered since at least the 1970's, when early proposals by Siegman^[18] and Auston^[19] sought to take advantage of short optical pulse-widths for sampling purposes, Fig. 2.9. Siegman's scheme envisaged sampling the input electronic signal via an electro-optic (EO) modulator, whereas Auston suggested triggering photoconductive switches with short optical pulses for high-bandwidth sampling of the input electrical signals. Both of these arrangements exploited mode-locked lasers and their very short pulsewidths (sub ps) and extremely low timing jitter, which can be as low as ~10's of fs, as discussed in the review of mode-locked laser sources in Appendix A. A significant benefit of the optical clock

2. Optical sampling and photonic analogue to digital conversion

distribution is the fact that the pulses can be transmitted to multiple nodes without a consequential increase in clock amplitude or timing jitter, due to the inherent robustness of optical transmission through fibre. The advent of high repetition rate low jitter laser pulses provided a direct solution for the aperture uncertainty problem which plagues high-speed all-electronic ADC implementations.

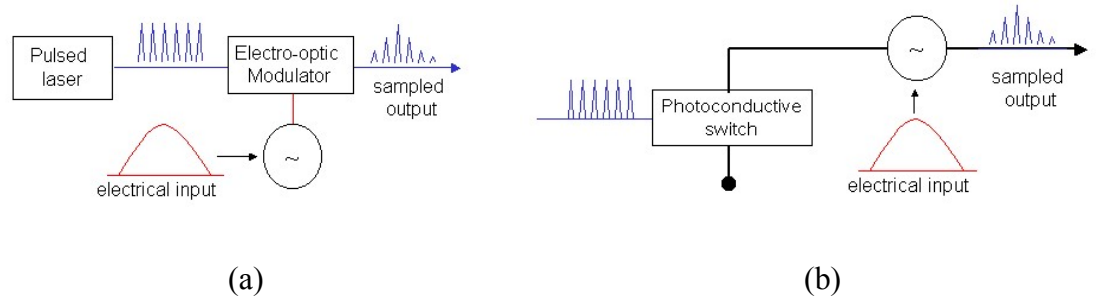


Fig. 2.9. Some of the earliest photonic sampling schemes, (a) Siegman's method for encoding the electrical signal onto a train of optical pulses using an EO modulator and (b) Auston's photoconductive switch triggered by short optical pulses.

The parallelism of optics was exploited in the mid-1970's when Taylor proposed splitting mode-locked laser pulse trains and using an array of EO modulators to represent each individual bit of the conversion, Fig. 2.10, with the output from each modulator captured via an avalanche photodiode (for amplification) and a comparator^[20,21]. Each successive bit of resolution (i.e. each extra least significant bit (LSB)) requires an EO modulator with a path length of double the previous bit's modulator. Ultimately the limit on this system becomes the electrode length of the LSB electrode, which for LiNbO₃ modulators leads to a limit of around 6 bits at 1 GHz. The main advantage of this system is that it decouples the input analogue signal from the optical sampling signal and therefore avoids distortion effects common to electronic diode-bridge sampling circuits, which tend to couple the sampling signal into the conversion circuitry.

2. Optical sampling and photonic analogue to digital conversion

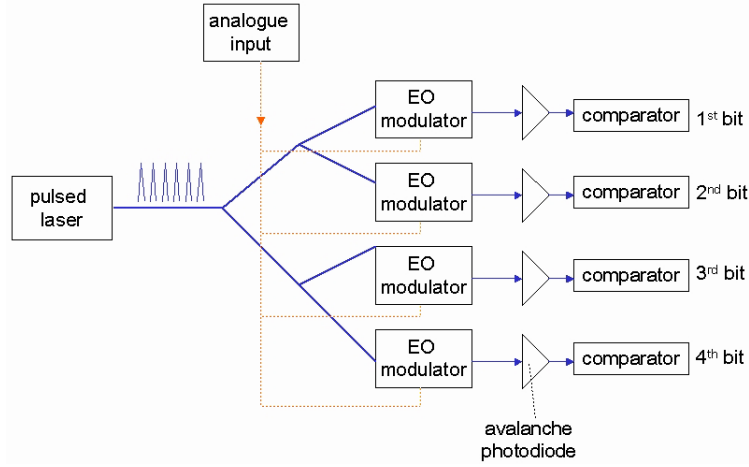


Fig. 2.10. Taylor's photonic ADC system, based on a pulsed laser and an array of EO modulators, with each modulator representing 1-bit of the output code. Each incremental bit requires a doubling of the modulator electrode length.

Since these early opto-electronic ADC implementations, a range of novel and varied systems have been proposed and demonstrated over the subsequent three decades. These methods can be grouped into two main categories: time-interleaved and frequency-interleaved architectures. The most successful of these will now be introduced to complete this overview of ADC technologies. Examples of some of the best performance parameters will be given but it should be noted that most of the results published for photonic ADCs are not based on complete ADC systems but are instead research results, which focus on overcoming particular limiting processes.

2.9 Time-interleaved photonic ADCs

In time-interleaved photonic ADC systems, the input analogue signal is generally encoded onto a train of optical pulses by passing them through an EO modulator, while it is being modulated by the electronic analogue input signal. Time interleaving is subsequently implemented by demultiplexing every n^{th} pulse to the n^{th} channel, up to N total channels. Each channel then consists of a photodetector, often some suitable filtering and then an electrical ADC to perform the quantisation. Each individual ADC samples at one- N^{th} of the total photonic ADC sampling rate. Options for the serial to parallel converter include a bank of binary switch trees as shown in Fig 2.11, usually implemented as a series of Mach Zehnder modulators^[12]. State-of-the-art performance

2. Optical sampling and photonic analogue to digital conversion

for time-interleaved ADCs includes a 40 GHz input bandwidth arrangement with 160 MSamples/s giving 4 bits resolution based on photoconductive sampling^[22].

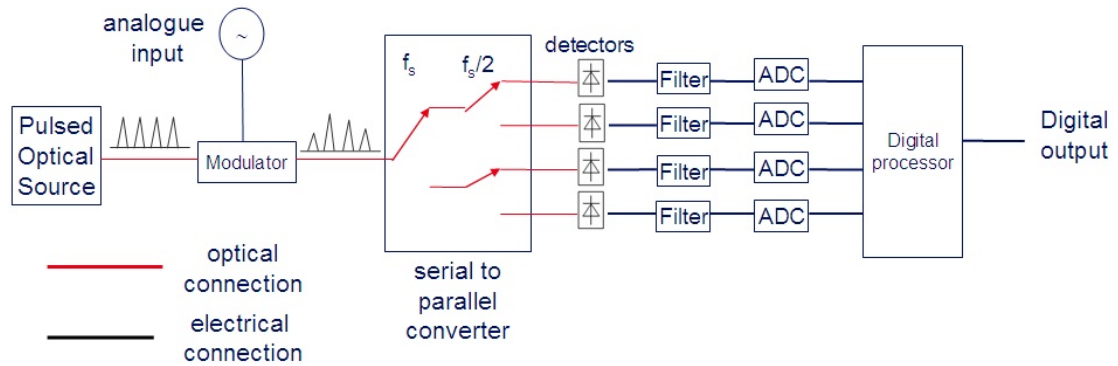


Fig. 2.11. Time-interleaved photonic ADC generic structure.

The time-interleaved work by Juodawlkis et al.^[12] is notable for employing a phase encoded optical sampling approach to overcome the nonlinearities introduced by LiNbO₃ Mach Zehnder (MZ) interferometers, the most commonly used EO device for modulating the sampling pulse intensities. The dynamic range of previous photonic ADC implementations using only a single output modulator had been limited by the sinusoidal nonlinearities of the MZ modulator. A number of approaches had sought to overcome this problem, for example by modifying the input electrical signal to limit the modulator non-linear terms^[23] or instead computationally manipulating the digital output from the ADC to invert the modulator transfer function^[24]. However Juodawlkis et al. use a dual-output MZ modulator to combine the energy from the complementary outputs and therefore allow the inversion of the modulator transfer function^[25]. This phase encoded approach has allowed them to realise a proof-of-principle system with over 8-bits resolution at 505 MSamples/s, with 12-bit resolution at multi-GHz sample rates predicted. The only drawback with their approach is that it requires twice the number of detection and quantisation components as a single output modulator scheme.

2.10 Frequency-interleaved photonic ADCs

Wavelength is an additional signal parameter which is often exploited in photonic systems to improve functionality or performance. In terms of photonic ADC technology, architectures have been implemented which use multi-wavelength or alternatively wavelength interleaved pulse sources which are then passively routed by

2. Optical sampling and photonic analogue to digital conversion

wavelength division multiplexing (WDM) set-ups such as arrayed waveguide gratings (AWGs), Fig. 2.12, as opposed to having a bank of actively addressed binary switches to perform the time-interleaved implementation. The demultiplexing operation then becomes a passive and potentially very compact solution. The challenge then becomes generating the multiple wavelength source, which can either consist of multiple lasers operating at different wavelengths which are then multiplexed, a supercontinuum source spectrally sliced to generate a stream of equally spaced pulses at different wavelengths, or alternatively a single laser capable of being reliably wavelength tuned at high speeds.

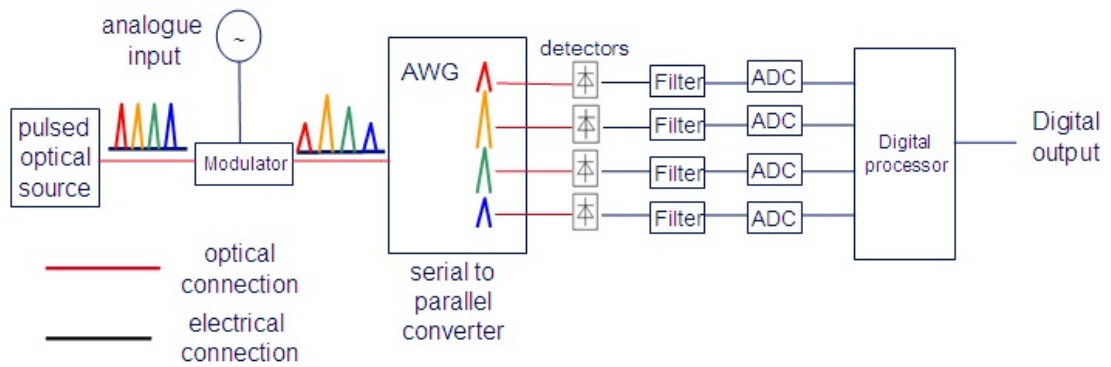


Fig. 2.12. Generic frequency-interleaved photonic ADC. Note that the pulse source can be frequency interleaved as shown, or consist of spectrally broad pulses.

Whilst frequency interleaving may appear to be an elegant solution to the problem of demultiplexing the pulse source before channelisation, problems exist with all three options for the realisation of the multiple wavelength sources mentioned. If multiple lasers operating at different wavelengths are multiplexed then the individual sources must have identical operating characteristics, including low jitter performance and identical power outputs to ensure gain flatness across all channels, at sufficiently high powers. In addition, each laser element must have accurate wavelength control to avoid drift since components downstream in the system are now critically wavelength dependent.

An alternative approach would be to use a very fast tuneable laser which must be capable of switching its operating wavelength at the rate 10's of GHz for high-end photonic ADC systems. To date, such devices have not yet been realised although the telecommunications industry has shown much interest in their development^[26] and devices based on Fabry-Perot laser pairs with optical interinjection have demonstrated

2. Optical sampling and photonic analogue to digital conversion

<7 ns switching speeds and over 20 dB sidemode suppression ratio^[27]. Other implementation methods suggested have included using the quantum confined Stark effect (QCSE) devices which can have ± 0.5 dB flat FM response over 10 kHz - 6 GHz^[28], or injection locking of Fabry-Perot or external cavity lasers^[29]. However, these methods have not yet provided the speeds, number of channels, channel stability and repeatability required for photonic ADC applications^[26].

An alternative approach is to use a supercontinuum source, which offers the potential for more than 100-channel carriers with 12.5-or-25 GHz spacing, as used by wavelength division multiplexing (WDM) telecommunication systems^[30]. Here an intense pump pulse is spectrally broadened in fibre through self-focussing, self-phase modulation, cross-phase modulation and parametric four-wave mixing. The result is the generation of multiple carriers with frequency spacing equal to the initial pulse frequency. The individual carriers can then be separated into discrete channels by the WDM setup. The limitations of this source for use in an ADC system are the variations in amplitude uniformity across all the channels. The timing of each channel is limited by the timing jitter of the original pulse source.

2.11 Time-stretched photonic ADCs

Another promising approach to photonic ADC implementation exploits the dispersive nature of optical fibres to extend the performance of electronic ADCs^[31]. It is based on the idea that if an analogue signal can be stretched in time then the effective sampling rate and effective bandwidth of the electronic ADC can be extended, Fig. 2.13.

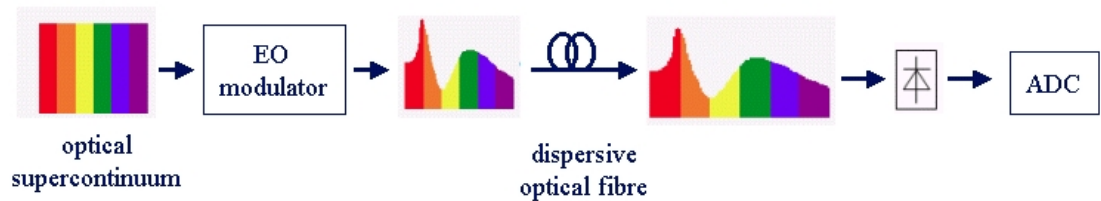


Fig. 2.13. Generic time-stretched photonic ADC system. The analogue signal is superimposed on a wideband optical pulse before being stretched through optical fibre, detected and then converted by an electronic ADC.

2. Optical sampling and photonic analogue to digital conversion

For the photonic time-stretch ADC approach, initially an optical supercontinuum is generated with a wavelength spread that is a linear function of time. In practice this has been achieved by amplifying a mode-locked laser and passing it through appropriate fibre to generate the supercontinuum source^[32]. The optical supercontinuum is then transmitted through a Mach-Zehnder modulator which encodes the input electrical analogue signal onto the source. Subsequent propagation through a chromatically dispersive optical fibre (or waveguide) linearly scales the optical signal in time, essentially expanding the modulated envelope of the signal. By photonic pre-processing the input signal in this way, the effective sampling rate and input bandwidth of the electrical ADC are increased by the stretch factor while the aperture uncertainty requirement is relaxed. The main drawback with this system is the inability to digitise continuous input signals, although for some applications such as digitising discrete radar returns this may not be a problem. Schemes employing parallelism through time-interleaving of this time-stretch technique have been suggested as a solution^[31]. One of the main challenges associated with the time-stretch approach is overcoming the non-uniform spectrum of the distortion introduced by the nonlinear dispersion, although this was achieved with active tracking via a dual output modulator approach. One of the most impressive implementations noted to date has been 480 GSamples/s giving 5.7 bit resolution over a 9.6 GHz bandwidth centred on a 26 GHz carrier^[33], for a 2 ns record length.

2.12 All optical detection and quantisation

For the interleaved photonic ADC schemes described, following the sampling of the analogue waveform by the optical pulse train and the subsequent demultiplexing, the optical pulses are then directed to photodetectors which integrate the energy in each optical sampling pulse. The response time of the photodetectors must be suitably fast such that the photocurrent generated by the sampling pulse has decayed to a negligible value before the next pulse arrives at the detector. The photodetector can then be used to charge a capacitor whose stored value can then be quantised to complete the analogue to digital conversion process.

2.13 Photonic ADC resolution limitations

There are three main limitations which could influence or limit the resolution of the photonic ADC^[34]: the linearity of the optical modulator used to sample the input electronic signal, the speed and sensitivity of the photodetectors, and the stability of the optical sampling source.

As discussed previously, the dual output modulator approach for phase encoded sampling^[12] can overcome the modulator nonlinearities. Photodetectors are available commercially (Discovery, U2T, New Focus and others) which meet the requirements of the latest photonic ADC requirements.

Therefore the performance or resolution of the optical sampling process can be directly attributed to the performance of the optical sampling pulse train, or optical clock^[34]. The stability of the optical clock can be characterised by three main parameters: the pulse duration, the amplitude fluctuation from pulse to pulse (the amplitude jitter), and the variation of the pulse sampling rate from pulse to pulse (the timing jitter). All three of these mechanisms contribute to inaccuracies in the sampled waveform as compared to the ideal waveform if sampled by a perfect optical clock.

References for Chapter 2

1. Walden R.H., "Analog-to-digital converter survey and analysis," IEEE J. Select. Areas Commun., vol. 17, pp. 539-550, 1999
2. Shoop B.L., "Photonic Analog-to-Digital Conversion", New York, Springer-Verlag Berlin Heidelberg, 2001
3. Agilent DSO/DA90000A real-time oscilloscope datasheet, retrieved on 20/04/2008 from Agilent website: <http://cp.literature.agilent.com/litweb/pdf/5989-7819EN.pdf>
4. Valley G.C, Hurrell J.P., Seidler G.A., "Photonic analog-to-digital converters: fundamental and practical limits", Proc. SPIE on Integrated Optical Devices, Nanostructures, and Displays, 5618, pp. 96-106, 2004

2. Optical sampling and photonic analogue to digital conversion

5. Kang J.U., Frankel M.Y., Esman R.D., "Highly parallel pulsed optoelectronic analog-digital converter", IEEE Phot. Tech. Lett., 10(11), pp. 1626-1628, 1998
6. Frankel M.Y., Kang J.U., Esman R.D., "High performance photonic analogue-digital converter", Elec. Lett., 33(25), pp. 2096-2097, 1997
7. Clark T.R., Dennis M.L., "Toward a 100-Gsample/s time-stretch analogue-to-digital converter", Elec. Lett., 36(18), pp. 1526-1527, 2000
8. Bushan A.S., Kelkar P.V., Jalali B., Boyraz O., Islam M., "130-Gsa/s photonic analog-to-digital converter with time stretch preprocessor", IEEE Phot. Tech. Lett., 14(5), pp. 684-686, 2002
9. DePriest C.M., Braun A., Abeles J.H., Delfyett P.J. Jr., "10-GHz ultralow-noise optical sampling stream from a semiconductor diode ring laser", IEEE Phot. Tech. Lett., 13(10), pp. 1109 - 1111, 2001
10. Clark T.R., Kang J.U., Esman R.D., "Performance of a time- and wavelength-interleaved photonic sampler for analog-digital conversion", IEEE Phot. Tech. Lett., 11(9), pp. 1168 - 1170, 1999
11. Twichell J.C., Wasserman J.L., Juodawlkis P.W., Betts G.E., Williamson R.C., "High-linearity 208-MS/s photonic analog-to-digital converter using 1-to-4 optical time-division demultiplexers", IEEE Phot. Tech. Lett., 13(7), pp. 714-716, 2001
12. Juodawlkis P.W., Twichell J.C., Betts G.E., Hargreaves J.J., Younger R.D., Wasserman J.L., O'Donnell F.J., Ray K.G., Williamson R.C., "Optically sampled analog-to-digital converters", IEEE T. Microw. Theory, 49(10), pp. 1840 – 1853, 2001
13. Nathawad L.Y., Urata R., Wooley B.A., Miller D.A.B., "A 40-GHz bandwidth, 4-b photoconductive-sampling time-interleaved CMOS A/D converter," IEEE J. Solid-State Circuits, 38(12), pp. 2021-2030, 2003
14. Yanik M.F., Fan S., Soljacic M., Joannopoulos J.D., "All-optical transistor action with bistable switching in a photonic crystal cross-waveguide geometry", Opt. Lett., 28(24), pp. 2506 – 2508, 2003
15. Clare B.A., Corbett K.A., Grant K.J., Atanackovic P.B., Marwood W., Munch J., "Investigation of critical slowing down in a bistable S-SEED", J. Lightwave Tech., 21(11), pp. 2883 – 2890, 2003

2. Optical sampling and photonic analogue to digital conversion

16. Boyd G.D., Fox A.M., Miller D.A.B., Chirovsky L.M.F., Dasaro L.A., Kuo J.M., Kopf R.F., Lentine A.L., "33-ps optical switching of symmetrical self-electro-optic effect devices", Appl. Phys. Lett., 57 (18), pp. 1843-1845, 1990
17. Oda S., Maruta A., Kitayama K., "All-optical quantization scheme based on fiber nonlinearity", IEEE Photon. Tech. Lett., 16(2), pp. 587-589, 2004
18. Siegman A.E., Kuizenga D.J., "Proposed method for measuring picosecond pulsewidths and pulse shapes in CW mode-locked lasers," IEEE J. Quantum. Electron., vol. QE-6, no. 4, pp. 212-215, 1970
19. Auston D.H., "Picosecond optoelectronic switching and gating in silicon," Appl. Phys. Lett., 26(3), pp. 101-103, 1975
20. Taylor H.F., "An electrooptic analog-to-digital converter," Proc. IEEE, vol. 63, pp. 1524-1525, 1975
21. Taylor H.F., "An optical analog-to-digital converter – Design and analysis," IEEE J. Quantum Electron., vol. QE-15, pp. 210-216, 1979
22. Nathawad L.Y., Urata R., Wooley B.A., Miller D.A.B., "A 40-GHz-bandwidth, 4-bit, time-interleaved A/D converter using photoconductive sampling", IEEE J. Solid-St. Circ., 38(12), pp. 2021-2030, 2003
23. Chiu Y., and Jalali B., Garner S., Steier W., "Broad-band electronic linearizer for externally modulated analog fiber-optic links," IEEE Photon. Technol. Lett., 11(1), pp. 48–50, 1999
24. Clark T.R., Currie M., Matthews P.J., "Digitally linearized wide-band photonic link," J. Lightwave Technol., 19(2), pp. 172–179, 2001
25. Twichell J.C., Helkey R., "Phase-encoded optical sampling for analog-to-digital converters," IEEE Photon. Technol. Lett., 12(9), pp. 1237–1239, 2000
26. Coldren L.A., Fish G.A., Akulova Y., Barton J.S., Johansson L., Coldren C.W., "Tunable semiconductor lasers: a tutorial", J. Lightwave Technol., 22(1), pp. 193-202, 2004
27. Yeh C-H, Lee C-C, Hsu Y-W, Chi S., "Fast wavelength-tunable laser technique based on a Fabry-Perot laser pair with optical interinjection", IEEE Photonic. Tech. L., 16(3), pp. 891-893, 2004

2. Optical sampling and photonic analogue to digital conversion

28. Huang, X., Seeds A.J., Roberts J.S., Knights A.P., "Monolithically integrated quantum-confined stark effect tuned laser with uniform frequency modulation response", IEEE Photonic. Tech. L, 10(12), pp. 1697-1699, 1998
29. Bergonzo A., Brenot R., Picq M., Legouezigou O., Landreau J., Sillard H., Jacquet J., "Fast wavelength switching using digitally tunable external cavity laser", Electron. Lett., 40(10), pp. 617–618, 2004
30. Mori K., Sato K., Takara, H., Ohara, T., "Supercontinuum lightwave source generating 50 GHz spaced optical ITU grid seamlessly over S-, C- and L-bands" Electron. Lett., 39(6), pp. 544–546, 2003
31. Asuri B., Han Y., Jalali B., "Time-stretched ADC arrays," IEEE T. Circuits-II, 49(7), pp. 521-524, 2002
32. Boyraz O., Kim J., Islam M.N., Coppinger F., Jalali B., "Broadband, high-brightness 10-Gbit/s supercontinuum source for A/D conversion", Conf. On Lasers and Electro-Optics, 2000 (CLEO 2000), pp. 489-490, 2000
33. Han Y., Boyraz O., Jalali B., "Real-time A/D conversion at 480 GSample/s using the phase-diversity photonic time-stretch system", Conf. On Microwave Photonics 2004 (MWP 2004), 2004
34. Delfyett P.J., DePriest C., Yilmaz T., "Signal processing at the speed of lightwaves [photonic ADCs]", Circuits and Devices Magazine, IEEE , 18(5), pp. 28 – 35, 2002

3. Optical metrology implemented using tuneable optical pulses

This chapter introduces optical metrology (range finding), a second and entirely separate application to photonic ADCs which also requires highly stable optical pulses. The compression pulse source, which is modelled and experimentally characterised later in this thesis, was used as the basis of an entirely novel approach to optical metrology, developed to meet a European Space Agency requirement for range finding for formation flying satellite missions. In this new metrology arrangement the electrically tuneable nature of the optical pulse repetition rate is exploited to ensure that the return pulses from the outlying satellite exactly overlap with a set of reference pulses on the master hub satellite. A heterodyne detection scheme allows slow-speed electronic circuitry to detect the specific repetition rates which provide overlapping pulses. Two separate pulse repetition rates providing the pulse overlap condition unambiguously provide the range from the pulse source to the target (the distance from the hub satellite to the outlying satellite). The metrology system range accuracy improves as the pulse stability improves, i.e. as pulse-to-pulse timing jitter and frequency drift is minimised, and as the pulse duration decreases.

3.1 Introduction to formation flying satellite requirements for optical metrology

Formation flying is an operational technique by which separate satellites operate as a single entity to enable new missions, which would otherwise be unfeasible or simply impossible to achieve with a single structure. The European Space Agency (ESA) has a long-term ambition to undertake a series of formation flying missions, with the aim of performing a range of demanding operations such as the search and analysis of terrestrial exo-planets which orbit nearby stars (Darwin), the search for the first giant black holes (XEUS), and other high accuracy formation flying missions such as the X-ray telescope observations planned for SYMBOL-X, Fig. 3.1. Absolutely core to the success of these missions is the ability of extended satellite constellations to perform autonomous and timely alignment to facilitate high precision formation flying, with inter-satellite alignments and orientations required to micron accuracies over hundreds of metres separation.

3. Optical metrology using tuneable optical pulses

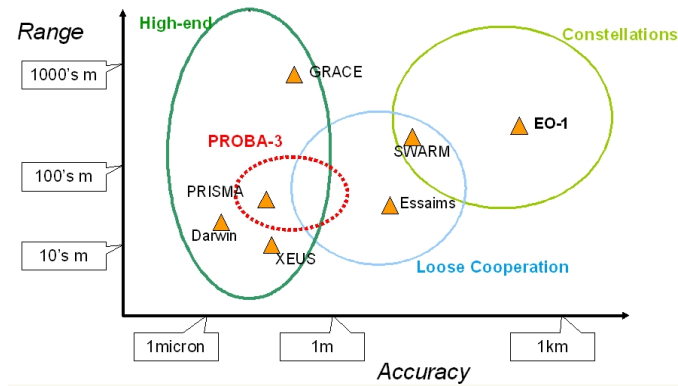


Fig. 3.1. ESA's formation flying applications encompass a wide range of separates and accuracies requiring flexible, scalable solutions.

The increasing use of micro-satellites ($\leq \sim 100$ kg) for earth observation and planetary exploration emphasises the need for much more compact, rugged, optical systems of lower mass and lower cost. Conventional optical and laser systems are often heavy, bulky, sensitive to misalignment and expensive to manufacture. Consequently, ESA is seeking highly functional and cost effective innovative technologies capable of delivering scalable metrology performance for its future range of missions.

PROBA-3 is a two-satellite test-bed mission which primarily aims to prove the feasibility of formation flying instrumentation systems^[1]. It will also carry a scientific payload in the form of a coronagraph, which will exactly block the observation satellite's view of the sun to facilitate imaging of the coronosphere. The PROBA-3 mission is planned to last for two years with the launch date scheduled as 2012. During the mission it will orbit the Earth twice daily, and will therefore experience relatively high levels of radiation as it passes through the Van Allen Belt on each orbit.

Paraphrasing ESA's mission aim

"PROBA-3 is the third in ESA's series of missions for validating developments in space systems while carrying an 'added value' user payload which can directly benefit from the innovations under test. PROBA-3 will demonstrate the technologies required for formation flying of multiple spacecraft. An instrument to observe the solar corona is being used for the ongoing design phase. PROBA-3 will comprise two independent,

3. Optical metrology using tuneable optical pulses

three-axis stabilised spacecraft flying close to one another with the ability to accurately control the attitude and separation of the two craft.

Utilising either cold-gas or electrical thrusters for agile manoeuvring, and both radio-frequency and optical (laser-based) metrology techniques for accurate position measurement and control, the combined system is expected to achieve a relative positioning accuracy of the order of 100 microns or better over a separation range of 25 to 250 metres.”

Following initial star tracker based position techniques, active radar control will be used to position the hub and coronagraph satellites to within 10 mm of their required positions during the observation cycle. The optical metrology system is then expected to take over and refine the relative positioning of the satellites to the order of 100 microns accuracy. A cascaded suite of increasing resolution lateral and longitudinal sensors is responsible for the optical metrology based positioning. In September 2007, QinetiQ was awarded a 12 month contract to address ESA’s longitudinal optical metrology sensor requirement. A parallel programme running at EADS Astrium had previously developed an alternative approach to optical metrology (known as the HPOM system – High Precision Optical Metrology^[2]), the specifications for which are given in Table 3.1. The majority of these specifications must be exceeded by the QinetiQ system in order for it to be considered for the PROBA-3 mission.

Metrology Sensor	Range	Accuracy	Drift capability	Update frequency	Volume [mm]	Mass [kg]	Power [Watt]
Longitudinal	±25 mm	32 µm	10 mm/sec	10 Hz	400 x 200 x 100	9	53
Fringe tracking	TBD	1 nm	0.1 mm/sec	10 Hz	300 x 200 x 100	12	53

Table 3.1: Technical specification of the HPOM optical metrology sensors.

3.2 Optical metrology approaches – the basic concepts

In general, optical metrology is the science and technology of performing measurements using the properties of light. In the specific case of formation flying, optical metrology is the measurement of the lateral, longitudinal and rotational displacement of two or more satellites in a constellation, relative to a common point in space. In the brief review of the principal longitudinal metrology approaches which follows, the techniques are listed roughly in order of increasing accuracy and precision.

The triangulation metrology method exploits the highly collimated nature of laser light over large distances. Typically, the laser beam illuminates a point located at the unknown target distance. Diffuse or specular reflections from that point are then monitored on a detector which is laterally displaced from the laser. A lens focuses the reflected light onto the detector which reveals the direction of the incoming light, thus providing the angle between the laser beam and the returning light and therefore the distance to the target under interrogation. This approach can be limited by the amount of reflected light over long distances. As the fundamental process is angle measurement, the range accuracy deteriorates with increasing range.

The time of flight approach involves transmitting an optical pulse and accurately measuring the round trip time for a reflected portion of the pulse to return to the source, hence providing a round trip distance. The time-of-flight method is typically used for measuring large distances. For example the distance between the Earth and the moon has been measured with this technique to an accuracy of a few centimetres. Typical accuracies of simple arrangements over short distances are a few millimetres due to the 10's of ps timing error on the pulse capture^[2]; more advanced arrangements employing time correlated single photon counting techniques (TCSPC) to increase the measurement count can achieve accuracies of $\sim 10 \mu\text{m}$ ^[3], see below. In a repetitively pulsed system, the maximum range that can be unambiguously determined is limited by the period between pulses. Therefore, if the period corresponding to the required measurement update rate is higher than the round trip time, the range ambiguities must be resolved in some other fashion (such as by varying the repetition rate). Unlike the triangulation techniques, the range resolution does not necessarily depend on the absolute range. Instead, the accuracy of a range measurement depends on the duration

3. Optical metrology using tuneable optical pulses

of the optical pulse, the speed of the timing circuitry and the signal-to-noise ratio (SNR).

Time Correlated Single Photon Counting (TCSPC), is a statistical sampling technique where the time of arrival of a train of individual photons is logged with high precision. Each measurement of arrival time corresponds to an independent range measurement; therefore, the precision improves with increased sample number according to $N^{1/2}$, where N is the number of photons (counts). The intrinsic temporal precision is determined by the duration of the laser pulses and the detector and counting circuit response times. For example, if the intrinsic response time of the detector is 50 ps, which results in a 7.5 mm range uncertainty, the range precision can be reduced by a factor of 10^{-3} (i.e. reduced to 7.5 microns) after 1 second of counting with a count rate of 10^6 Hz. As the name implies, TCSPC offers the ultimate in sensitivity since it measures discrete photons, however the count rate is limited by technological issues. In particular, the typical recovery time of current detectors limits the maximum count rate to ~ 10 MHz^[3]. It is therefore unlikely that TCSPC can solely be used to provide the sub-micron accuracies required for some formation flying missions.

A variant of the time of flight approach is to periodically modulate a cw (continuous wave) optical source and compare the return signal with a portion of the outgoing signal. This technique transfers the measurement from the time domain to the frequency domain. The phase relationship between the outgoing and the return signal is used to determine the range. Some range ambiguity may remain, as it may not be possible to determine how many multiples of the periodic signal span the unknown range, particularly for rapidly changing ranges. The range resolution is limited by the accuracy of the phase measurement and may be improved by using high modulation frequencies at the expense of reducing the range of unambiguous measurements.

The ultimate in range resolution is achieved by the use of an optical interferometer, which utilises the effect of interference to realise high accuracy optical metrology. This may be regarded as an extension of the modulation scheme described above to the highest possible modulation frequency. In order to perform distance measurement, a laser is split into two beams, with one beam travelling the return path to and from the unknown target. The second beam is reflected through a very stable reference distance.

3. Optical metrology using tuneable optical pulses

When the beams are recombined, interference fringes are observed as the optical path difference between the two arms varies by distances on the order of the optical wavelength. Basic interferometer configurations suffer from the drawback that, although the **change** in distance to the target may be determined to within a fraction of a wavelength, the order of interference may be very large and the **absolute** distance remains ambiguous as it is impossible to determine how many multiple integers of the wavelength span the round trip distance to the unknown target. The dual wavelength interferometry approach, as employed by the High Precision Optical Metrology (HPOM) system^[2], can be used to extend the ambiguity range of an interferometer by generating a synthetic wavelength related to the beat frequency between the two lasers. For a 3 GHz beat frequency the ambiguous range can be extended from the optical wavelength of around 1 micron, to the synthetic wavelength of 100 millimetres. In practice, a range measurement within the unambiguous synthetic wavelength band is usually capable of achieving 100 – 1000 ppm accuracy, resulting in an accuracy of order 10 – 100 microns^[2]. By generating a synthetic wavelength, the upper measurement limit of the HPOM system is then compatible with the handover from the initial RF range finding to the optical metrology stage.

Using the techniques introduced in this section, optical metrology can be extremely precise and is ultimately limited by a combination of frequency source drift and instabilities, optical spontaneous emission and laser noise, thermal drift of optical cavities and reference lengths, and environmental vibration leading to timing variations.

3.3 Scanning Interferometer Pulse Overlap Detection (SIPOD)

This section provides an overview of the SIPOD system and explains the requirement for a highly stable pulse source possessing a tuneable repetition rate. A full mathematical analysis of the SIPOD operation is given in Chapter 8 and is omitted from this introductory chapter.

A highly promising technique which has been investigated at QinetiQ to assess its suitability for meeting the ESA requirements is a novel technique named Scanning Interferometer Pulse Overlap Detection (SIPOD). This approach utilises the electronically tuneable nature of the highly stable optical pulse source, originally

3. Optical metrology using tuneable optical pulses

developed for performing high bandwidth opto-electronic sampling of military radar signals. This pulse source offers a novel approach to metrology, based on the fact that the repetition rate of the pulses can be electronically varied (by tuning the ultra-stable oscillator) to provide a precisely known repetition rate of highly stable optical pulses. This approach is not feasible with traditional pulsed laser sources such as Q-switched lasers and mode-locked lasers (see the review of optical pulse sources in Appendix A) which do not generally offer tuneable repetition rates at known frequencies in a robust package.

In SIPOD, the pulse repetition rate is varied to find the frequency which allows the return pulses from the outlying satellite to *exactly* overlap, and hence interfere, with pulses propagating through a stable reference length on the source satellite, Fig. 3.2. As the optical pulse rate is electronically scanned, two separate frequencies providing the overlapping condition provide unambiguous coarse range finding over a range of up to many kilometres, limited only by the oscillator frequency resolution and stability and the laser coherence length. The frequency spacing, Δf , of adjacent frequencies satisfying the overlapping (constructively interfering) pulse condition range indicates the unknown round trip distance (e.g. $\Delta f = 6 \text{ MHz} \rightarrow 50 \text{ metres round trip}$, $\Delta f = 0.6 \text{ MHz} \rightarrow 500 \text{ metres round trip}$). Once the overlapping pulse technique has established the coarse range (~ 100 's of microns), the range estimate can be refined by interpolation within the pulse envelope. Finally, the optical carrier underneath the pulse envelope could be used to perform fringe tracking to sub-wavelength accuracy using the same source arrangement. In this way, the SIPOD system offers unambiguous optical metrology over ranges limited only by the coherence length of the laser and the oscillator stability, to accuracies of 10 's of microns or better. The SIPOD system has been filed as a patent, GB0715368.7^[4].

3. Optical metrology using tuneable optical pulses

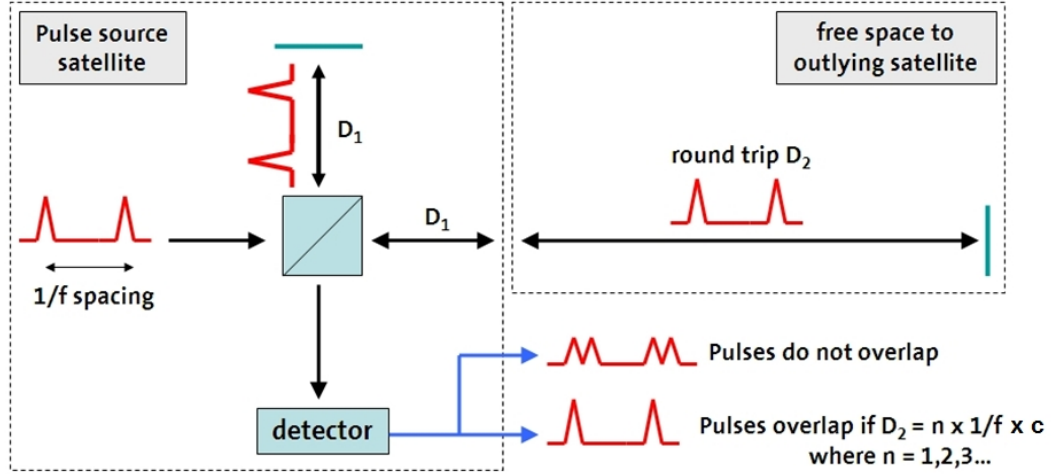


Fig. 3.2. For the correct optical pulse repetition rate, f , the return pulses from the unknown satellite outlier can be made to overlap and hence interfere with a second set of pulses generated by the same optical source. By scanning the frequency to find two separate pulse repetition rates which provide the overlapping condition, the coarse longitudinal range can be determined unambiguously over many hundreds of metres. The optical carrier underneath the pulse envelope can then be used to perform wavelength accuracy interferometry.

3.4 SIPOD system architecture

A proposed implementation of the optical metrology system based on the tuneable pulse compression scheme is shown in Fig. 3.3. The stability of the whole system could be governed by a frequency standard; Perkin Elmer's RFS-IIF space qualified rubidium clock at 6.834 GHz has been identified as a possible commercially available option^[5], with a quoted stability of 3×10^{-12} over one second, although other commercial frequency standard options exist in addition to those offered by Perkin Elmer. For a practical breadboard demonstrator, a low phase noise, high stability signal generator source with a microwave frequency output will be acceptable, at the expense of lower long-term stability.

The optical pulses are generated, as will be described in Chapter 4 (in particular Section 4.2.3), and then propagated along the return path from the outlying satellite. The pulse repetition rate is then scanned until the return pulses overlap and therefore interfere with a set of reference pulses. The overlapping condition is detected by the following method; two phase shifters are used to balance the arms of the optical interferometer, with one or both arms being modulated. When the pulses from the two arms of the

3. Optical metrology using tuneable optical pulses

interferometer interfere at the detector, the detector signal will be modulated at the drive frequency (2-5 MHz in Fig. 3.3). To find the range, the pulse repetition rate is scanned to find the peak output of the lock-in amplifier. The frequency separation of adjacent maxima gives an approximate range; the absolute repetition rate frequency gives an accurate range.

The majority of the electronic functions required to implement optical metrology using the pulse compression scheme could be integrated onto a single field programmable gate array (FPGA) arrangement. This would include a direct digital synthesiser which, together with the reference clock and a single-sideband mixer, would set the tuneable microwave frequency which drives the optical amplitude modulator and hence generates the optical pulse train. A tuning range of less than 10 MHz is required at a frequency offset from the reference clock to cover the 500 metre hub to outlying satellite range for ESA's PROBA-3 mission. FPGA manufacturer Xilinx supply a commercially available direct digital synthesiser (DDS) core for use with their FPGA boards, providing 0.02 Hz tuning resolution and 108 dB spurious free dynamic range (SFDR). Although not necessarily required for this programme, a 6.834 GHz rubidium standard could be used to provide a precise reference clock, accurate to $\sim 3 \times 10^{-12}$.

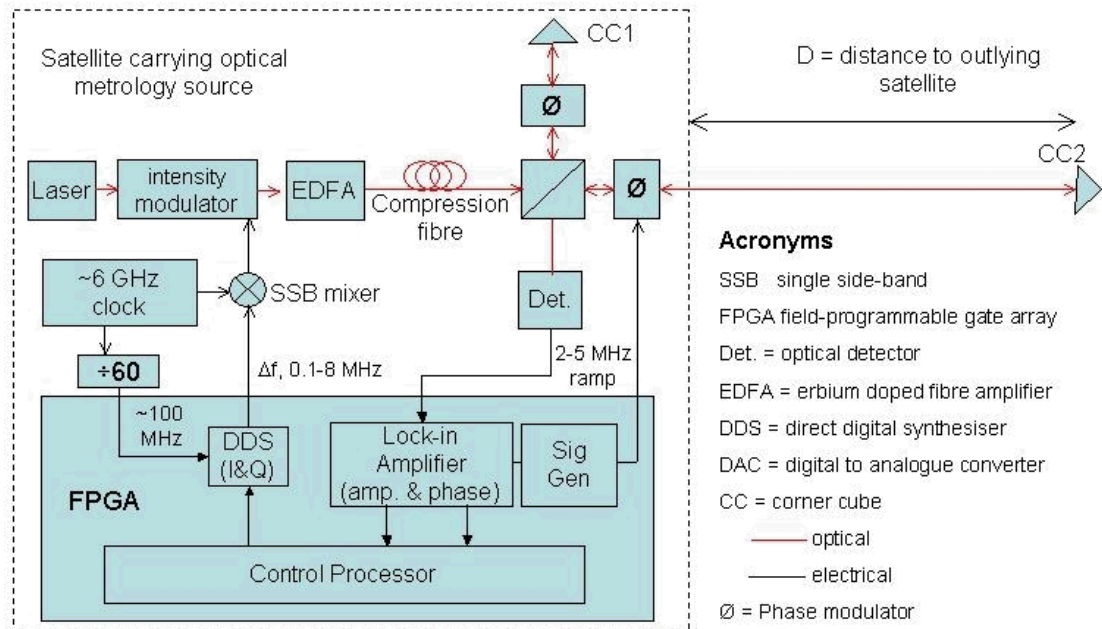


Fig. 3.3. FPGA version of the optical metrology system based on a tuneable pulse compression source. Current FPGAs can perform the DDS, lock-in amplifier and signal generator functions all on one custom board.

Although the system could be designed and built using a space-qualified FPGA, the breadboard implementation has been designed and implemented using discrete components due to reduced cost and lead time. The design and implementation is discussed in Chapters 8 and 9 of this report. In the most compact implementation, a single FPGA would be responsible for the DDS function, the lock-in amplifier and a digital to analogue converter (DAC). The DAC will provide a ramp function to drive the optical phase modulator through a 2π phase shift. The photo-detector signal has a complex spectrum, consisting of the fundamental and harmonics of the ramp frequency. When the total phase excursion is $2\pi N$ radians, most of the interference pattern is concentrated in the N th harmonic^[6], i.e. 2 MHz in the 2π case shown in Fig. 3.4.

Bandpass filtering around the chosen harmonic then produces a strong carrier which is free of the higher harmonics associated with the ramp flyback. The instantaneous phase of the carrier is equivalent to the optical phase between the arms of the interferometer. Random and signal induced optical phase shifts directly phase modulate the carrier. The final recovery of the signal is achieved using conventional FM or PM demodulation techniques. One key advantage of this proposed technique is that, although the interference effects only occur when an overlap of the pulses occurs, the detector bandwidth need only be dimensioned to correspond to the rate of change of phase. This allows the detectors to be larger in area, allowing better light gathering and SNR characteristics. The high precision, short duration pulses allow high accuracy range-finding, due to the well defined overlap characteristics, but the system only requires to perform low bandwidth detection of the resultant carrier amplitude.

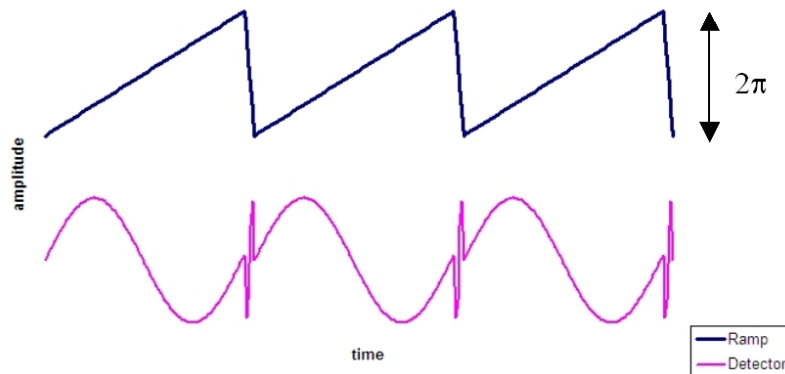


Fig. 3.4. A phase ramp of amplitude 2π radians produces a “phase generated carrier” at the output of the interferometer.

3. Optical metrology using tuneable optical pulses

In summary, the highly stable optical pulses initially developed to perform optical sampling for the first time with a compression source have also been used as the pulse source for a novel optical metrology system. This metrology technique has been filed as a patent. A more detailed investigation of the theoretical and experimental SIPOD system performance is detailed later in this report in Chapters 8 and 9.

References for Chapter 3

1. "PROBA-3: Formation Flying Technologies", European Space Agency, British National Space Council Workshop at RCDS:- Technologies for Satellite formation Flying: Opportunities for the UK, 23 February 2006
Retrieved on 10/02/2008 from:
[http://www.bnsc.gov.uk/assets/channels/resources/formation_flying/Paper 11 - ESA.ppt](http://www.bnsc.gov.uk/assets/channels/resources/formation_flying/Paper_11_-_ESA.ppt)
2. Haupt C., Kudiella K.H., Fischer E., and Johann U., "High-precision optical metrology system for the SMART-2 mission as precursor for the DARWIN satellite constellation", Proc. SPIE Interferometry XI: Techniques and Analysis 4777, 143 (2002)
3. Buckley S.J., Bellis S. J., Rosinger P., and Jackson J. C., "Fully integrated sub 100ps photon counting platform", Proc. SPIE Ultrafast Phenomena in Semiconductors and Nanostructure Materials XI and Semiconductor Photodetectors IV, 647116 (2007)
4. Lewin A.C., McDonald G.J., and Orchard D.A., "Range-Finding Method and Apparatus", GB patent number 0715368.7, filed 7th August 2007
5. Perkin Elmer's space qualified rubidium clock datasheet, product ID: RFS-IIF, retrieved on 10/10/2008 from Perkin Elmer's website:
<http://optoelectronics.perkinelmer.com/catalog/Product.aspx?ProductID=RFS-IIF>
6. Kersey A.D., Lewin A.C., and Jackson D.A., "Two wide-dynamic range signal-recovery schemes for the fiber-optic gyroscope," Proc. Instr. Elec. Eng, vol. 132, pp. 271-276, Oct. 1985.

4. Soliton and soliton-effect pulse compression

As part of a UK Ministry of Defence funded photonic ADC programme, an optical sampling source based on soliton-compression of a repetitive waveform was developed, with the aim of producing high repetition rate pulses with timing jitter values rivalling those of other methods of generating short duration optical pulses, such as gain-switched, Q-switched and mode-locked lasers. Before modelling and constructing such a compression scheme, based on a modulator driven with a single frequency from a microwave synthesiser, a literature survey was undertaken to determine if this technique had been previously demonstrated elsewhere. In particular, the literature study revealed that there does not appear to have been any detailed timing jitter analysis performed on a soliton-compression scheme before.

4.1 Introduction to theory

When a short intense pulse travels through a fibre, its duration and shape can be altered by non-linear effects and group velocity dispersion (GVD), Fig. 4.1.

An important mechanism which acts on short pulses with high peak intensities is the phenomenon known as self-phase modulation (SPM), which occurs due to the non-linear response of the fibre's refractive index [$n = n_0 + n_2 I(t)$]. The higher intensity regions of the pulse see a different refractive index than the rest of the pulse, and hence an instantaneous frequency shift occurs, down-shifting the frequency of the leading edge of the pulse and up-shifting its trailing edge.

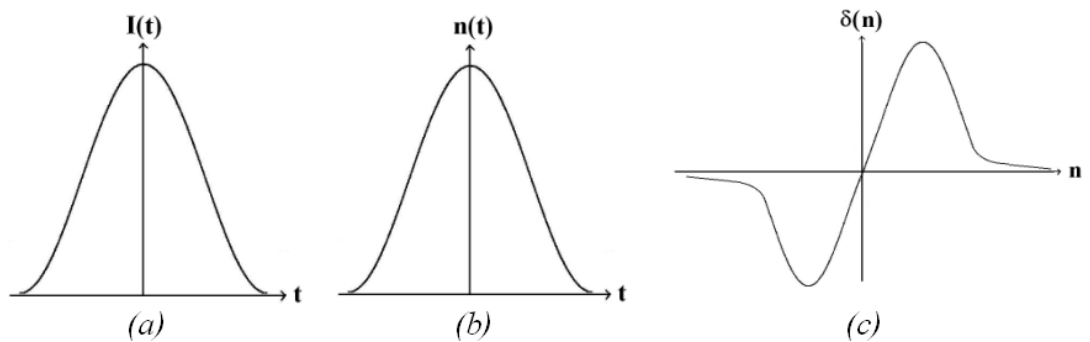


Fig. 4.1 (a) the pulse intensity with time, (b) refractive index variation across the pulse, (c) the corresponding instantaneous phase shift

When the optical wavelength corresponds to the anomalous region of the fibre (>1300 nm for standard telecommunications fibre), the pulse experiences negative dispersion, with the result that the duration of the pulse decreases since the leading edge of the pulse travels at a slower velocity than the trailing edge. This compression effect can be exaggerated by the self phase modulation downshifting the leading edge of the pulse, Fig. 4.2.

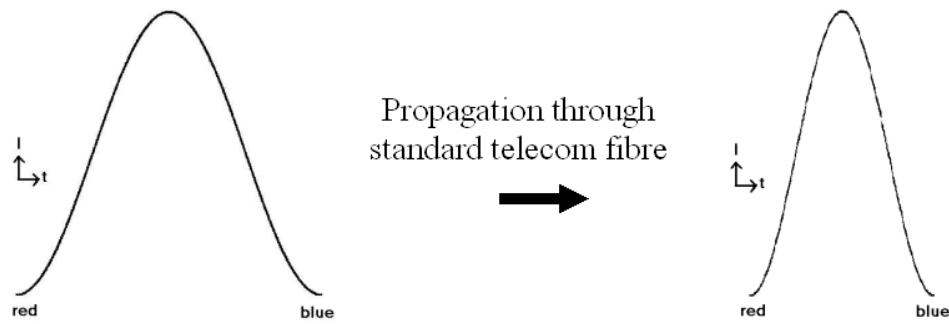


Fig. 4.2. Negative group velocity dispersion leading to pulse shortening

A special type of pulse known as a soliton can exist when the dispersion balances the non-linear effect and in theory these pulses can travel “forever” with constant duration (assuming a loss-less fibre). In practise, these soliton pulses can travel long distances undistorted and remain unaffected after collisions with other solitons. They were first described by John Scott Russell, who observed a wave propagating from a canal boat’s bow and then travelling with constant amplitude and speed (at a horse’s gallop) along a Glasgow canal in the 19th century. The first publication reporting the observation of solitons in optical fibre was by Kruskal in the 1960’s^[1].

A pulse compression technique known as soliton compression relies on the fact that for optical solitons, a small variation in the dispersion has a similar perturbative effect as an amplification or loss. The dispersion variation upsets the equilibrium between the dispersion and nonlinearity and so the soliton pulse length varies. Therefore, under the correct conditions the pulse can be compressed as the dispersion decreases and vice versa^[2]. In practise the pulse compression is often not an adiabatic process since the pulse energy is not maintained due to the methods employed to implement the compression, and in this case the process is referred to as soliton-effect compression.

Dispersion decreasing fibres (DDF's) have been recognised as being very useful for high-quality, stable, polarisation-insensitive, adiabatic soliton pulse compression and soliton train generation^[3]. The basis for the DDF operation is that the waveguide's contribution to the group velocity dispersion parameter depends on the core size. In a DDF, the dispersion is smoothly decreased monotonically from an initial core diameter to a smaller final value at the end of the fibre. This is achieved during manufacture through careful drawing of the fibre so that the core diameter is gradually tapered. Hence, as the pulse travels through the fibre it encounters a gradually decreasing core diameter and so the pulse shortens.

If the dispersion variation in the DDF is sufficiently gradual then the soliton compression can be an adiabatic process, whereby an input fundamental soliton can be ideally compressed as it propagates, thus conserving its soliton character and energy. If the process is not adiabatic (i.e. if the pulse energy is not maintained) then the process is referred to as soliton-effect compression. There are many papers which deal with considerations regarding higher order effects^[4] and in addition the behaviour of different pulse shapes, such as hyperbolic secant and Gaussian for example^[5].

Since DDF is not in widespread use, by the telecommunications industry for example, its manufacturing involves a custom process which can be costly, and so an alternative and more economic approach is to approximate dispersion decreasing fibre with a comb-like dispersion profiled fibre (CDPF)^[6]. Basically two different types of fibre are alternated in a CDPF compressor, alternating between high and low dispersion fibre. The effects of fibre non-linearity and dispersion are effectively spatially separated with dispersion dominating in the high dispersion fibre and nonlinearity dominating in the low dispersion segments. In practise a CDPF can be constructed for use at 1.55 μm using alternating lengths of standard telecommunications fibre (high dispersion), and dispersion shifted fibre (DSF) (low dispersion). These alternating sections are then spliced together to form the CDPF.

Soliton-effect compression can achieve high compression factors using short fibre lengths. Compression of 3.6 ps DFB gain switched laser pulses down to 185 fs by propagation through only 30 metres of fibre has been achieved using soliton-effect

compression^[7]. In this case the required input peak power was very high at around 50W (with an average power $\sim 50\text{mW}$) to compress the 100 MHz repetition rate gain switched pulses. As this example illustrates, one drawback with soliton-compression is that the required input powers can be high, too high to be obtained directly from a semiconductor laser, thus large optical amplification is required, increasing system complexity and power requirements. Another, significant, disadvantage with this technique is that it often produces a poor quality of compressed pulse, since a substantial proportion of the pulse energy can be contained in a broad pedestal rather than in the compressed central peak. For example, for pulse compression factors of 60, up to 80% of the pulse energy can be contained in the pedestal component^[8].

In general there is a trade-off between compression factors and the pulse quality. Adiabatic compression, the alternative technique for generating short soliton pulses, achieves virtually pedestal free pulses of less than 200 fs duration using DDF^[9,10]. For adiabatic compression the maximum compression factor is determined by the ratio of the input to output dispersion. The benefits of this technique are the possibility of very high quality pulse compression and the significantly lower input power required (100's of mWs). The drawback however is that the maximum compression factor is typically limited to about 20 and also the fibre length required for compression of pulses of initial length 5 ps or more can be long (a few kilometres). Incidentally, as the required length of DDF increases it becomes increasingly attractive to use comb-like fibre to approximate the DDF due to the difficulties in manufacturing the DDF (and the cost of a custom production fibre draw, as mentioned previously).

4.2 Practical implementation of a soliton compression scheme

The fundamental idea is to generate a periodic optical signal and use the non-linear propagation of the fibre to generate compressed optical pulse trains. Input waveform options include pulsed lasers, the beat frequency of two lasers or a modulator generated periodic waveform.

4.2.1 Pulsed lasers

The timing jitter performance and implementation method of low jitter mode-locked, gain-switched and Q-switched lasers are discussed in some detail in Appendix A. If very short pulse durations are desired then many of the pulsed lasers outlined in Appendix A could benefit from soliton or soliton-effect pulse compression techniques, for example gain switched lasers with pulses of around 20 ps. Pulses as short as 20 fs have been generated using multi-stage fibre compression schemes and gain switched pulses^[11].

4.2.2 Beat frequency from two laser sources

By beating together two very stable laser sources and propagating the result through the correct combination of fibres, it is possible to convert the input beat frequency into a series of short, high repetition rate pulses, Fig. 4.3. The benefit of the two-laser source is that it allows the generation of very high repetition rate sources without the need for high frequency electronics. Some authors report that a disadvantage with this method is that the technique is limited by the timing jitter that arises from the relative frequency noise between the two lasers. This however can be overcome using an optical injection phase lock loop (OIPLL) as developed at UCL^[12], whereby a very pure single frequency source is obtained. The laser beat frequency itself can be sub-GHz, such as the 600 MHz implementation reported by QinetiQ^[13]. Therefore, soliton compression of the beat frequency of two stabilised lasers promises to be a low jitter method of generating optical pulse trains with repetition rates ranging from hundreds of MHz to hundreds of GHz.

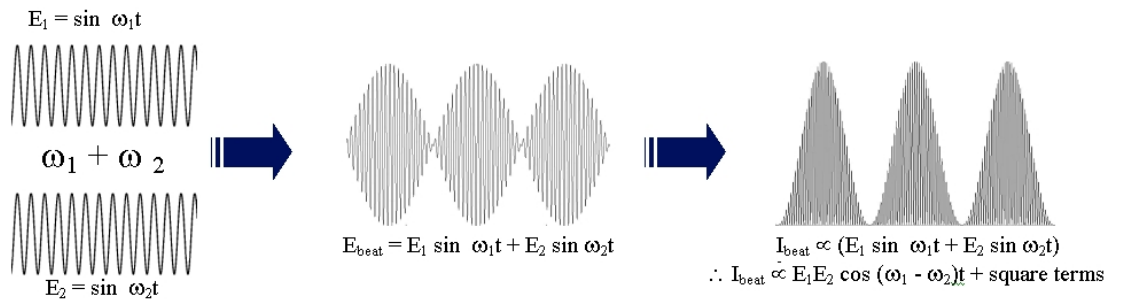


Fig 4.3. Generating a beat frequency using two stable lasers.

Mathematically, the beat field is given by:

$$E_{\text{beat}} = E_1 \sin \omega_1 t + E_2 \sin \omega_2 t \quad (4.1)$$

With the beat envelope given by:

$$E_{\text{env}} = 2E_1 \sin\left[\frac{1}{2}(\omega_1 - \omega_2)t\right] \quad (\text{with } E_1 = E_2) \quad (4.2)$$

4.2.3 Periodic waveform generated using a modulator

Fig. 4.4 demonstrates the generic set-up to generate a repetitive input by driving a modulator with a single frequency, f_c , from a microwave source. The maximum possible repetition rates here are lower than that for the beat frequency set-up, limited by the maximum output frequency of the signal generator and/or the modulator bandwidth. Also, it is expected that as the microwave source frequency increases, so will the jitter as the microwave source approaches its performance limit. Note that the beat frequency approach in Section 4.2.2 also demonstrates increasing phase noise as the beat frequency increases, since an OIPLL also requires a microwave source.

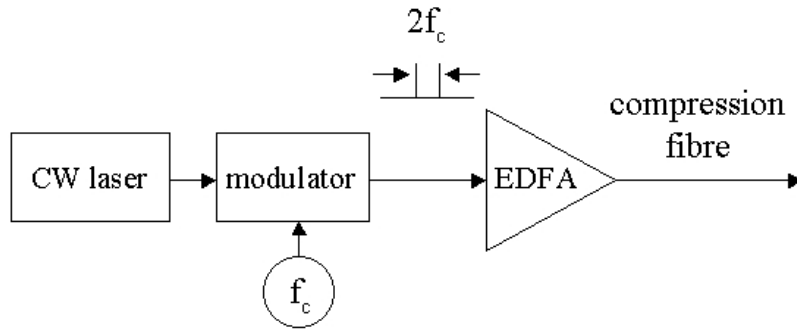


Fig. 4.4. Modulator biased-at-null set-up, generating a pulse train source at twice the microwave source frequency f_c .

The modulator should be biased at extinction and driven with a sinusoid at half the required sampling rate. In this case, the field is given by:

$$E_{\text{out}} = \frac{1}{2} E_{\text{in}} (1 + e^{i\Delta\phi}), \text{ where } \Delta\phi = \text{peak phase modulation} \quad (4.3)$$

$$\text{giving, } I_{out} = I_{in} \left[\frac{1 + J_0(\Delta\phi)}{2} + \sum_{n=1}^{\infty} J_{2n}(\Delta\phi) \cos(2n\pi f_c t) \right] \quad (4.4)$$

Eq. 4.4 does not appear to have been published in the literature regarding modulator based compression schemes, and seems to have first been introduced to this subject in Ref. [14] (see Appendix E for derivation). Fig. 4.5 visually depicts the modelled and experimental fields described by Eq. 4.4.

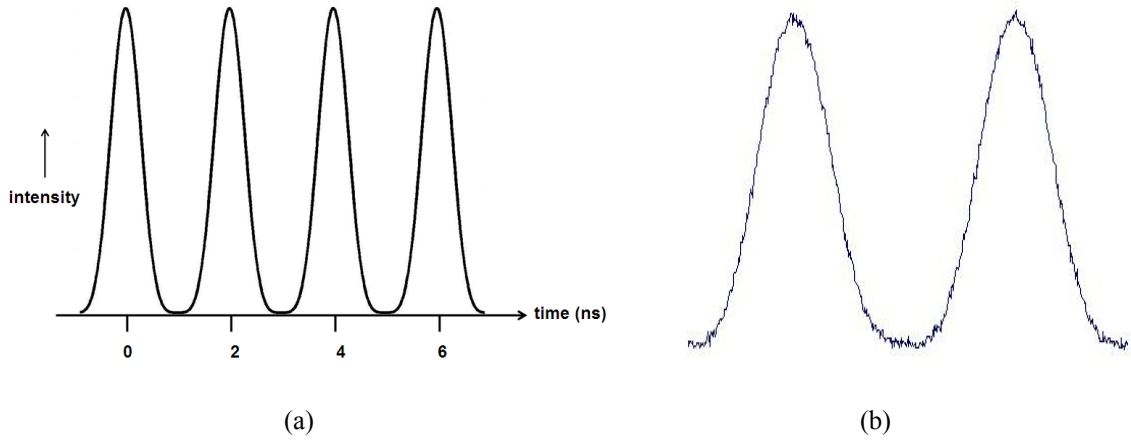


Fig 4.5. The modulator intensity output, (a) modelled, (b) experimentally.

It is this modulator based approach to pulse compression which has been modelled and demonstrated experimentally at QinetiQ, with the aim of creating a pulse source with timing jitter limited by that of the microwave drive electronics. This new pulse source was initially developed to provide the sampling stream for the QinetiQ photonic ADC programme, before it was also developed and integrated for use as the pulse source for a novel optical metrology system under the European Space Agency PROBA-3 micro-satellite mission programme.

The later chapters of this thesis detail the modelling, experimental implementation and characterisation of the compression source and its subsequent use for the first time to perform two very different functions in two separate programmes: optical sampling and optical range finding. However, before commencing the modelling and experimental work, it was necessary to investigate the wider literature to establish whether or not the compression of the modulator biased-at-null approach, had been attempted before. Two authors in particular are prominent in this field of soliton-effect compression:

Chernikov, of the General Physics Institute in Moscow, and Eric Swanson, from MIT. After the survey, detailed in the remainder of this chapter, it did not appear that the modulator-at-null compression technique has been implemented before using a LiNbO_3 modulator to generate pulses at <10 GHz repetition rates, and that no compression source had been characterised in any detail, particularly not in terms of the timing jitter performance. The following papers however have similarities to the proposed scheme and are of interest in terms of compression fibre arrangements, pulse peak input powers and pulse pedestal implications.

4.3 Survey of published pulse compression schemes

Compression of laser beat frequencies

Swanson and Chinn reported the laser beat frequency technique in 1994^[15], with pulse compression achieved through 6.45 km of standard single-mode telecommunications fibre (Corning SMF-28) for a 23 GHz beat frequency. A beat frequency of 123 GHz was also compressed, this time using 5 km of commercially available dispersion shifted fibre (DSF).

The two CW lasers (linewidths ~ 100 kHz) are combined in a 50/50 coupler and passed through a single polarisation isolator to ensure the alignment of their polarisation and to balance their powers. A LiNbO_3 phase modulator is used to spectrally broaden the signal and increase the stimulated Brillouin scattering threshold – since this is applied to both laser fields there is no additional phase shift applied. A phase modulation of 100 MHz was applied at $\pm\pi$. No timing jitter analysis of the 1.3 ps duration output pulses was performed.

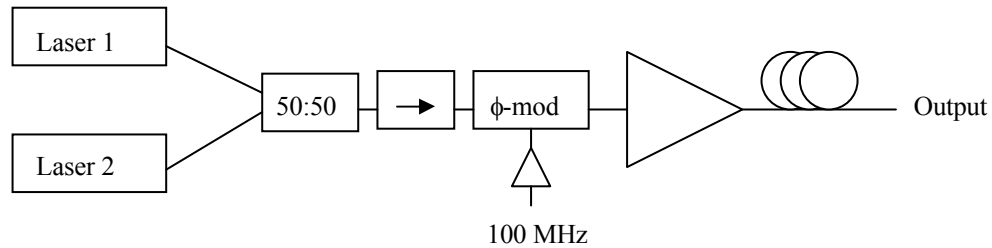


Fig.4.6. Beat frequency approach.

Avoiding two source timing jitter

To avoid the timing jitter that arises from the relative frequency noise between the two lasers, an alternative is to modulate a single source to create two optical carriers which then create a beat frequency. The use of a single laser source and an external phase modulator has the potential of very low timing jitter since the two sidebands share a common frequency noise.

Swanson et al.^[16] generated a 100 GHz near-transform-limited pulse train using this approach. They modulated the drive current of the laser (a DFB) to broaden its linewidth to ~ 200 MHz to overcome stimulated Brillouin scattering (SBS). The output from this laser was then modulated at 16.9 GHz and then amplified by an erbium doped fibre amplifier (EDFA), Fig. 4.7. After propagation through 9 km of DSF, the pulses were compressed to 1.37 ps using an input power of 33 mW per carrier.

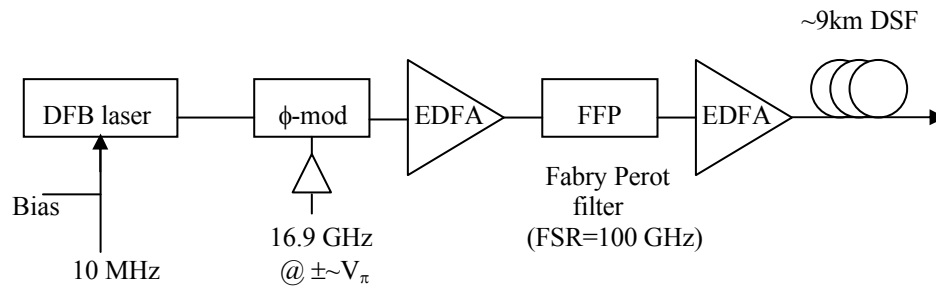


Fig.4.7. Beat frequency using sidebands of same source to avoid two source jitter.

Another variation is to generate the beat frequency using a single coupled cavity, for example using a single coupled erbium fibre laser^[17]. The source in Ref. [17] provides a dual frequency beat signal at 1545 nm with a selected frequency separation of $\nu=59.1$ GHz. The average linewidth was ~ 16 kHz, with the stability of the frequency separation $\Delta\nu=3$ MHz (limited by the measuring instrument). The resulting phase noise parameter $\Delta\nu/\nu$ characterising the relative fluctuations of the beat signal period is less than 5×10^{-5} . In this example, a train of pulses at 59.1 GHz is generated with widths of 2.2 ps, with no obvious pedestals. No more detailed timing jitter analysis was given other than stating the beat frequency phase noise parameter. The launch power into the compression fibre was 190 mW. A major drawback however with this approach is that the laser is free-running, so the pulse repetition rate is not controllable, and hence the

set-up simply settles to an arbitrary rate. Also, the coupled cavity is temperature dependent and requires polarisation control, which is not ideal for a practical system to be deployed in a military or space environment.

Comb-like dispersion-profile fibre (CDPF) for pulse compression

Chernikov et al.^[18] avoid the manufacturing problems associated with dispersion decreasing fibre (DDF) by using comb-like dispersion-profiled (CDPF) fibre, based on alternating standard telecom fibre and dispersion shifted fibre. The result is a simple comb involving 6 fibre segments. By propagating a laser beat frequency through the comb, Fig. 4.8, they obtained a 100 GHz repetition rate series of pulses as short as 670 fs for 800 mW launch power, and 505 fs for 400 mW (no pedestals were observed on the autocorrelation traces).

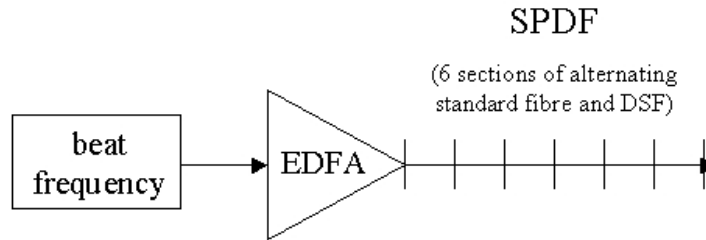


Fig. 4.8. Alternating lengths of standard fibre and dispersion shifted fibre (DSF) to simulate dispersion decreasing fibres (DDF). Specific lengths were not given.

To maintain adiabatic pulse shaping, without adding any background or pedestal artefacts, they state that the ratio of the dispersion at each fibre interface should be less than around 1.5.

Shipulin et al.^[19], modelled a two-section fibre set-up involving dispersion increasing fibre (DIF) followed by a dispersion decreasing fibre (DDF), since they argue that DDF alone is not practical for compressing beat frequencies as low as 10's of GHz. They state that for repetition rates of less than 50 GHz, a length of over 10 km of DDF is required. As discussed, such long lengths of DDF are difficult and expensive to source, and therefore a section of DIF is used before the DDF to create high quality compressed pulses with a residual SPM, ideal for further compression in the DDF. They suggest that

this approach brings the total fibre length down to around a more realistic 5 km for 40 GHz repetition rates.

Pedestal elimination

As pulses become narrower after compression, higher order effects such as stimulated Raman scattering (SRS) and third-order dispersion (β_3) become more important. There is a trade-off associated with trying to overcome SRS using dispersion shifted fibres, since the SRS depends on the soliton power levels which are related to the fibre dispersion, however this is at the expense of increased third order effects.

It has been suggested that the pedestals which can occur for some compression arrangements could be eliminated by performing the soliton-effect compression whilst intensity discrimination occurs in the fibre^[20]. The technique involves the manipulation of the fibre birefringence, achieved with a polarisor, a polarisation controller and a wave-plate. The intensity discrimination occurs depending on the polarisation state of the light in the fibre, the aim being to optimise the effects of β_3 while keeping the power requirements at reasonably low levels.

Due to intensity dependent non-linear birefringence, the pedestal and the peak experience different phase shifts and hence will have different phase shifts at the fibre output. With subsequent manipulation the peak and pedestal can be separated with the help of a polariser and wave-plate.

The fibre can be optimised for this application by choosing a sufficiently high value of intensity dependent birefringence. Analysis demonstrates that the optimised fibre should also possess an optimal value of GVD so that the detrimental effects of β_3 and stimulated Raman scattering (SRS) can be minimised. Alternatively, dispersion flattened fibre can be used to optimise the GVD value.

Although this technique has demonstrated pulses as short as 185 fs without any discernable pedestal present on the autocorrelation trace, this technique would appear to be very experimentally sensitive. Along with another pedestal removal technique, fibre

loop mirrors^[21], this environmental sensitivity would appear to discount the technique for use in harsh military and space environments. It is far more preferable to avoid the generation of pedestals in the first place by using adiabatic compression techniques.

Frequency tuneable pulse generation using an electro-absorption modulator

The electroabsorption modulator (EAM) provides a compact method of generating picosecond optical pulses around 1.55 μm , with a repetition rate continuously tuneable to as high as around 40 GHz, with potentially ultra-low timing jitter.

Usually the shortest pulse obtainable from an EAM is greater than 10 ps. Methods for generating pulses of a few picoseconds duration at high frequencies from an EAM include either a very large modulation extinction frequency, extremely large bias and modulation voltages, and/or chirp compensation. All of these methods are undesirable and it is preferable to generate longer duration pulses if at all possible (>20 ps).

However, in order to generate adiabatic soliton pulse compression, the initial pulse width should be only a few picoseconds at most to ensure a slow dispersion decreasing rate relative to the DDF length. As mentioned previously, in terms of manufacturing, it is practical to keep the length of the DDF short.

Instead a method to generate a soliton pulse train has been successfully achieved using pulses as broad as 30 ps from an EAM, followed by standard fibre and DDF^[22]. The idea here is that 2 km of standard telecommunications fibre (STF) is used to perform an initial compression of the EAM pulses, from 20-30 ps to around 2 ps, before the pulses then propagate through 250 metres of DDF, which performs adiabatic compression down to 130-140 fs with no obvious pedestal creation, Fig. 4.9. Peak powers are large, of the order of 1.5 Watts for the tuneable repetition rate range of 6.67 GHz to 18 GHz. The input to the EAM is phase modulated at 100 MHz to overcome stimulated Brillouin scattering (SBS).

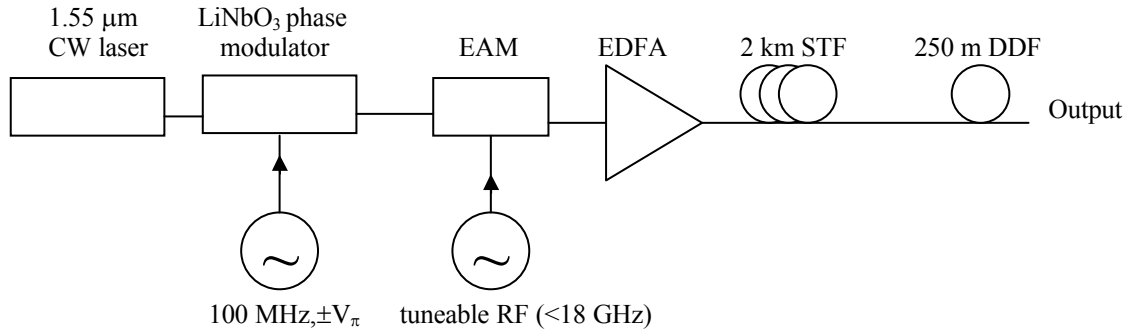


Fig. 4.9. Compression of an electro-absorption modulator output.

Chernikov's group have published a variation on this EAM set-up, using 1 km of standard fibre followed by 1.6 km of DDF fibre^[23], quoting pulses as short as 189 fs.

Frequency tuneable pulse generation using a Mach-Zehnder modulator

Swanson et al.^[24], describe the approach discussed in the introduction to this chapter, whereby a Mach-Zehnder modulator is biased at null (or a peak) and driven with a sinusoidal waveform, Fig. 4.10. They then compress the resultant waveform using either comb-like dispersion fibre or standard telecommunications fibre, depending on the repetition rate of the modulator output train (40 GHz for the CLDF and 20 GHz through the STF). The laser was directly phase modulated at 50 MHz to overcome SBS. An undesirable detail of their set-up is the use of two stages of optical amplification. Presumably this could be overcome by the use of lower loss components and a higher output EDFA (>5 Watt optical output EDFAs are now commercially available). Whilst they state that this should be a low jitter approach to pulse generation, they do not characterise the jitter.

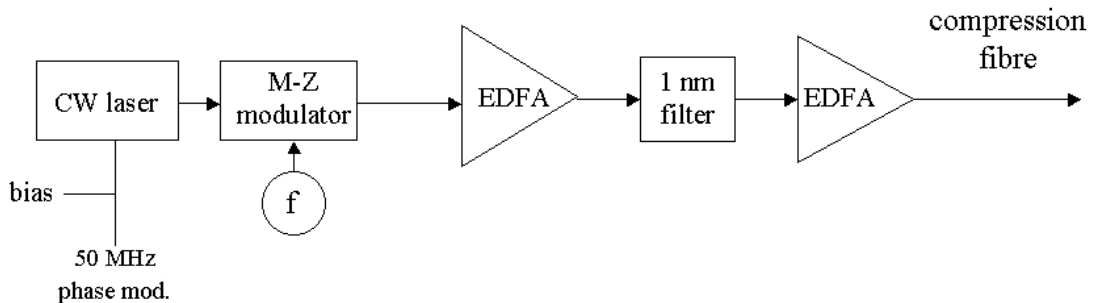


Fig. 4.10. Modulator biased-at-null output compressed.

4.4 Pulse compression jitter implications

While many papers state that their various compression schemes inherently possess low jitter, only Tamura and Nakazawa appear to actually measure this property^[25]. They performed a theoretical analysis of soliton jitter due to compression in dispersion decreasing fibre (DDF), which argues that Gordon-Haus jitter is applicable to these schemes. Since high powers are required, EDFAs are usually employed at some point before the DDF, and so a level of amplified spontaneous emission is present. This additive noise perturbs the centre frequency of the soliton which translates into timing shifts (or jitter) through the dispersion in the fibre (Gordon-Haus jitter). They apply soliton perturbation theory to generate a model for this process which is then verified with 3.5 ps modelocked pulses at 10 GHz, which are compressed through the DDF after amplification by an EDFA and filtering through a 10 nm filter. By predicting timing jitter using an autocorrelator approach, they found that the timing jitter of the modelocked laser is <100 fs whereas the Gordon-Haus jitter adds between 300-700 fs of timing jitter for high power soliton pulses travelling through DDF. The total Gordon-Haus jitter is related to the total dispersion of the set-up and the input pulse condition, and it appears from the modelling that short DDF sections and certain tapering profiles minimise the jitter. For example, an exponentially tapering DDF leads to lower jitter than a linearly tapering version.

This appears to be the only characterisation of soliton pulse compression jitter in the literature, with no experimental characterisations being performed until the author of this thesis published Ref. [26]

4.5 Conclusion on published pulse compression schemes

Following a review of soliton and soliton-effect compression schemes, it seems that a pulse source of repetition rates as low as a few gigahertz has not been implemented before, either by laser beat frequency compression, compressing the output of a modulator (EAM or Mach-Zehnder) or by beating and compressing modulation orders from a single modulated source.

There do however appear to be a wide range of fibre combinations used to achieve compression, for example Chernikov et al. put forward a dual frequency source using a comb-like dispersion profiled fibre to generate the soliton compression. Other papers use dispersion shifted fibre, dispersion increasing fibre, dispersion decreasing fibre and combinations of these with standard telecommunications fibre.

Curiously, while most of the papers discuss the potential for low jitter pulses, there does not appear to be any published jitter characterisation on any of the compression schemes. Only the phase noise factor of the beat frequency is quoted (in Chernikov's papers) and no single-sideband (SSB) phase noise measurements are performed for example (see Appendix B for a discussion on timing jitter measurement techniques). This is in stark contrast to wealth of analysis performed on the pulsed laser options detailed in the Appendix A (gain-switched, Q-switched and mode-locked lasers).

Following the literature survey, it appeared that there was the possibility of creating and characterising, for the first time, a compression scheme which generated ultra-low timing jitter, ultra-short duration pulses at only a few gigahertz repetition rate. The remainder of this report discusses the modelling, experimental implementation and characterisation of such a pulse source, based on biasing a modulator at null and compressing the output through the correct combinations of fibre. A detailed study of the timing jitter of this fibre compression scheme has been performed and published [Ref. 26], a topic almost always entirely ignored in other papers in the field.

References for Chapter 4

1. Zabusky, N. J., Kruskal, M. D., "Interaction of solitons in a collisionless plasma and the recurrence of initial states." *Phys. Rev. Let.* **15**, pp. 240-243, 1965.
2. Agrawal G.P., "Nonlinear Fiber Optics", Academic Press, 1995
3. Mamyshev P.V., Chernikov S.V., Dianov E.M., "Generation of fundamental soliton trains for high-bit-rate optical fiber communication lines", *IEEE J. Quantum Elect.*, 27(10), pp. 2347 – 2355, 1991

4. Pelusi M.D., Liu H., "Higher Order Soliton Pulse Compression in Dispersion-Decreasing Optical Fibers", J. Quantum Elect., 33(8), pp. 1430-1439, 1997
5. Mostof A., Hatami-Hanza H., Chu P.L., "Optimum dispersion profile for compression of fundamental solitons in dispersion decreasing fibres", J. Quantum Elect., 33(4), pp. 620-628, 1997
6. Chernikov S.V., Taylor J.R., Kashyap R., "Comblike dispersion-profiled fibre for soliton pulse train compression", Opt. Lett., 19(8), pp. 539-541, 1994
7. Ahmed K.A., Chan K.C., Liu H., "Femtosecond pulse generation from semiconductor lasers using the soliton-effect compression technique", IEEE J. Sel. Top. Quant., 1(2), pp. 592-600, 1995
8. Chan K.C., Liu H.F., "Short pulse generation by higher order soliton-effect compression: Effects of optical fiber characteristics", J. Quantum Electron., 31(12), pp. 2226-2235, 1995
9. Chernikov S.V., Dianov E.M., Richardson D.J., Payne DN "Soliton pulse-compression in dispersion-decreasing fiber", Opt. Lett., 18(7), pp. 476-478, 1993
10. Guy M.J., Taylor J.R., Moodie D.G., Kashyap R., "200 fs soliton pulse generation at 10 GHz through nonlinear compression of transform-limited pulses from an electroabsorption modulator", Electron. Lett., 31(9), pp. 740-741, 1995
11. Matsui Y., Pelusi M.D., Suzuki A., "Generation of 20-fs optical pulses from a gain-switched laser diode by a four-stage soliton compression technique", IEEE Photonic. Tech. L., 11(10), pp. 1217-1219, 1999
12. Johansson L.A., Seeds A.J., "Millimetre-wave modulated optical signal generation with high spectral purity and wide-locking bandwidth using a fiber-integrated optical injection phase-lock loop", IEEE Photonic. Tech. L., 12(6), pp. 690-692, 2000
13. Etem Y., Lewis M.F., Sample P., "An optical microwave source for frequency synthesizer applications", Proc. Conf. Microwave Photonics 1996 (MWP96), pp. 161-164, 1996
14. "Sampling Pulse Generators for Optical Analogue to Digital Converters", prepared by Alwyn Seeds Technical Services under QinetiQ contract CU016 11154 (March 2002)

15. Swanson E., Chinn S.R., "23-GHz and 123-GHz soliton pulse generation using two CW lasers and standard single-mode fiber. IEEE Photonic. Tech. L. 1994;6:796-798.
16. Swanson E., Chinn S.R., Hal K., Rauschenbach K.A., Bondurant R.S., Miller J.W., "100-GHz soliton pulse train generation using soliton compression of two phase side bands from a single DFB laser", IEEE Photonic. Tech. L, 6(10), pp. 1194-1196, 1994
17. Chernikov S.V., Taylor J.R., Kashyap R. "Integrated all optical fibre source of multigigahertz soliton pulse train", Electron. Lett., 29(20), pp.1788-1789, 1993
18. Chernikov S.V., Taylor J.R., Kashyap R. "Experimental demonstration of step-like dispersion profiling in optical fibre for soliton pulse generation and compression", Electron. Lett., 30(5), pp. 433-434, 1994
19. Shipulin A.V., Fursa D.G., Golovchenko E.A., Dianov E.M., "High repetition rate CW fundamental soliton generation using multisoliton pulse compression in a varying dispersion fibre", Electron. Lett., 29(16), pp. 1401-1403, 1993
20. Ahmed K.A., Chan K.C., Liu H., "Femtosecond pulse generation from semiconductor lasers using the soliton-effect compression technique", IEEE J. Sel. Top. Quant., pp. 592-600, 1995
21. Hall K.L., Rauschenbach K.A., Swanson E.A., Chinn S.R., Raybon G., "Picosecond-accuracy all-optical bit phase sensing using a nonlinear loop mirror", IEEE Photonic. Tech. L., 7(8), pp. 935-937, 1995
22. Pelusi M.D., Matsui Y., Suzuki A., "Frequency tuneable femtosecond pulse generation from an electroabsorption modulator by enhanced higher order soliton compression in dispersion decreasing fibre", Electron. Lett., pp. 734-736, 1999
23. Chernikov S.V., Guy M.J., Taylor J.R., Moodie D.G., "Sources for ultra-high bit rate telecommunication based on an EA modulator in conjunction with soliton compression", IEE Colloq. On Optical Solitons: Principles and Applications, pp. 2/1 – 2/5, 1996
24. Swanson E.A., Chinn S.R., "40-GHz pulse train generation using soliton compression of a Mach-Zehnder modulator output", IEEE Photonic. Tech. L., 7(1), pp. 114-116, 1995
25. Tamura K., Nakazawa, "Timing jitter of solitons compressed in dispersion-decreasing fibers", Opt. Lett., 23(17), pp. 1360-1362, 1998

26. McDonald G.J., Seeds A.J., "A novel pulse source for low-jitter optical sampling: a rugged alternative to mode-locked lasers", SPIE Proc. on Advanced Free-Space Optical Communication Techniques/Applications II and Photonic Components/Architectures for Microwave Systems and Displays, Vol. 6399, 63990J, Oct 2006

5. Modelling pulse compression through fibre

A modulator biased at a carefully selected bias point and driven with a single frequency was selected as a method of generating a periodic waveform, which is then compressed through appropriate fibre with the aim of generating ultra-low jitter, ultra-short pulses at gigahertz repetition rates. The generic arrangement is shown in Fig. 5.1, where the output from a continuous laser is modulated by an external optical modulator (such as a LiNbO₃ Mach Zehnder) before amplification and subsequent compression through suitable fibre. This chapter details modelling of this arrangement with a modulator biased at null, for propagation through both standard telecommunications fibre and dispersion decreasing fibre (DDF).

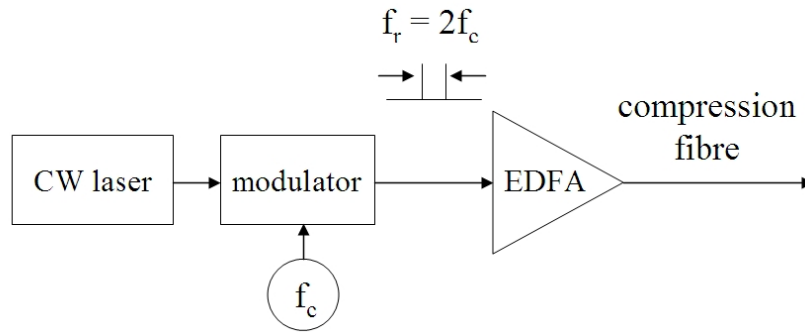


Fig. 5.1. Generic modulator biased-at-null set-up, generating a periodic pulse train source f_r at twice the microwave source frequency f_c .

For the remainder of this chapter the microwave synthesiser has the frequency f_c and the pulse repetition frequency $f_r = 2f_c$. As mentioned in Section 4.2.3, the output field from the modulator (and EDFA) is:

$$E_{out} = \frac{1}{2} E_{in} (1 + e^{i\Delta\phi}), \text{ where } \Delta\phi = \text{peak phase modulation} \quad (5.1)$$

5.1 The split-step Fourier algorithm

To evaluate system feasibility, modelling of the system was performed using the split-step Fourier algorithm, as described mathematically in Agrawal's "Non-linear Fibre Optics"^[1], implemented in Matlab. At discrete steps through the fibre the pulse amplitude distribution is calculated to take into account fibre loss, dispersion and non-linearities. For each step, the dispersion effects are evaluated in the frequency domain

before the amplitude distribution is Fourier transformed to the time domain, where the self-phase modulation is calculated, Eqs. 5.2-5.4. For small enough steps through the fibre it is acceptable to consider the dispersion and non-linearity acting independently in this way. The accuracy of the model is governed by the number of points used to model the pulse at each step through the fibre and also the fibre step size.

$$\frac{\partial A}{\partial z} = (\hat{D} + \hat{N})A \quad \text{propagation equation} \quad (5.2)$$

$$\hat{D} = -\frac{i}{2}\beta_2 \frac{\partial^2}{\partial^2 T} + \frac{1}{6}\beta_3 \frac{\partial^3}{\partial^3 T} - \frac{\alpha}{2} \quad \text{differential operator} \quad (5.3)$$

$$\hat{N} = i\gamma \left[|A|^2 + \frac{2i}{A\omega_0} \frac{\partial}{\partial T} (|A|^2 A) - T_R \frac{\partial |A|^2}{\partial T} \right] \quad \text{non-linear operator} \quad (5.4)$$

where $T = t - \frac{z}{v_g} = t - \beta_1 z$ $A = \text{pulse amplitude}$
 $|A|^2 = \text{optical power}$

- group velocity $v_g = \beta_1^{-1}$, the speed at which the pulse envelope propagates
- β_2 , the group-velocity parameter, is responsible for pulse broadening
- γ , the non-linear parameter $= \left(\frac{n_2(\omega_0)\omega_0}{cA_{eff}} \right)$ $A_{eff} = \text{effective area}$
 $n_2 = \text{nonlinear index coefficient}$
 $\omega_0 = 2\pi c/\lambda$
- $\alpha = \text{fibre loss}$
- T_R is related to the slope of the Raman gain, assumed to vary linearly with frequency in the vicinity of the carrier frequency ω_0 , estimated to be ~ 5 fs

Note that for the modelling, only the first order non-linearities in Eq. 5.4 were used in the approximation. The β_3 term in Eq. 5.3 was included in the model since it can be important for ultrashort pulses due to their wide bandwidth, even when the wavelength is relatively far away from the zero-dispersion wavelength.

5.2 Model implementation

Initially the modelling was attempted on a time window with at least two discrete points per cycle of the optical carrier frequency. However, this number of points proved to be too computationally demanding to run on even a high specification desktop computer. Instead, the amplitude envelope was considered over a time window of between 16,384-131,072 points per pulse time-slot at each step through the fibre, depending on the final pulse width. For modelling the standard single-mode fibre propagation, where pulses are compressed to the order of around 16 ps, as will be discussed shortly, 16,384 points proved adequate. However if a more complex fibre arrangement is used to compress the pulses to <1 ps, then more points per pulse time-slot are required to avoid introducing substantial errors due to the limited time step size resulting in the pulse being inadequately sampled.

Fig. 5.2 shows the typical modelled evolution of a pulse envelope as it propagates through a standard telecommunications fibre such as Corning's SMF-28 (the envelope in this example corresponds to a 3 GHz repetition rate pulse launched at 500 mW peak power). After 8 km of propagation, compression of the pulse has begun and this compression becomes more pronounced as the pulse peak intensity increases and the resulting non-linear effects become stronger. At 8 km the pulse is developing a pedestal, as discussed in Chapter 4 of this report. The maximum pulse compression occurs at 9.1 km, and a narrow sharp pulse is observed, with some pedestal present. As the pulse propagates further through the fibre, the pulse shape displays multiple peaks and a high level of attenuation after the long lengths of fibre.

5. Modelling pulse compression through fibre

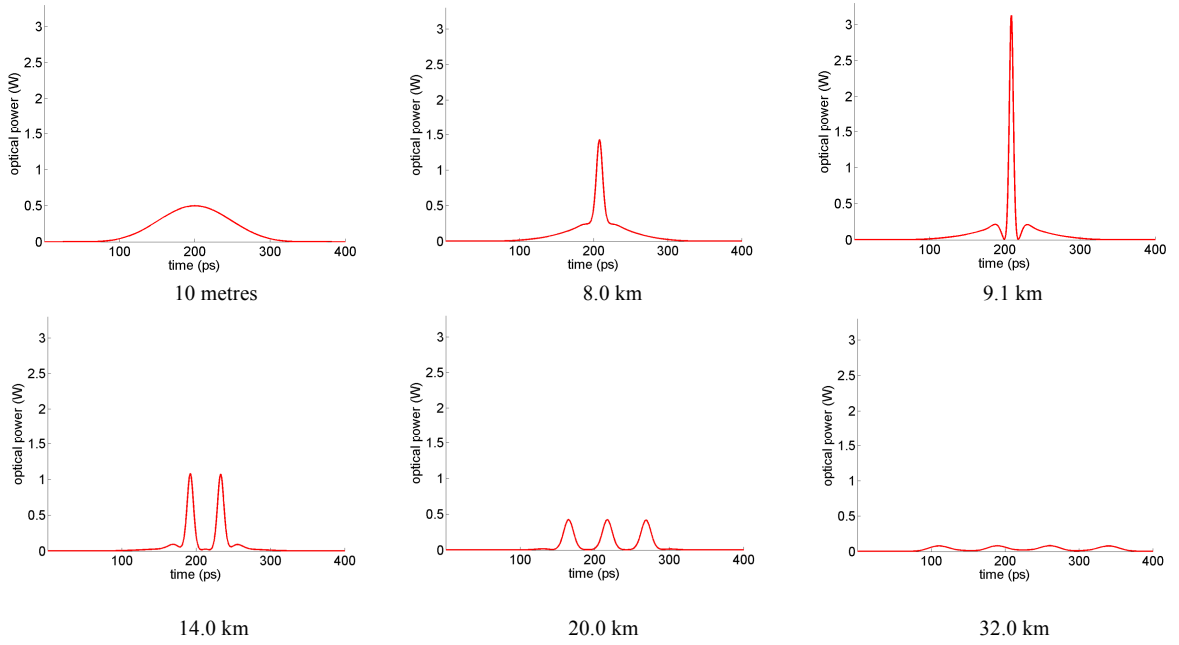


Fig 5.2. The intensity distribution of a beat envelope through the fibre at various lengths of fibre (3 GHz repetition rate input at 500 mW peak input launch power). The compressed, high peak power pulse at 9.1 km is potentially of interest for sampling and metrology applications.

The goal is to generate single peak pulses with durations as short as possible, such as at 9.1 km in Fig. 5.2. Ideally the pulses will not display pedestals, or at least these pedestals should be minimised. Fig. 5.3 summarises the basic pulse characteristics of interest: the full width half maximum (FWHM), peak power and peak pedestal power. From these, a peak to pedestal power ratio can be evaluated to provide a useful metric indicating pulse quality. Note that the term pedestal has been used in much of the soliton literature reviewed in Chapter 4 and will be used in this report – this could also be termed as a sidelobe peak.

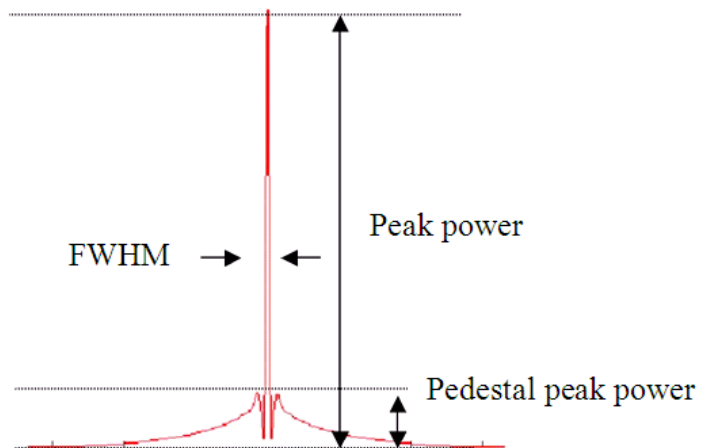


Fig. 5.3. Pulse parameters, to be evaluated from the model for every step through the fibre.

As will be discussed in more detail later in this chapter, split-step Fourier algorithm modelling predicts that a 3 GHz repetition rate pulse will compress to a pulse width of the order of 16 ps, from an initial launch width of 111 ps, when launched into 19.5 km of Corning's SMF-28 fibre. Fig. 5.4 shows the evolution of the pulse in the temporal domain, in the form of a 3D plot through up to 70 km of fibre. The pulse narrows to a single peak around 19.5 km before it rapidly broadens into a series of low amplitude side-lobes and effectively disappears, smeared across the time window as a temporally broad series of pedestal ripples. The effect of fibre loss becomes substantial through such long lengths of fibre, even through low-loss telecommunications fibre, with a total attenuation of around 8 dB after 40 km and 14 dB after 70 km. The non-linear coefficient used for Fig. 5.4 was 0.0013 W.km^{-1} and the group velocity dispersion was $16 \text{ ps}^2/\text{km}$.

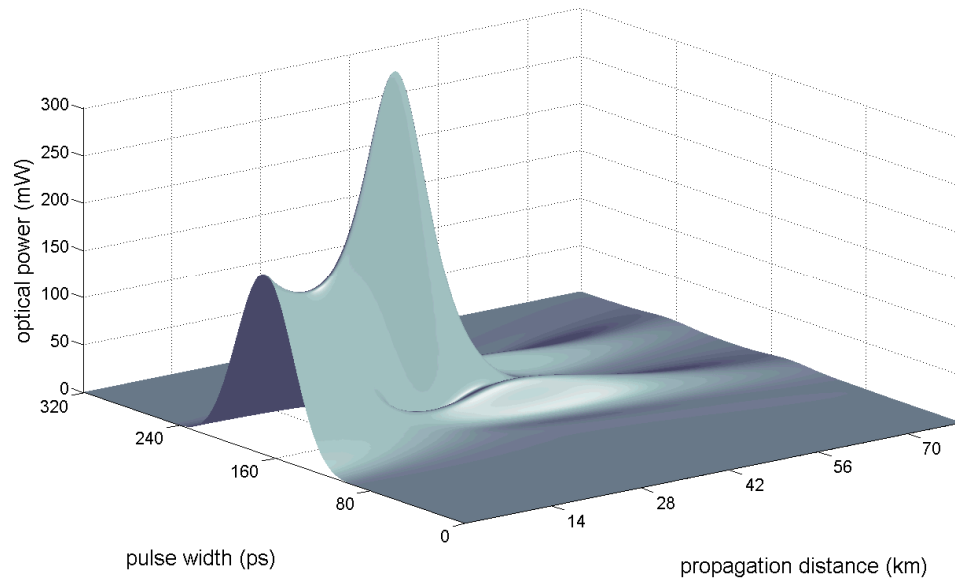


Fig. 5.4. 3D evolution of a 3 GHz repetition rate pulse through 70 km of Corning's SMF-28. The pulse narrows to a ~ 16 ps peak around 19.5 km before experiencing rapid pulse broadening and substantial attenuation through long lengths of fibre.

Fig. 5.5 shows the effect of setting the fibre attenuation to zero and considering the evolution of a 3 GHz repetition rate pulse through a hypothetical loss-less fibre with the same non-linear and dispersion properties as Corning's SMF-28 fibre. After 150 km the pulse has evolved through several similar but different periodic cycles, whereby it narrows to a single short central pulse, before evolving into a pair of lower intensity pulses, before coming back to a single narrow central pulse further down the fibre.

5. Modelling pulse compression through fibre

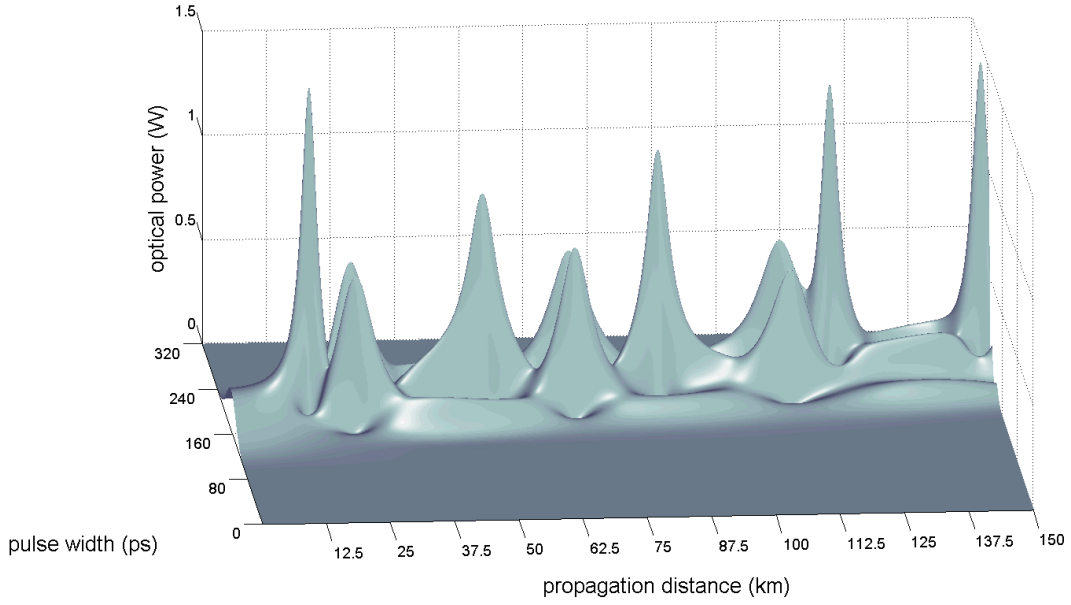


Fig. 5.5. 3D evolution of a 3 GHz repetition rate pulse as it propagates through a hypothetical loss-less version of Corning's SMF-28 (i.e. loss = 0 dB/km, non-linear coefficient = 0.0013 W.km^{-1} and $\text{GVD} = 16 \text{ ps}^2/\text{km}$).

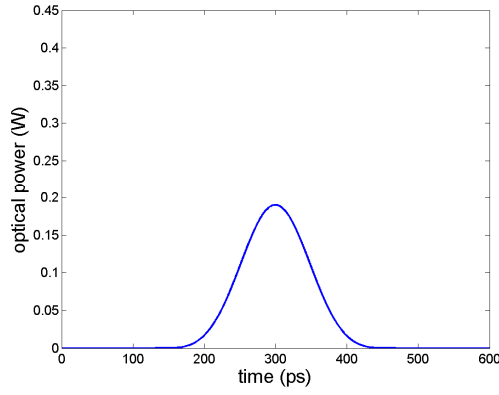
Eq. 5.5 describes the soliton order of a pulse, N , based on its launch parameters of peak power, P_o , and pulse duration, T_o , into a fibre with a given non-linear coefficient and GVD. Its derivation can be found in Ref. [1].

$$N^2 = \frac{\gamma P_o T_o^2}{|\beta_2|} \quad (5.5)$$

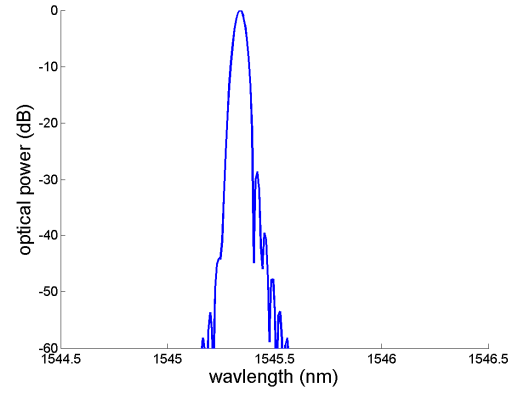
Based on the launch parameters used in Fig. 5.4 of 190 mW and 110 ps, the soliton order given by Eq. 5.5 is $N = 13.7$, i.e. a relatively high order soliton.

Fig. 5.6 shows the spectral broadening associated with the pulse compression, for the 190 mW peak power pulse at 3 GHz repetition rate, through 19.5 km of Corning's SMF-28 fibre. The launch pulse has a 3 dB width of 0.049 nm in the spectral domain, which broadens to 0.245 nm after propagation and compression through 19.5 km of fibre. These spectral widths are consistent with experimental observations described in Section 6.8 of this thesis.

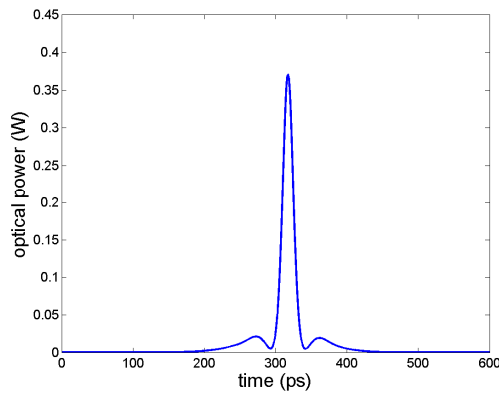
5. Modelling pulse compression through fibre



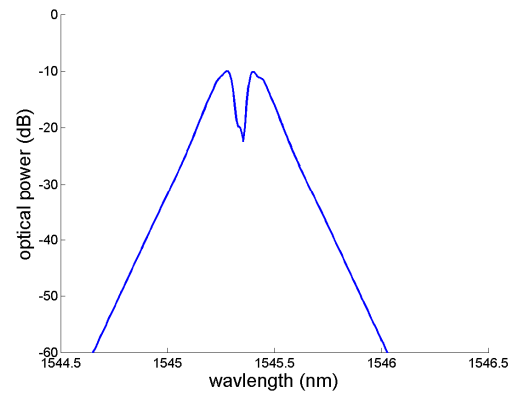
(a) Temporal domain. Launch pulse.
FWHM ~ 110 ps.



(b) Spectral domain. Launch pulse.
Spectral width = 0.049 nm.



(c) Temporal domain. Pulse after 19.5 km of
Corning's SMF-28. FWHM ~ 17 ps.



(d) Spectral domain. Pulse after 19.5 km of
Corning's SMF-28. Spectral width = 0.245 nm.

Fig. 5.6. A direct comparison of the time domain and frequency domain pulse representations for the input and output pulses for a 3 GHz repetition rate pulse launched into 19.5 km Corning SMF-28 fibre, with a peak launch power of 190 mW. Note that the axes are the same for both the input and output sets of plots.

5.3 Model accuracy

In terms of model accuracy, both the number of points per pulse time-slot and the step size through the fibre are important. As with any numerical modelling, the trade-off with improved resolution is the increased computational time required to perform the modelling.

5.3.1 Global relative error

The global relative error, ε , is one method described in the literature^[2] for evaluating the error introduced by an increased fibre step size when using the split-step Fourier method to model pulse propagation. This error analysis method compares the E-field after a long propagation length through the fibre, i.e. after many thousands or millions of FFTs and dispersion/SPM calculations, for both a step size under test and a very small step size limited by machine precision. Ideally, the E-field for a given step size would be compared to the true solution of the nonlinear Schrödinger equation. However in practice true solutions are only known for the few special cases which can be solved analytically, so when a real experimental arrangement is being modelled it is necessary to compare the numerical solution to the E-field for a very small step size.

The global relative error is given by:

$$\varepsilon = \frac{\|u_n - u_a\|}{\|u_a\|} \quad (5.6)$$

where u_a is a solution limited by machine accuracy precision and u_n is the solution for a step size larger than that used to generate the solution u_a , and the following norms are defined as:

$$\|u_n - u_a\| = \sqrt{\sum_{i=1}^N |u_n(i) - u_a(i)|^2} \quad (5.7)$$

$$\|u_a\| = \sqrt{\sum_{i=1}^N |u_a(i)|^2} \quad (5.8)$$

where N = number of points across pulse envelope

5.3.2 Fibre step size through SMF-28

The global relative error was evaluated for a range of step sizes, for a pulse generated by a modulator biased at null and driven with a 3 GHz sinusoid with V_π amplitude. The peak launch power was 190 mW. As will be discussed here and in later chapters

5. Modelling pulse compression through fibre

describing the experimental work, these pulse parameters are representative of the parameters used to generate the soliton-effect pulse trains which have been used to perform optical sampling, where the compression fibre is Corning's SMF-28.

Various step sizes were modelled propagating through 19.5 km of SMF-28 on a 3 GHz PC with 750 MB RAM, ranging from 0.01 m (1.95 million steps) through to 500 m (39 steps). The global relative error for each step size was then compared to the minimum step size of 0.01 m. Fig. 5.7 shows the model output after 19.5 km for a step size of 0.01 m and 100 m. Visually they appear identical.

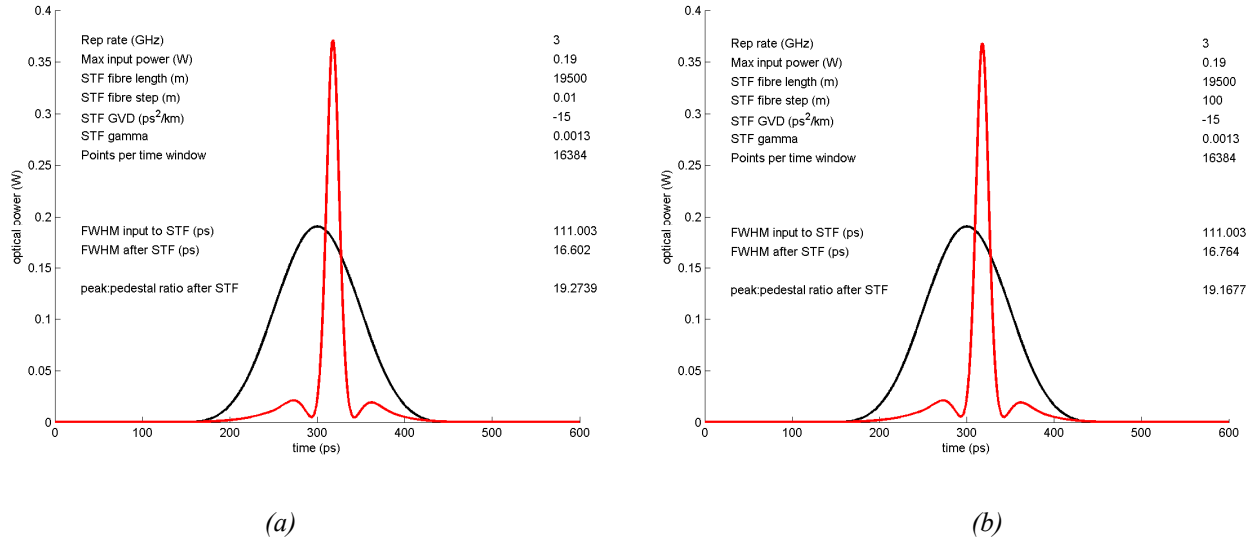


Fig. 5.7. Modelled 3 GHz repetition rate pulse (FWHM = 111 ps launch), propagated through 19.5 km of SMF-28 for (a) a 0.01m step size (1.95 million steps), and (b) a 100 m step size (195 steps). The resulting compressed pulses have FWHMs of 16.602 ps and 16.764ps respectively. Visually the resulting pulses from the two different step sizes appear identical. The black plot is the waveform launched into the fibre, and the red plot is the compressed pulse after 19.5 km of SMF-28.

Table 5.1 shows the massive variation in run-time required depending on step size, with a step size of 0.01 m requiring approximately 18 hours to model a single input power and repetition rate through a 19.5 km length of fibre, compared to <2 seconds for a 500 m step size. The 0.01m step size is clearly not practical for evaluating a large combination of fibre arrangements (such as with a comb-like fibre), and a wide range of launch powers and repetition rates. A step size of 10 m results in a modest global

relative error in the modelled E-field of only 0.0012 (0.12%), which is well below the measurement resolution of a high-speed sampling oscilloscope (<8-bits resolution). Even a crude step size of 500 m yields a global relative error of only 6.5%. A realistic trade-off between high-accuracy modelling and manageable run-times is to use a 10 m step size through the fibre. If high-precision lengths of fibre are required, as may be the case when constructing a comb-like fibre for example, then multiple combinations of fibre arrangements could be modelled with a 10 m step size to gain an understanding of the generic arrangement required. This could then be followed by modelling with a step size of <1 m to ensure the modelling is performed with minimum step size related errors prior to fibre fabrication.

Step size (m)	No steps	Run-time (hours:min:sec)	Global relative error
0.01	1,950,000	18:18:19.0	n/a
0.1	195,000	1:49:50.0	1.1242e-5
1	19,500	10:59.0	1.2367e-4
10	1,950	1:05.0	1.2443e-3
100	195	7.0	1.2641e-2
500	39	1.6	6.5992e-2

Table 5.1. Global relative error for step sizes ranging from 0.01 m to 500 m, resulting in a very wide range of computational steps required to model 19.5 km of SMF-28, with correspondingly large variations in run-times. The maximum global relative error due to even a very crude step size of 500 m is 0.0659 (6.59%), an unacceptably high error for detailed analysis, but low enough to still crudely indicate generic pulse behaviour. A step size of 1 m or 10 m would appear to be a reasonable compromise between numerical accuracy (0.012% and 0.12% respectively) and run-time, if many parameters are to be varied. A step size of 0.01 m or 0.1m should be used for the final detailed run once parameters have been finalised.

Although not as rigorous an evaluation method as the global relative error, looking at the actual pulse parameters at 19.5 km for the different step sizes also demonstrates the gradual decline in model accuracy, Table 5.2. Using 16,384 points gives a time-step of ~20 fs across the 3 GHz pulse time-slot. The FWHM values in Table 5.2 remain constant at 16.602 ps for step sizes ranging from 0.01 m to 10 m, as the cumulative effect on the FWHM of the modelling errors is less than the 20 fs time-step size. Even for the largest crude step size of 500 m, requiring only 39 steps to cover the 19.5 km of

SMF-28, the FWHM is only 0.97 ps or 5.9% larger than for the 0.01 m fibre step size. Similarly the variation in the peak:pedestal power ratio only varies by the small amount of 4.3% over the step size range of 0.01 m to 500 m, while the number of steps through the fibre varies considerably from a mere 39 to a computationally intensive 1.95 million. Variations of a few percent in the power and pulse durations are very close to the measurement accuracy of high-speed sampling oscilloscopes which would be used to visualise the pulses experimentally. Therefore, a step size of 10m would appear to be a good balance between computational time and E-field accuracy.

Step size (m)	No. of steps	FWHM (ps)	Peak:pedestal power ratio
0.01	1,950,000	16.602	19.2379 (12.841 dB)
0.1	195,000	16.602	19.2378 (12.841 dB)
1	19,500	16.602	19.2738 (12.850 dB)
10	1,950	16.602	19.2650 (12.848 dB)
100	195	16.764	19.1677 (12.826 dB)
500	39	17.578	18.4030 (12.649 dB)

Table 5.2. Varying SMF-28 fibre step size. Pulse parameters for a 3 GHz pulse launched into 19.5 km of SMF-28 for a wide range of step sizes. Despite the massive variation in number of steps required through the fibre for each step size, the FWHM and peak:pedestal power ratios only vary by up to 6%.

5.3.3 Number of points per pulse window through the SMF-28

The number of points per time window was varied in powers of two to allow direct comparison of the errors introduced to the E-field when the pulse time-slot is represented by too few points (using powers of two also allows for the most efficient computation of the Fourier transform of the pulse window). The overall time-slot remains constant, but the number of points equally distributed across this time window is doubled for each successive run in Table 5.3. By doubling the number of points each time, every timing step across the 8,192 point window corresponds exactly to every second point in the 16,384 point window, every fourth point in the 32,768 point window, and so on. In this way the global relative error in the E-field can be evaluated for the different number of points per time-slot.

5. Modelling pulse compression through fibre

No. points per pulse time-slot	FWHM (ps)	Peak:pedestal power ratio	Global relative error
8192	16.602	19.2652 (12.848 dB)	4.7835e-008
16384	16.602	19.2650 (12.848 dB)	8.4710e-009
32768	16.683	19.2650 (12.848 dB)	1.4929e-009
65536	16.724	19.2650 (12.848 dB)	2.5009e-010
131072	16.764	19.2650 (12.848 dB)	n/a

Table 5.3. Varying number of points across pulse time-slot. Pulse parameters for a 3 GHz pulse rate launched with a 190 mW peak power into 19.5 km of SMF-28 for various numbers of points across a fixed time window. The resulting global relative error for common time points across the window is negligible. The variation in the FWHM is due to quantisation of the time steps when too few points are used.

Table 5.3 shows that the global relative error due to the number of points per pulse time-slot is negligible for pulses compressing to the order of 16 ps. Analysis of the FWHM shows that the accuracy is limited by discrete quantisation of the time-step and the peak to pedestal power ratio is constant to 5 significant figures. Given the limited resolution of high-speed sampling oscilloscopes, 16,384 points appears to be an acceptable value for modelling the pulse evolution through the SMF-28 section. However, when the pulses compress to sub-ps duration, it is necessary to use a larger number of points as will be discussed in Section 5.8.2.

5.3.4 FFT windowing

Two different FFT windows (Hanning and quadratic) were applied to the FFT process for the case where single pulses were propagated, but they had no effect on the global relative error – it was exactly the same with and without the windowing. This result is perhaps not surprising, as there is no E-field present at the start and end of the pulse-slot for the perfectly nulled modulator. Originally the pulse train was padded on either side with 5 pulse intervals of zeros to ensure no “wrap around” of the Fourier transform process. Multiple temporally adjacent pulses were also considered to ensure no pulse interaction due to spreading into adjacent pulse time-slots. However, it became apparent after investigating the behaviour of many pulse input conditions that it was not necessary to include any additional zero padding or FFT windowing and that a single pulse time-slot was sufficient. This was confirmed by the FWHMs and peak:pedestal

power ratios being identical with and without FFT windowing in Tables 5.2 and 5.3. Therefore to ensure computational efficiency it has been verified that no zero padding or windowing is required.

5.3.5 Verifying the model with a soliton input

A fundamental soliton pulse has a hyperbolic secant (sech) profile and should travel indefinitely in a lossless fibre if it has a width T_0 and peak power $P_I^{[1]}$, if:

$$P_1 = \frac{|\beta_2|}{\gamma T_0^2} \approx \frac{3.11|\beta_2|}{\gamma T_{FWHM}^2} \quad (5.9)$$

Three separate solitons with different FWHMs and input powers were launched into the modelled fibre with the fibre loss set to zero:

- FWHM = 1.7 ps and $P_1 = 5$ Watts
- FWHM = 6.8 ps and $P_1 = 1$ Watt
- FWHM = 13.8 ps and $P_1 = 190$ mW

In all three cases, the pulse intensity envelopes travelled virtually unchanged for 19.5 km of SMF-28, for fibre step sizes 0.01, 0.1, 1, 10, 100 and 500 m, Fig. 5.8, except for machine precision errors.

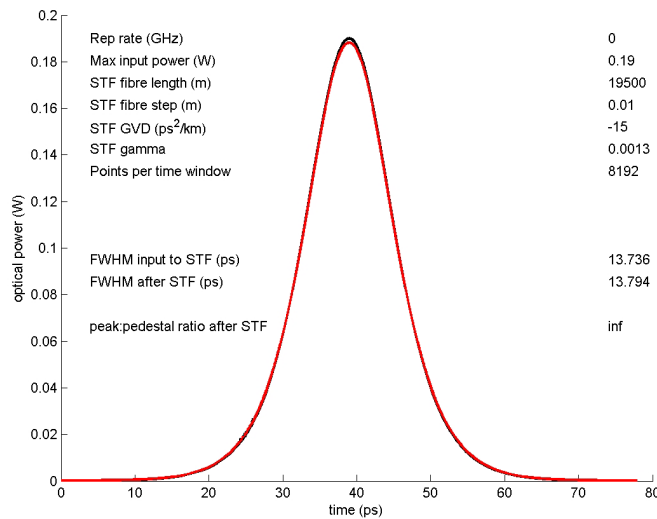


Fig. 5.8. Fundamental soliton (sech) pulse input and output from 19.5 km are identical except for machine precision error. Both plots overlap in the figure.

5. Modelling pulse compression through fibre

The global relative errors for the sech profile soliton, Table 5.4, and the compressed pulse from the modulator biased at null, show very comparable performance, Fig. 5.9. It appears therefore that the error in the E-field introduced by the step size for these pulse parameters is independent of pulse shape and subsequent compression behaviour, and is instead dominated by the accumulation of rounding errors in the numerical model.

Step size (m)	No steps	Global relative error
0.01	1,950,000	n/a
0.1	195,000	8.6739e-6
1	19,500	9.5434e-5
10	1,950	9.6509e-4
100	195	9.9903e-3
500	39	5.3933e-2

Table 5.4. **Varying fibre step size.** Global relative error for modelled sech pulse propagating through 19.5 km for step sizes ranging from 0.1-500 m.

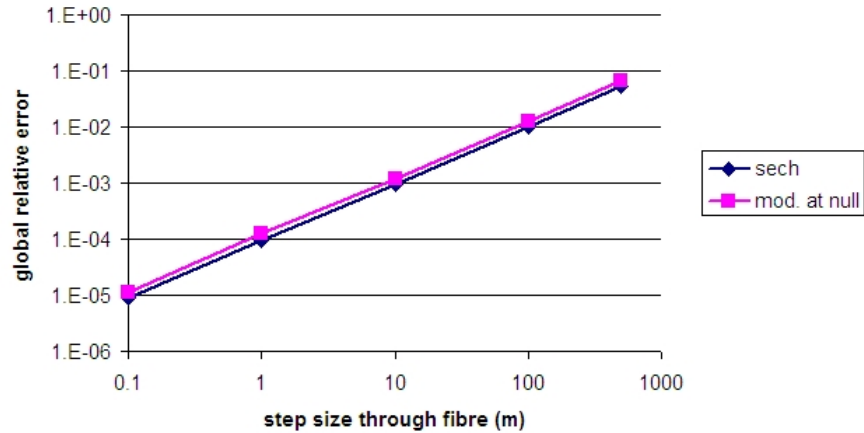


Fig. 5.9. Comparison of the global relative error after 19.5 km for the compressed modulator-at-null pulse and the sech pulse. The very close behaviour of the global relative error suggests that the error is due to numerical precision as opposed to pulse characteristics.

Closer inspection of the real and imaginary E-fields for the two cases (the sech pulse and the modulator-at-null pulse) after 19.5 km reveals that the sech pulse real and imaginary E-fields are both sech profiles, whereas the modulator-at-null compressed pulse has developed a detailed structure, quite different from its launch profile, Fig. 5.10. The unchanged propagation of the fundamental soliton is as expected from

theory and, coupled with the compression behaviour of the modulator-at-null pulse, suggests that the model is performing as expected with no obvious coding errors.

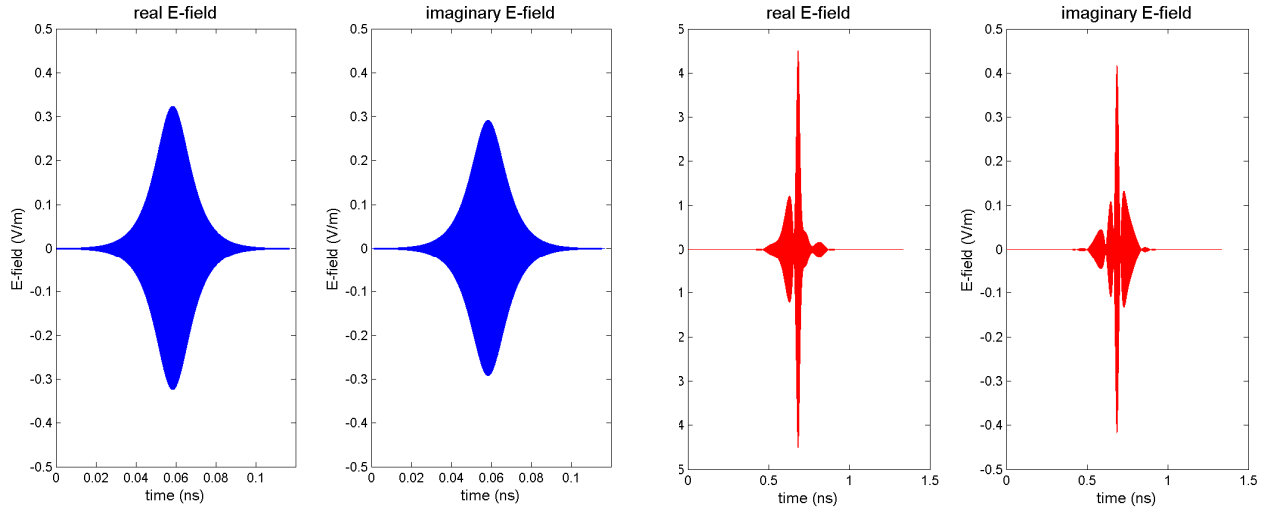


Fig. 5.10. Modelled E-field envelopes (real and imaginary) after 19.5 km for sech pulse (blue plots) and 3 GHz modulator biased at null compressed pulse (red plots). In both cases peak launch power = 190 mW, step size = 10 m, and number of points = 16,384.

5.4 Evaluating viable pulse repetition rates and launch powers

It is desirable to know which combination of repetition rates, peak input intensities and fibre lengths convert the modulator output into a desirable pulse train. In order to perform the task of assimilating viable input pulse parameters automatically, code was written to analyse and characterise the intensity distribution for every step through the fibre. For every step of every input parameter combination, the intensity distribution was examined to measure FWHM and also the ratio of the central peak intensity to the pedestal intensity.

In many cases the modulator-at-null input does not converge to single peak and often the result after propagation through the fibre is a corruption of the input, Fig. 5.11.

5. Modelling pulse compression through fibre

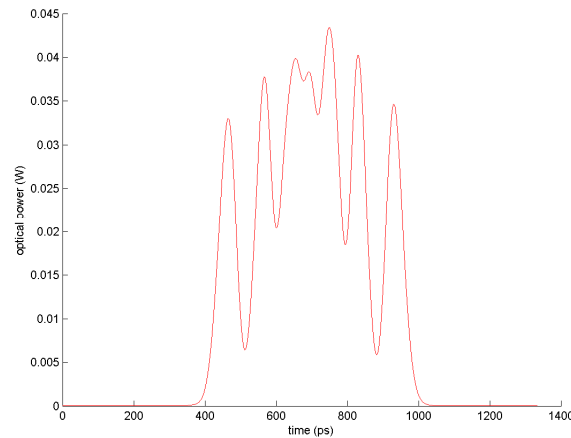


Fig. 5.11. Example of a corrupted pulse. There is little point in continuing the model run beyond this point, as this waveform will not converge back to a single clean pulse, therefore an optional corruption monitor was written into the model code to break the routine if a pulse is considered to have become corrupted.

The model allows the output from the standard fibre section to be passed to a dispersion decreasing fibre (DDF) for further compression if required. Optional thresholding criteria can be applied at any point along the fibre, for example the routine can be told to pass the output from the SMF-28 to the DDF section only if the pulse width is less than, say, 10 ps. This helps reduce the modelling run-time. Similarly, to minimise run-time, it is substantially quicker (in Matlab) to save only those images which provide desirable pulses after the SMF-28 or SMF-28 & DDF. An optional “corruption monitor” can be switched on, such that if the pulse envelope becomes multi-peaked after propagation through the fibre, then the routine breaks and begins again at the start of the fibre with the next set of pulse input parameters.

To understand how significant the pedestal is for a given run, the option exists in the model code to measure the power in either a given time window around the pulse peak, or alternatively to measure the power in a given multiple of the pulse width.

The following model run information can be saved to file as the user defines:

- A summary of input parameters and fibre lengths meeting user defined FWHMs
- Detailed tables of FWHMs for both SMF-28 and DDF sections, peak-to-pedestal power ratios, pulse energies for given time windows, required fibre lengths and input pulse parameters

Also, specific pulse envelope images can be saved, meeting any of the following:

- At user defined lengths through the fibre for each input pulse set-up
- Any pulse meeting a given FWHM at any point through the fibre
- For each pulse, the user can plot any of:
 1. The input pulse (i.e. the modulator-at-null output)
 2. The output from the SMF-28
 3. The output from the DDF (if applicable)
 4. Textual information detailing that specific pulse run

Fig. 5.12 overleaf shows a snapshot of the user interface in Matlab.

GUI for_pulse_model_sech

Pulse compression modelling suite

Standard fibre

Fibre loss (dB/km)

Beta 2 (GVD) (ps^2/km)

Beta 3 (ps^3/km)

Refractive index *

Non-linear coefficient

(* average of core and cladding)

DDF parameters

☐ Only model if input FWHM < (ps):

☐ Only model if STF length = (m):

No. of DDF segments

DDF segment length (m)

Input core radius (μm)

Output core radius (μm)

Core refractive index

Cladding refractive index

Material dispersion

Profile dispersion

N2 ($\times 10^{-20}$)

Pulse type

Bias-at-null

bias away from null V_{pi}

Modelling run-time parameters

Number of pulses

No. points/pulse

Wavelength (nm)

STF length (m)

STF step (m)

Pulse repetition rates

Start (GHz)

End (GHz)

Step (GHz)

Min. (W)

Max. (W)

Step (W)

Run

Rep. rate (GHz)

Power (W)

Fibre length

FWHM

Start model

Stop

Pulse plotting

Threshold STF output?

Threshold values (ps)

Plot only first pulse meeting each threshold?

Plot DDF output (if applicable)?

Manual timespan on plots?

Timespan (ps)

Save plot at specific lengths?

(in metres)

Pulse plot content:

File save details

Save viable input parameters?

If so, save for pulses shorter than (ps):

Save detailed pulse parameters?

For every step through the fibre?

For pulses under (ps):

Save E-field?

For short pulses?

For pulses under (ps):

After length (m)

After fibre length (m)

DDF output (if applicable)

Fig. 5.12. Graphical user interface front-end for the pulse modelling code.

5.5 Modelling compression through standard telecommunications fibre (SMF-28)

The aim of this section of the modelling is to establish which combinations of peak input powers, P_0 , and pulse repetition rates f_r lead to compressed pulses and which generate corrupted multi-peaked envelopes. Also of interest is the corresponding length of fibre required for the pulse to compress to a given width for a given f_r and P_0 . An enormous amount of data could potentially be generated detailing all the possible combinations. In an attempt to provide a concise summary, this section gives the results for input parameters leading to pulses shorter than 30 ps, 20 ps, 10 ps and 5 ps. The model runs were from 100 MHz to 5 GHz repetition rates in 100 MHz frequency steps, and 50 mW to 5 Watt peak powers in 50 mW power steps, Fig. 5.13. The maximum possible fibre length considered was 50 km. These parameters were chosen since EDFAs with up to 5 Watts peak outputs are commercially available and fibre lengths of 50 km are available as standard commercial items, although fibre lengths much shorter than 50 km are preferable to work with for compactness and packaging reasons. The repetition rate range is of interest for the QinetiQ ADC sampling function and the optical metrology application.

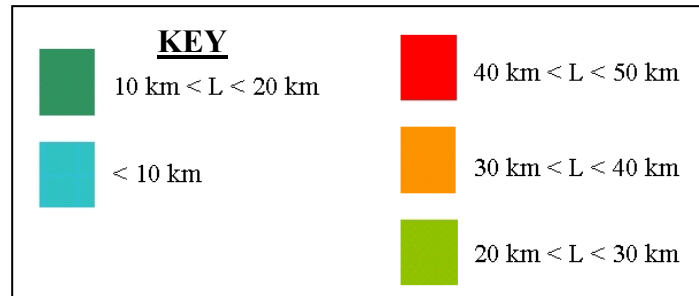
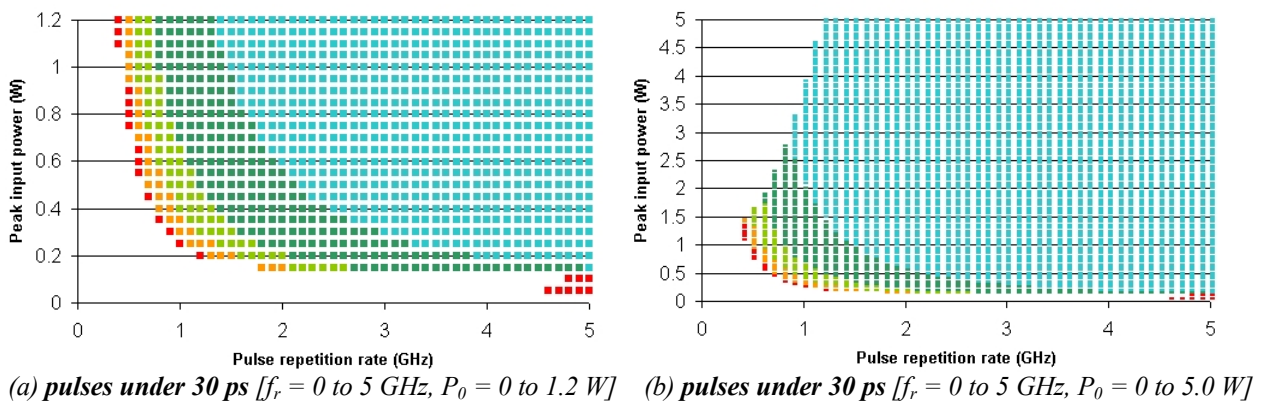


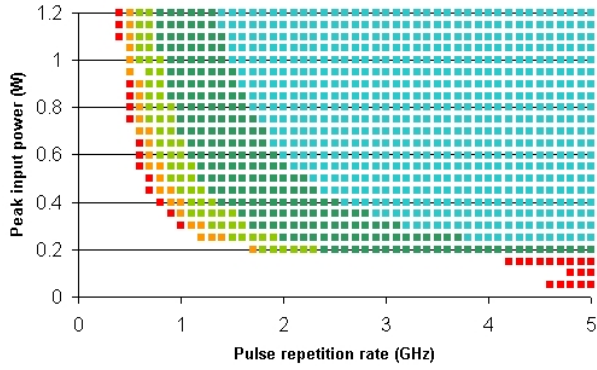
Fig. 5.13. Combinations of pulse repetitions f_r and input peak powers P_0 giving pulses with FWHMs shorter than the stated value for the colour coded length of SMF-28 (note source frequency $f_c = \frac{1}{2} f_r$).

Number of points = 16,384 and fibre step size = 10 m.

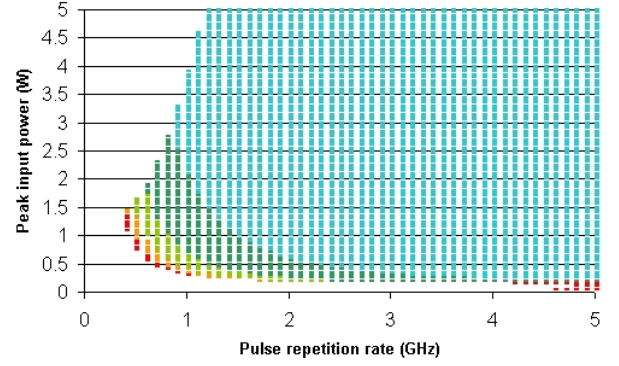
Note: the left hand column of plots is a “zoomed in” version of the right hand column.



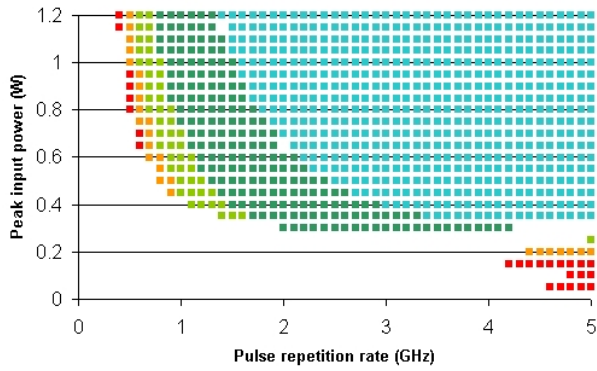
5. Modelling pulse compression through fibre



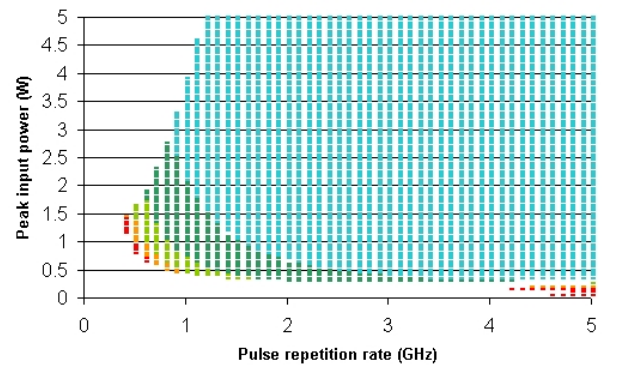
(c) pulses under 20 ps [$f_r = 0$ to 5 GHz, $P_0 = 0$ to 1.2 W]



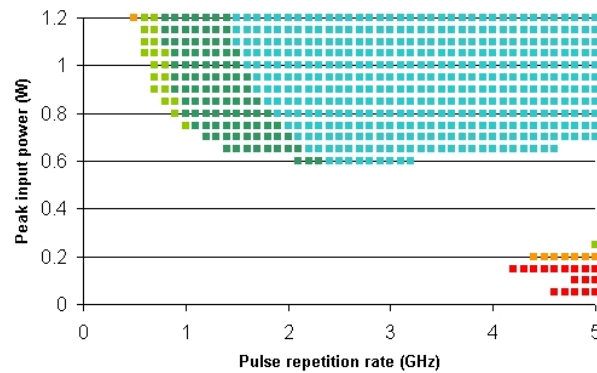
(d) pulses under 20 ps [$f_r = 0$ to 5 GHz, $P_0 = 0$ to 5.0 W]



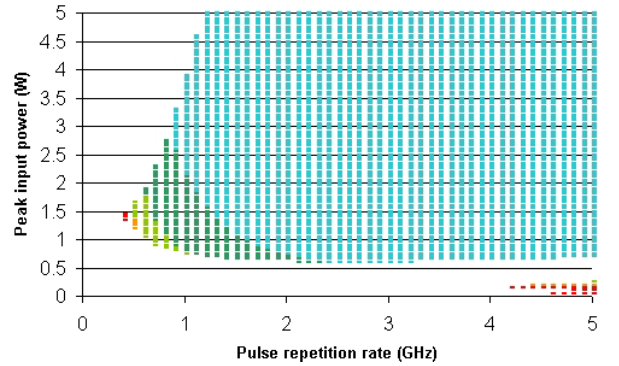
(e) pulses under 10 ps [$f_r = 0$ to 5 GHz, $P_0 = 0$ to 1.2 W]



(f) pulses under 10 ps [$f_r = 0$ to 5 GHz, $P_0 = 0$ to 5.0 W]



(g) pulses under 5 ps [$f_r = 0$ to 5 GHz, $P_0 = 0$ to 1.2 W]



(h) pulses under 5 ps [$f_r = 0$ to 5 GHz, $P_0 = 0$ to 5.0 W]

The multiple batch run plots, Fig. 5.13(a)-(h), show the predicted combinations of pulse repetition rates and peak input powers which compress the modulator-at-null output after some length of SMF-28 fibre to give the FWHM indicated for each plot, either <30 ps, <20 ps, <10 ps or <5 ps. The length of fibre required for each repetition rate and input power is given by the colour contours, in 10 km steps to ease visualisation.

These plots suggest that sub-20 ps pulses can be obtained for around 200 mW peak input powers and fibre lengths of 30 km and under. The shortest predicted pulse widths of under 10 and 5 ps pulses require higher powers of >600 mW, which is not ideal due

to the stimulated Brillouin scattering effects encountered by some of the pulse compression schemes discussed in Chapter 4.

5.6 Specific SMF-28 input power and repetition rate example

Using Fig. 5.13 as a guide for feasible parameters for generating a desired compressed pulse width, it is then possible to look in more detail at the pulse evolution through the fibre for a specific input power and repetition rate combination. For illustration, a 3 GHz repetition rate pulse launched with 190 mW peak power is modelled through SMF-28 only (i.e. the same parameters used in the 3D pulse evolution plot, Fig. 5.4).

Fig. 5.14 shows the compression of the pulse as it propagates through the fibre, with a minimum pulse width of 16.5 ps observed for 20.14 km of fibre. After this fibre length, the pulse width actually starts to increase. This corresponds to the start of the transition from a single peak to a double peak, as in Fig. 5.2.

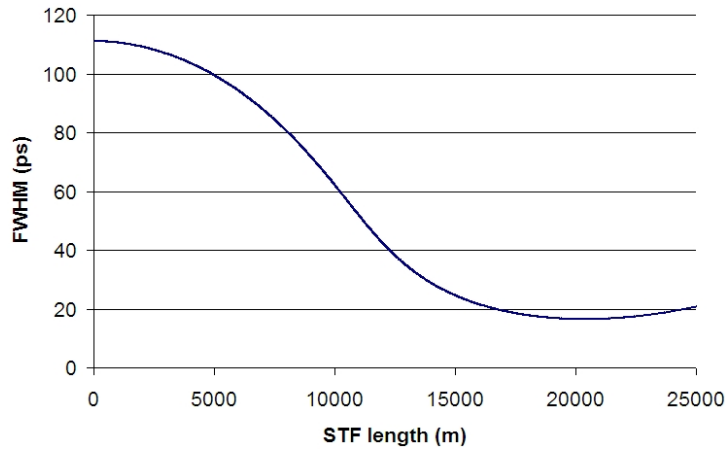


Fig. 5.14. Decreasing FWHM as the pulses are compressed through fibre to under 20 ps.

The minimum pulse width obtained for this combination of 190 mW peak input power at a 3 GHz repetition rate is 16.5 ps, after 20.14 km of SMF-28 fibre. There is a noticeable pedestal at this length of fibre, Fig. 5.15, with a peak to pedestal power ratio of 19.79 (13 dB), Fig. 5.16. However, despite the presence of a pedestal, it is important to note that the vast majority, almost 80%, of the total time-slot energy is contained in the central pulse, Fig. 5.17.

5. Modelling pulse compression through fibre

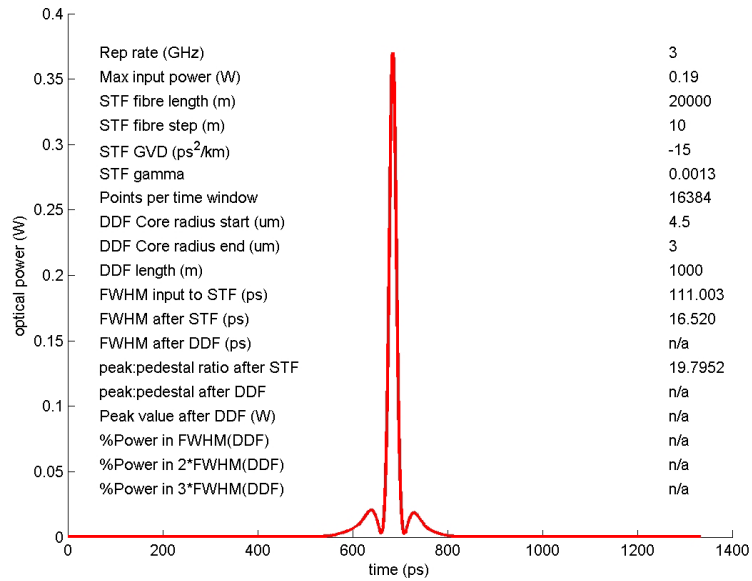


Fig. 5.15. A snapshot of the pulse envelope at the fibre length corresponding to the optimally compressed pulse for 190 mW peak input power and a 3 GHz repetition rate, after 20 km of fibre.

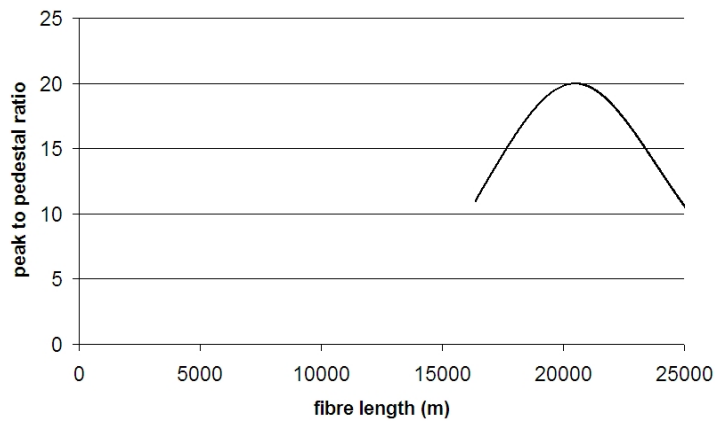


Fig. 5.16. Peak to pedestal power ratio. Note there is no distinct pedestal up until 16.34 km, although this does not necessarily mean that the total pulse power is contained in only a narrow central portion of the pulse, only that there are no sidelobes on the main pulse.

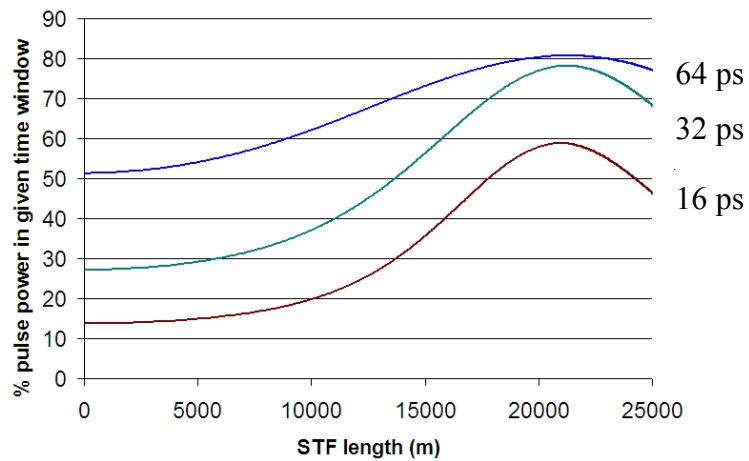


Fig. 5.17. Power contained in stated time windows around the pulse peak. 16 ps is the pulse FWHM and 32 ps is the full width of the main central peak (without the pedestal).

5.7 Dispersion decreasing fibre (DDF) model implementation

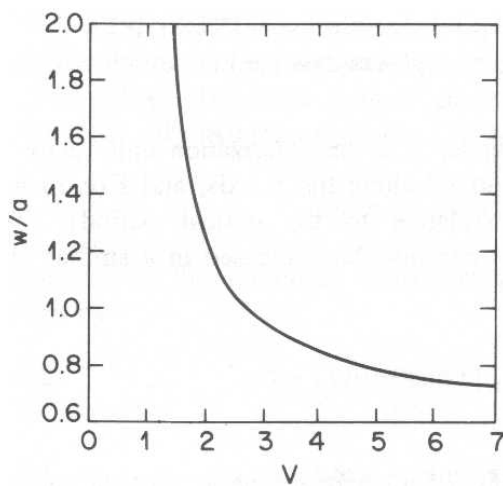
The input to the dispersion decreasing fibre (DDF) section is the output from the SMF-28 section discussed in the previous section.

The DDF section is modelled as a series of short constant diameter fibres, each of diameter slightly narrower than the previous DDF section. The split-step Fourier method is then applied to each section as before.

The nonlinearity and dispersion coefficients, γ & β_2 , are both related to the fibre radius. The radius is gradually reduced over the length of the DDF section, and γ & β_2 must be calculated for use by the split-step Fourier algorithm for each subsection of the DDF length.

As defined in Eq. 5.4, the nonlinear coefficient γ is given by:
$$\gamma = \frac{n_2(\omega_0)\omega_0}{cA_{eff}} \quad (5.4)$$

The effective width parameter, w , can be calculated from a numerical solution such as Fig. 5.18. Fitting a polynomial to such a numerical solution gives Eq. 5.10, related to the normalised frequency, V (commonly known as the V number), given by Eq. 5.11.



$$\frac{w}{a} \approx 0.65 + \frac{1.619}{V^{1.5}} + \frac{2.879}{V^6} \quad (5.10)$$

for $0.8 < V < 2.5$

Fig. 5.18. The effective width parameter variation with V number

5. Modelling pulse compression through fibre

The normalised frequency, V (5.11)

$$V = k_0 a (n_1^2 - n_2^2)^{\frac{1}{2}}$$

where $k_0 = 2\pi/\lambda$, $n_1 = 1.450$ & $n_2 = 1.445$

So to model γ for each DDF section: 1) reduce core radius a

2) calculate $V \propto a$

3) interpolate width parameter w , for V

4) calculate $\gamma \propto A_{\text{eff}} \propto w$

The group velocity dispersion coefficient, β_2 , is given by: (5.12)

$$\beta_2 = -\frac{\lambda^2}{2\pi c} D_T$$

Where (5.13)

$$D_T = D_W + D_M + D_P = \frac{\lambda}{c} \left| \frac{d^2 n_1}{d\lambda^2} \right| - \left(\frac{n_1 - n_2}{\lambda c} \right) V \frac{d^2(Vb)}{dV^2} + D_P$$

total
dispersion

material
dispersion

waveguide
dispersion

profile
dispersion

For typical fibre, the material dispersion is $\sim 13.5 \text{ ps nm}^{-1} \text{ km}^{-1}$ and the profile dispersion is $\sim 0.4 \text{ ps nm}^{-1} \text{ km}^{-1}$ at 1550 nm. The waveguide dispersion, D_{wg} , varies however as the normalised frequency varies with fibre radius:

$$D_{\text{wg}} = \frac{\partial}{\partial \lambda} \frac{\tau_{\text{wg}}}{L} = - \left(\frac{n_1 - n_2}{\lambda c} \right) V \frac{d^2(Vb)}{dV^2} \quad (5.14)$$

waveguide
parameter

To find the waveguide parameter, once again a numerical solution is used. In the modelling two polynomials were fitted, one for when $V < 1.25$ and one for $V \geq 1.25$

Having calculated the waveguide dispersion D_{wg} , and hence the total dispersion, D_T , the group velocity parameter β_2 is calculated using Eq. 5.12. Note that D_T is in ps/nm/km

5. Modelling pulse compression through fibre

whereas β_2 is in ps^2/km , hence a scaling factor of 10^6 is required to convert from $\text{ps}/\text{nm}/\text{km}$ to ps^2/km using Eq. 5.12 (Appendix F).

Using Eqs. 5.4 and 5.12 it is then possible to obtain the group velocity dispersion, β_2 , and the non-linearity γ as functions of the core radius a , Fig. 5.19.

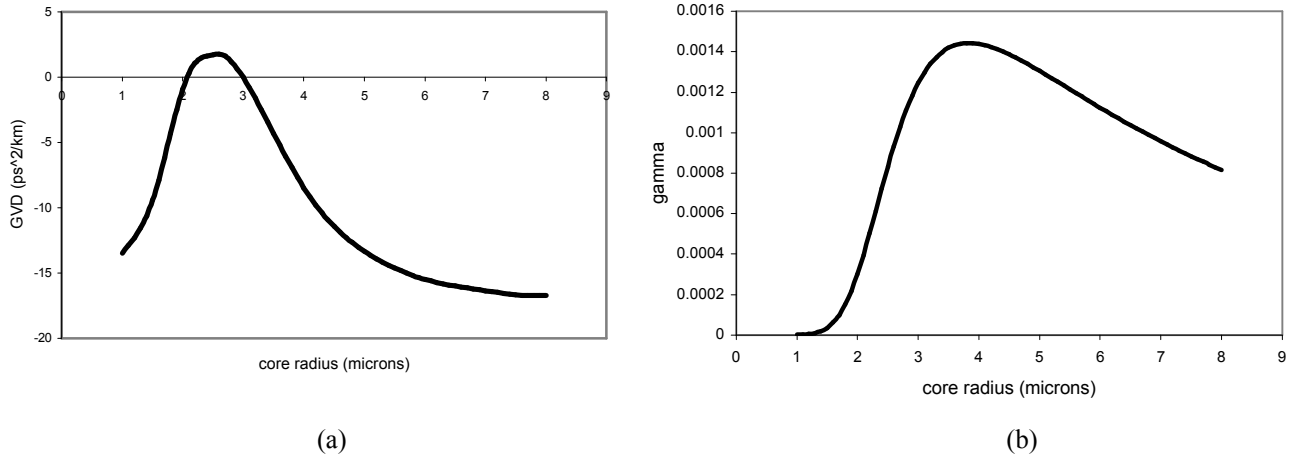


Fig. 5.19. Calculated (a) $GVD \beta_2 \propto \text{core radius } a$, and (b) $\text{non-linearity } \gamma \propto \text{core radius } a$.

The next step was to investigate which DDF set-up provided the shortest, best quality pulses. The variables of interest were: DDF length, DDF core start and end radius and the length of SMF-28 after which the DDF should be implemented.

Simulations demonstrated that the optimum core radius variation was from 4.5 to 3.0 μm , giving a variation in β_2 of approximately -13 to 0 ps^2/km , with γ remaining relatively constant, varying from 0.0012 to 0.0014 over the same radius change. Simulations suggest that it is not necessary to have a larger core variation, as results are very promising with the 4.5 to 3.0 μm variation, as discussed in the next section. Interestingly, when the core radius was increased (rather than decreased) the pulse duration was seen to increase as expected. The length of the DDF was largely unimportant, for lengths over at least several hundred metres.

5.8 DDF model runs

The pulse envelope was propagated through a length of DDF after *every* 10 m step through the 19.5 km of SMF-28, to gain an understanding of the DDF pulse compression performance. The step size through the SMF-28 was initially chosen to be 10 m when evaluating all the possible core diameter variations to keep the runtime manageable. After iterative investigations, the DDF considered was 1 km long, *initially* modelled as 50 x 20 m sections to gain an understanding of the generic behaviour, with the core radius decreased at a constant rate from 4.5 to 3.0 μm over the 50 DDF steps, Fig. 5.20(a).

After iteratively investigating many different DDF fibre runs (not detailed in this thesis), the following fibre parameters in Table 5.5 were finalised as they provide short duration (~ 100 fs) pulses with very little pedestal present, as will be discussed.

SMF-28 parameters	DDF parameters
SMF-28 $\gamma = 0.0013$ SMF-28 $\beta_2 = -15 \text{ ps}^2/\text{km}$ SMF-28 step size = 10 m	DDF core radius = 4.5 to 3.0 μm DDF $\beta_2 = 13 \text{ ps}^2/\text{km}$ to 0.1 ps^2/km DDF $\gamma = 0.0012$ to 0.0014 DDF length = 1 km
Parameters common to SMF-28 and DDF	
cladding refractive index, $n_{\text{clad}} = 1.45$ core refractive index, $n_{\text{core}} = 1.445$ (i.e. $\Delta n = 0.005$) core nonlinear refractive index $n_2 = 3 \times 10^{-20} \text{ m}^2/\text{W}$	

Table 5.5. *Fibre parameters used in the model for the SMF-28 and DDF sections*

Fig. 5.20(a) shows that in terms of pulse compression it is only worthwhile considering implementing the DDF section if the input to the DDF is already compressed to around 20 ps duration, as no significant compression occurs otherwise.

Following the initial generic run to gain an understanding of the DDF characteristics, a second more detailed run was performed with more points per time-slot (65,536) and

the DDF was modelled more accurately as 1,000 x 1 m sections, Fig. 5.20(b). This modelling suggests that an appropriate DDF section after the SMF-28 can compress the pulses to durations as short as 100 fs. Reassuringly from an implementation point of view, the SMF-28 length does not have to be highly precise and a range of SMF-28 lengths of around 19,250-19,750 m provides the shortest post-DDF pulse duration of ~100 fs.

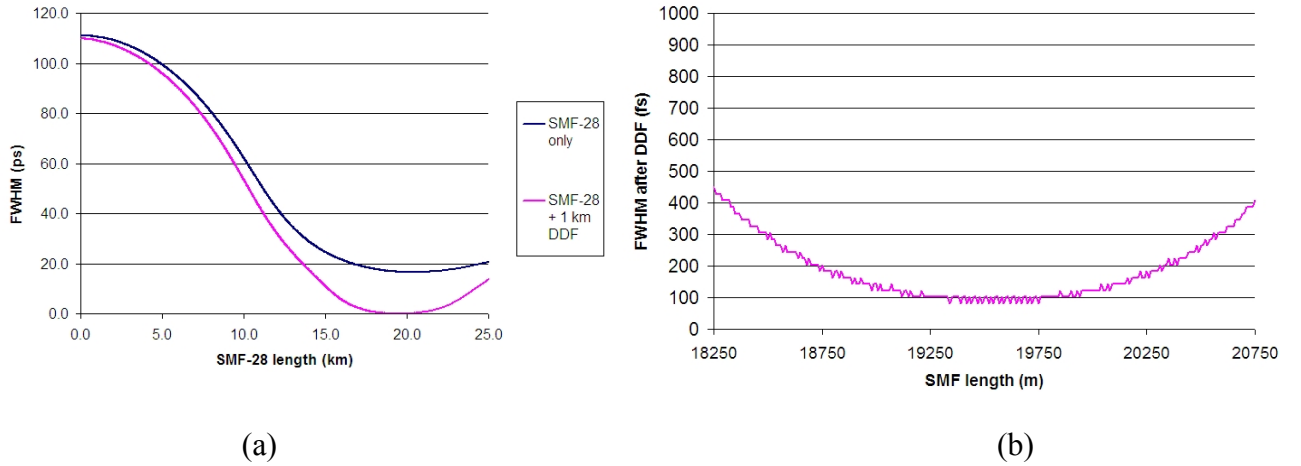


Fig. 5.20. (a) **Generic run.** The pulse FWHM from the given length of SMF-28 (blue plot) is propagated through DDF fibre (pink plot), modelled as 50 x 20 m sections. Substantial pulse compression through the DDF only occurs when the SMF-28 has already compressed the pulse to around 25 ps. Number of points = 16,384. (b) **Detailed run.** The output from the SMF-28 is propagated through the DDF only if the pulse is <17.5 ps. For this run the DDF is modelled as 1,000 x 1 m steps and the number of points = 65,536.

5.8.1 DDF step size accuracy

In the previous section, Fig. 5.20 demonstrates that a 1 km DDF section with core radius varying from 4.5 to 3.0 microns is predicted to produce compressed pulses as short as ~100 fs. This was demonstrated for modelling where the core size was uniformly decreased over 1,000 x 1 m sections.

Table 5.6 shows the global relative error and various DDF output pulse parameters for a range of different fibre step sizes through the DDF. The number of points per time-slot for these runs was 16,384. The global relative error is only reduced to an insignificant level when using at least 10,000 sections of 0.1 m steps. However for large batch runs, the DDF arrangement of 1,000 sections of 1 m provides a modest global relative error of <1% which is acceptable to establish generic pulse behaviour.

DDF section length (m)	No of DDF sections	FWHM (ps)	Peak power after DDF (W)	Peak:pedestal power ratio	Global relative error
0.01	100,000	0.081	15.6394	105.5740 (20.236 dB)	n/a
0.1	10,000	0.081	15.6279	105.4890 (20.232 dB)	5.7909e-4
1	1,000	0.081	15.4730	104.3728 (20.185 dB)	6.5676e-3
4	250	0.081	14.4908	97.7039 (19.899 dB)	3.5565e-2
10	100	0.081	11.5757	76.5273 (18.838 dB)	1.4254e-1
20	50	0.244	8.0182	43.2125 (16.356 dB)	3.3098

Table 5.6. Varying the length of the DDF step size from 0.01 m to 20 m illustrates that a step size of at most 0.1 m is necessary to avoid introducing significant numerical errors. Step sizes of 0.1 m and 0.01 m lead to pulse parameters that are identical to at least 3 significant figures and a global relative error of only 5.8e-4 (0.06%). [Run parameters: number of points = 16,384, SMF-28 length = 19.5 km, DDF length = 1 km, 3 GHz pulse launched at 190 mW peak power].

5.8.2 DDF number of points per time-slot

Once the pulse has compressed to <1 ps after the DDF, the time-step across the pulse time-slot starts to become significant in terms of quantising the FWHM and also adding to the global relative error in the E-field envelope. In a previous section discussing the SMF-28 output, Table 5.3 showed that the global relative error of the SMF-28 output was insignificant for all number of points tested, where 8,192 points was the minimum test size. However in Table 5.7 below, using only 8,192 points leads to a significant global relative error of 0.0552. The FWHM is also measured as zero for this number of points, since the peak only occupies a single time point and so it is “infinitely short”. Once the number of points is increased to 65,536, the FWHM remains constant at 102 fs. The global relative error for the DDF output becomes insignificant for pulse envelopes $\geq 32,768$ points.

5. Modelling pulse compression through fibre

Number of points per window	FWHM (ps)	Peak power after DDF (W)	Peak:pedestal power ratio	Global relative error
8,192	0.000	13.0169	85.8321 (19.337 dB)	5.5263e-2
16,384	0.081	19.2650	104.3728 (20.186 dB)	1.1002e-2
32,768	0.081	20.0124	136.2038 (21.342 dB)	1.7193e-4
65,536	0.102	20.0088	136.2382 (21.343 dB)	9.2506e-7
131,072	0.102	20.1776	136.2431 (21.343 dB)	n/a

Table 5.7. Varying number of points across pulse time-slot. A 190 mW peak power 3 GHz pulse is launched into 19.5 km of SMF-28, followed by a 1,000 x 1 m length of DDF, for various numbers of points across a fixed time window. The global relative error suggests that at least 32,768 points are required to accurately model the propagation through the DDF section.

5.8.3 Example of high quality DDF output pulse

Following analysis of the generic behaviour of the DDF output for different DDF step sizes and numbers of points, a final high accuracy run was performed using 131,072 points per time-slot. The DDF was modelled as a 1 km long fibre with a core radius which tapers uniformly from 4.5 to 3.0 microns in 100,000 x 0.01 m sections. The DDF output pulse shape is shown in Fig. 5.21, and notably it does not exhibit the same level of sidelobes as the output from the SMF-28. The DDF output pulse has a peak:pedestal power ratio = 136, i.e. the pedestal is 21.3 dB down on the pulse peak. The temporal pulse shape is visually very clean and looks highly suitable for applications including optical sampling.

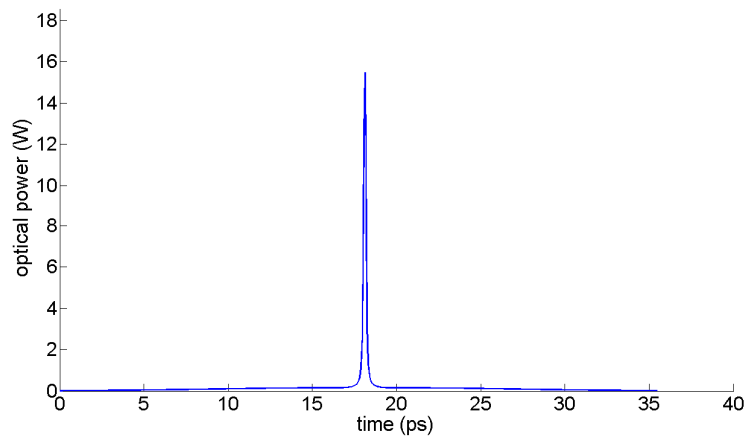


Fig. 5.21. Output pulse from 19.5 km of SMF-28 followed by 1 km of DDF. The DDF is modelled as 100,000 x 0.01 m sections of uniformly tapering core radius from 4.5 to 3 microns. The number of points per time-slot is 131,072. The DDF output pulse has FWHM of 102 fs, and a 21 dB peak to pedestal ratio.

Fig. 5.22 shows the corresponding spectral content of the ~ 100 fs pulse after propagation through both the SMF-28 and DDF fibres. In comparison to Fig. 5.6, which shows the spectra of the launch pulse and the SMF-28 output pulse, there is broad spectral content surrounding the central carrier wavelength. In the case of the ~ 16 ps pulse output from the SMF-28 fibre in Fig. 5.6, the optical power at >1 nm offsets from the carrier is 60 dB lower than the carrier. The ~ 100 fs output pulses from the DDF however, Fig. 5.22, possess a spectral pedestal sloping from 20 dB to 40 dB, relative to the carrier, at offsets up to 50 nm from the carrier.

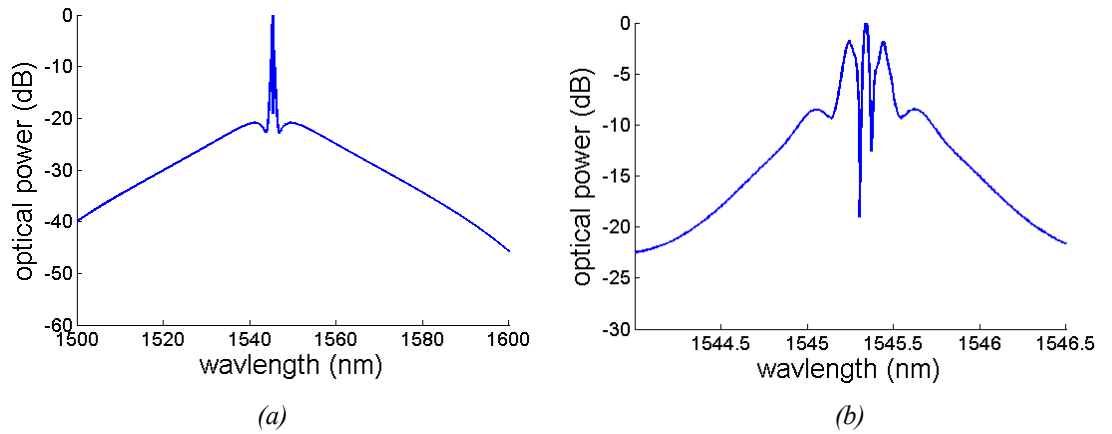


Fig. 5.22. The spectral content of the ~ 100 fs pulse output from the DDF section. Plots (a) and (b) show the pulse spectra over two different frequency and power ranges. Plot (b) is a close-up of the detailed structure around the carrier wavelength.

5.9 DDF performance summary

Pulses as short as 102 fs were modelled for a 1 km DDF section which immediately follows a 19.5 km SMF-28 fibre. The final model run used 131,072 points per pulse time-slot, and a very short incremental decrease in the core diameter to accurately approximate a truly tapering DDF section (100,000 sections of 0.01 m). The modelled pulse pedestal is very well suppressed (21.3 dB down on the main peak). Importantly, for a 190 mW peak launch power into the SMF-28, the 1 km DDF section generates ~ 100 fs pulses after an SMF-28 section of $19.5 \text{ km} \pm 250 \text{ m}$, suggesting that the experimental arrangement generating ~ 100 fs pulses would be fairly stable since fibre lengths (or alternatively peak launch powers) can be defined to relatively low precision ($19,500 \pm 250 \text{ m}$, i.e. around 1%).

5.10 Conclusions from pulse modelling

In conclusion, repetition rates as low as around 1.5 GHz are predicted by the modelling, for the modulator biased-at-null approach for generating soliton-effect compressed pulses. Detailed modelling was performed on a 3 GHz pulse train using the optimum number of points per time-slot and fibre step size, as confirmed by global relative error analysis. The initial waveform is launched through 19.5 km of SMF-28, to compress the pulses to around 16.6 ps. The waveform is then launched through a 1 km section of DDF, the core radius of which tapers uniformly from 4.5 to 3.0 microns. For the 3 GHz pulse train, the required peak launch power is 190 mW, which is easily achievable with commercially available EDFAs, and the 19.5 km of SMF-28 fibre is an easily procured commercial item. After the SMF-28 fibre section, the pulse exhibits pedestals at 12.8 dB relative to the pulse peak, which may prove to be limiting factor for high bandwidth sampling. However, after compression through both SMF-28 and a 1 km section of DDF, the pedestal has been reduced to 21 dB below the pulse peak power. The key pulse characteristics observed in the modelling are summarised in Table 5.8.

Input Frequency	3.0 GHz
Peak Input Power	190 mW
Pulse FWHM input to SMF-28	111.0 ps
Pulse FWHM output from SMF-28	16.6 ps
Pulse FWHM after DDF	102 fs
Pulse compression ratio: input:SMF-28	6.7
SMF-28:DDF	166
Peak:pedestal power ratio: SMF-28	19 (12.8 dB)
DDF	136 (21.3 dB)
Max. power of pulse after DDF	20.1 W
SMF-28 length	19.5 km
SMF-28 range providing 102 fs pulses after DDF	19.5 km \pm 250 m

Table 5.8. Key pulse performance parameters for a waveform launched in 19.5 km of SMF-28 followed by a 1 km section of DDF. The initial launch waveform is generated by a modulator-at-null driven with a 1.5 GHz single tone, to generate 3 GHz optical pulses. The peak power launched into the SMF-28 is 190 mW.

Analysis of the number of points required and the fibre step size, using the relative global error approach, gives confidence that the model has been implemented using high enough precision. The unperturbed sech waveform after tens of kilometres of propagation also provides confidence that the model has been correctly implemented. Further, the demonstration of the DDF fibre implementation and subsequent 100 fs pulses shows that the model can in theory generate very short pulses with negligible global relative error. The main source of discrepancies between the modelling and experimental realisation is therefore assumed to stem from inaccurate modelling parameters for the fibre attenuation, dispersion and non-linear coefficient.

References for Chapter 5

1. G. P. Agrawal, "Nonlinear Fibre Optics", 2nd edition, Academic Press (1995)
2. Sinkin O.V., Holzlohn R., Zweck J., Menyuk C.R., "Optimization of the split-step Fourier method in modeling optical-fiber communications systems", J. Lightwave Technol., 21(1), pp. 61-68, 2003

6. Experimental pulse source implementation

This chapter details the successful experimental implementation of the optical pulse source which was modelled in the previous chapter, using 25 km of Corning's SMF-28 telecommunications fibre to provide compressed pulses at gigahertz repetition rates. Pulse durations as short as 10-15 picoseconds were measured using an autocorrelator. Various methods for overcoming stimulated Brillouin scattering (SBS) were investigated, with phase modulation selected as the preferred option since it adds the least timing jitter artefacts to the optical pulse train. The experimental performance compares well with the modelled predictions using a variety of measurement techniques, including autocorrelation and fast oscilloscope captures in the time domain, and analysis in the wavelength domain using optical spectrum analyser measurements.

6.1 Generic experimental arrangement

The generic arrangement shown in Fig. 6.1 was first implemented using components sourced for the QinetiQ photonic ADC programme. A CW operation DFB laser with suitable temperature control was employed to ensure wavelength stability to better than 0.1 nm. Several intensity modulators were evaluated for long-term drift, before a JDS Uniphase device was selected for its stability. An IPG Photonics ≤ 1 W EDFA provided amplification of the modulator output before compression through a length of Corning SMF-28 standard telecommunications fibre (reels of 8.8 km, 12.8 km and 25.2 km were purchased for the programme). A New Focus detector with 45 GHz bandwidth then provided input to either a 34 GHz bandwidth hp 54120B sampling oscilloscope or an hp 8565E spectrum analyser.

6. Experimental pulse source implementation

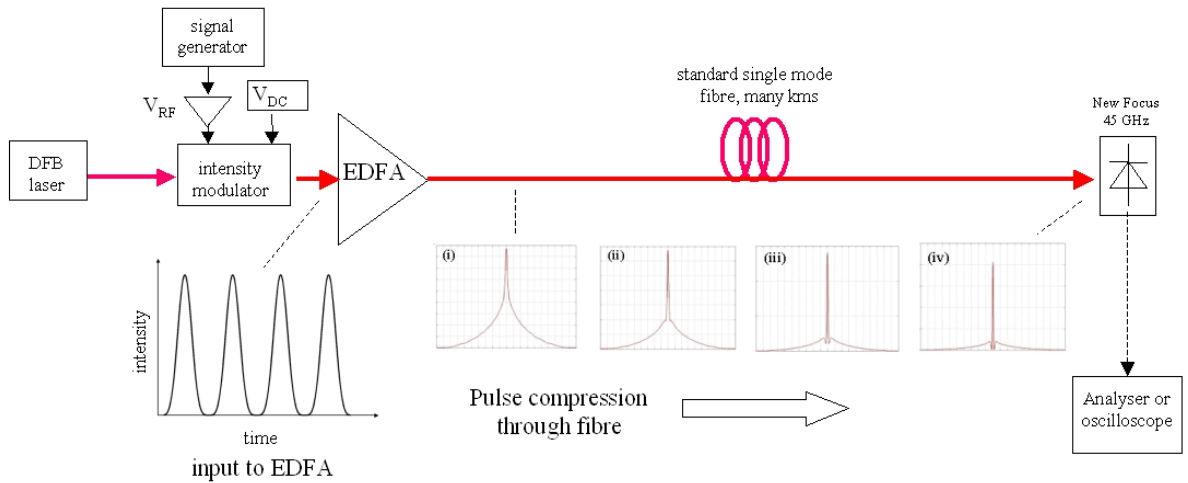


Fig. 6.1. Generic experimental arrangement. An intensity modulator biased at null modulates the output from a CW DFB laser and the resultant waveform is then amplified before compression through fibre.

An example of 3 GHz output pulse is given in Fig. 6.2. The ringing effect on the trailing edge is believed to be due to the detector, and is not present on autocorrelation traces, shown later in Fig. 6.18. Pulse duration measurements are limited using the 34 GHz sampling scope to of the order 25-30 ps, requiring the use of an autocorrelator to make more detailed measurements. Autocorrelator measurements and timing jitter are discussed shortly.

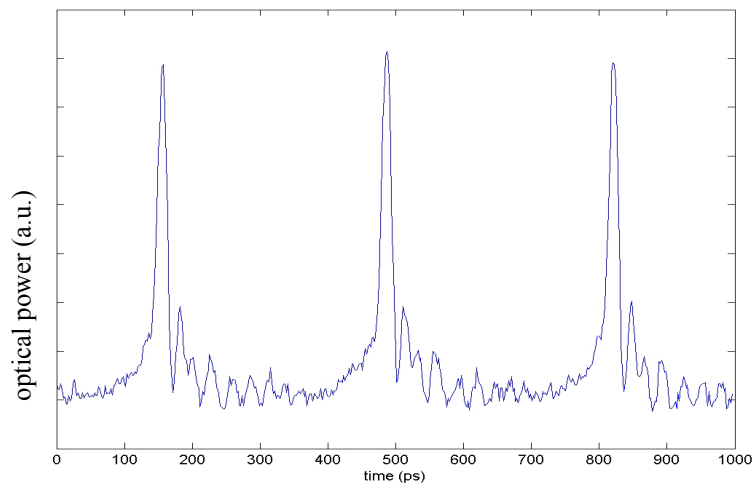


Fig. 6.2. Example of 3 GHz pulse obtained after compression through 25 km of SMF-28 fibre.

6.2 Removing EDFA amplified spontaneous emission

A fibre Bragg grating (FBG) was implemented into the system immediately after the EDFA, to minimise the effects of amplified spontaneous emission (ASE) through the compression fibre. It was hoped this would reduce Gordon Haus jitter, where a change of pulse centre frequency translates into a change of group velocity which will subsequently affect the pulse timing^[1]. To eliminate this problem, the DFB wavelength was tuned to match a 0.35 nm FBG, such that with the use of a circulator only the DFB wavelength was reflected back into the compression fibre and the majority of the ASE was simply discarded (the FBG arrangement is shown on the final system diagram, Fig. 6.13). In this way a (wavelength dependent) reduction of up to 18 dB was observed at wavelengths other than the DFB wavelength of 1543.5 nm. However, it was found that the contribution of the EDFA ASE to the timing jitter was irrelevant, as will be discussed in Chapter 7, so the FBG could optionally be omitted from the system with no obvious detriment to performance.

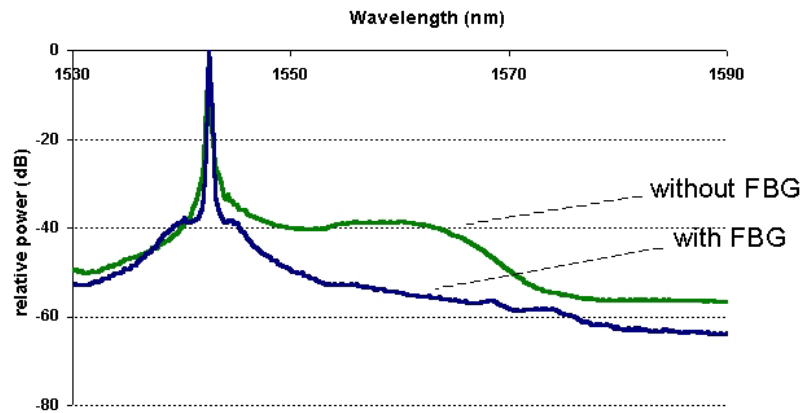


Fig. 6.3. Reduction of ASE by up to 18 dB (wavelength dependent) through the use of a FBG and circulator.

6.3 Stimulated Brillouin scattering (SBS)

As indicated by many of the soliton compression papers reviewed in Chapter 4, stimulated Brillouin scattering (SBS) is often a major problem when launching into long lengths of fibre, and this proved to be the case when the set-up in Fig. 6.1 was

implemented. The effects of SBS therefore had to be overcome before any pulses resembling those in Fig. 6.2 were realised.

SBS is a nonlinear process, more precisely a backward propagating Stokes wave, which carries most of the input power once the SBS threshold has been reached. Unlike stimulated Raman scattering (SRS), SBS only propagates backwards in the fibre rather than in both directions. Practically, it is therefore sensible to use an isolator after any component which propagates powers higher than the SBS threshold into long lengths of fibre, to avoid unwanted reflections.

In order to reduce the effects of SBS, either the pulse width should be shorter than the phonon lifetime (16 ns) or the linewidth should be broader than the Brillouin threshold linewidth of around 17 MHz^[2]. The linewidth can effectively be broadened for a single mode pump whose phase varies at a higher frequency than the Brillouin linewidth.

In the proposed pulse compression scheme in Fig. 6.1, a DFB laser is used as it provides single-mode operation to avoid dispersion problems due to different modes propagating through the compression fibre. However, the drawback of the DFB laser is that it has a linewidth of <3 MHz, and so inevitably SBS was experimentally found to be a major problem, as will be discussed shortly. Several methods were tried (or considered) to overcome the scattering:

- Firstly a tuneable laser with a variable cavity length was used as the CW source instead of the DFB, but the tuning frequency of several kHz was not fast enough to overcome the SBS.
- In order to generate a broadband source, a 0.8 nm fibre Bragg grating (FBG) was used to select ~100 GHz of the ASE of an EDFA, far exceeding the 30 MHz linewidth of the SBS, Fig. 6.3. Although this source did overcome the SBS, the source was too broad to allow the non-linear and dispersive effects to compress the input waveform as modelled, and the input waveform was simply propagated through the fibre virtually unaltered.

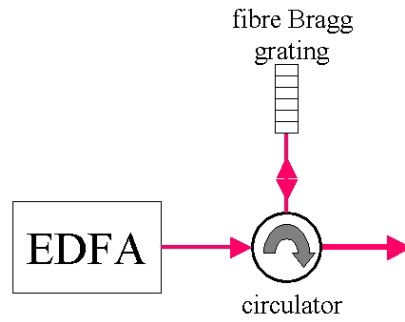


Fig. 6.4. Broadband source: an FBG selects a 100 GHz linewidth of the ASE of an EDFA.

However, two other options were implemented which did prove successful for SBS suppression and subsequent generation of high quality compressed pulses: phase modulation and injection dithering.

- The **phase modulation** approach for overcoming SBS has been widely used in the soliton literature described in Chapter 4, and was used effectively to broaden the linewidth of the input to the fibre in the experimental set-up described here. The phase modulator was added to the system before the intensity modulator and driven with a single tone frequency. An advantage with the phase modulation approach is that it should add only negligible intensity modulation if a suitable phase modulator is implemented.
- A second method which successfully suppressed the SBS was **injection dithering** applied to the DFB drive current source. This method involves periodically varying the DFB drive current, thus slightly varying the carrier density and so broadening the output linewidth. It is essential that the current dithering amplitude is negligible compared to the bias current level as variable launch powers will lead to variable pulse compression and an irregular pulse stream. Ignoring any compression problems, for sampling applications the dithering amplitude should be less than half a bit (i.e. less than 1 part in 10^4 for 12-bit accuracy), to avoid introducing sampling errors, although it is possible that any small scale amplitude dither could be calibrated out since the dither waveform could be known accurately, however it would seem preferable to avoid this complication if possible.

The SBS was observed in two ways. Firstly, the output power from the fibre was much lower than expected for a given input and also fluctuated wildly. When a coupler was added to allow the backscattered light to be viewed on the spectrum analyser, Fig. 6.5, there were strong features at around 11GHz, corresponding to known artefacts due to SBS^[2], Fig. 6.6. These should be expected since the frequency shift backwards, ν_B is related to the acoustic frequency ω_A and in turn the refractive index and wavelength via:

$$\nu_B = \frac{\omega_A}{2\pi} = \frac{2n\nu_A}{\lambda} \quad (6.1)$$

For a typical value $\nu_A = 5.96$ km/s, at 1550 nm wavelengths in fibre (refractive index $n = 1.45$), this gives a frequency shift backwards of $\nu_B \sim 11.1$ GHz.

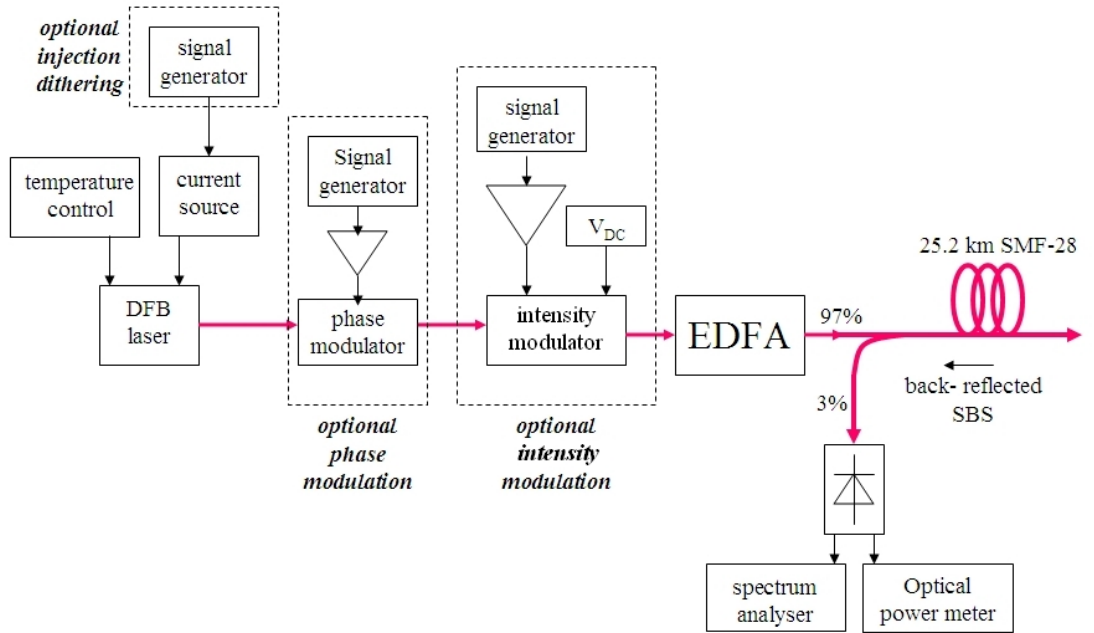


Fig. 6.5. Schematic experimental set-up used to observe the backscattered SBS on either a spectrum analyser or an optical power meter. 3 methods can optionally be applied to try and overcome SBS:

- (i) injection dithering by applying sinusoidal modulation to the laser current source
- (ii) phase modulation
- (iii) using short pulses (intensity modulation)

6. Experimental pulse source implementation

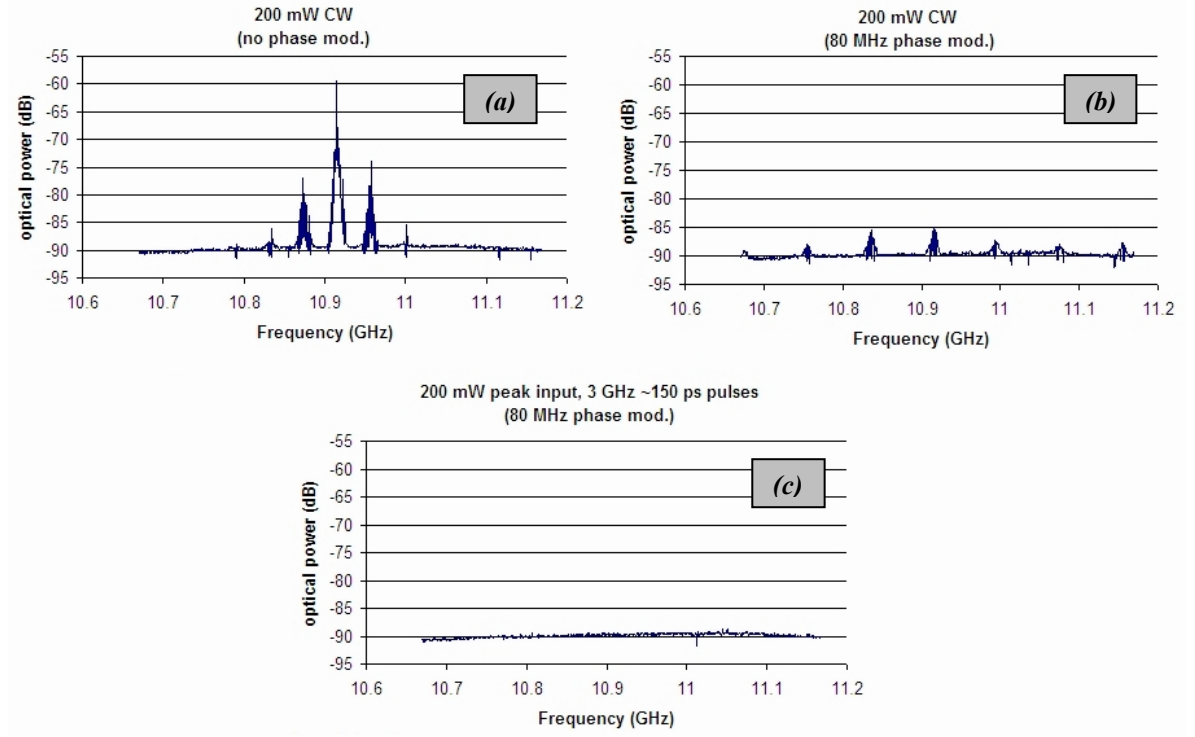


Fig. 6.6. Backscattered spectra from 25.2 km SMF-28 fibre, for the following launch conditions:

- (a) 200 mW CW launch (no phase modulation)
- (b) 200 mW CW launch with 80 MHz phase modulation applied
- (c) 200 mW (peak power) pulses of duration ~150 ps at 3 GHz repetition rate with 80 MHz phase modulation ($\sim V_\pi$ modulation depth).

Fig. 6.6(a) shows strong peaks at 10.92 GHz corresponding to SBS backscattered effects for 200 mW CW launch powers into the 25.2 km fibre. Using 80 MHz phase modulation, Fig. 6.6(b), the magnitude of the backscattered light was reduced, but at the expense of introducing artefacts related to the phase modulation. A combination of short pulses (~150 ps duration) and phase modulation removed any detectable SBS artefacts from the backscattered path, Fig. 6.6(c). Therefore the SBS would appear to have been suppressed.

Unexpectedly, SBS artefacts were also observed in the **output** from the 25.2 km fibre for CW input Fig. 6.7, contrary to theory (such as in Ref. [2]) which states that SBS is only a backward propagating wave. However, despite the use of isolators at either end of the fibre, this may only be a reflected portion of the backscattered wave reflected

onto the output, or it could be Stokes light generated in the forward direction due to a relaxation of the wave-vector rule due to the guided nature of the acoustic waves.

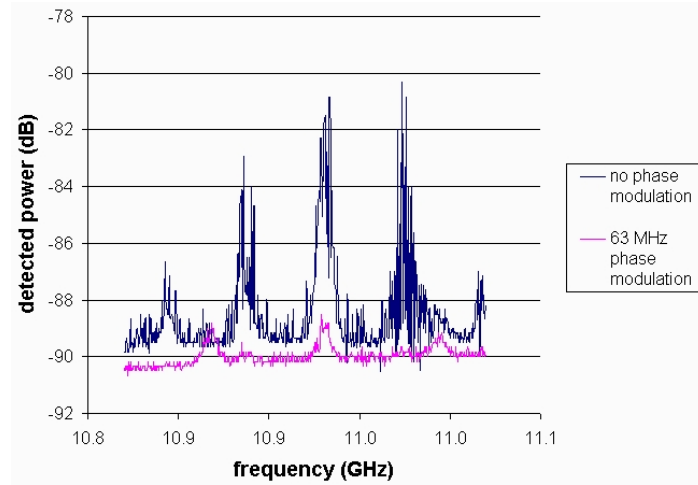


Fig. 6.7. Forward propagating SBS artefacts, with CW launch and no phase modulation (blue plot) and with CW input and 63 MHz phase modulation (pink plot). These artefacts disappear when short pulses (>150 ps) are propagated through the fibre.

The single-tone frequency used to drive the phase modulator was varied, Fig. 6.8, with the aim of having a frequency deviation, $\omega_m \Delta\phi_p$, greater than the Brillouin threshold. Fig. 6.8 shows the fibre output for $\Delta\phi_p = 110^\circ$ ($\approx 0.6V_\pi$) for various frequencies. No SBS suppression was observed for frequencies of the order of kHz, with significant suppression only noted for frequencies greater than around 40 MHz. Four Ramar (now JDS Uniphase) 7 GHz phase modulators were sourced and it was found that the SBS was suppressed for **virtually** the entire frequency range 40 MHz – 4 GHz (limited to 4 GHz only by the signal generator and amplifier arrangement). Notable frequency exceptions at which phase modulation does not significantly suppress the SBS is where the phase modulation frequency is also a multiple of the frequency used to drive the intensity modulator which generates the initial periodic waveform, Fig. 6.9. In this special case the phase modulation lines exactly overlap with the optical carrier frequency lines and therefore there is no effective broadening of the optical launch into the compression fibre, and hence no reduction in the SBS level is observed.

6. Experimental pulse source implementation

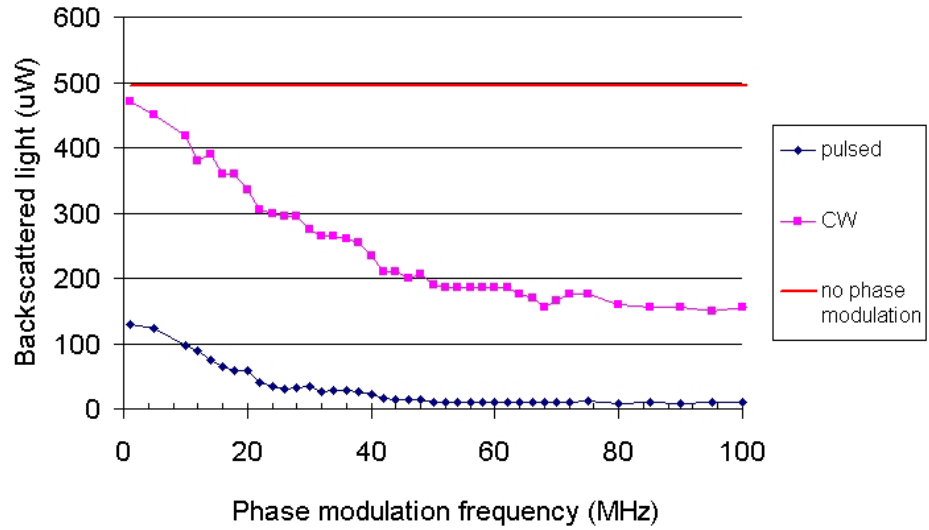


Fig. 6.8. The effect on the SBS of varying the frequency of the phase modulation (200 mW EDFA peak output and a 3% back-scatter coupler).

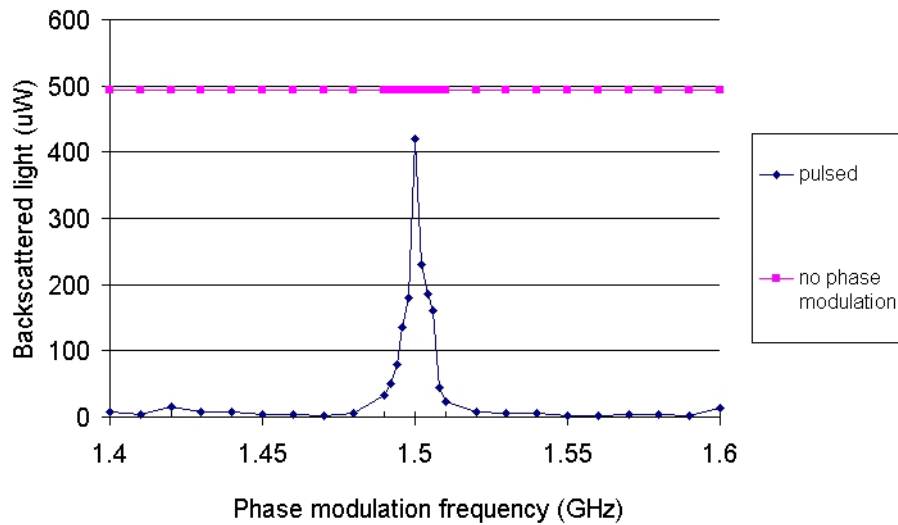


Fig. 6.9. The SBS is suppressed for phase modulations greater than around 40 MHz, with the exception of when the phase modulation frequency is a multiple of the frequency used to generate the period waveform. Here 1.5 GHz phase modulation only slightly suppresses the SBS on 3.0 GHz optical pulses generated from a 1.5 GHz source.

The drawback of using phase modulation is the addition of extra features on the pulse spectra, which ultimately add to the total timing jitter. It is therefore desirable that the minimum possible phase modulation depth is used to overcome the SBS. Fig. 6.10 demonstrates the effect on the measured spectra of increasing the phase modulation

6. Experimental pulse source implementation

depth for 3 GHz repetition rate pulses, measured on a spectrum analyser over the frequency range 0-20 GHz.

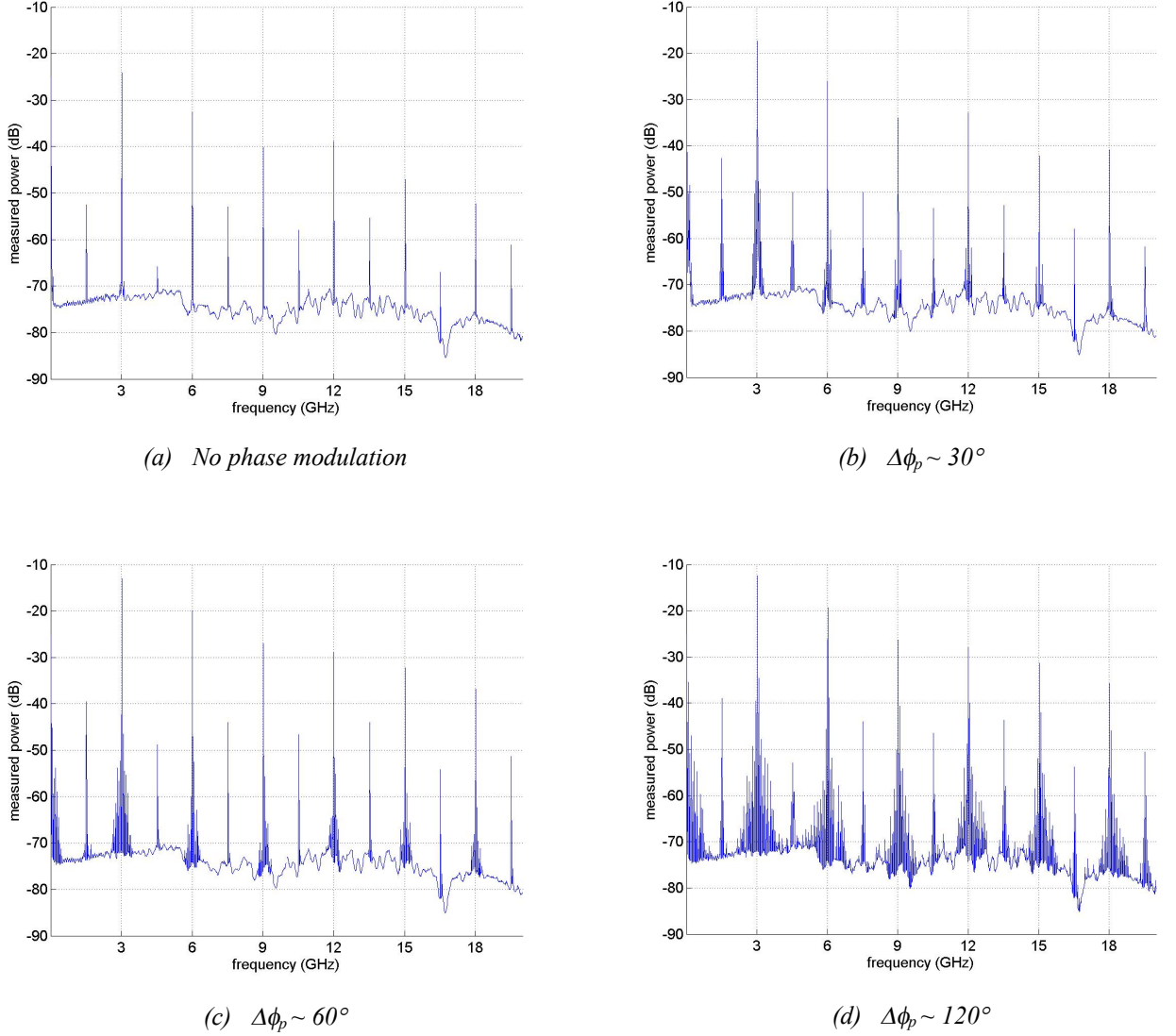


Fig. 6.10. Spectra showing the effect of increasing the phase modulation depth $\Delta\phi_p$. In all 4 cases a 3 GHz pulse train is launched into 25 km of SMF-28.

- In (a), for no phase modulation, the harmonics are clearly reduced due to presence of SBS, when compared to (b)-(d).
- When 63MHz phase modulation is applied, the SBS is suppressed by differing amounts. Note the harmonics in (b) are lower than when $\Delta\phi_p$ is increased in (c) and (d).
- The harmonics increase with larger $\Delta\phi_p$ due to reduced backscattering, up to the point at which SBS becomes negligible. For larger $\Delta\phi_p$ large phase modulation artefacts are present on the optical signal noise floor – compare (d) with (c) and (b).

Fig. 6.11(b) illustrates that when the phase modulation is not sufficient to broaden the linewidth greater than the SBS threshold, coherent noise features are present around the harmonics. However once the threshold linewidth is reached then the phase modulation and frequency components appear as discrete finite spectral lines.

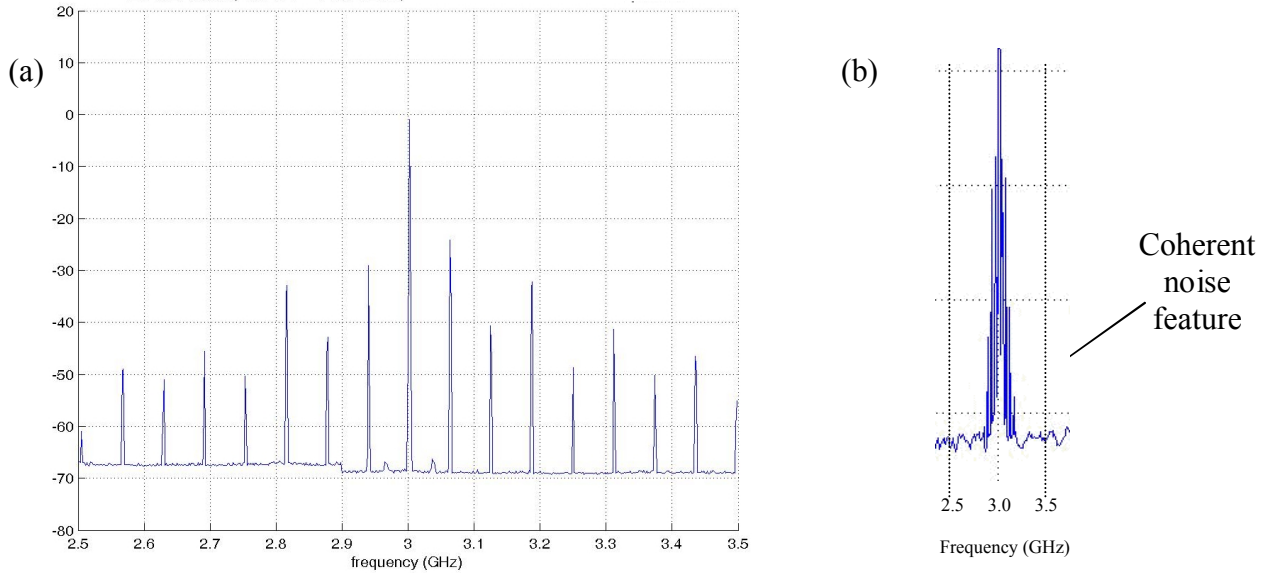


Fig. 6.11. 3GHz repetition rate pulses. (a) For phase modulation depths and frequencies which suppress the SBS, the phase modulation appears as discrete lines as opposed to (b) a coherent noise feature

Similar successful removal of the backscattered SBS effects around 11 GHz was observed when the DFB drive current was periodically modulated via **injection dithering**. For a laser drive current of 245 mA, injection dithering of ± 0.25 mA was sufficient to remove all evidence of SBS on both the analyser and the backscattered light observed on the optical power meter. This level of injection dithering is equal to 0.2% of the DC current level, which would allow optical sampling to be performed with this source to around 9-bit resolution. When the injection dithering level was lowered further to 0.1% of the total drive current, some backscattered power was observed, although this backscattered level was still negligible, at around $1/40000^{\text{th}}$ (~ 46 dB reduction) of the backscattered power when no suppression method was applied. Fig. 6.12 shows the effect of the injection dithering frequency on the backscattered power level, with frequencies of the order 1 kHz to ~ 200 kHz proving successful at removing SBS.

6. Experimental pulse source implementation

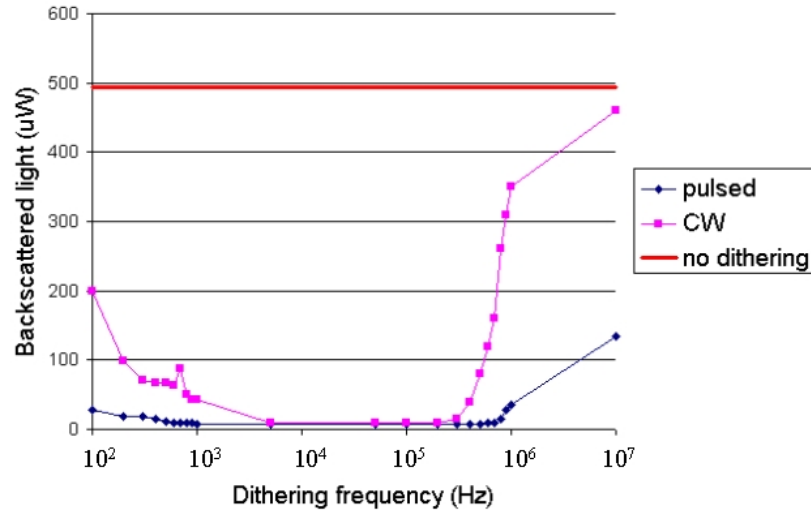


Fig. 6.12. Back-scattered power versus injection dithering frequency. The injection dithering amplitude is 0.2% of the DC current drive level. The input source is a CW DFB amplified to 200 mW launch power into the fibre by an EDFA, with a 97:3 coupler directing back-scattered light onto the optical power meter.

In summary, both phase modulation and injection dithering have been used to successfully reduce the effects of SBS, with only the most negligible levels of backscattered light detected. The implications that these two methods have for the total timing jitter of the pulse stream will be discussed in detail in the next chapter, since injection dithering and phase modulation each introduce different frequency related artefacts to the pulse stream. However, before the timing jitter issues are discussed, some other important pulse parameters will be reported.

6.4 Final system for experimentally generating short ultra-stable pulses

Fig. 6.13 shows a more detailed version of the generic experimental set-up shown in Fig. 6.1 at the start of this Chapter. This new system diagram is updated to include:

- (Optional) phase modulation to overcome SBS
- (Optional) injection dithering to overcome SBS
- (Optional) fibre Bragg grating and circulator to attempt to reduce the effects of amplified spontaneous emission

6. Experimental pulse source implementation

A range of methods are then used to evaluate and characterise the pulse train:

- Capture on a high speed sampling oscilloscope (hp 54120B) to evaluate pulse to pulse uniformity and pulse shape (34 GHz sampling head option)
- Autocorrelator capture to measure the duration of pulses shorter than ~ 25 ps, the limit of the sampling scope
- Spectrum analyser measurements (hp 8656E) to observe noise features around the harmonics and also the optical noise floor across the whole measurable spectrum
- Phase noise measurements (hp E5500) to measure timing jitter

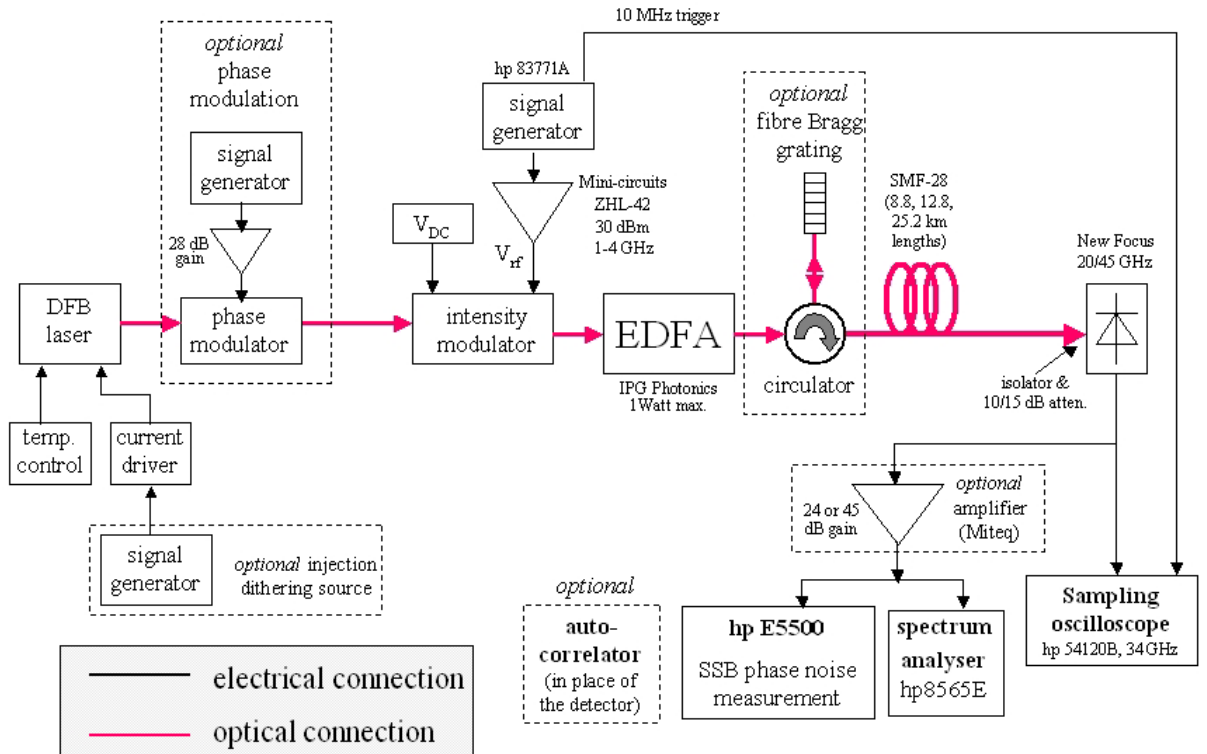


Fig. 6.13. Final experimental configuration, used to generate and characterise the optical pulse train. Phase modulation and/or injection dithering is used to overcome SBS and a fibre Bragg grating can be used to reduce EDFA amplified spontaneous emission.

6. Experimental pulse source implementation

The lowest repetition rate pulse train generated experimentally was ~ 1.5 GHz, although these pulse displayed large pedestals, Fig. 6.14.

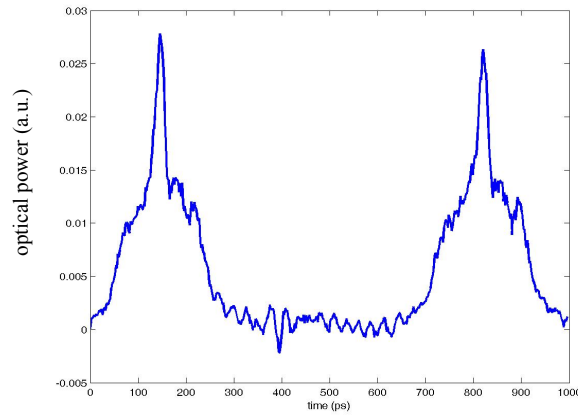


Fig. 6.14. Lowest repetition rate compressed pulses demonstrate large pedestals and are therefore of limited interest.

When operating in the biased at null regime, it is important that the modulator is strictly kept biased at null. If this bias deviates from this position then successive pulses are no longer identical, Fig 6.15. A very useful method for maintaining the biased-at-null criteria was to tune the bias voltage to ensure the third harmonic of the microwave source, f_c , was minimised (pulse repetition rate $f_r = 2 \times f_c$). It is also essential that the modulator is a “push-pull” device to avoid successive pulses experiencing positive and negative chirp corresponding to different phase conditions on each arm of the modulator, leading to non-identical successive pulses.

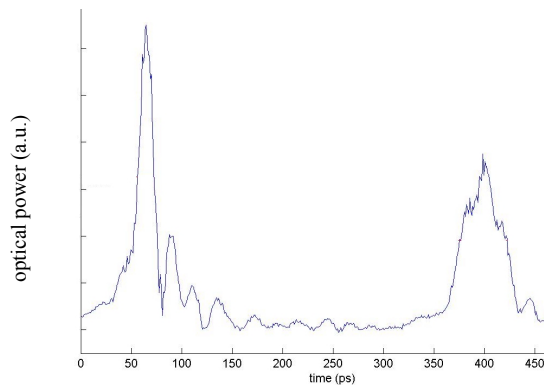


Fig. 6.15. Example of highly irregular successive pulses, if modulator bias is not maintained at null. This is an extreme example for illustration.

A method for avoiding irregular successive pulses is to bias the modulator away from null and modulate to null, only using one side of the modulator, Fig. 6.16(b). This

approach generated regular pulses which were more robust to bias drift than the biased-at-null approach, from the point of view that the drift does not lead to irregular pulses but merely non-optimised compression.

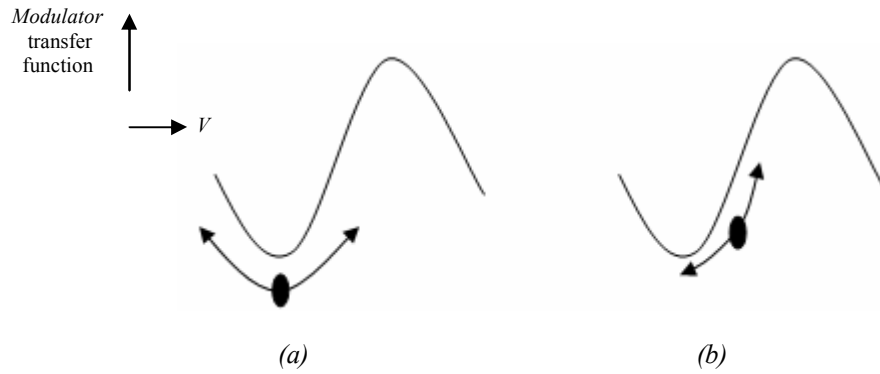


Fig. 6.16. (a) The modulator is biased at null and the applied voltage varies the modulator transmission such that consecutive optical pulses correspond to different arms of the modulator, or (b) the modulator is biased on one side of the null and the applied voltage is set such that the full-scale modulation reaches the transmission null of the modulator.

An observation is that for repetition rates around 2 GHz, the pulse compression and pulse shape appears to be slightly better for the biased at null mode of operation, however for repetition rates of the order 3 GHz and higher either mode of operation provides very similar pulse shapes and so either bias regime can be used.

6.5 Pulse tuneability

The pulse repetition rate is electronically tunable to the precision of the microwave source, although in practice it was preferable during development to use a multiple of 10 MHz since this is required to allow triggering of the sampling scope for visualisation of the pulses. Often after large repetition rate changes, the modulator bias must be adjusted to optimise the pulses. This variation is presumed to be due to the varying thermal response of the modulator depending on the drive level. 3.8 GHz and 8 GHz repetition rate pulses are shown in Fig. 6.17.

6. Experimental pulse source implementation

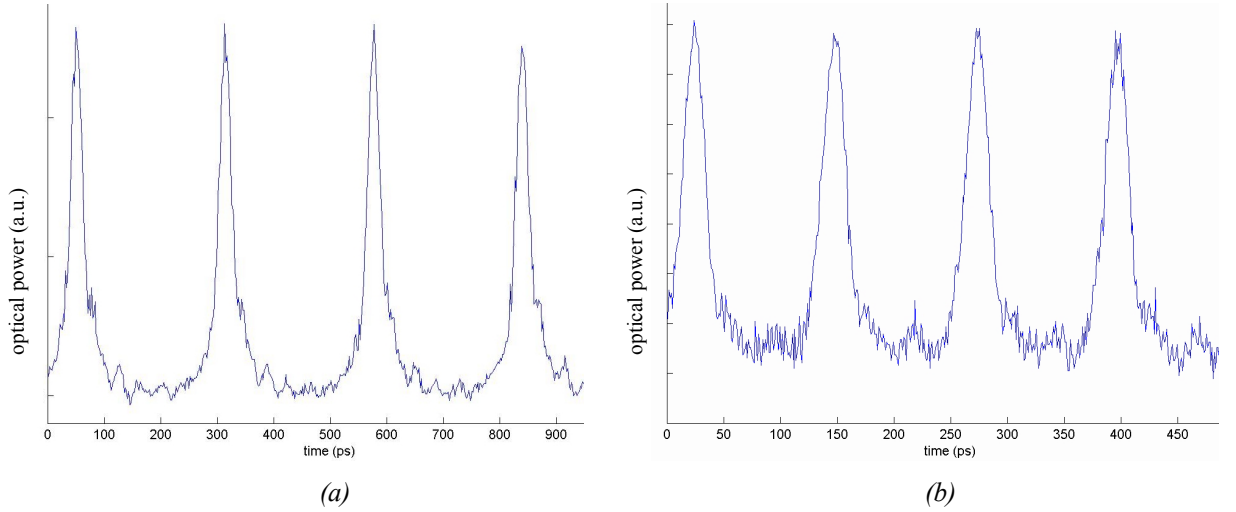


Fig. 6.17. (a) 3.8 GHz repetition rate pulses and (b) 8 GHz repetition rate pulses (note, different time-scales for the two plots).

6.6 Autocorrelation measurements

Since the pulse duration was too short to resolve properly on the high-speed sampling oscilloscope, the pulses were also captured on an autocorrelator, Fig. 6.18. These autocorrelator traces show the narrow central pulse section surrounded by a long pedestal. The narrow central region was measured from the trace as being around 10 ps, so the true width of this compressed region is likely to be 10-15 ps.

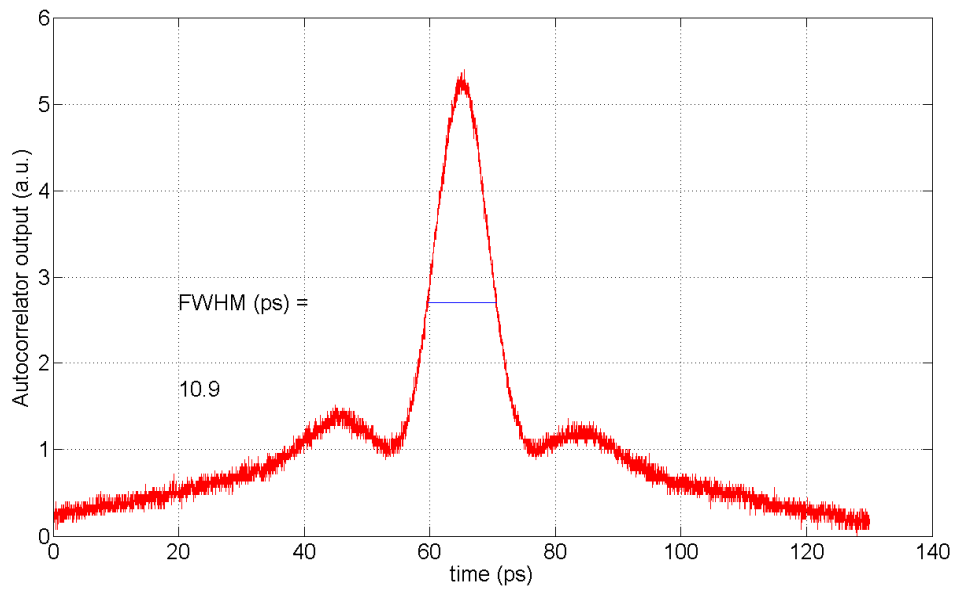


Fig. 6.18. Autocorrelation trace of a 3 GHz repetition rate pulse train after 25.2 km fibre.

6.7 Higher order pulses

As the launch power is increased beyond the optimum level for generating a train of high quality narrow pulses, multiple peaks similar to higher order solitons occur, Fig. 6.19. This behaviour was expected from the modelling described in Chapter 5.

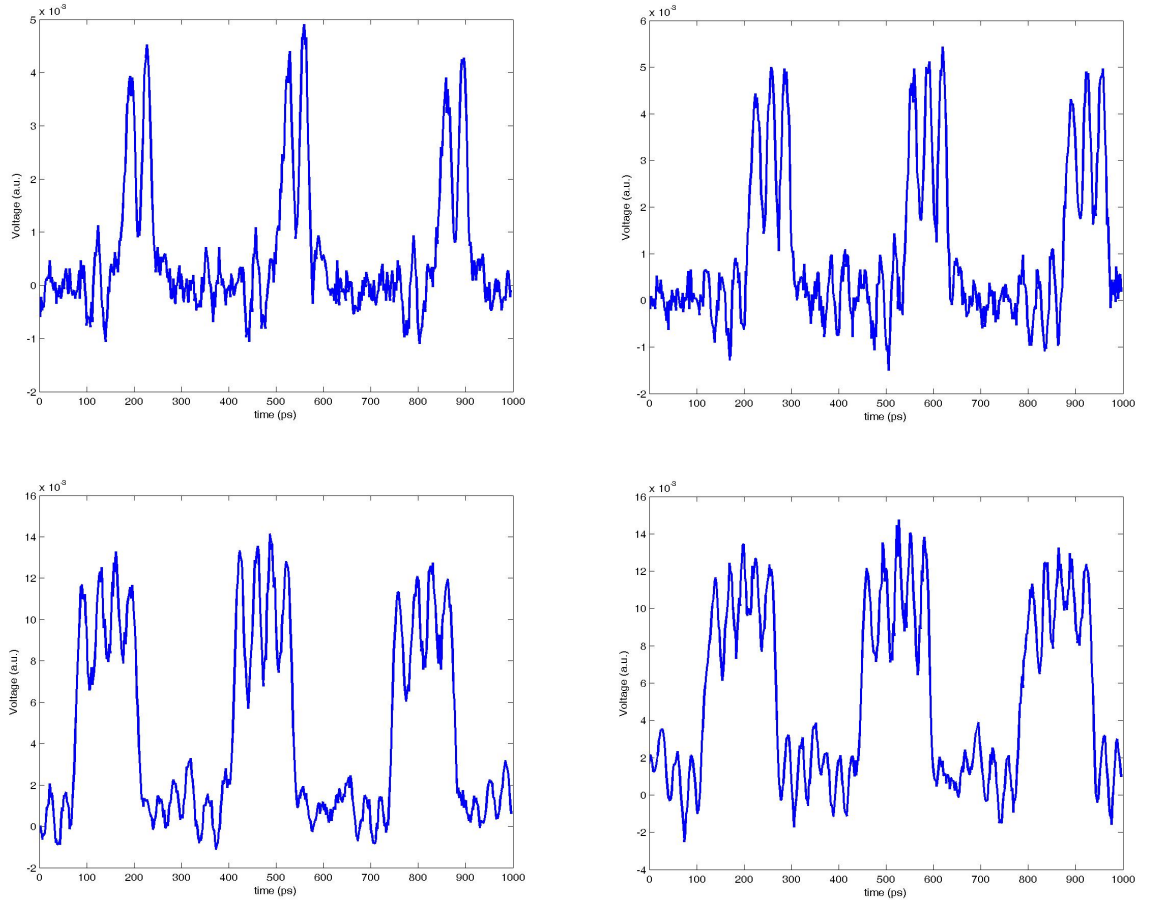


Fig. 6.19. As the launch power increases, higher ordered pulses are observed, as expected.

6.8 Comparison with modelling

Table 6.1 demonstrates the correlation between the modelled and experimental peak input powers required for a 3 GHz repetition rate pulse train to exhibit the single and multi-peaked behaviour shown generically in Fig. 6.19 (through 25.2km of SMF-28). The experimental values for the single, double and triple peaks all lie within the region predicted by the modelling, but they do not cover nearly such a broad range of input

6. Experimental pulse source implementation

powers as the modelling suggests. For example, there is only a brief range of experimental launch powers around 150 mW which provides single peak pulses of <30ps duration. It is also very difficult on the sampling oscilloscope to visually determine the transition point at which the pulse changes from a double to a triple peak due to increasing the launch power.

In addition, the values used for the various parameters in the modelling may not be exactly correct for the specific fibre, as γ and β_3 in particular are not often widely quoted by fibre manufacturers.

In summary, using *a time domain* measurement approach, the predicted performance of the pulse train given by the modelling in Chapter 5 appears to be a very useful guide to the experimental performance, in terms of the minimum possible frequency of ~1.5 GHz and the required launch powers for each repetition rate to achieve <30 ps pulses.

	Modelled (mW)	Experimental (mW)
Single peak < 30 ps	120 – 200	140 - 160
Double peak	240 – 350	300 – 330
Triple Peak	390 – 500	~450

Table 6.1. Modelled and experimental peak input powers for 3 GHz repetition rate pulses through 25.2 km of SMF-28 with modulator drive at $\pm V\pi$

The pulses modelled using the split-step Fourier algorithm have been described up until now in terms of their appearance in the time domain. Due to the difficulties in capturing very short duration pulses in the time domain, even when using the fastest available sampling oscilloscopes, it is therefore perhaps more useful to observe the output from the compression fibre in the frequency domain.

6. Experimental pulse source implementation

Shown below are the experimental captures on a Yokogawa AQ6370 optical spectrum analyser for a 3 GHz pulse amplified to 150 mW peak power and propagated through 25.2 km of SMF-28 compression fibre. Figs. 6.20 & 6.21 show:

- DFB laser output prior to any modulation
- the input to the EDFA after the phase and intensity modulation is applied to the CW DFB
- the output from the EDFA, demonstrating approximately 10 dB increase in optical noise floor at wavelengths away from the DFB carrier
- the output from the 25.2 km of SMF-28, demonstrating significant spectral broadening

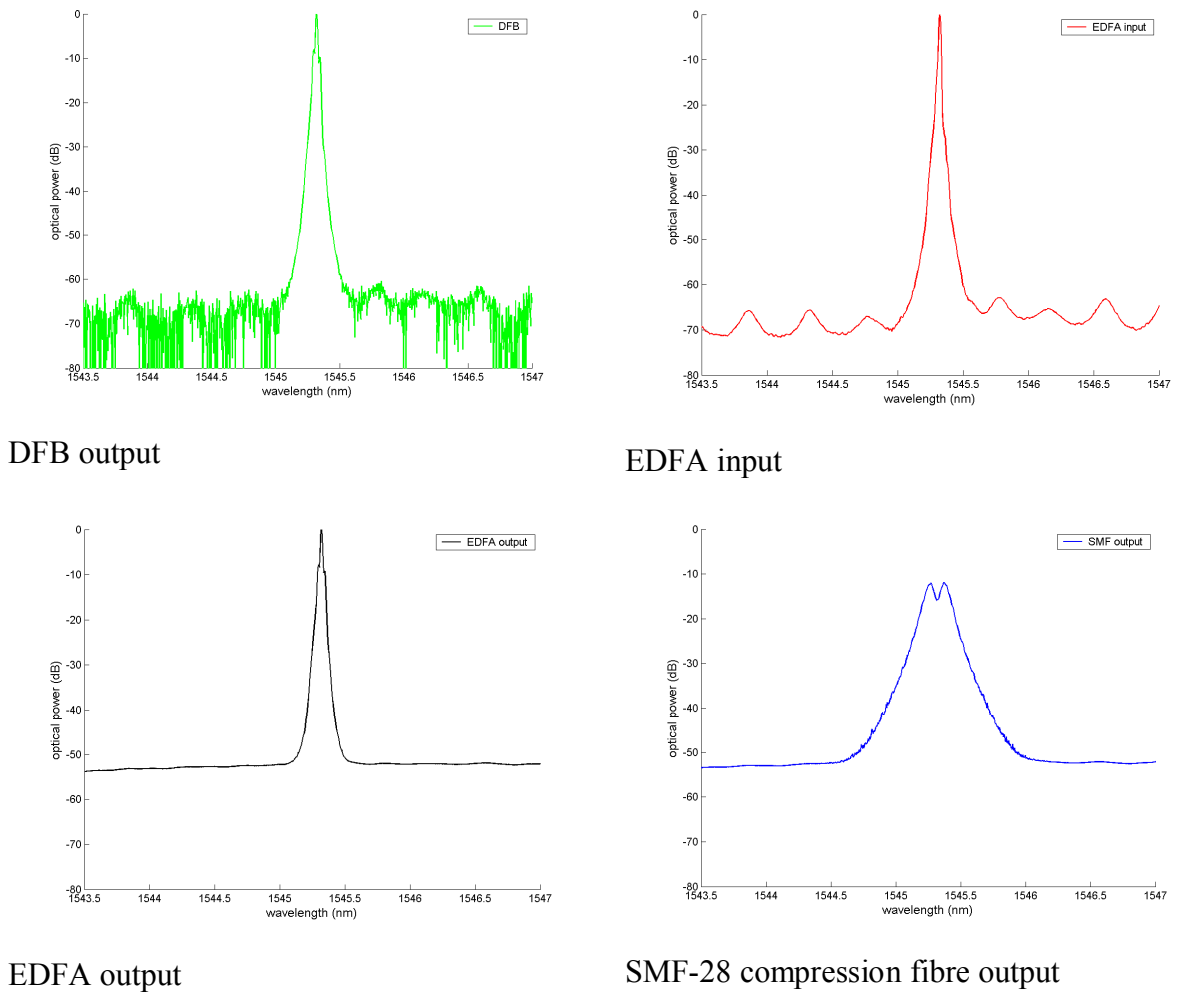


Fig. 6.20. Spectrum analyser captures at various points throughout the experimental pulse source arrangement which generates 3 GHz pulses: DFB output, EDFA input (intensity and phase modulated DFB laser), EDFA output, compression fibre output.

6. Experimental pulse source implementation

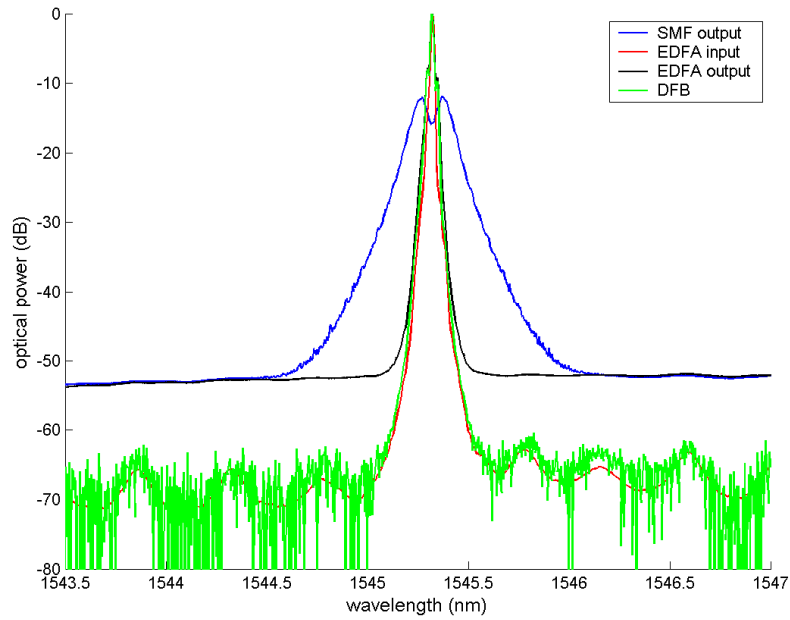


Fig. 6.21. Combining Fig. 6.20 onto one plot.

Focussing in particular on the modelled input and output spectra from the compression fibre, we see that visually the modelled spectrum matches the experimental performance very well, with the exception of the EDFA gain curve at <-40 dBc which is not currently included in the model, Fig. 6.22. The 3 dB widths are 0.038 nm (experimental, red plot) and 0.044 nm (modelled, blue plot).

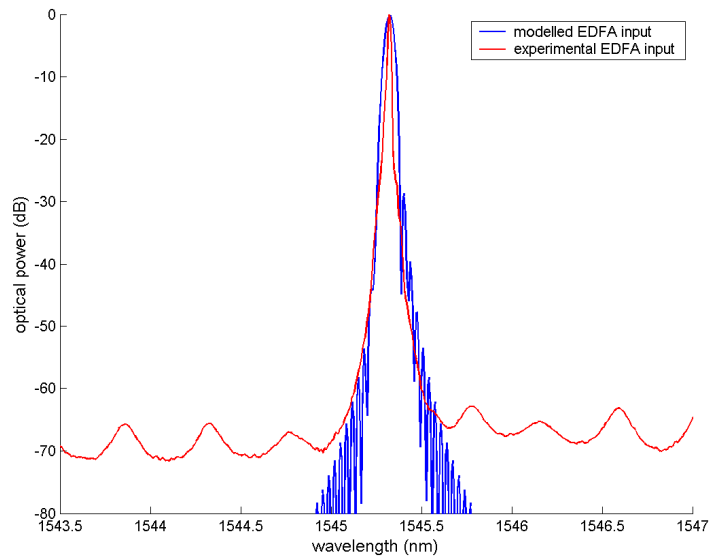


Fig. 6.22. Modelled and experimental input to the EDFA. Blue: modelled EDFA input. Red: experimental EDFA input following DFB phase and intensity modulation. The plots show a close match, with the exception of the noise floor at ~ 70 dBc, which is not included in the model.

The output from the compression fibre is shown in Fig. 6.23. Both experimental and modelled pulses exhibit a “notch” at the central wavelength, although this is more pronounced on the modelled pulses. The spectral widths are 0.269 nm (modelled) and 0.197 nm (experimental)

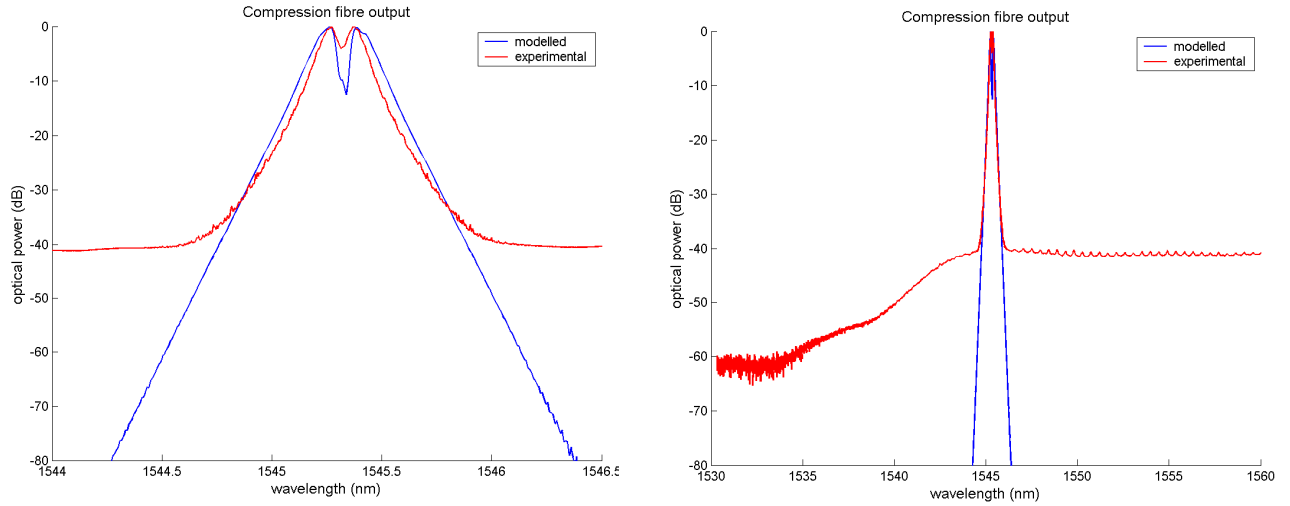


Fig. 6.23. Modelled and experimental output from the compression fibre (SMF-28). Red: modelled compression fibre output. Red: experimental compression fibre output. The two plots show the same captures on different wavelength scales (left hand plot 1544-1546.5 nm, right hand plot 1530-1560 nm). Note the EDFA gain curve is not including in the model.

6.9 Summary of pulse compression implementation

The output from a modulator biased-at-null was successfully compressed through standard telecommunications fibre, to realise pulses as short as 10-15 ps. The lowest possible repetition rate was around 1.5 GHz, although at this lower rate the pulses demonstrate large pedestals. By increasing the repetition rate to around 2 GHz, very respectable pulse shapes were observed.

Experimentally, the region of viable repetition rates and required fibre lengths was very similar to those predicted by the modelling, with the peak input power required to observe single, double and triple peaks for a 3 GHz pulse train lying within the predicted range. In practice however, this range of input powers which generated the single, double or triple peaks was much narrower than predicted by the modelling.

Spectral analysis also identified a close match between the modelled and experimental spectra at various points throughout the pulse source arrangement.

In order to generate the experimental pulse trains, various methods were attempted to overcome stimulated Brillouin scattering (SBS) due to the relatively high EDFA launch powers into the long length of SMF-28 fibre (25.2 km). A tuneable laser was investigated but its tuning rate was too slow (kHz rates) to adequately broaden the carrier linewidth. A broadband source was then constructed by selecting ~ 100 GHz of an EDFA's ASE using a FBG, but although the SBS was suppressed, the linewidth was too broad to allow compression to occur as modelled. Instead injection dithering at $\sim 0.2\%$ of the DC current drive level was applied to the DFB, periodically slightly heating the laser and hence broadening the linewidth as the cavity length varied. Injection dithering in the frequency range ~ 1 kHz to a couple of 100 kHz was required. A second approach, which successfully overcame SBS, involved phase modulating the DFB output with an external phase modulator. Phase modulation at frequencies greater than around 40 MHz out to the amplifier limited system limit of 4 GHz successfully suppressed the SBS, with the exception of the case where the phase modulation frequency equalled the microwave source frequency (and its harmonics) used to generate the periodic waveform.

References for Chapter 6

1. J. P. Gordon and H. A. Haus, "Random walk of coherently amplified solitons in optical fiber transmission", *Opt. Lett.* 11 (10), 665 (1986)
2. G. P. Agrawal, "Nonlinear Fibre Optics", 2nd edition, Academic Press (1995)

7. Pulse timing jitter performance (SMF-28 compression fibre)

In this chapter, characterisation of the pulse timing jitter is extensively investigated, using both single-sideband phase noise measurements and harmonic analysis, with particular focus on the jitter implications of the various methods available for overcoming stimulated Brillouin scattering (SBS). The single-sideband phase noise measurements identify that the microwave source used to generate the periodic waveform (hp 83711A) limits the optical pulse performance at phase noise frequency offsets below around 100 kHz, with the optical noise floor dominating at offsets larger than this. For a 3 GHz repetition rate optical pulse stream, the total pulse timing jitter was found to be 3.135 ps for the frequency offset range 10Hz-Nyquist, 3.893 ps for 10Hz-3GHz, and only 257 fs for the widely published offset range 100Hz–10MHz. The harmonic analysis jitter measurement technique yielded timing jitters between 4-5 ps, depending on which harmonics were used in the calculation, in close agreement with the 3.893 ps value obtained by SSB phase noise integration over almost the entire offset range of 10Hz-3GHz. The superior timing jitter performance of the compression pulse source compared to a gain switched laser is demonstrated when both are implemented to perform optical sampling in the QinetiQ opto-electronic ADC scheme. It is believed that this is the first time that a soliton-compression source has been used to perform optical sampling.

7.1 Timing jitter measurement options

A literature survey presented in Appendix B discusses the three main methods employed to determine the amplitude and timing jitter of pulsed laser sources. By far the crudest of these is the use of a sampling oscilloscope with a long persistence display time so that many successive pulses are overlapped and the amplitude or timing jitter is simply the width of the resulting trace. However, this method is not accurate enough to measure timing jitter of the order of a few picoseconds, even with the fastest available oscilloscopes.

Instead, two accurate jitter measurement techniques widely used involve either integrating the relative harmonic powers captured on a spectrum analyser or

alternatively integrating the single-sideband (SSB) phase noise of the pulse train using a phase noise measurement set-up.

A fourth approach is to use a photonic ADC to sample a known input sinusoidal waveform to determine the accuracy of the sampling pulse train. The phase encoded method employed by the MIT group^[1] has the benefit that it inherently performs a high level of amplitude modulation suppression, therefore allowing isolation and measurement of the timing jitter only. This was verified by intentionally amplitude modulating the input sampling pulse train and observing that the phase encoded set-up suppressed the added amplitude jitter by 48 dB. Using this technique they experimentally measured an upper bound of 55 fs for the modelocked fibre laser used to perform the optical sampling.

7.2 Single-sideband phase noise measurements

SSB phase-noise measurements were performed on the optical pulse train using an Agilent E5500 phase-noise measurement system, a New Focus 20 GHz detector and a Miteq 0.1 to 20 GHz bandwidth electronic pre-amplifier. The Agilent E5500 manual states that the mixer has an amplitude modulation reduction of the order of 30 dB. The robustness of the E5500 to optical intensity fluctuations was experimentally confirmed by purposely adding a few percent (up to ~3%) asynchronous intensity modulation to a 3 GHz optical pulse stream, using a range of frequencies (few MHz through to ~3 GHz), Fig. 7.1. The captured SSB plots remained unchanged for every arrangement tested for $\leq 3\%$ intensity modulation, however the E5500 failed to phase lock and perform measurements when the intensity modulation was increased towards 10%.

7. Pulse timing jitter performance (SMF-28 compression fibre)

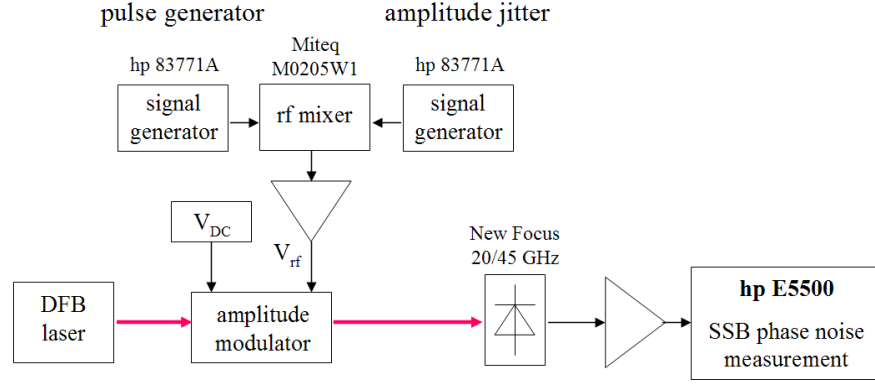


Fig. 7.1. Arrangement used to test the robustness of the E5500 to <3% intensity modulation on the optical pulse stream.

As discussed in Appendix B, the RMS timing jitter is typically calculated over a specified frequency range using the equation

$$\sigma_{\tau} = \sqrt{2.L(\phi)} \approx \frac{1}{2\pi f_R} \sqrt{\int_{f_{\min}}^{f_{\max}} 2.L(f)df} \quad (7.1)$$

where f_{\max} and f_{\min} are the boundaries of the frequency range.

Reassuringly, the SSB phase noise plot obtained for the hp 83711A microwave synthesiser with the E5500 measurement system, Fig. 7.2, matched the published SSB phase noise in its datasheet. Every available microwave source within QinetiQ was measured on the E5500 and the 83711A had the lowest phase noise performance. Unfortunately only the standard 83711A model was available for use, as there is an additional high stability timebase option which has SSB phase noise of -90 dBc/Hz at 10 Hz offset (compared to -45 dBc/Hz at 10 Hz used here). Note that for most output single tone frequencies, there were large spikes at 117.5 and 236 kHz which were also present on the subsequent optical pulses (as well as mains 50 Hz and its harmonics). The origin of these spikes is unknown, however they are intrinsic to the specific signal generator model (or perhaps even unit) employed, as they were not present on any other source tested.

7. Pulse timing jitter performance (SMF-28 compression fibre)

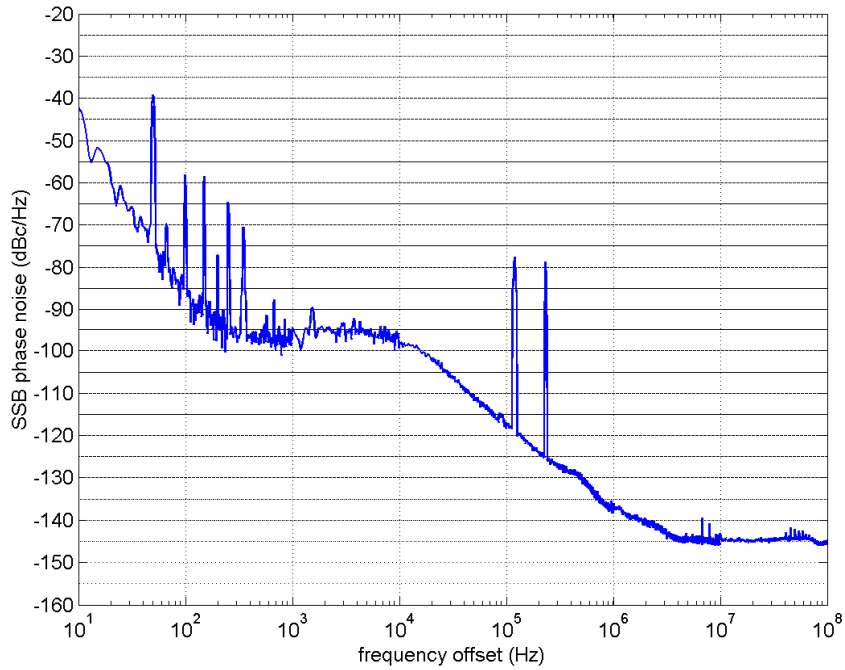


Fig. 7.2. SSB phase noise plot of the 83711A signal generator at 1.5 GHz (note that this is the same power level and frequency as used to generate the 3.0 GHz optical pulses). This plot matches the published SSB phase noise spectrum in the 83711A specifications sheet.

The SSB phase noise plot in Fig. 7.2 was integrated over the various ranges shown in Table 7.1 (Section 7.8). The E5500 phase noise measurement system only measures to a maximum frequency offset of 100 MHz. Interpolated jitters out to the carrier frequency of 1.5 GHz assume that the SSB phase noise level is -145 dBc/Hz from 100 MHz to 1.5 GHz and that there are no spikes present in this range.

As discussed in the previous chapter, it proved necessary to use either injection dither or of the DFB laser or phase modulation of the DFB output in order to overcome SBS. Both of these methods generate unwanted artefacts on the SSB phase noise spectra.

7.3 Overcoming stimulated Brillouin scattering using injection dithering

Fig. 7.3 shows the dramatic effect that injection dithering has on the SSB phase noise plots, with a forest of peaks added at the injection dithering frequency and its harmonics, even when the injection dithering is only $\sim 0.2\%$ of the DC drive current. Clearly therefore injection dithering is not an attractive method of overcoming the SBS for precision sampling applications requiring low timing jitter.

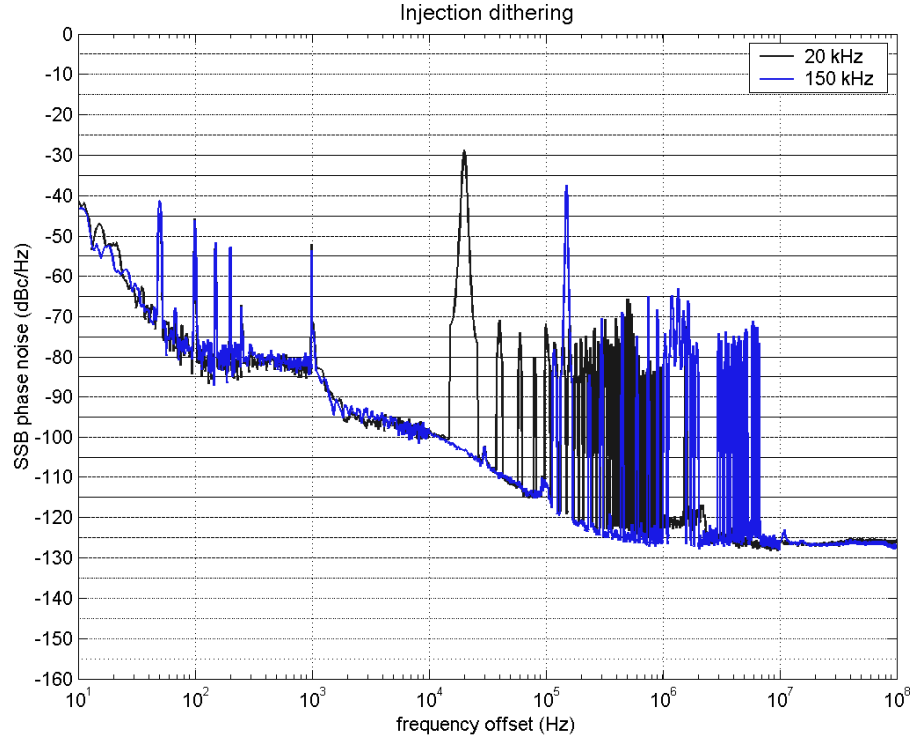


Fig. 7.3. SSB phase noise spectra where injection dithering is used to overcome SBS. Very large SSB phase noise spikes are observed at the injection dithering frequency and its harmonics.

7.4 Overcoming stimulated Brillouin scattering using phase modulation

Given the presence of large spikes on the SSB phase noise spectra with injection dithering, it is not surprising that the phase modulation approach to SBS suppression also generates significant artefacts at the phase modulation frequency and its harmonics. Phase modulation around the minimum frequencies (~ 30 MHz) required to overcome SBS generates artefacts on the SSB phase noise spectrum at offset frequencies equal to the phase modulation frequency. For example, 30 MHz phase modulation in Fig. 7.4(a) generates SSB phase noise spikes at 30, 60 and 90 MHz. These artefacts are not simply removed by applying phase modulation at any arbitrary frequency beyond the frequency offset region over which the SSB phase noise is integrated in Eq. 7.1, as phase modulation artefacts can still be present on the SSB phase noise spectrum as intermodulation frequencies. In Fig. 7.4(b), 950 MHz phase modulation appears at 50 and 100 MHz frequency offsets (i.e. sum and difference frequencies of 950 MHz and 1.5 GHz).

7. Pulse timing jitter performance (SMF-28 compression fibre)

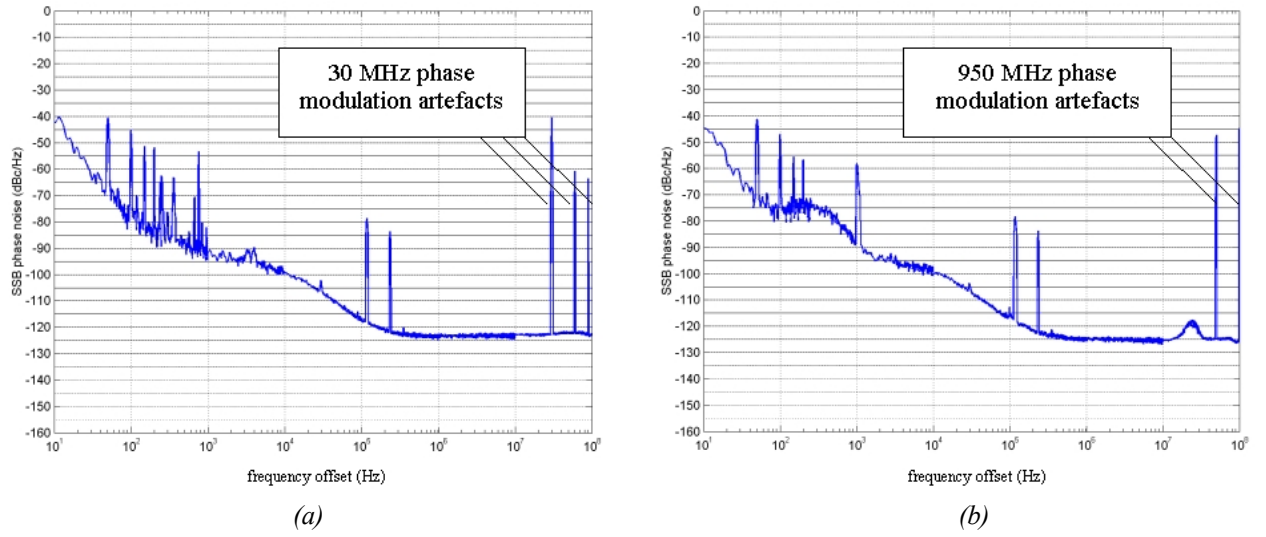


Fig.7.4. (a) 30 MHz phase modulation, generating artefacts at 30, 60 and 90 MHz on the SSB phase noise spectrum and (b) 950 MHz phase modulation which results in artefacts at 50 MHz and 100 MHz on the SSB phase noise spectrum, corresponding to intermodulation frequencies with the 1.5 GHz pulse generator frequency.

As discussed in Appendix B, if the pulse train is to be used to perform optical sampling, timing jitter calculations using the SSB phase noise approach should be performed over the offset range 10 Hz to the Nyquist frequency of the sampling rate. Observations based on Fig. 7.4 above suggest that in order to avoid significant phase modulation artefacts occurring within the range 10 Hz to Nyquist, then the phase modulation must be applied at the Nyquist frequency itself, e.g. phase modulation must be applied at 1.5 GHz for 3 GHz pulse trains. However, as discussed in Section 6.3 in the previous chapter (see Fig. 6.9), phase modulation at the same frequency as the pulse signal generator frequency does not sufficiently suppress SBS adequately when operating the modulator in the biased-at-null regime where the output pulse rate is double the microwave drive frequency. Therefore, when using the biased at null mode of operation, the next best option is to phase modulate at half the Nyquist frequency and then halve the optical pulse train repetition rate by pulse picking using a second intensity modulator. For example, apply 1.5 GHz phase modulation to 6 GHz optical pulses, propagate these pulses through the compression fibre, and then pulse pick the output pulses down to a 3.0 GHz repetition rate, hence the phase modulation is at the Nyquist frequency of the output optical pulse train. The SSB phase noise plot and resulting timing jitters are given for this set-up in Fig. 7.5 and Table 7.2. When operating the

modulator biased away from null and then driving it to null, the pulse rate equals the microwave drive frequency and so the phase modulation used to suppress the SBS can be applied at a frequency equal to half the pulse repetition rate (Nyquist) with no pulse picking required.

A patent has been filed which describes this frequency specific phase modulation method of overcoming SBS without adding to the pulse timing jitter for optical sampling applications^[2].

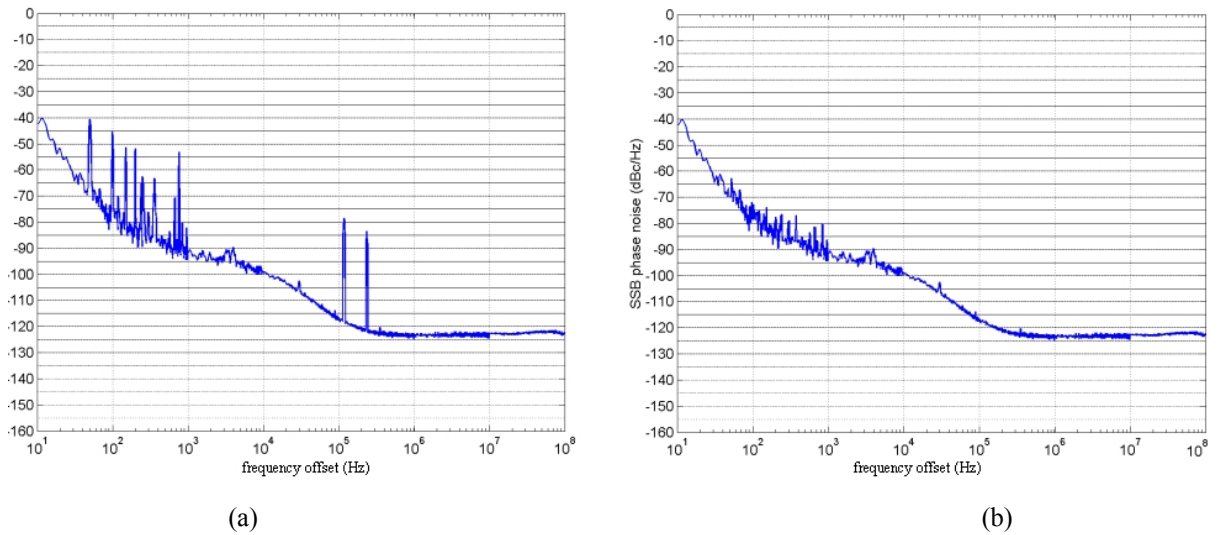


Fig. 7.5. Single-sideband phase noise plot of 3 GHz optical pulse train with 1.5 GHz phase modulation (a) raw and (b) with spikes due to signal generator removed (see Fig. 7.2, the signal generator SSB phase noise plot). Note, this result was obtained by generating 6 GHz optical pulses with 1.5 GHz phase modulation, performing pulse compression through 25 km of fibre, and then pulse picking down to 3 GHz (modulator biased-at-null mode of operation) using a second intensity modulator.

7.5 Fibre Bragg Grating effect on SSB phase noise

The inclusion of the FBG to remove the EDFA ASE at unwanted wavelengths, as discussed in Section 6.3, did not have any effect on the SSB phase noise spectra for any experimental arrangement investigated, including injection dithering and phase modulation. Intuitively, it would seem desirable to remove these unwanted wavelengths as they can only be detrimental to the optical pulse quality, but for the current system the effect they have on the timing jitter is of no consequence. Perhaps if the far-out SSB phase noise was lower, say -145 dBc/Hz for offsets >1 MHz, then the EDFA ASE would become an issue.

7.6 Analysis of SSB phase noise timing jitter measurements

Fig. 7.6 shows the SSB phase noise plots of 3 GHz repetition rate optical pulses and the 3 GHz microwave source (hp 83711A) used to create these optical pulses. The microwave source can be seen to largely dominate the optical pulse SSB phase noise at offset frequencies less than ~ 100 kHz, however beyond this point the SSB phase noise is dominated by the optical pulse train. A more stable microwave source would therefore be highly desirable for reducing the jitter contribution at offsets under ~ 100 kHz. Over the frequency offset range 10 Hz to ~ 1 kHz the phase noise measurements of the optical pulses is 5 to 10 dB higher than that of the microwave source; the source of this additional phase noise has not currently been identified.

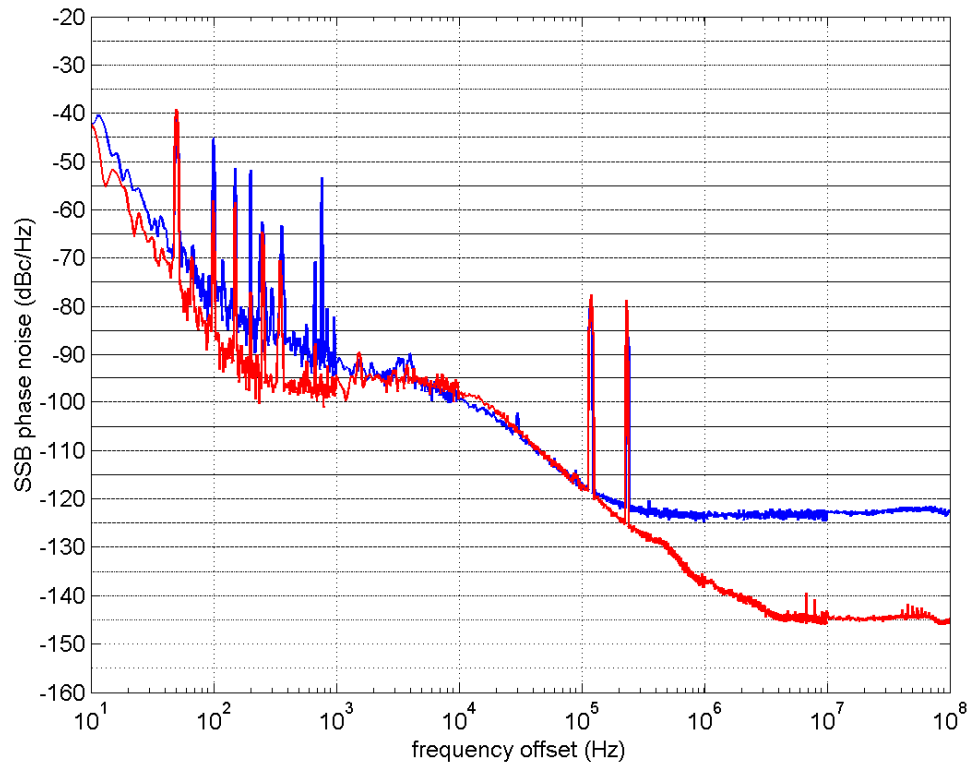


Fig 7.6. SSB phase noise spectra of:

Blue plot: 3 GHz optical pulses picked from a 6 GHz optical pulse train, with 1.5 GHz phase modulation applied to overcome SBS.

Red plot: 3 GHz microwave source and amplifier set-up used to drive the LiNbO_3 amplitude modulator which generates the 6 GHz periodic waveform prior to amplification and compression.

Tables 7.1 and 7.2 show the timing jitters obtained from integrating the SSB phase noise spectra shown in Fig 7.6, for the output optical pulse train, and also for the microwave source and amplifier used to generate the initial periodic waveform, prior to compression through the fibre. Since the E5500 only allows measurements for offsets up to 100 MHz, the SSB phase noise has been assumed to remain at -123 dBc/Hz for the optical pulses and -145 dBc/Hz for the signal generator plus amplifier for offsets from 100 MHz to Nyquist. In addition, the timing jitters are quoted for the raw capture, and for a smoothed capture in which the pulse generator spikes are removed from the spectra.

As was discovered in the review of published timing jitters undertaken in Appendix A, the frequency offset range is very important for making comparisons between different sources, and therefore the jitter of the compressed soliton-effect pulses has been calculated over a range of offsets.

7.7 Microwave source jitter observations

A substantial portion of the microwave source's timing jitter is due to the contributions over the 10Hz-100Hz offset range: the timing jitter is 1.757 ps over 10Hz–1MHz, but only 0.906 ps over 100Hz–1MHz (as calculated from the raw capture). The contribution of the large SSB phase noise spikes to the microwave source jitter is evident from the dramatic reduction in timing jitter values in Table 7.1 between the raw and smoothed columns for every offset range: for example the timing jitter over 10Hz–1MHz is 1.757 ps for the raw capture and 0.756 for the smoothed capture.

7.8 Optical pulse jitter observations

The total timing jitter value of the optical pulses is given by integrating the SSB phase noise from DC to the repetition rate of the pulse train. However the E5500 measurement system can only measure offsets over 10 Hz, so an approximation of the total timing jitter of the pulse train can be obtained from the frequency offset range 10Hz-3GHz, which gives 3.893 ps (raw) and 3.42 ps (smoothed), Table 7.2. In terms of the sampling application, the important integration range is 10Hz-Nyquist, which gives 3.135 ps (raw) and 2.687 ps (smoothed). These figures are an order of magnitude higher than the

7. Pulse timing jitter performance (SMF-28 compression fibre)

best timing jitter values for the gain and Q-switched lasers surveyed in Appendix A. Integrating over the familiar published mode-locked laser integration range of 10Hz-10MHz and 100Hz-10MHz does give much lower timing jitters of 204 fs and 257 fs respectively (microwave source spikes removed), which is much more favourable in comparison to the published values in Appendix A.

Offset range	Timing jitter (ps)	
	Raw	Smoothed
10 Hz – 1 MHz	1.757	0.756
10 Hz – 10 MHz	1.757	0.756
10 Hz – 100 MHz	1.757	0.757
10 Hz – Nyquist	1.764	0.773
10 Hz – carrier freq.	1.771	0.791

Offset range	Timing jitter (ps)	
	Raw	Smoothed
100 Hz – 1 MHz	0.906	0.167
100 Hz – 10 MHz	0.906	0.168
100 Hz – 100 MHz	0.907	0.173
100 Hz – Nyquist	0.921	0.235
100 Hz – carrier freq.	1.035	0.286

Table 7.1. Timing jitter from SSB phase noise spectrum of the 83711A signal generator over various frequency offset ranges (as shown in Fig 7.2). The results for the offset ranges from 100 MHz out to the carrier frequency assume that the floor remains at -145 dBc/Hz and that there are no spikes in this range.

Offset range	Timing jitter (ps)	
	Raw	Smoothed
10 Hz – 1 MHz	2.129	1.388
10 Hz – 10 MHz	2.135	1.397
10 Hz – 100 MHz	2.203	1.499
10 Hz – Nyquist	3.135	2.687
10 Hz – carrier freq.	3.893	3.542

Offset range	Timing jitter (ps)	
	Raw	Smoothed
100 Hz – 1 MHz	1.110	0.204
100 Hz – 10 MHz	1.121	0.257
100 Hz – 100 MHz	1.247	0.602
100 Hz – Nyquist	2.550	2.309
100 Hz – carrier freq.	3.443	3.265

Table 7.2. Timing jitter from SSB phase noise spectrum of the 3 GHz optical pulse train with 1.5 GHz phase modulation (as shown in Fig 7.6). Note, this set-up was obtained by generating 6 GHz optical pulses with 1.5 GHz phase modulation, performing pulse compression through 25 km of fibre, and then pulse picking down to 3 GHz. For offsets over 100 MHz, the SSB phase noise is assumed to remain at -123 dBc/Hz out to the carrier frequency.

7.9 General comments on SSB phase noise timing jitters measured

An important observation when comparing the SSB phase noise spectra in Fig. 7.6, and the mode-locked laser spectra in the wider literature (Appendix A) is that the

microwave source used here has much poorer performance at offsets less than around 1kHz-10kHz. Also, the optical noise floor at offsets around 10 kHz and beyond is much higher for the compression pulses detailed in this report compared with the mode-locked lasers. The mode-locked lasers with low published timing jitters^[3,4] have SSB phase noises around -150 dBc/Hz at 100 MHz offsets for 10 GHz repetition rates pulses, where as the SSB phase noise at a 100 MHz offset for the compression pulses is around -125 dBc/Hz. Given that the 10 GHz pulses are roughly 4 times the repetition rate of the 3 GHz, that equates to an effective difference in large offset SSB phase noise of somewhere around 35-40 dBc/Hz.

7.10 SSB phase noise jitter measurements summary

The two methods investigated for overcoming the SBS, injection dithering and phase modulation, both added artefacts to SSB phase noise plots at the modulation frequencies used by each regime. Since the optical pulses are to be used to perform sampling, it is important that the timing jitter calculated from the SSB phase noise should be obtained by integrating from 10 Hz to the Nyquist frequency. For this frequency offset region of interest, phase modulation at the Nyquist frequency would ensure no SSB phase noise spikes occur due to the phase modulation frequency or any intermodulation frequencies. Unfortunately however, this is the one frequency (and its harmonics) which cannot be used since it corresponds to the signal generator frequency used to generate the pulse train itself, and so the carrier is not broadened by applying phase modulation at this one specific frequency (and its harmonics). The solution therefore is to apply phase modulation at a frequency equal to a quarter of the optical pulse frequency, propagate the pulses through the compression fibre and then halve the optical repetition rate by pulse picking. In this way the phase modulation is at half of the optical pulse rate, i.e. Nyquist.

7.11 Timing jitter measurements using spectral analysis

To make jitter measurements based on harmonic analysis, the optical noise floor must be clearly defined above the system noise floor, which is likely to mean operating the spectrum analyser without any internal attenuation. Also, the harmonic levels should be determined without overloading the spectrum analyser. If the optical noise floor and the power in the fundamental cannot be resolved simultaneously, then filters would have to be used to measure the values separately to avoid introducing non-linearities in the measurement.

The spectrum analyser used here was an hp 8565E, and in order to observe the optical noise floor with zero attenuation, the total power input from the detector and any electronic pre-amplifier must not exceed -10 dBm for any frequency. For an average optical input power of $270\text{ }\mu\text{W}$ onto a 20 GHz New Focus detector, the power in the fundamental frequency is -38 dBm, without any electronic amplification. Therefore, the maximum gain of the analyser pre-amplifier must not exceed 28 dB to ensure that the analyser is not saturated.

The analyser floor is around -92 dBm for 300 kHz resolution bandwidth ($-147 + 55$ dBm). This bandwidth was selected as it allows for a continuous frequency sweep in 80 seconds. Although a lower bandwidth would have been preferable in order to lower the noise floor, it would have resulted in unacceptably long sweep times, during which the pulses may have drifted significantly. Obviously, an amplifier with as low a noise figure as possible is desirable (3 dB).

Taking these amplifier requirements into account, Fig. 7.7, a Miteq amplifier with a 3 dB noise figure and 24 dB gain, 0.1-20 GHz response, was sourced as a suitable amplifier for attempting timing jitter measurements using spectral analysis (Leep and Holm method^[5], Appendix B).

7. Pulse timing jitter performance (SMF-28 compression fibre)

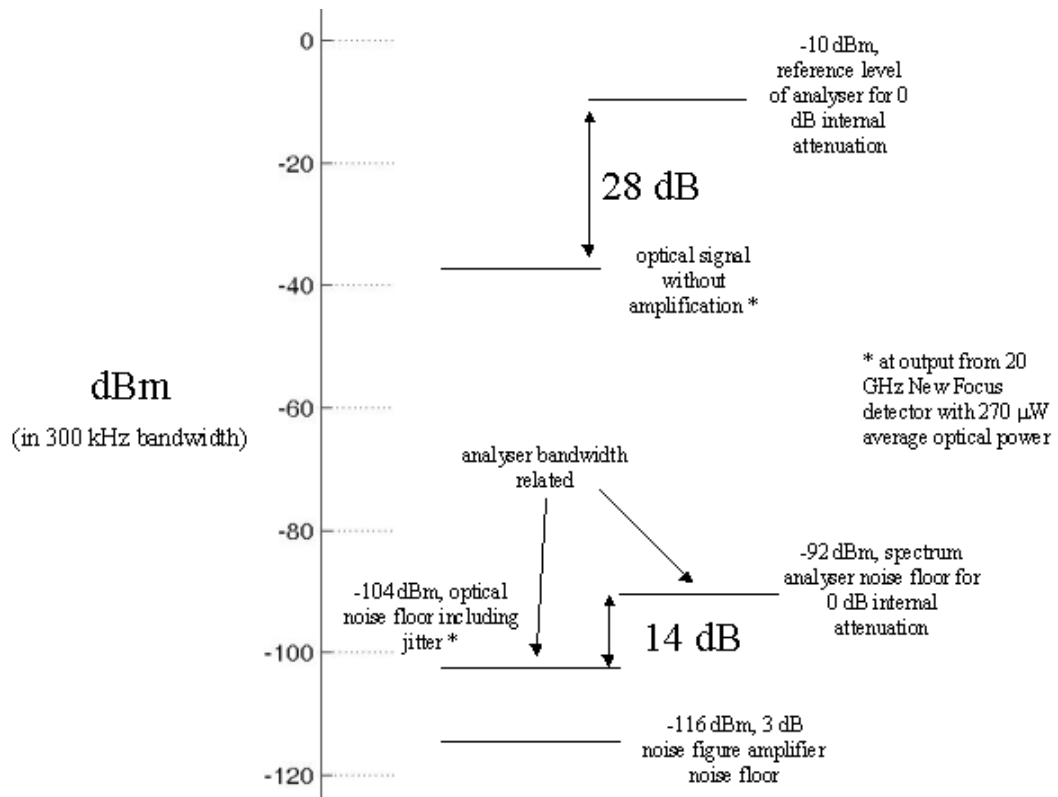


Fig.7.7. Amplifier gain requirements given analyser considerations and optical and signal noise floors, if the harmonic spectra are captured in one sweep with no filtering applied to avoid saturation of the spectrum analyser (resolution bandwidth = 300 kHz; trade-off between acceptable sweep time and noise floor).

Fig. 7.8(a) is an example of a frequency spectrum obtained with and without optical power onto the detector. The reason for measuring the spectra with no optical input is to correct for variable system gain across the 0.1-20 GHz range. The Leep and Holm method for jitter calculation, as discussed in Appendix B, can then be applied to the adjusted harmonic spectra, Fig. 7.8(b). Each harmonic level is measured and the power in each harmonic region is integrated, taking into account the spectrum analyser bandwidth. Fig. 7.8(a) shows the relative integrated harmonic power (RIHP) for each harmonic. For a perfect pulse train this will be a parabola, and hence the RIHP plotted against the harmonic squared will be a straight line in the perfect case. Fig. 7.9(b) shows a reasonable approximation to a straight line.

7. Pulse timing jitter performance (SMF-28 compression fibre)

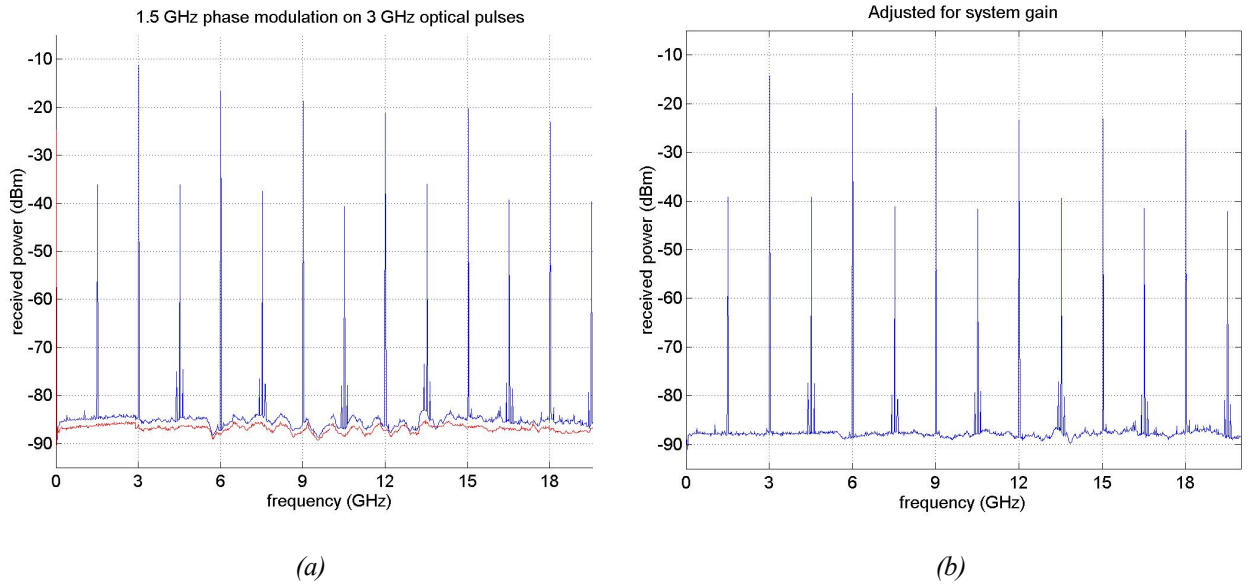


Fig. 7.8(a) The harmonic spectrum captured for 1.5 GHz phase modulation on 6 GHz optical pulses, pulse picked to a 3 GHz output repetition rate. The blue plot is the optical pulse train as captured by the spectrum analyser after detection and amplification. The red plot is the spectrum analyser capture with no light incident on the detector (i.e. the system floor). Analyser set-up: 300 kHz RBW, 1 kHz VBW, 0 dB attenuation, -10 dBm ref. level. (b) Harmonic spectrum corrected for system gain.

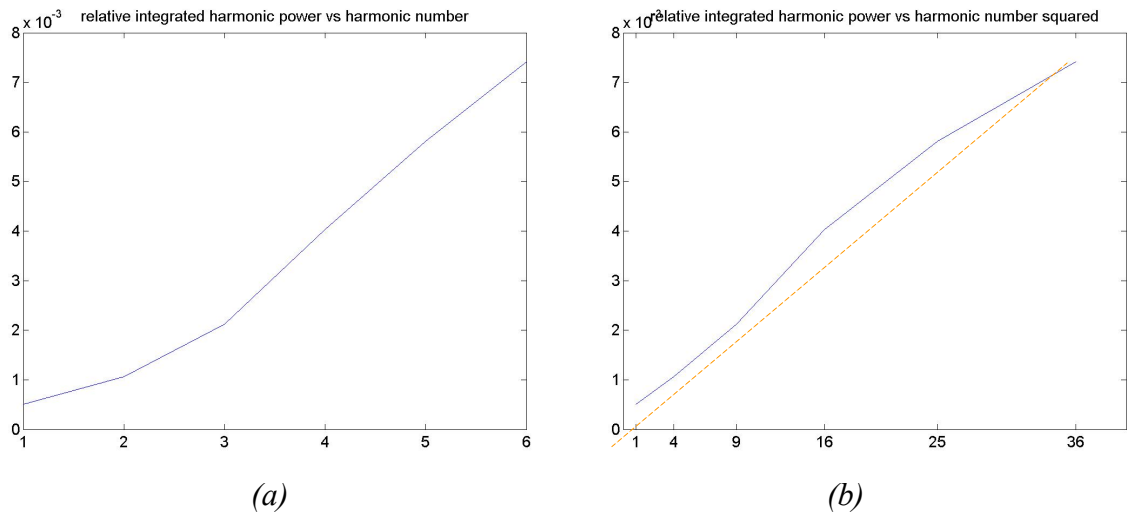


Fig. 7.9(a) Relative integrated power versus harmonic number and (b) relative integrated harmonic power squared versus harmonic number. In the ideal case plot (a) will be parabolic, meaning that plot (b) will be a straight line. Visually, it is apparent that plot (b) is a reasonable approximation to the linear fit.

It is then possible to calculate the amplitude and timing jitters from the RIHPs, Fig. 7.10. Irrespective of which harmonics are used, the timing jitters are found to be between 4 and 5 ps, and the amplitude jitter is around 2-3%. The value of 4 ps is in

7. Pulse timing jitter performance (SMF-28 compression fibre)

keeping with the 3.893 ps obtained using the SSB phase noise approach over for the frequency offset range 10Hz-3GHz.

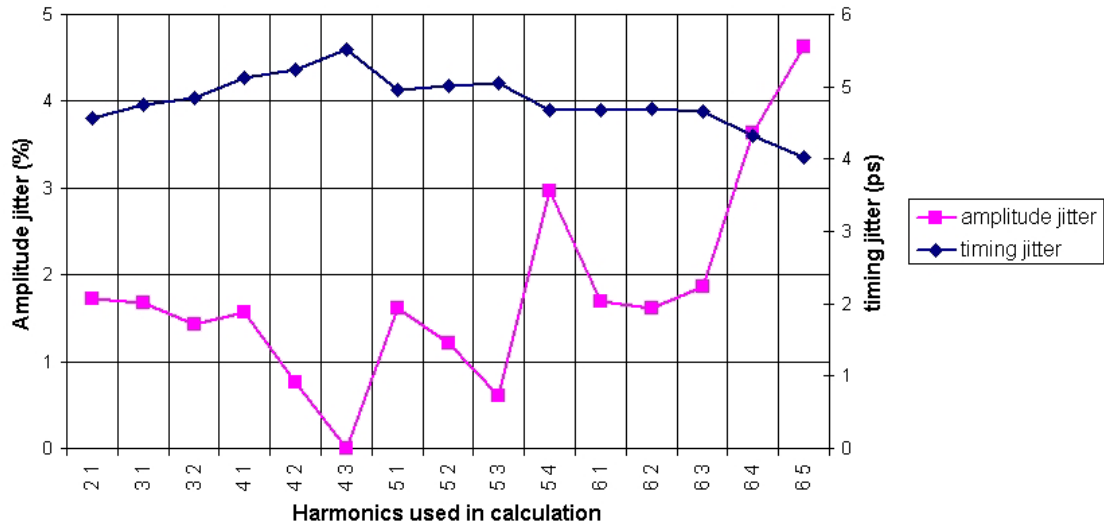


Fig. 7.10. Timing and amplitude jitter for 3 GHz optical pulses with 1.5 GHz phase modulation applied, calculated from RHIP values in Fig.7.8.

Fig. 7.11 shows the harmonic spectra obtained for various other phase modulation frequencies and also for injection dithering. The abundance of phase modulation artefacts can be seen in Fig. 7.11(iii)-(vi).

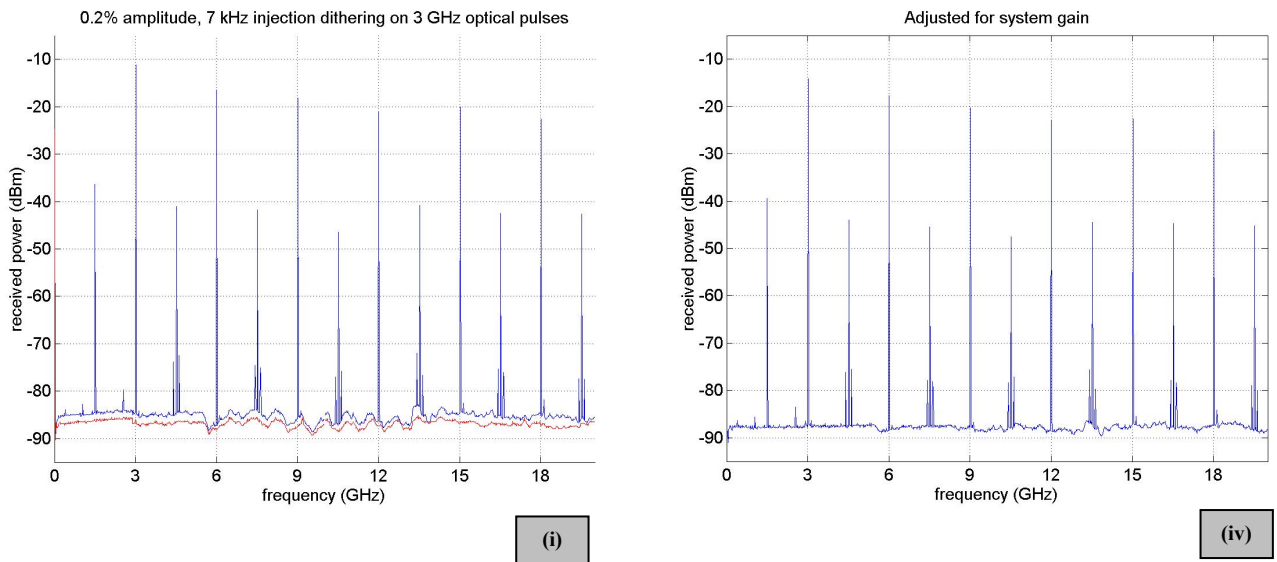


Fig. 7.11 - continued onto next page.

7. Pulse timing jitter performance (SMF-28 compression fibre)

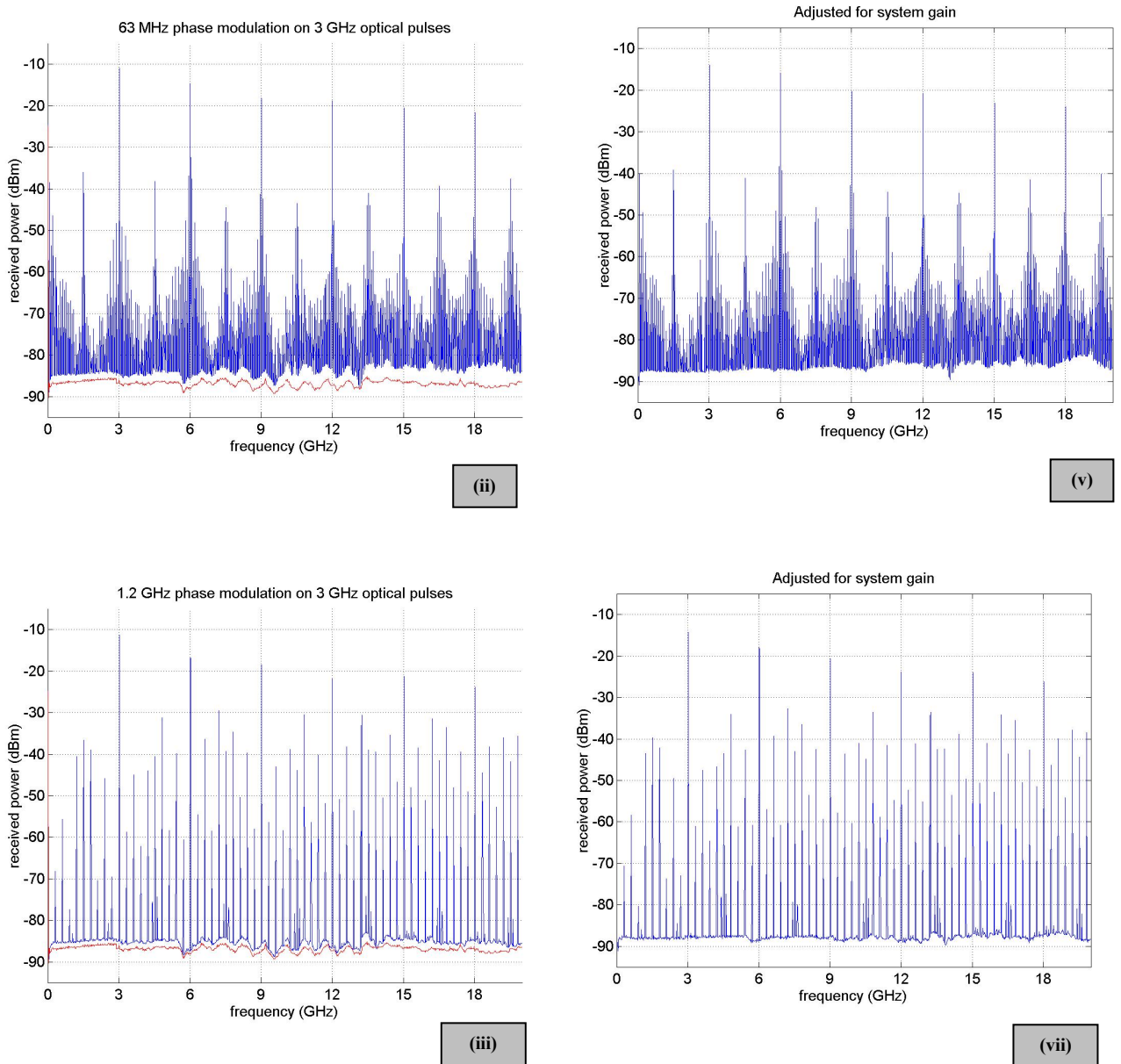


Fig. 7.11. Spectra illustrating the different artefacts for different methods of SBS suppression obtained when 200 mW peak power, 3 GHz pulses are launched into 25.2 km SMF-28:

- (i) 7 kHz injection dithering on 3 GHz optical pulses, at 0.2% amplitude of the DC current
- (ii) 63 MHz phase modulation on 3 GHz optical pulses
- (iii) 1.2 GHz phase modulation on 3 GHz optical pulse
- [(iv)-(vi) show the 3 plots above corrected for system gain]

7.12 Analyser method “sanity check”

As a “sanity check” to confirm that the spectra obtained experimentally were providing sensible jitter values, an approximation was performed which assumed that the floor was constant across the 0-20 GHz range. The harmonic levels were then taken from the analyser captures. Using this crude approximation, the timing jitters are calculated to be around 3.5 to 4.0 ps when the harmonic values are [-14, -17, -20, -22, -22, -24 dBm] and the floor is -87 dBm, roughly matching the values found in the previous section (amplitude jitter is 1.5-2.0%).

If the pulses were to be made more stable and the noise floor dropped by 10 dB (or the harmonics increased by 10 dB), then the timing jitter becomes 1.0 to 1.3 ps and the amplitude jitter would be 0.5 to 1.0 %, depending on which harmonics are used, Fig. 7.12 and Table 7.3.

Spectrum analyser captures could not be found in the literature to compare values calculated for this report with those published. Ng et al publish harmonics but their optical noise floor is beneath the signal noise floor (30 fs timing jitter).

Noise floor	Timing jitter	Amplitude jitter
-87	3.5 to 4.0 ps	1.5 to 2.0%
-97	1.0 to 1.3 ps	0.5 to 1.0%
-107	300 fs	0.1 to 0.5%
-117	120 fs	<0.1%

Table 7.3. Timing reduction due to increase in harmonic to floor separation. The analyser bandwidth was 300 kHz.

7. Pulse timing jitter performance (SMF-28 compression fibre)

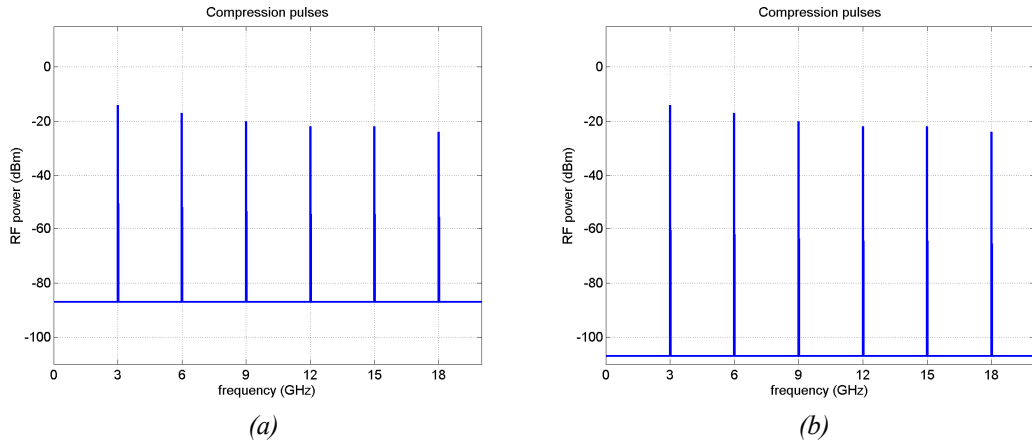


Fig. 7.12. Compared to (a), in (b) the noise floor has dropped by 20 dB, but the harmonics are at the same level. This gives a reduction in timing jitter from 3.5-4 ps down to 300 fs.

7.13 Comparison of compressed pulse performance with a gain switched laser

The amplitude and timing jitter values of a gain switched laser were measured using both the SSB phase noise and the harmonic analysis approaches. The gain switched laser outputs ~30 ps pulses at a 1 GHz repetition rate, Fig. 7.13. The gain switching is achieved by driving the laser with a 1 GHz sinusoid which periodically allows the laser to experience a large population inversion, which is then pumped hard to enable rapid gain depletion.

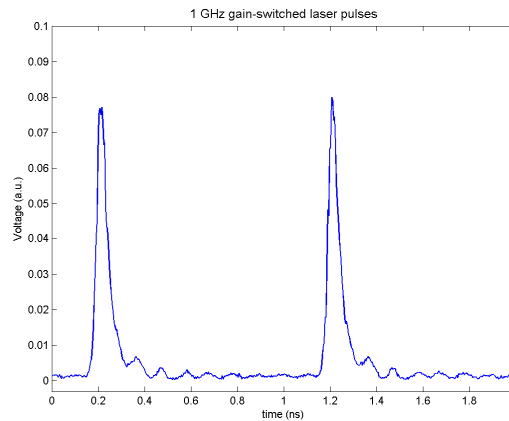


Fig. 7.13. 1GHz repetition rate gain switched laser pulses.

As with the compression pulses, the gain switched laser's SSB phase noise plot shows that its performance is limited by the microwave source for lower frequency offsets, up to around 20 kHz for the gain switched laser, as opposed to ~100 kHz for the compression pulses, Fig. 7.14. For frequency offsets over 20 kHz, the gain switched

7. Pulse timing jitter performance (SMF-28 compression fibre)

SSB phase noise remains around -115 dBc/Hz, in comparison with -125 dBc/Hz for the 3 GHz compression pulses. Therefore the gain switched laser has significantly higher timing jitter values than the compression pulses when its SSB phase noise spectrum is integrated, Table 7.4. For example the timing jitter (for the raw captures) is 11.40 ps and 2.20 ps over 10Hz-100MHz, and 13.93 ps and 3.14 ps over 10 Hz-Nyquist, for the gain switched laser and the compression pulses respectively (assuming that the gain switched SSB phase noise remains at -115 dBc/Hz out to Nyquist).

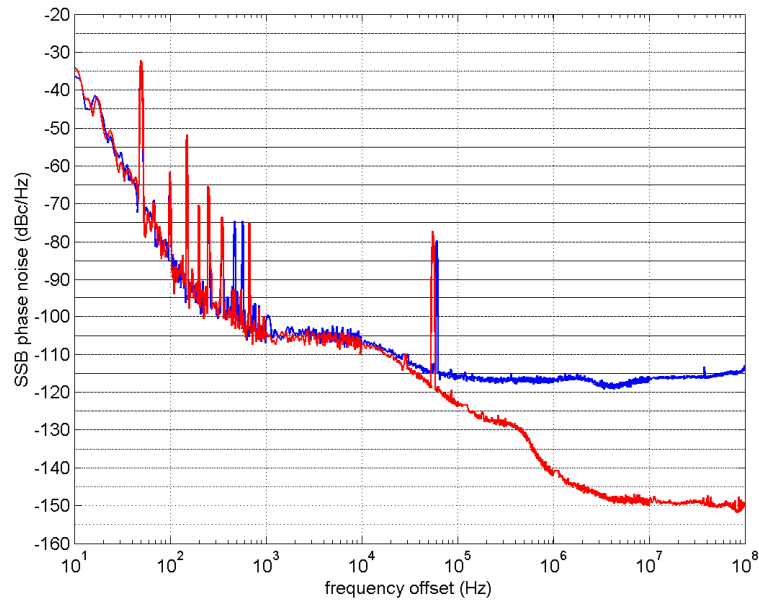


Fig. 7.14. SSB phase noise spectra of:

Blue plot: 1 GHz gain switched laser pulses

Red plot: 1 GHz microwave source and amplifier used to drive the 1GHz gain switch laser

Offset range	Timing jitter (ps)
10 Hz – 1 MHz	10.73
10 Hz – 10 MHz	10.77
10 Hz – 100 MHz	11.40
10 Hz – Nyquist	13.93
10 Hz – carrier freq.	16.55

Offset range	Timing jitter (ps)
100 Hz – 1 MHz	1.36
100 Hz – 10 MHz	1.65
100 Hz – 100 MHz	4.08
100 Hz – Nyquist	8.98
100 Hz – carrier freq.	12.68

Table 7.4. The 1 GHz gain switched laser timing jitter values obtained by integrating the SSB phase noise plot in Fig. 7.13. The SSB phase noise for offsets over 100 MHz is assumed to remain at -115 dBc/Hz. The spikes due to the signal generator have not been removed.

Fig. 7.15 shows the frequency spectrum of the gain switched laser, captured using the same optical power level ($\sim 270 \mu\text{W}$ onto the detector) and analyser set-up as used previously to capture the frequency spectrum of the compression pulses, c.f. Fig. 7.8. The gain switched laser's frequency spectrum is dramatically different to that of the compression pulses, with the optical noise floor up to 25 dB higher than the system floor, as opposed to ~ 3 dB with the compression pulses. The general form of the harmonic spectrum is visually very similar to theoretical studies of pulse trains exhibiting high levels of both uncorrelated and correlated amplitude and timing jitter, Fig. 7.16.

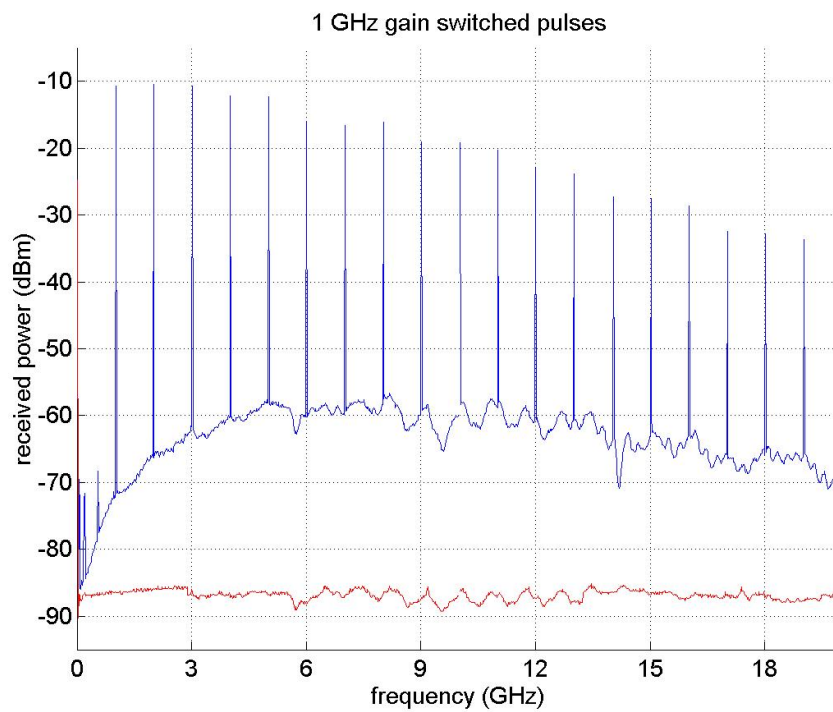


Fig. 7.15. Harmonic spectrum of the gain switched laser. Note that the optical noise floor is now ~ 25 dB higher than the system floor, compared with the ~ 3 dB difference for the soliton effect compressed pulses. (Spectrum analyser resolution bandwidth = 300 kHz, video bandwidth = 1 kHz).

7. Pulse timing jitter performance (SMF-28 compression fibre)

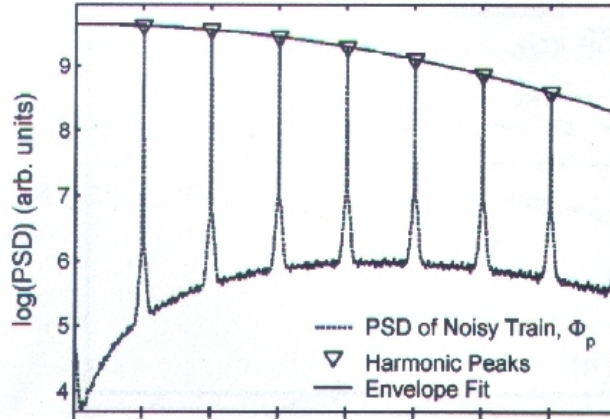


Fig. 7.16. Spectrum of a simulated pulse train exhibiting uncorrelated and correlated amplitude and timing jitter (image reproduced from *Appl. Phys. Lett.* 2002, Ref. [6]). Note visual similarity to Fig. 7.15 above.

Performing calculations on the frequency spectrum of the gain switched laser gives values of 50-60 ps for the timing jitter and around 5-10% for the amplitude jitter, depending on which harmonics are used in the calculations, Fig. 7.17. The timing jitter values obtained are therefore higher than the 16.5 ps obtained via SSB phase noise integration from 10Hz-1GHz. This could be because the SSB phase noise is actually higher than -115 dBc/Hz at offsets larger than 100 MHz. This could perhaps be expected since the pulse source study in Appendix A of this report identifies that gain switched lasers can have a substantial element of uncorrelated jitter, primarily due to spontaneous emission noise during pulse build-up. Due to the different method of generating the pulses, this is not an issue for the compression system.

7. Pulse timing jitter performance (SMF-28 compression fibre)

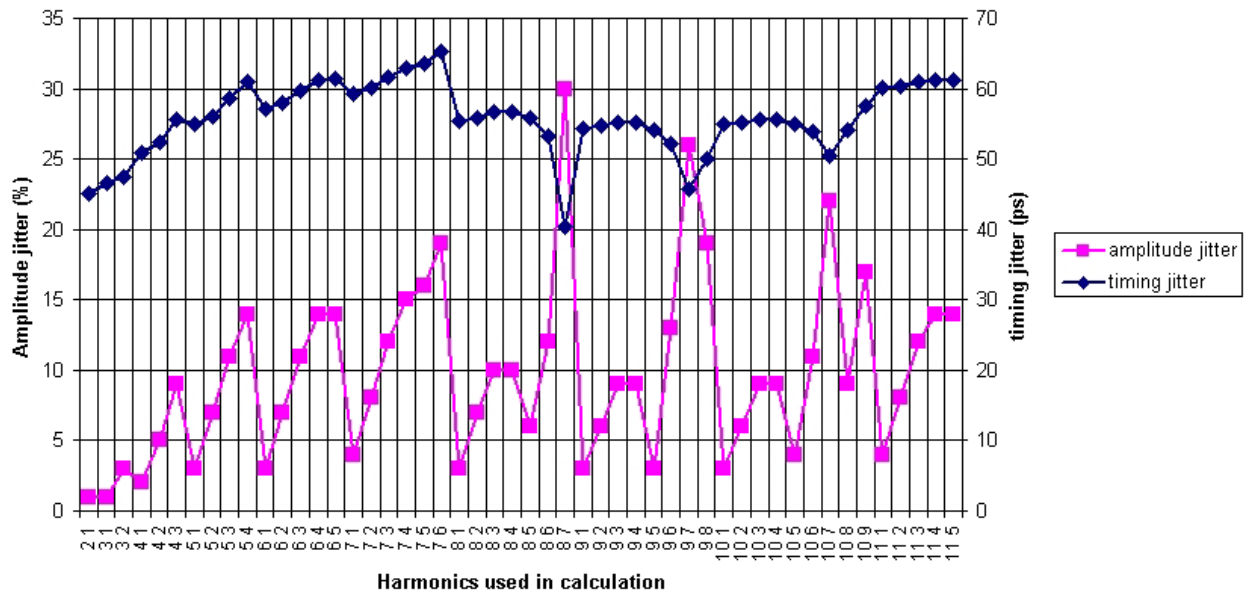


Fig. 7.17. Amplitude and timing jitter values calculated using the Leep and Holm method on the relative integrated harmonic values. The timing jitter can be seen to be in the range 40-60 ps and the amplitude jitter is 5-15%, depending on which harmonics are used in the calculation.

7.14 Implementing the pulse compression scheme into an ADC system

The QinetiQ ADC system is based on optical sampling using a dual output modulator, which overcomes the problem of modulator non-linearities by allowing dual decoding, which also has the benefit of cancelling laser amplitude noise, Fig. 7.18. Over 70 dB linearity is predicted based on DC measurements. There are two options for the back-end electronic digitisation, either a 1 Gs/s 8-bit COTS board or a custom-built high resolution quantiser based on Analog Devices' AD6645 100 Ms/s, 14 bits, 90 dB linearity ADC circuits.

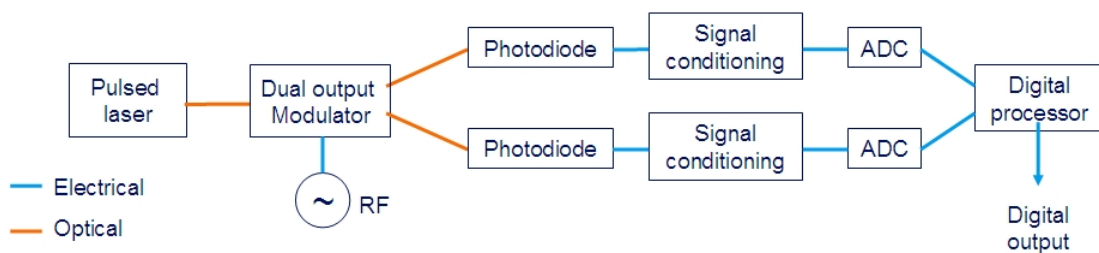


Fig. 7.18. Schematic of the QinetiQ opto-electronic ADC using a dual output modulator to linearise the sampling gate and cancel amplitude noise.

The performance of the ADC system using the pulse compression scheme to perform the sampling is compared with the system performance when the basic gain switched laser from Section 7.13 is used instead, Fig. 7.19. Here 16 separate 1024 point sample windows were averaged for various signal input frequencies. Fig. 7.19 clearly shows the huge benefit of the lower timing jitter compression pulse source for the sampling application, with an improvement of up to 3 bits resolution when sampling higher input frequencies.

In order to make both the gain switched laser and the pulse compression system repetition rates compatible with the QinetiQ electronic ADC digitisers, two methods were employed. The first involved using an amplitude modulator driven with a 1 GHz sinusoid to pulse-pick 2 GHz compressed pulses down to 1 GHz. A separate approach involved using a 100 MHz step recovery diode to pick a 100 MHz train from the 1 GHz gain switched laser or pulse-picked 1 GHz pulse compression set-up.

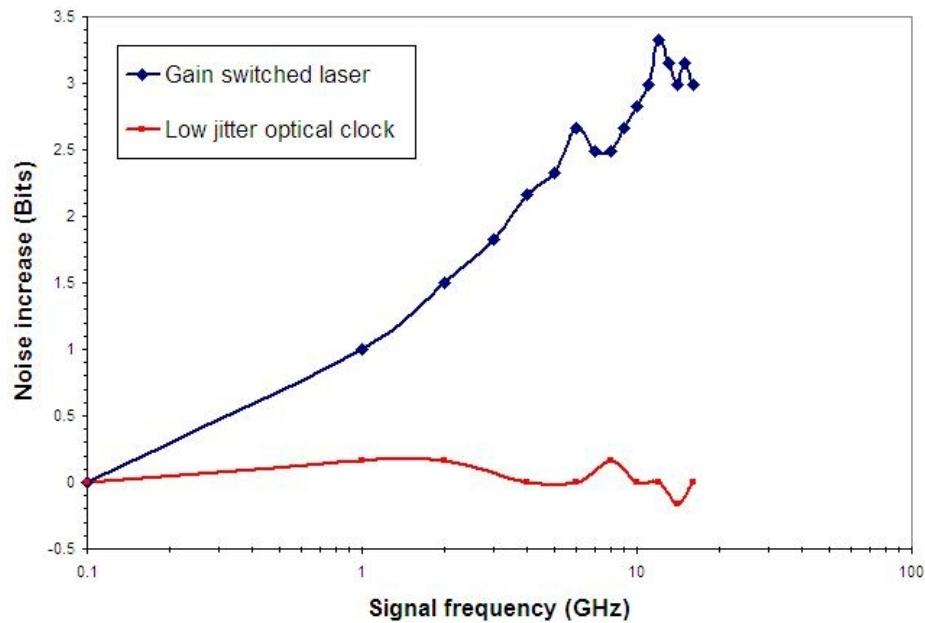


Fig. 7.19. Comparison of the QinetiQ ADC noise performance with a standard gain switched laser and with the lower timing jitter pulse compression scheme. The superior performance of the pulse compression scheme is clear, especially for higher input frequency signals.

7.15 Summary of compression pulse timing jitter performance

The pulse jitter of the soliton-effect compression source was measured using two approaches, SSB phase noise measurements and harmonic analysis. The SSB phase noise spectra of several microwave sources were measured and an hp 83711A signal generator was selected as having the best performance. It did however generate several spurious spikes at offsets of several 100 kHz, and these were also present on the optical pulse train SSB phase noise spectrum. The compressed pulse timing jitter was found to be limited by the microwave source at frequency offsets under around 100 kHz. At higher frequency offsets, the optical pulse noise floor dominated the SSB phase noise spectrum. Table 7.5 gives the timing jitter performance of the 3 GHz soliton-effect compression pulses, as integrated over various frequency offset ranges. For sampling applications, the most important frequency offset range is 10Hz-Nyquist, which gave a timing jitter of 3.135 ps for the raw capture and 2.687 ps with the microwave source spikes removed. This assumed that the SSB phase noise at offsets over 100 MHz remains at -125 dBc/Hz. This figure of 3.135 ps does not compare favourably with the published values for state-of-the-art mode-locked laser setups, however over the more commonly quoted frequency offset range of 100Hz-10MHz, and with the spurious microwave source spikes removed, the timing jitter value reduces substantially to 257 fs.

Offset range	Timing jitter (ps)	
	raw	Smoothed
10 Hz – 1 MHz	2.129	1.388
10 Hz – 10 MHz	2.135	1.397
10 Hz – 100 MHz	2.203	1.499
10 Hz – Nyquist	3.135	2.687
10 Hz – carrier freq.	3.893	3.542

Offset range	Timing jitter (ps)	
	Raw	Smoothed
100 Hz – 1 MHz	1.110	0.204
100 Hz – 10 MHz	1.121	0.257
100 Hz – 100 MHz	1.247	0.602
100 Hz – Nyquist	2.550	2.309
100 Hz – carrier freq.	3.443	3.265

Table 7.5. Summary of 3 GHz optical pulse timing jitters derived from the SSB phase noise spectrum for various offset frequency ranges, for the raw capture and also where the microwave source spikes are removed/smoothed.

Both injection dithering and phase modulation add artefacts to the SSB phase noise spectrum. The injection dithering frequency and its harmonics add large SSB phase noise spikes at kHz offset frequencies and therefore the use of injection dithering to overcome SBS has to be discounted for high precision sampling applications. Phase modulation at 10's of MHz similarly adds spikes to the SSB phase noise at corresponding frequency offsets. Applying much higher frequency phase modulation leads to intermodulation frequencies occurring at lower offset frequencies, for example 950 MHz phase modulation adds SSB phase noise spikes at 50 MHz and 100 MHz (intermodulation frequencies of the 950 MHz phase modulation and the 1.5 GHz microwave source used to generate the periodic input waveform). Phase modulation at the *same* frequency as the microwave source does not suppress SBS as the phase modulation and pulse generation frequencies overlap. For the modulator biased-at-null mode of operation (i.e. the pulse repetition frequency equals twice the microwave drive frequency), the solution is to apply phase modulation at half the microwave source frequency, compress the pulses through the fibre and then halve the repetition rate via pulse-picking. In this way, the SSB phase noise spikes due to the phase modulation used to overcome the SBS only occur at SSB phase noise offset frequencies equal to the Nyquist frequency of the pulses. For example, one can generate 6 GHz optical pulses with 1.5 GHz phase modulation to overcome SBS, compress the pulses through the fibre and then pulse pick to 3 GHz. The phase modulation used to overcome the SBS is at 1.5 GHz, which equals the Nyquist frequency of the sampling pulse train. In this way, the phase modulation does not contribute any artefacts to the offset integration range of interest, 10Hz-Nyquist. For the modulator biased away from null and driven to null mode of operation (i.e. pulse repetition frequency equals the microwave drive frequency), the phase modulation can be applied at Nyquist with no pulse picking of the output pulse required.

A fibre Bragg grating was tested in the system to filter out unwanted EDFA amplified spontaneous emission it but its inclusion did not affect the SSB phase noise spectrum of the 3 GHz optical pulse train.

Applying Leep and Holm's method to the harmonic spectrum of the compression pulses gave timing jitter values of between 4-5 ps and amplitude jitters of around 2-3%, depending on which harmonics were used in the calculation. This timing jitter value

was in close agreement with the 3.893 ps value obtained by integrating the SSB phase noise over extended frequency offset range 10Hz-3GHz.

A basic 1 GHz gain switched laser was also evaluated using both the SSB phase noise method and analysis of its harmonic spectrum. The SSB phase noise approach gave a timing jitter value of 16.55 ps for the frequency offset range 10Hz-1GHz. This was lower than the harmonic analysis value of between 50-60 ps. This could be due to the fact that the SSB phase noise approach assumed that the SSB phase noise remained at -115 dBc/Hz at offsets greater than 100 MHz, when in fact the uncorrelated nature of the gain switch operation may mean this is not a valid assumption.

Both the pulse compression source and the 1 GHz gain switch laser were integrated into the QinetiQ opto-electronic ADC prototype system, and the new compression pulse source showed distinctly improved sampling resolution performance over the gain switched laser source. This is believed to be the first time that soliton-effect compression pulses have been used to perform optical sampling.

The timing jitter value of 257 fs measured over the offset range of 100Hz-10MHz is comparable to the very best gain-switched and Q-switched laser values published in the literature and two orders of magnitude higher than the best mode-locked laser figures, see Table A.4 in Appendix A

Given the findings of the literature survey of soliton and soliton-effect schemes in Chapter 4, the analysis performed in this report appears to be the first detailed timing jitter study performed on this type of pulse compression system. The timing jitter findings discussed in this chapter have been presented in a comprehensive conference proceeding paper^[7]. The technique for overcoming stimulated Brillouin scattering without adding to the pulse timing jitter for optical sampling applications, by applying phase modulation at the Nyquist frequency, has been filed as a patent^[2].

References for Chapter 7

1. Juodawlkis P.W., Twichell J.C., Wasserman J.L., Williamson R.C., “Measurement of mode-locked laser timing jitter using phase-encoded optical sampling”, Conf. on Lasers and Electro-Optics, 2000. (CLEO 2000), pp. 78 – 79, May 2000
2. McDonald G.J., “Low jitter optical pulse source for sampling applications”, GB Patent 0618021.0, 11th Sept. 2006
3. Clark T.R, Carruthers T.F., Mathews P.J., Duling I.N., “Phase noise measurements of ultrastable 10 GHz harmonically mode-locked fibre laser”, Electron. Lett., 35(9), pp. 720-721, 1999
4. Grein M.E., Jiang L.A., Haus H.A., Ippen E.P., McNeilage C., Searls J.H., Windeler R.S., “Observation of quantum-limited timing jitter in an active, harmonically mode-locked fiber laser”, Opt. Lett., 27(11), pp. 957-959, 2002
5. Leep D.A. and Holm D.A., “Spectral measurement of timing jitter in gain-switched semiconductor lasers”, Leep and Holm, Appl. Phys. Lett., **60** (20), pp 24512 – 2453, 1992
6. Gross M.C., Hanna M., Patel K., Ralph S.E., “Spectral method for the simultaneous determination of uncorrelated and correlated amplitude and timing jitter”, Appl. Phys. Lett., 80(20), pp. 3694-3695, 2002
7. McDonald G.J., Seeds A.J., “A novel pulse source for low-jitter optical sampling: a rugged alternative to mode-locked lasers”, SPIE Proc. on Advanced Free-Space Optical Communication Techniques/Applications II and Photonic Components/Architectures for Microwave Systems and Displays, Vol. 6399, 63990J, Oct 2006

8. Optical metrology system design

This chapter summarises an Architectural Design Document which was written by the author of this thesis to define the Scanning Interferometer Pulse Overlap and Detection (SIPOD) proof-of-principle demonstrator system which is being developed and manufactured by QinetiQ for the European Space Agency. The aim of the SIPOD system is to realise optical range finding functionality in a compact and rugged system for use on micro-satellite missions. The Architectural Design Document described the system in a hierarchical manner, covering the various sections (optics, mechanics, analogue electronics, digital electronics and software) at the appropriate level.

This chapter is divided into six main sections:

- Introduction to the SIPOD system and its goals
- Top level system architecture
- Design of electronic hardware modules
- Design of optical hardware modules
- Design of control software & algorithms
- System performance analysis (model)

8.1 Introduction to SIPOD

SIPOD is an optical measurement system being developed for the PROBA-3 formation flying mission to measure the longitudinal separation of the satellites. The system utilises the highly stable properties of the compression pulse source, and its electronically tuneable pulse repetition rate, thus realising a novel approach to optical metrology which is based on the rapid scanning of the optical pulse repetition rate to determine the exact frequencies which allow the return pulses from an outlying satellite to exactly overlap with a set of reference pulses on the hub satellite; heterodyne detection is used to measure the specific repetition rates which provide the maximum overlapping pulse condition. From the start of the programme it was anticipated that the inter-satellite spacing would be determined to ≤ 30 microns absolute accuracy at ranges

from ~25 metres to hundreds of metres and at update rates of at least 10 Hz, thus meeting or exceeding the PROBA-3 optical metrology requirements. The unambiguous measurement range is limited only by the coherence length of the laser and therefore the system will be appropriate for future formation flying missions, which may require longitudinal range measurements over many kilometres with accuracies limited only by the frequency reference. Every system component of this new metrology system already exists as either a military or space qualified version, allowing rapid prototyping of a mission ready system. One final important feature of the system is that it can, in principle, switch between pulsed and continuous wave operation to enable variations in the satellite formation spacing to be tracked with interferometric resolution.

8.2 Target / preliminary specifications for SIPOD system

The following table summarises the target/predicted performance of the SIPOD breadboard system.

No.	Property	Value
1	Operating range	25 ... 250m
2	Maximum Laser Power	500mW
3	Laser Power Control	10-500mW (non-compressed)
4	Optical system size	10 litres
5	Optical system weight	10 kg
7	Beam diameter	~30mm diameter
8	Beam divergence	>1mrad desired >0.05mrad required
9	Range Accuracy (non- interferometric)	30 microns
10	Recovered bandwidth	>10Hz
11	Data-logging	via Labview generated files
12	Optical Head volume	<10 litres
13	Signal Processor size	PC based
14	Signal Processor weight	<15 kg
15	Power consumption	<30 W
16	Power format	Auto-ranging 100-250 V AC mains
17	Control Interface	Labview front-panel
18	Interferometric resolution	<50nm
19	Operating Conditions	5 – 35 deg C, <80% non-condensing

Table 8.1. Predicted performance of the SIPOD breadboard system, prior to build.

8.3 Top level system architecture

SIPOD is a near infra-red laser based range-finding system that has two modes of operation. The “Pulse Overlap Detection” principle utilises an interferometric carrier signal to indicate the overlap condition, which allows micron level absolute range-finding. The interferometric signal can also be used for fringe-tracking, although this feature does not constitute part of the programme of work being undertaken for ESA. Due to the fact that the fringe tracking feature may be valuable for future missions, some requirements for this mode of operation are considered here, but will not necessarily be developed further. Fig. 8.1 shows a generic SIPOD system diagram.

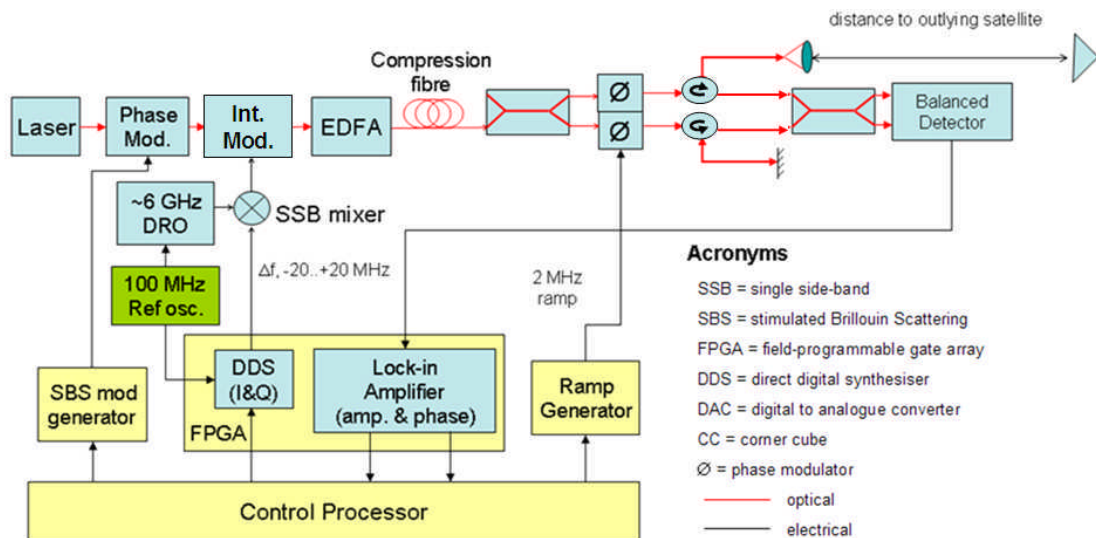


Fig. 8.1. The SIPOD system configuration

The system can be broken down into 6 key sections, namely:

1. Frequency reference unit with up-converter, which is the high frequency RF section.
2. Laser pulse generation system consisting of laser, phase modulator (for elimination of SBS), intensity modulator, EDFA and compression fibre
3. Interferometer head, which contains the fibre splitter/combiner, phase modulator(s), reference mirror, telescope (collimator) lens assembly and balanced detector.
4. Frequency sweep and detect system, which generates the I & Q offset frequencies and detects the carrier strength signal indicating the overlap condition

8. Optical metrology system design

5. Signal generation instrumentation. This section encompasses the ramp generator and an RF generator required for the elimination of SBS. These components would eventually be incorporated into the same FPGA board as the “sweep & detect” components, however development of a single processor board is beyond the scope of this programme.
6. Control system / software, comprising the Labview based control of the AM frequency sweep, Phase modulator frequency etc.

Based on these functional blocks, the system is then relatively modular, as shown in Fig. 8.2 below.

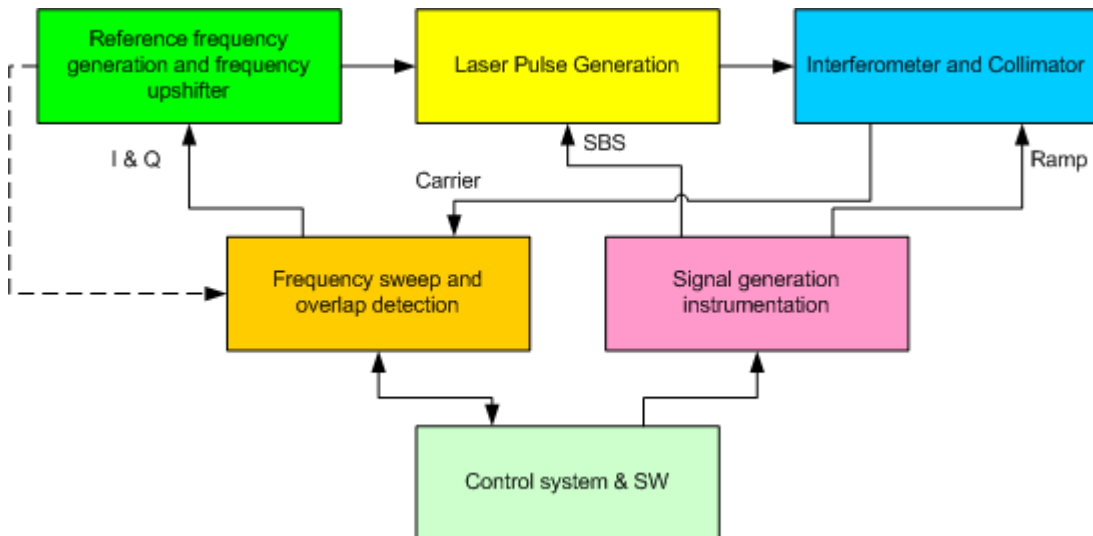


Fig. 8.2. Top level block diagram of the SIPOD system

8.4 Initial optical range finding using repetition rate tuneability

In order to perform the initial coarse optical range finding, the tuneable pulse source must be used to determine the special case where an integer number of optical pulses exactly spans the hub to outlier round trip distance D , Fig. 8.3.

8. Optical metrology system design

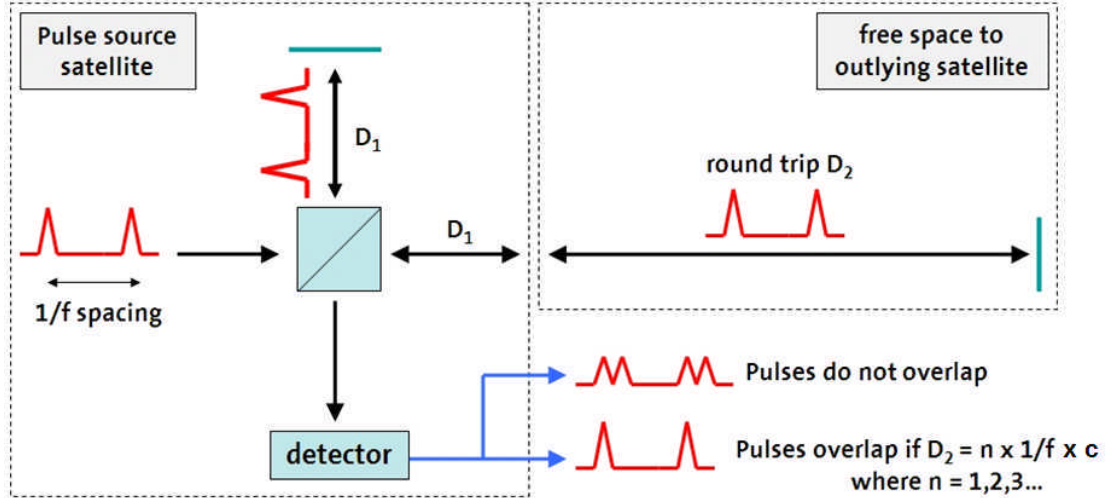


Fig. 8.3. For the correct optical pulse repetition rate, f , the return pulses from the unknown satellite outlier can be made to overlap and hence interfere with a second set of pulses generated by the same optical source. By scanning the frequency to find two separate pulse repetition rates which provide the overlapping condition, the coarse longitudinal range can be determined unambiguously.

If the pulses have a repetition rate R equal to the microwave oscillator frequency f_{RF} :

$$\text{Pulse spacing in seconds} = 1 / R$$

$$\text{Pulse spacing in metres} = c / R$$

$$\text{Pulses must satisfy: } D = n \frac{c}{R} \text{ where } n = 1, 2, 3, \dots \quad (8.1)$$

The repetition rate is scanned to find the frequency R_1 providing an integer multiple of the pulse-to-pulse spacing which exactly equals the hub to satellite round trip spacing D .

By simultaneous equations the nearest repetition rate, R_2 , satisfying the integer multiple requirement is given by Eq. 8.4.

$$n = \frac{DR_1}{c} \quad (8.2)$$

$$n+1 = \frac{DR_2}{c} \quad (8.3)$$

$$R_2 = \frac{c}{D} + R_1 \quad (8.4)$$

$$\text{Re-writing for } D \quad D = \frac{c}{R_2 - R_1} \quad (8.5)$$

Once the round trip distance D has been determined from two frequencies providing adjacent overlapping peaks, Eq. 8.5, then Eq. 8.2 gives the pulse order. Re-writing Eq. 8.5 as Eq. 8.6, it is observed that the frequency spacing between the two repetition rates which satisfy the adjacent integer spacing requirement varies only with round trip distance D . For the PROBA-3 range requirement of 25-250 metres (50-500 metre round trip), the scan range is 650 kHz to 6.5 MHz, Fig. 8.4. This scan requirement is a small fraction (10^{-3} - 10^{-4}) of the nominal pulse repetition rate of 6 GHz.

$$R_2 - R_1 = \frac{c}{D} \quad (8.6)$$

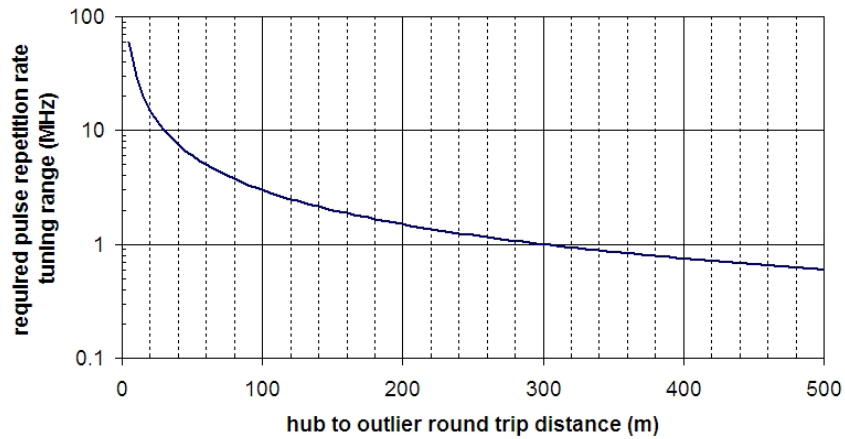


Fig. 8.4. The frequency scan range requirement of the optical pulse repetition rate R , for PROBA-3's 25-250 metre hub to outlier operating range (note round trip distance = twice the hub to outlier range).

Once the integer number of pulses, n , has been determined then the absolute frequency to the n th peak is given by $F_n = nR_1$. Now the distance is provided by d where:

$$d = \frac{n_1 c}{R_1} = \frac{n_2 c}{R_2} \quad (8.7)$$

This represents an n -fold improvement in range accuracy over that derived using the frequency difference between successive overlapping peaks, Eq. 8.5. Once the integer number of pulses is known, the error in d is reduced to the uncertainty in either R_1 or R_2 , since the integer value is an exact figure and the speed of light in vacuum is known to very high accuracy.

The increase in range accuracy due to knowing the integer number of pulses spanning from the hub to outlier is an important SIPOD feature and is repeated to emphasis its significance. Once the coarse range D has been determined (by the RF metrology or by an initial optical scan) and subsequently the pulse order n is determined, then the range measurement accuracy is improved by the order of the pulse, n . The absolute frequency of the n th peak, F_n , is given by $F_n = nf$ where n is an integer. An improved estimate for d is then given by $d = nc/F$. The value of n is obtained using Eq. 8.8 rounded to the nearest integer. For n to be unambiguously determined, the fractional uncertainty in f must be much less than n^{-1} . For large values of n , it may be necessary to perform an additional scan over an extended frequency range to achieve this precision.

$$n_1 = \frac{R_1}{|R_2 - R_1|} \quad (8.8)$$

Additionally, PROBA-3's RF metrology will be able to provide a coarse range to around 1 cm accuracy. Since 6 GHz pulses have 5 cm pulse-to-pulse spacing in vacuum, the pulse order n could be inferred using this RF metrology cue, although SIPOD does not require any such external range cue.

The maximum possible refresh rate of the system is governed by the round trip time of the pulses. In the extreme case, the repetition rate cannot be varied until at least one pulse has propagated through the compression fibre and returned from the outlier to the hub satellite and overlapped with a reference pulse. As will be discussed, it is preferable that many pulses overlap to reduce the measurement error significantly.

8.5 Component specifications / requirements

An error analysis has been carried out to identify which points in the signal processing “flow” may contribute detrimental signals or effects. Both the pure range-finding and interferometric fringe tracking system requirements are considered in the analysis, and where possible, system components will be chosen to enable both modes of operation. The diagram overleaf, Fig. 8.5, shows the front-end processing steps and their critical properties.

The white boxes on the left and right of the flow diagram describe the type of contribution or issue to be analysed with respect to the process/step/component at that point in the flow. In each case, the properties of the respective process step are assessed and specifications for the critical component defined to keep the performance as close to the theoretical limit as possible. Boxes O1-11 refer to potential optical sources of error/noise, and E1-9 potential electronic sources.

8. Optical metrology system design



Fig. 8.5. System Flow Diagram showing error analysis points. Points E1-E9 are potential electronic limitations or error sources, and points O1-O11 are potential optical noise or error sources.

8.6 System error analysis

This section summarises on the error sources identified in Fig. 8.5 above.

The optical carrier E-field is given by:

$$E(t) = E_0 \sin(2\pi f_c t) \quad (8.9)$$

Where the carrier frequency $f_c \approx 1.9 \times 10^{14}$ Hz ($\lambda = 1.55 \mu\text{m}$)

E_0 = peak E-field

Applying sinusoidal phase modulation to the carrier to overcome SBS:

$$E(t) = E_0 \sin[2\pi f_c t + \phi(t)] \quad (8.10)$$

Where:

- The applied phase modulation is given by $\phi(t) = \phi_0 \sin(2\pi f_{PM} t)$ (8.11)
- ϕ_0 is the peak phase deviation
- The phase modulation frequency $f_{PM} \approx 65 \times 10^6$ Hz

Intensity transmission from a Mach- Zehnder modulator is given by T_{MZ} :

$$T_{MZ} = \frac{1}{2} \left[1 + \sin \left[\frac{\pi}{V_\pi} (V_{RF}(t) + V_{BIAS}) \right] \right] \quad (8.12)$$

$$\text{The RF signal applied to the intensity modulator is } V_{RF}(t) = V_0 \sin(2\pi f_{RF} t) \quad (8.13)$$

Where: $f_{RF} \approx 6.6 \times 10^9$ Hz

V_0 = peak drive voltage

V_π = modulator's half-wave voltage

V_{BIAS} = modulator's bias voltage

Modes of operation:

1. Biased at null when $V_{BIAS} = 1.5 V_{\pi}$, output pulse repetition rate $f_{rep} = 2 \times f_{RF}$
2. Biased away from null and driven to null, e.g. $V_{BIAS} = 1.6 V_{\pi}$ and RF signal drive $V_0 = 0.1 V_{\pi}$, output repetition rate $f_{rep} = f_{RF}$

Therefore, combining Eqs. 8.9-8.12, the optical waveform launched into the EDFA is given by:

$$I(t) \propto \underbrace{\left[\frac{E_0}{2} \sin[2\pi f_c t + \phi_0 \sin(2\pi f_{PM} t)] \right]^2}_{\text{phase modulated carrier}} \underbrace{\left[1 + \sin\left[\frac{\pi}{V_{\pi}} (V_0 \sin(2\pi f_{RF} t) + V_{BIAS}) \right] \right]}_{\text{intensity modulation}} \quad (8.14)$$

O1: Laser intensity and phase noise

Optical carrier frequency instabilities

- Short-term laser instabilities manifest themselves as laser linewidth broadening, Δf , resulting in reduced laser coherence length and therefore shorter longitudinal range capability.

$$\text{SIPOD range} = \text{coherence length}/2 = c/(2\Delta f) \quad (8.15)$$

- Longer-term laser wavelength drift must not exceed 2×10^{-8} over the time of the return flight to the outlier ($\leq 1.6 \mu s$) plus the measurement time $t_{\text{measurement}}$ (for PROBA-3 the desired update rate is ≥ 10 Hz, giving a scan time of ≤ 0.1 seconds)]. The round trip time only becomes significant for round trips of many thousands of kilometres, so the measurement time is the important factor. The figure of 2×10^{-8} relates to 10 microns accuracy over 500 metres. More generally (in terms of future missions), the long-term laser stability requirement for the SIPOD system is given by:

$$\lambda_{stability} \geq \left(\frac{range_resolution}{max_range} \right) per \left(\frac{D}{C} + t_{measurement} \right) seconds \quad (8.16)$$

Commercially available stable fibre lasers (such as those manufactured by Koheras^[1]) were shortlisted as the CW source which would be intensity modulated and launched into the compression fibre. The Koheras offering has a Relative Intensity Noise (RIN) specified to be below -115 dB/Hz at 1 MHz dropping to -140 dB/Hz at 10 MHz. Due to the use of a balanced detector configuration in the SIPOD system, the intensity noise should be reduced by a factor of 20 dB or more, via the common mode rejection effect. Assuming that the pass band for the lock-in section is >10kHz, this will still lead to a negligible intensity noise contribution from the laser.

The theoretical limits on the achievable position sensitivity for the heterodyne interferometer are governed by the carrier to noise ratio (CNR) available. Even in non-interferometric mode, the SIPOD system relies on a constant and reasonably high visibility interference signal, and thus also a given CNR. This performance is governed by three values, namely the reference signal strength (a constant), the recovered optical signal strength, and the noise at the input. The noise level cannot be lower than the shot noise level, and is typically influenced by laser relative intensity noise (RIN).

Phase noise measurements published by Koheras state that their E15 laser exhibits a 1/f characteristic, implying that it is dominated by frequency jitter. A set of phase noise values will be specified as acceptance criteria for the laser, corresponding exactly to the properties required in the final system. Supplier data shows that the phase noise is of order 50 dBmicrorad/ $\sqrt{\text{Hz}}$ at ~100 Hz signal frequency, corresponding to ~0.04 nm noise equivalent displacement in a 1 Hz bandwidth. Although this noise level is easily sufficient to allow the system to **resolve** AC motion signals, the lack of absolute stability of the wavelength undermines the ability to determine **absolute** range.

O2 & O5: Phase noise

As discussed in Chapter 7, the current compression source pulse arrangement has been characterised using single-sideband phase noise analysis to derive timing jitter values due to phase noise. As discussed below, the single-sideband frequency offset range 600 kHz to 100 MHz is the important range of interest for the SIPOD application. At these offsets the optical pulse source phase noise is dominated by contributions from the optical amplifier and not the microwave frequency source for the source implemented using SMF-28. A value of 380 fs RMS timing jitter has been measured for the current compression source using SMF-28 as the compression fibre.

The short-term stability of the microwave frequency f_{RF} applied to the intensity modulator can be measured by the single-sideband phase noise

- Instabilities in the microwave frequency f_{RF} are directly translated into instabilities in the repetition rate of the microwave pulse envelope. These instabilities can be measured by integrating the single-sideband phase noise over the appropriate frequency offset range of interest for the application, using Eq. 8.17.
- Minimum single-sideband frequency offset: the maximum round-trip time of the pulses from the hub to the outlier = 1.6 μ s for the maximum round trip of 500 metres, hence the corresponding minimum single-sideband phase noise offset frequency of interest for PROBA-3 is 60 kHz.
- Maximum single-sideband frequency offset: the SIPOD system proposes to use a 100 MSamples/s digitiser, e.g. a maximum sampling aperture duration of <10 ns. Therefore the maximum single-sideband phase noise offset frequency of interest is 100 MHz.
- The single-sideband phase noise frequency offset range 600 kHz to 100 MHz is therefore narrow in comparison to the pulse repetition rate of \sim 6 GHz. Based on actual single-sideband measurements of the current pulse compression source, if a worst case single-sideband phase noise of -122 dBc/Hz is integrated over the offset

8. Optical metrology system design

range 600 kHz – 100 MHz, the RMS pulse-to-pulse timing jitter contribution for a 6 GHz pulse train is 380 fs. Note that this timing jitter is independent of pulse width, and therefore is more significant for highly compressed pulses.

$$\sigma_{\tau} = \sqrt{2.L(\phi)} \approx \frac{1}{2\pi f_{RF}} \sqrt{\int_{f_{min}}^{f_{max}} 2.L(f)df} \quad (8.17)$$

where

$L(f)$ = single sideband phase noise relative to the carrier $L(\phi)$

$f_{min} = c/D$

f_{max} = sample rate

A very important difference between the optical sampling application and the SIPOD system operation is that SIPOD is not critically dependent on the timing jitter between individual pulses. The optical sampling arrangement discussed in Chapter 7 captures a series of one-time only samples of an unknown waveform. The SIPOD system however is not measuring the overlap of a single pulse with another pulse, but instead it is looking at the time-averaged overlap of many pulses (6.6×10^5 pulses if 100 frequency steps are made per scan and the scan rate is 100 Hz), and so the effect of the timing jitter is reduced by square root of the number of measurements/overlaps per sampling slot: $\sqrt{6 \times 10^5} = \sim 800$. Therefore the *effective* timing jitter becomes ~ 0.5 fs, corresponding to a negligible 75 nm range error.

Therefore the effective SIPOD timing jitter is given by:

$$\sigma_{t(SIPOD)} = \frac{\sigma_{t(pulse)}}{\sqrt{\left(\frac{f_{RF}}{freqsteps \times scanrate} \right)}} \quad (8.18)$$

O3: Bias point drift of the intensity modulator

A low frequency (<1 Hz say) control loop should be used to monitor and adjust the bias point of the intensity modulator to ensure optimised compressed pulses. Bias drift will be too slow to affect measurement accuracy (at ≥ 10 Hz scan rates) but will result in non-optimum pulse compression resulting in reduced range resolution. Bias monitoring can be achieved by tapping off a small fraction of the intensity modulator output and monitoring the RMS level on a slow detector and/or monitoring the shape of the overlapping heterodyne signal.

Variations in the null transmission point, V_{NULL} , of the intensity modulator have implications for the microwave waveform launched into the compression fibre, unless the transmission function is monitored and V_{BIAS} corrected appropriately.

- Biased at null operation, $V_{\text{BIAS}} = V_{\text{NULL}}$. As the modulator transmission null point deviates from the applied bias voltage, the successive pulses become irregular.
- For the arrangement where the modulator is biased away from the null transmission point and driven to the null point, $V_{\text{BIAS}} = V_{\text{NULL}} + V_0$, the pulse envelope will not experience optimum compression and the range resolution will decrease. This regime is preferred to biasing at null, as a bias drift results in slightly broader consistent pulses as opposed to irregular successive pulses.

The required V_{BIAS} tracking rate of <1% per minute is too slow to adversely impact specific samples at 100 MSample/s or complete scans at ≥ 10 Hz refresh rates. A low bandwidth bias control loop should prevent long-term bias drift and subsequent non-optimised pulse compression.

O4: Optical pulse intensity jitter

The intensity jitter of the current compression source pulse arrangement has been characterised using harmonic analysis, and was found to be <2%. As with the timing jitter, this value becomes negligible when integrating the carrier signal value over

$\geq 6 \times 10^5$ pulses (i.e. 100 samples per scan at 100 Hz scan rates with 6 GHz pulses). The effective intensity jitter drops to 2.5×10^{-3} % due to the square root of the number of measurements.

O6: Polarisation issues

Only one polarisation must be launched into the measurement interferometer to avoid ambiguous range measurements arising from multiple possible polarisation orientation recombinations. In the ideal scenario the pulse compression source will be polarisation maintaining throughout, however for the SIPOD system it may not be economic to develop a custom fibre with all the necessary parameters. Therefore the initial proof-of-principle SIPOD system uses a non-polarisation maintaining COTS highly non-linear fibre followed by active polarisation control.

O7 & O9: Technology for interferometer splitter/combiner & reference mirror

In order to demonstrate the operation of the SIPOD system, a fibre interferometer could be used with a COTS phase modulator spliced into the reference arm. Metal coatings on the reference fibre end are an easy option to provide the reference mirror. Although this is a simple and effective solution for proof-of-principle, an integrated optics solution (i.e. GaAs waveguide) would be more compact and would minimise thermal drift effects which would complicate verification of system performance. A fibre solution will be the primary system design, however, should a simple & low cost method for generation of the integrated optic solution become available, this will be considered.

O8: Bandwidth for ramp

In order to generate a carrier frequency of between 1 and 10 MHz, a ramped modulation signal must be applied to the phase modulator. To produce a reasonably linear ramp, many higher (odd) harmonics are required. As telecommunications modulators are available in the 1-10 GHz bandwidth range, the opto-electronic component should not place any limitations on the ramp quality.

O10: FM Signal, Background Doppler, Drift

The bandwidth required to allow correct operation of the system is defined by two effects, namely drift dependent Doppler shift and response time requirements. Agreed specifications for the ACOM programme have been defined as 50 mm/sec, generating a 66 kHz Doppler shift, which can easily be accommodated as an error band around the nominally 5 MHz carrier frequency.

The Doppler shift Δf is given by:

$$\Delta f = \frac{fv}{c} \quad (8.19)$$

where

f is the transmitted frequency (the optical carrier frequency $\sim 2 \times 10^{14}$)

v is the velocity of the transmitter relative to the receiver in metres per second

c is the speed of light

During laboratory testing, a fibre delay will almost certainly be used to simulate at least a large portion of the longer ranges to be measured, which will no doubt generate further drift effects, removal/compensation of which is a topic that requires further discussion with the ESA customer, *potentially requiring the use of a vacuum test facility for this stage.*

The phase information of interest is superimposed on a carrier which is nominally at 5 MHz. The sampling frequency can be locked to the external reference frequency (100 MHz), however this is not as critical in the lock-in section of the system. It may be beneficial to use a relatively high sampling frequency to allow frequency analysis of the pseudo-heterodyne carrier, as this may be used to automatically optimise the drive amplitude. Also, it may be convenient to use a multiple of the 44.1 kHz data rate typically used in WAV format files, to allow audio analysis of pick-up effects.

Drift compensation

Some aspects of system operation may be affected by drift of the target. Scanning the repetition rate in both directions will allow compensation of the error produced. It may, however, also be beneficial to differentiate the phase signal in the FPGA (simply subtract the phase from the previous clock cycle) to determine the drift velocity, and thus correct or optimise as appropriate.

O11: Divergence and Telescope Design

The free space optics design has been undertaken by Dr David Orchard at QinetiQ and not by the author of this thesis. At the start of the design process it was expected that a beam diameter of order 30 mm would be required. Optimum collimation will generate a divergence of order 70 microrads, i.e. a spot diameter of order 50 mm at 250 m range. In this configuration, the use of a 25 mm diameter corner cube will maintain good returns at all ranges, and will not generate large range dependent effects, nor be overly sensitive to lateral shifts. A single lens would be sufficient to achieve this requirement.

Larger divergences can be used. This would ease the bore-sighting and beam-pointing requirements of the system. However, the strength of the heterodyne signal depends strongly on the divergence of the transmitted beam. At distances large compared to the Rayleigh range, the power returned from the retroreflector falls as the fourth power of the divergence and the signal falls as the square of the divergence. Thus, the ADC would require a dynamic range of 100:1 to cope with ranges between 25 m and 250 m. This may require the addition of an adjustable gain amplifier prior to the ADC to enable to use of the full bit-depth of the ADC at all ranges.

E1 Phase noise & visibility issues related to the anti-SBS phase modulator

Care must be taken to ensure that the phase modulation used to overcome SBS does not detrimentally affect the interferometer signal. Since the two arms of the extended interferometer will be of different lengths, when recombined the phase modulation from the two arms may not be in phase. This will tend to result in a lower peak heterodyne signal than if they were both in phase.

However, as discussed below, given knowledge of the approximate range, a small adjustment can be made to the modulation frequency used to overcome SBS, which reduces the reduction of the peak heterodyne signal to a negligible level.

Deriving this effect mathematically, assuming a phase modulated CW input carrier to the interferometer (i.e. not pulsed) for simplicity:

$$E_{input}(t) = E_{input} \cos[\omega_c t + \phi_{SBS} \sin(\omega_{SBS} t)] \quad (8.20)$$

In arm 1 of the test interferometer, the ramp phase modulation is applied giving:

$$E_1(t) = E_1 \cos[\omega_c t + \phi_{SBS} \sin(\omega_{SBS} t) + \phi_H f_H t] \quad (8.21)$$

Assuming the ramp optimally drives the phase modulator through 2π , Eq. 8.21 becomes:

$$E_1(t) = E_1 \cos[(\omega_c + \omega_H)t + \phi_{SBS} \sin(\omega_{SBS} t)] \quad (8.22)$$

The E-field in arm 2 experiences a time delay corresponding to the hub to outlier distance D , $\delta t = D/c$:

$$E_2(t) = E_2 \cos[\omega_c(t + \delta t) + \phi_{SBS} \sin(\omega_{SBS}(t + \delta t))] \quad (8.23)$$

Re-writing in exponential form using the relationship $\cos \alpha = \frac{e^{i\alpha} + e^{-i\alpha}}{2}$

$$\begin{aligned} E_1(t) &= \frac{1}{2} E_1 [\exp[i((\omega_c + \omega_H)t + \phi_{SBS} \sin(\omega_{SBS} t))] + c.c.] \\ E_2(t) &= \frac{1}{2} E_2 [\exp[i(\omega_c(t + \delta t) + \phi_{SBS} \sin(\omega_{SBS}(t + \delta t)))] + c.c.] \end{aligned} \quad (8.24)$$

8. Optical metrology system design

The output intensity is related to:

$$\begin{aligned}
 I_{output} &\propto |E_1 + E_2|^2 \\
 &\propto e^{i(\omega_c + \omega_H)t} e^{i(\phi_{SBS} \sin(\omega_{SBS}t))} e^{-i(\omega_c(t+\delta t))} e^{-i(\phi_{SBS} \sin(\omega_{SBS}(t+\delta t)))} + c.c. \\
 &= e^{i\omega_H t} e^{-i\omega_c \delta t} e^{i\phi_{SBS} [\sin(\omega_{SBS}t) - \sin(\omega_{SBS}(t+\delta t))]} + c.c.
 \end{aligned} \tag{8.25}$$

$$I_{output} \propto e^{i\omega_H t} e^{-i\omega_c \delta t} e^{i\phi_{SBS} [\sin(\omega_{SBS}t) - \sin(\omega_{SBS}(t+\delta t))]} + c.c. \tag{8.26}$$

Using $\sin A - \sin B = 2 \cos\left(\frac{A+B}{2}\right) \sin\left(\frac{A-B}{2}\right)$

$$I_{output} \propto e^{i\omega_H t} e^{-i\omega_c \delta t} e^{i2\phi_{SBS} \cos(\omega_{SBS}(t+\frac{1}{2}\delta t)) \sin(-\frac{1}{2}\omega_{SBS}\delta t)} + c.c. \tag{8.27}$$

Band-pass filtering the detected signal around a central frequency ω_H removes the higher frequency, time dependent, terms leaving:

$$I_{output} \propto e^{i\omega_H t} e^{-i\omega_c \delta t} e^{-i2\phi_{SBS} \sin(\frac{1}{2}\omega_{SBS}\delta t)} + c.c. \tag{8.28}$$

The SBS phase modulation term disappears when:

$$\begin{aligned}
 \omega_{SBS} \delta t &= 2\pi n & \text{where } n = 1, 2, 3, \dots \\
 \text{Or } f_{SBS} &= \frac{nc}{D}
 \end{aligned} \tag{8.29}$$

Therefore the phase modulation used to overcome the SBS effects should be tuned to a frequency satisfying Eq. 8.29, to avoid superimposing phase modulation of amplitude

$\leq 2\phi_{\text{SBS}}$ (depending on δt) onto the heterodyne signal. Typically $\phi_{\text{SBS}} \leq \pi/6$, is a sufficient amplitude of phase modulation to successfully eliminate SBS. Fig. 8.6 shows the tuning range required to guarantee that optimum phase modulation is applied, for a given round trip range. Since the satellites will be slowly drifting relative to each other, the phase modulation frequency will not require rapid updating.

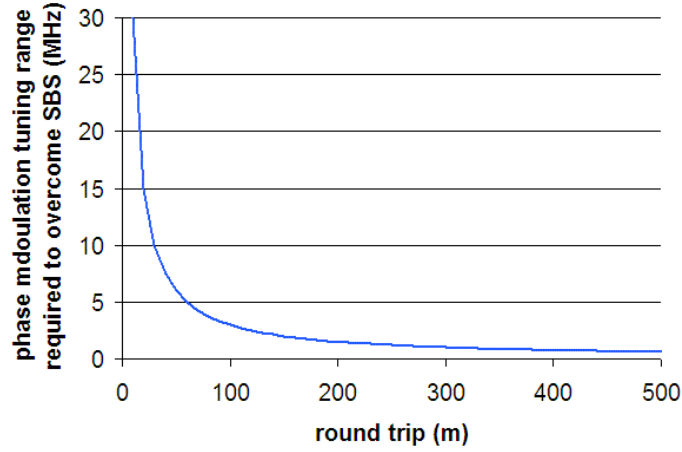


Fig. 8.6. Minimum required tuning range of the phase modulation used to minimise the effects of SBS on the heterodyne signal, given the interferometer path length difference.

E2: Reference frequency accuracy

Long-term stability of the microwave frequency f_{RF} applied to the intensity modulator:

- 10 microns range resolution over a 500 metre round trip requires 2×10^{-8} stability in the microwave reference frequency over the duration of each measurement plus the round trip time of flight.

The microwave drive frequency at ~ 6 GHz comprises the 6 GHz reference mixed with the 0.1 MHz to 8 MHz frequency generated by the FPGA core.

In order to achieve the 2×10^{-8} stability requirement for PROBA-3, the microwave frequency f_{RF} of around 6 GHz applied to the intensity modulator must be stable to 120 Hz. This places a 2×10^{-8} stability requirement on the 6 GHz reference source, and a 1.5×10^{-5} stability requirement on the FPGA signal generator core.

An accuracy of 2.5 microns at a range of 250 m will require a system clock accuracy of 0.01ppm, and will easily allow realisation of the <30 micron target accuracy. When operated at 25 metre range, this may allow investigation of system accuracy in the 0.25 micron band, i.e. at sub-wavelength levels. Oven stabilised reference oscillators are available to provide the 0.01 ppm accuracy at 100 MHz (e.g. Miteq's XTO range), thus fulfilling this requirement.

E3: Upshifter carrier feed-through

The I/Q modulator (or frequency upshifter) takes the nominal frequency (6 GHz) and the I and Q inputs to generate a new frequency which is up (or down) shifted by an amount equal to the frequency of the I and Q signals. A small portion of the nominal frequency at 6 GHz will still be visible on the drive signal applied to the optical intensity modulator. This will appear on the optical pulse stream as coherent intensity jitter with a periodicity of the beat frequency between the nominal frequency and the shifted frequency. The proposed I/Q modulator (Miteq SDM0307LI1CDQ 3.7 to 6.4 GHz direct satellite I/Q test modulator²) has a typical carrier rejection of 30 dB and so the resulting output voltage fluctuations will be smaller than the least significant bit of the 12-bit sampling ADC. This low level of optical intensity modulation is not expected to significantly detrimentally affect the pulse compression process.

E4: DDS phase noise and LUT bit depth

The same DDS IP cores are used in an existing QinetiQ sub-nanometre performance interferometric system^[3], suggesting that the performance required for SIPOD is readily achievable.

E5: Frequency shifter Phase noise

The interferometer in the system uses a pseudo-heterodyne operating principle with a ramped phase modulator in one arm^[4]. This device is a telecommunications component which has a bandwidth of many GHz, and should therefore be able to cleanly generate the high frequency harmonics of the (~5 MHz) phase ramp. In simple terms, if the phase

ramp shifts the interferometric phase by 360 degrees each period of the ramp, the rate of change of phase (i.e. the carrier frequency) observed at the detector will be equal to the ramp frequency. Any jitter on the phase modulation signal will be seen as a phase shift; however this should only affect the interferometric measurement, not the pulse overlap detection range finding.

E6: Saturation and dynamic range of the detectors

The divergence parameters designed into the telescope optics will combine with the maximum range requirement (250 m) to generate an attenuation value that will be applied to the optical signal received at full range compared to short range. Under the current low divergence design, this will be minimal and easily covered by the dynamic range of the detectors, and more importantly, the fixed gain ADC configuration. Use of a larger divergence will result in the need to revisit this section, possibly needing a programmable gain component, with a control signal based on approximate range information from the RF metrology system.

E7: Bandwidth for slew rate requirements

The system slew rate (drift) requirement of 50mm/sec constitutes a Doppler shift at 1550 nm of 66 kHz. The lock-in bandwidth of ~100 kHz will easily allow these signals to pass through to the carrier strength evaluation section, and is therefore the issue of Doppler shift is not a concern for the SIPOD system.

E8: ADC bit depth and Aperture error at ADC

As with the DDS IP cores, the same ADC IP cores are used in an existing QinetiQ sub-nanometre performance interferometric system^[3], suggesting that the performance required for SIPOD is readily achievable.

E9: Interpolation of the pulse overlap frequency value

The intrinsic resolution of the SIPOD system is 150 μm per picosecond of pulse width. A conservative estimate for the pulse width is 5 ps, i.e. 750 μm . Thus, in order to

8. Optical metrology system design

achieve the desired resolution of $<30\text{ }\mu\text{m}$, it will be necessary to locate the centre of the heterodyne pulse envelope to better than one part in 25 of the pulse width. Computer models suggest that correlation techniques can be used to achieve a resolution of $<1\text{ }\mu\text{m}$ based on a signal to noise ratio of 100 and 50 points in the pulse envelope.

8.7 SIPOD error analysis summary

Noise source	Value	Comment
Laser RIN	-115 dB/Hz at 1 MHz dropping to -140 dB/Hz at 10 MHz	Negligible - ignore
Optical carrier (wavelength) stability	10 microns accuracy over 500 metres = 2×10^{-8} over measurement time of ≤ 0.1 s.	COTS laser will satisfy this.
Microwave oscillator stability	Need stability 2×10^{-8} over measurement time of ≤ 0.1 s.	Requires: <ul style="list-style-type: none"> 2×10^{-8} stability from the 6 GHz reference source 1.5×10^{-5} stability from FPGA offset freq Components which meet both specifications have been sourced.
Intensity modulator bias point drift	Slowly varying over timescale \gg measurement duration	Impact on system is a slight broadening of pulses and slight loss of resolution. Control loop can correct for this.
Polarisation issues	Typical fibre polarisation dispersion parameter ~ 0.2 ps/ $\sqrt{\text{km}}$ (= 8 to 28 microns range error over 50 to 500 metres)	Use PM interferometer to remove the problem.
Phase modulation to suppress SBS	Carrier strength slightly lower depending on the relative delay in the two interferometer arms.	Overcome by tuning frequency to satisfy: $f_{\text{SBS}} = \frac{nc}{D}$
DDS phase noise and LUT bit depth issues	Existing FPGA cores have been demonstrated in a previous QinetiQ interferometer system ^[3] to achieve sub-nanometre performance.	Negligible - ignore
Optical pulse timing jitter	~ 0.5 fs for the measurement window = 75 nm range error (6×10^5 pulses). ~ 380 fs for a single pulse.	Far exceeds accuracy requirement for PROBA-3 and accurate enough to allow hand-over to interferometric regime in future system.
Optical pulse intensity jitter	Due to EDFA ASE contributions, fibre vibration, launch waveform intensity jitter (including unwanted 6 GHz reference source contributions).	Averaging over 6×10^5 pulses, the average intensity jitter was measured as a negligible 2.5×10^{-3} %.

Table 8.2. Error analysis summary table.

8.8 Summary of uncertainty levels in frequency scan measurements

The SIPOD components must meet the stability requirements outlined above, namely better than 2×10^{-8} stability over ≤ 0.1 seconds (≥ 10 Hz update rate) in the microwave reference oscillator frequency and the laser wavelength stability.

Intensity and timing jitter of the current compression source (using SMF-28 as the compression fibre) has been measured using both the single-sideband phase noise approach and harmonic analysis. These figures comprise the contributions of all the noise sources mentioned, including the optical amplification contributions and the microwave oscillator instabilities. These values represent the jitter errors which would be observed for a series of single measurements based on a single pulse returning from the outlier and overlapping with a single reference pulse. In practice the measured value will be based on the average of many tens of thousands of overlapping pulses per measurement slot, and so the uncertainty will be greatly reduced as discussed below.

Typical operating parameters of the SIPOD system are expected to be 100 frequency steps per overlapping pulse, at perhaps up to 100 Hz scan rates. Therefore the number of pulses N_{pulses} observed by the detector per measurement (optical pulse repetition rate frequency step) is at least 6×10^5 using:

$$N_{\text{pulses}} = \frac{\text{pulse repetition rate}}{\text{scan rate} \times \text{number of frequency steps per scan}} \quad (8.30)$$

The effect on the measured overlap envelope of the RMS intensity and timing jitter, σ_A & σ_t respectively, is reduced by the square root of the number of pulses per measurement step, $\sqrt{N_{\text{pulses}}}$. For 100 frequency steps per overlapping pulse at 100 Hz with a 6 GHz repetition rate, the RMS jitters can be reduced by a factor of ~ 800 .

Assuming Gaussian E-fields for convenience and the centre of the time frame to be $t = 0$, individual overlapping pulses satisfy:

$$E_{\text{out}} = 2(A + \sigma_A) \exp \left[- \left(\frac{t + \sigma_t}{\kappa} \right)^2 \right] \quad (8.31)$$

Where A is the peak E-field and κ is the pulse full width half maximum, e.g. $\kappa = 1$ ps.

$$E_{out} = 2(A \pm \frac{\sigma_A}{\sqrt{N_{pulses}}}) \exp \left[- \left(\frac{t \pm \left(\frac{\sigma_t}{\sqrt{N_{pulses}}} \right)}{\kappa} \right)^2 \right] \quad (8.32)$$

For the jitter values measured for the current SIPOD compression source of $\sigma_A = 2\%$ and $\sigma_T = 380$ fs, the jitter contribution over the measurement window comprising 6.6×10^5 pulses and a subsequent reduction in the effective noise of ~ 800 is negligible. The intensity jitter for a given measurement sample is negligible at $\sigma_A < 2.5 \times 10^{-3}\%$ and the effective timing jitter for each measurement becomes $\sigma_t = 0.475$ fs, which again is a negligible fraction of a picosecond duration pulse and can effectively be ignored.

8.9 SIPOD sub-system modules

8.9.1 Frequency reference unit (with up-converter)

The first and probably key component in the SIPOD modular system is the frequency reference unit (FRU) which comprises 3 key components:

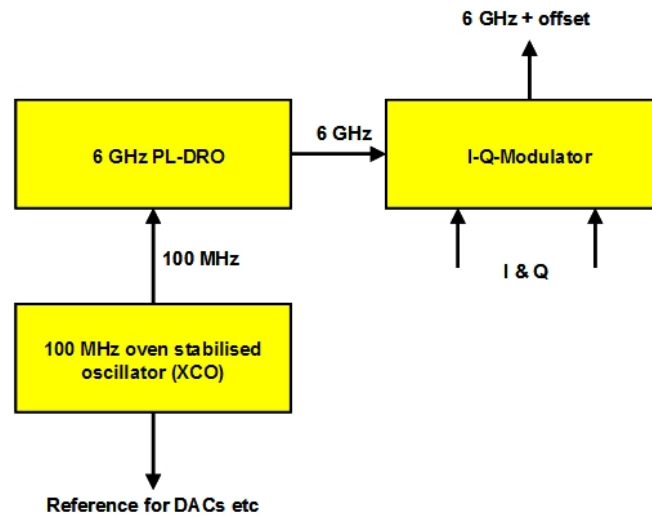
- 1) A reference oscillator with high accuracy and stability
- 2) A frequency upshifter or I/Q modulator and
- 3) A frequency divider (or multiplier) to provide a second phase locked reference

Based on the requirements discussed above and an analysis of available components, the use of dielectric resonant oscillator (DRO) running at 6 GHz phase locked to a 100 MHz 0.01 ppm reference oscillator (XCO) has been selected for the SIPOD breadboard implementation. The high accuracy of the XCO is transferred up to the 6 GHz oscillator, providing a clock related precision limit of 2.5 microns at 250 m

range. The choice of the relatively high frequency reference allows this also to be used to clock the DACs on the I & Q generation board (external input) providing a very good “over-sampled” output of the sine and cosine signals. A compatible I/Q modulator allows the 100 kHz – 8 MHz I & Q signals to add a precise offset frequency to the already high accuracy 6 GHz signal frequency. The 0.01 ppm accurate 6 GHz signal corresponds to a 60 Hz error, which is far easier to achieve on the 100 kHz – 8 MHz I&Q signal frequencies. The ~10 ppm accuracy required may be achievable with a free-running reference clock on the I&Q generation board without the need to provide the reference signal shown in Figure 5.1.

Longer term, a commercially available rubidium clock atomic clock could replace the crystal oscillator and DRO. Companies such as Perkin Elmer supply rubidium sources with 1×10^{-12} stability (0.3 nm stability over 300 metres).

The block diagram in Fig. 8.7 shows the layout of the FRU module.



22Fig. 8.7. Block Diagram of the Frequency reference unit.

The main function of the I/Q modulator is to preserve the accuracy of the reference frequency, even with the addition of a known offset value. The function is to take the reference frequency A (RF input) and the in-phase (I or Sine) and quadrature (Q or Cosine) representations of an offset frequency B, and combine them according to the trigonometric principle:

$$\sin A \cdot \sin B + \cos A \cdot \cos B = \cos(A - B) \quad (8.33)$$

8.9.2 Laser pulse generation sub-system

The main optical system in the SIPOD system is the Pulse Generation Sub-assembly. This unit comprises the compression pulse source discussed throughout this thesis, namely:

1. Long coherence length laser
2. Phase modulator (SBS)
3. Intensity modulator
4. Erbium Doped Fibre Amplifier (EDFA)
5. Pulse compression fibre

A telecommunications based 1550 nm laser is used as the source for the system, providing an output power of order 10-20 mW and a coherence length of many kilometres. The coherence length must significantly exceed the maximum optical path-length difference expected in the interferometer in order to produce a visible heterodyne signal, which then indicates the pulse overlap condition. The coherence length must be improved further if the phase noise is to be reduced to allow interferometric tracking with high precision. As the laser used here will not be stabilised (locked to a known frequency), this is of little value, so a particularly high coherence length will not be required.

Due to the requirement to launch peak powers of several hundred milli-Watts into the compression fibre, stimulated Brillouin scattering (SBS) will detrimentally affect system performance if steps are not taken to overcome it. SBS is a nonlinear process, more precisely a backward propagating Stokes wave that carries most of the input power once the SBS threshold has been reached, as discussed in Chapter 6. In order to reduce the effects of SBS, either the pulse width should be shorter than the resulting phonon lifetime (16 ns) or the linewidth should be broader than the Brillouin threshold linewidth of around 17 MHz. The linewidth can effectively be broadened for a single mode pump whose phase varies at a higher frequency than the Brillouin linewidth. This

phase modulation method has been successfully shown to overcome SBS effects, without adding significant timing jitter to the pulse stream.

The phase modulator component will immediately follow the laser itself. As discussed, care must be taken to ensure that the phase modulation used to overcome SBS does not detrimentally affect the interferometer signal. This is due to the fact that the two arms are different lengths, and so when recombined the phase modulation from the two arms may not be in phase unless the SBS suppression frequency is actively controlled.

The next component in the sequence is the intensity modulator, which generates the ~6 GHz intensity modulated waveform prior to the pulse compression process. This is a standard telecommunications component. The intensity modulator's bias point will drift with operating temperature, and so will require to reach a stable operating condition and will also require a relatively stable environmental operating temperature (stable to a few degrees C).

The erbium doped fibre amplifier boosts the relatively small signal up to a power level of order $\leq 500\text{mW}$, as required to realise the non-linear effects which generate the compression effect via soliton-effect compression.

Compression fibre

As described in the modelling section, Chapter 5, the propagation equation describing the pulse envelope evolution through the compression is a nonlinear partial differential equation which does not generally lend itself to analytical solutions:

$$i \frac{\partial A}{\partial z} + \frac{i}{2} \alpha A - \frac{1}{2} \beta_2 \frac{\partial^2 A}{\partial T^2} + \gamma |A|^2 A = 0 \quad (8.34)$$

Therefore to evaluate system feasibility, modelling of the system was performed using the split-step Fourier algorithm, as described in Chapter 5.

Pulse propagation has been modelled through a variety of different fibre types: Chapter 11 details the results for both commercially available fibres and also idealised fibres

which could be commissioned if modelling suggests exceptional performance. The aim of this work was to identify a fibre arrangement which would substantially reduce the weight and volume of the 25 km of Corning's SMF-28 fibre which is used in the current laboratory SIPOD test-bed system. Commercially available fibre products evaluated include those offered by OFS (Furukawa), Corning, Fibercore, Sumitomo and photonic crystal fibre manufacturer Crystal Fibre. In terms of the SIPOD application, the most important physical parameters are total fibre weight and volume, and the fibre's radiation susceptibility. In addition, it would be useful for the fibre to be polarisation maintaining to eliminate polarisation control as a potential concern when launching into the interferometer test arrangement.

Corning's SMF-28 fibre has already been shown to generate compressed pulses (Chapter 6), however the pulses were not particularly short at 10-15 ps. The other drawback was that long lengths of fibre are required, typically ~25 km which weighs approximately 2 kg.

It is expected that the two modulators can be located within a fibre coil of radius ~20cm, and that the laser/EDFA modules will be of order 200 x 90 x 25mm. Packaging of these elements could be achieved in a volume of order 200 x 300 x 60 mm. The CAD drawing Fig. 8.8, prepared by the author using Solidworks, shows the approximate layout proposed for this module with the additional electronic control components included.

8. Optical metrology system design

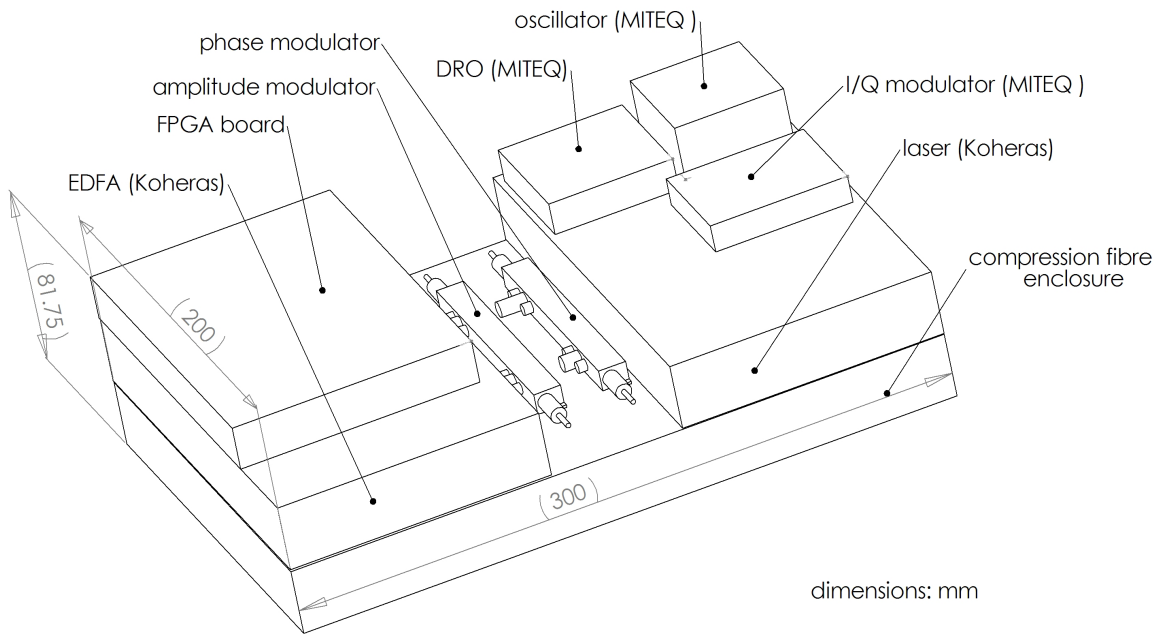


Fig. 8.8. Representative volumetric CAD drawing of a potential opto-mechanical layout for the pulse generator to illustrate relative component dimensions. Maximum dimensions as shown in the non-optimised layout are 200x300x85 mm = 5.1 litres. In practice the optical modulators and MITEQ components could be housed within the compression fibre enclosure to reduce the footprint further.

8.9.3 Interferometer head (including collimator)

The output from the pulse generator provides the light source for the measurement “interferometer”. Although the term “interferometer” is used, the interferometric phase is not used to “meter” the range or displacement, rather the presence of interference is used to indicate the overlap. In order to generate a continuous interferometric signal which can be monitored, a second phase modulator is required within the interferometer (as opposed to before, for the SBS removal). The interferometer was designed in a Michelson configuration as shown below, which like all dual beam interferometers provides two complementary outputs. The use of another telecommunications component, the circulator, allows the second output from the interferometer to be extracted whilst also stopping light feeding back to the laser source. One arm of the interferometer is termed the reference arm and contains the phase modulator and a reflective coated fibre end (or waveguide end), which acts as the reference mirror. The other path is termed the signal path, and is coupled out of the fibre for collimation and projection towards the target corner cube.

It is expected that a beam diameter of order 30 mm will be required, which with a fibre numerical aperture of 0.1 implies a focal length of 150 mm will be required. Optimum collimation will generate a divergence of order 70 microrads, i.e. a spot diameter of order 50 mm at 250 m range. In this configuration, the use of a 25 mm diameter corner cube will maintain good returns at all ranges, and will not generate large range dependent effects, nor be overly sensitive to lateral shifts.

One key consideration for the design of the interferometer head, Fig. 8.9, is the differential thermal expansion of the two arms of the interferometer. The block diagram Fig. 8.9 shows a simplistic fibre-optic configuration which would be suitable for demonstration of the principle of operation, but which may suffer thermal drifts due to the single phase modulator in one arm of the interferometer. The best solution would be to use a splitter and phase modulator similar to that used in a telecommunications Mach-Zehnder modulator.

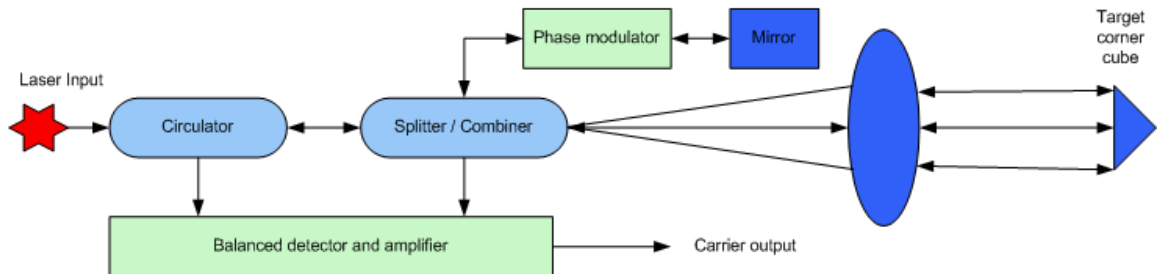


Fig. 8.9. Layout of the Interferometer head.

Fig. 8.10 shows the “cut-down” modulator, which could be used to fulfil this role, in which the two interferometer arms are of near identical length and experience almost identical thermal effects. This compact integrated optic design could later (in a custom component build) be designed to provide a compact and optimised interferometer head. If a suitable modulator can be obtained and divided as shown above, this may offer a simple solution.

Depending on mechanical constraints, the balanced detector may be switched to a location closer to the acquisition electronics.

8. Optical metrology system design

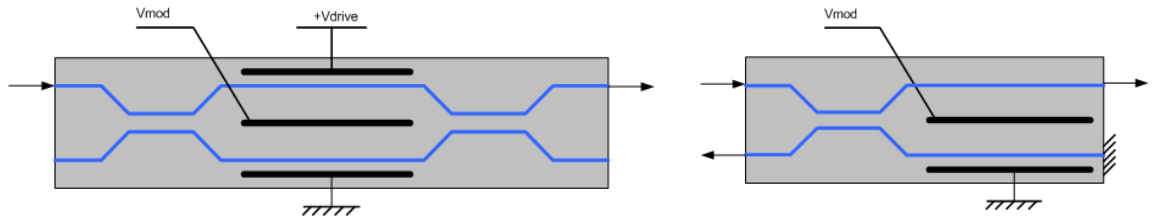


Fig. 8.10. A telecommunications Mach-Zehnder modulator (left) and a suitable integrated optic splitter / phase modulator (right).

8.9.4 Frequency sweep and overlap detection

The frequency sweep and (heterodyne based) overlap detection functions are the key elements of the system and will be performed on an FPGA board to optimise the speed of these dynamic processes. The National Instruments (NI) IF-RIO board has been chosen for this task, as it offers a high performance Xilinx platform which can be flexibly programmed from Labview building blocks which represent standard IP cores. Further FPGA code can be “dropped-in” via a HDL interface, which will be used to generate the more detailed and intelligent code.

The frequency generation part of this block is performed by generating the I and Q signals of the chosen offset frequency and applying those to the I/Q modulator. This is performed using a Xilinx IP-core known as the Direct Digital Synthesiser (DDS).

In order to generate a given offset frequency (represented by its sine & cosine signals), the FPGA must simply be programmed with the corresponding phase increment to be advanced at each clock cycle of the system. The phase offset and dither inputs are not required. This DDS IP core is a pre-programmed module that is ready to use.

The second portion of this block is the lock-in amplifier function which determines the amplitude present at the carrier frequency, which is a measure of the overlap level. In interferometric mode, the phase is also of interest, and should therefore also be determined. Again, there is an FPGA IP-core which is pre-destined for use in the realisation of the lock-in amplifier function. The Xilinx Direct Digital down-Converter (DDC) performs almost the inverse of the I/Q modulator function, in that it mixes a chosen signal down to base-band to provide the in-phase (I) and quadrature (Q)

components. The baseband signals can easily be low-pass filtered (LPF), which has the effect of removing signals which are more than that (LPF) frequency away from the local oscillator (LO) frequency chosen for the downmixing. The resultant outputs are the I and Q components of the signal strength in a frequency band around the LO frequency. The carrier strength is then given by $R = \sqrt{I^2 + Q^2}$, and the phase is given by $P = \arctan(I/Q)$. Note that the DDS IP-core is an integral part of the DDC, and this second copy of the DDS logic defines the LO frequency, and thus the “lock-in” frequency.

The final function operating on this board is the lowest level of scanning process, i.e. the Labview control programme will instruct the FPGA to scan a defined frequency range in defined steps, and the FPGA will return an array containing carrier strength values. This will minimise the communication traffic between the PC and the IF-RIO board.

The FPGA programming will be performed by QinetiQ’s FPGA expert Andy McCaffrey and not the author of this thesis.

8.9.5 Signal Generation Instrumentation

Unlike the “Frequency sweep and overlap detection” section, this module has two relatively benign functions in that it generates a fixed frequency ramp for carrier generation and a relatively well defined sinusoidal output which drives the SBS phase modulator. Fig. 8.11 shows the phase modulation signal required at the interferometer head (top trace) and the carrier signal which it generates (lower trace) during pulse overlap.

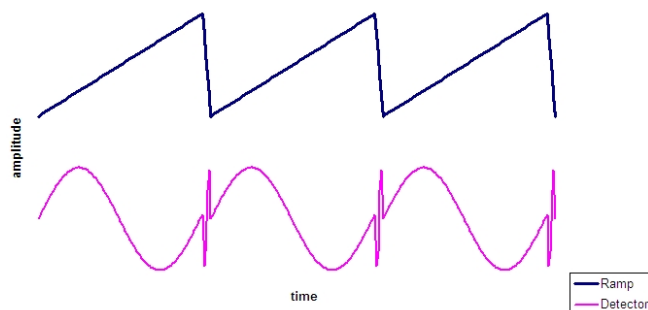


Fig. 8.11. Function of the ramped phase modulation.

In order to generate the required carrier at ~ 5 MHz, a waveform generator capable of reproducing several higher harmonics is required in order to reproduce the sine wave without distortion. This function will be performed by a 200 MSamples/s NI-5422 arbitrary waveform generator. At 5 MHz, the carrier is easily high enough to maintain Doppler shifts due to drift rates (50 mm/s or ~ 66 kHz) at a small fraction of the carrier frequency. Lower carrier frequencies would provide better (lower) harmonic distortion on the ramp function, however a compromise is required with the time (cycles) required for the lock-in to respond.

The second function performed by this block is the frequency generator for the phase modulator, which is used to dither the wavelength in order to inhibit the onset of SBS. As has been discussed, the ideal frequency lies between a chosen start frequency (greater than 35 MHz, see Fig. 6.8 in Chapter 6) and a value only $\sim 10\%$ higher. A good assumption would then be to use say 60-65 MHz generated by a second 100-200 MSamples/s board. The output of this board can be low-pass filtered using a simple analogue (mini-circuits) component to remove any digital effects. The signal generation board would also allow control of the signal amplitude if required. The NI-5404 signal generator has been chosen for this task.

In this configuration, the signal generation / processing system should reside on three to four NI boards occupying either a PC or PXI chassis. The main signal processing effort is then performed on the FPGA, and the other simpler tasks (signal generation & system control) could easily be realised on a custom FPGA board in a future programme. It should be noted, however, that the SRAM based FPGA technology in the Xilinx chips is not well suited to space qualification, and the VHDL code would need to be ported to a fuse-based technology such as the Actel product family.

8.9.6 Control System and Software

The SIPOD prototype's control software will be a very simple GUI, allowing the following functions:

8. Optical metrology system design

- System initialisation
- Approximate range input (equivalent to RF metrology)
- Setting of the laser output power
- Monitoring of system / laser status
- Display of the current range and plots of range vs. time

A top level diagram of the functional steps is shown below, Fig. 8.11. The software will run on a Windows PC.

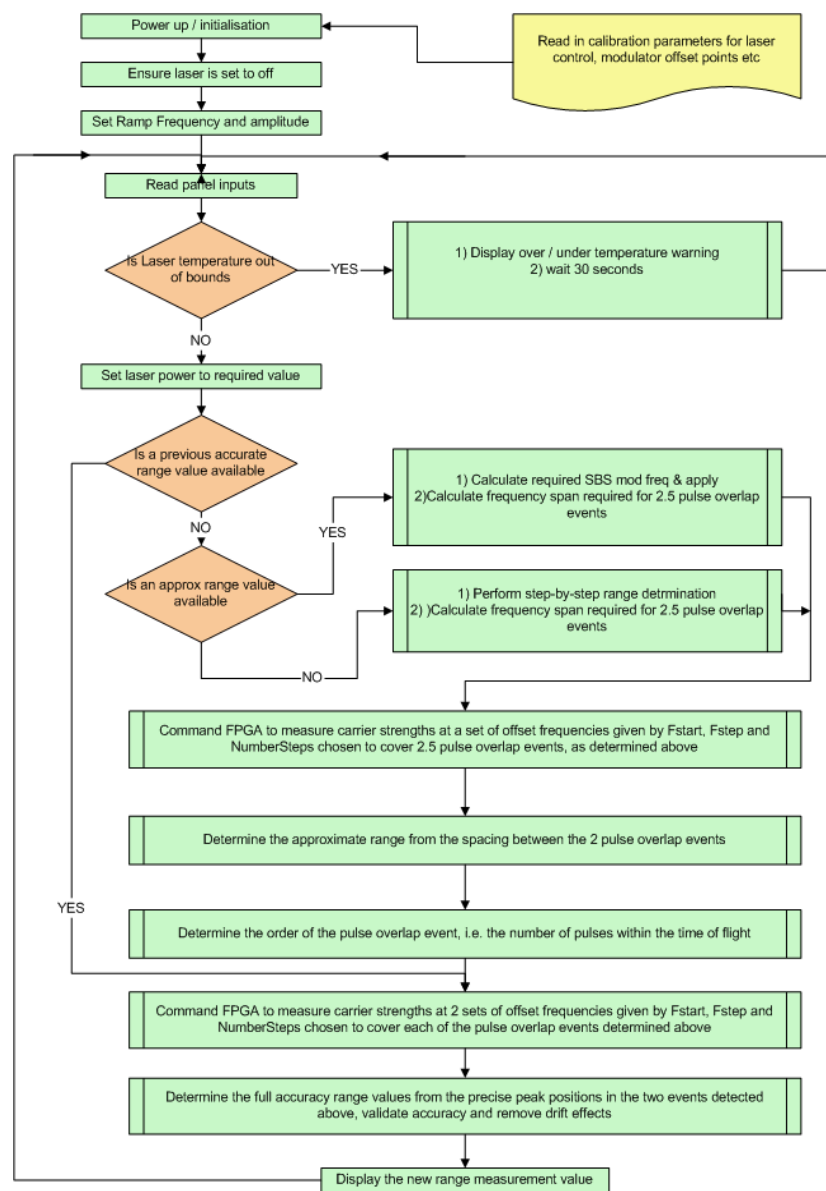


Fig. 8.11. Top level software flow.

8.10 SIPOD system size, weight and power summary

Table 8.4 provides a breakdown of the expected system component weights and power consumption during normal operation, based on chosen component datasheet specifications.

	Component	Weight (grams)	Power (Watts)
1	IQ mod	100	0.0
2	oscillator	100	0.4
3	DRO	100	0.4
4	fibre enclosure	500	0.0
5	3 km fibre + reel	250	0.0
6	Laser	600	2.5
7	EDFA	600	3.0
8	FPGA board	300	17.0
9	2 amplifiers for modulators	800	6.0
10	balanced detector (receiver)	400	0.3
11	cabling	500	0.0
	Sub-total	4250	29.6
12	NI-PXI5404 (100 MHz sig gen)	500	3.3
13	NI-PXI5422 (200 MSample/s AWG)	500	6.6
	Total	5250	39.7

Table 8.4. Breakdown of SIPOD breadboard component power and weight specifications.

Notes:

- The EDFA, item 7 in Table 8.4, is assumed to generate a peak optical output of 500 mW, i.e. an average power of around 250 mW. Based on typical 10% electrical to optical efficiency, a figure of 3 W has been used for its consumption.
- Items 12 and 13 could be performed by the FPGA board using far reduced power requirements (<2 Watts in total for the two functions). However for the SIPOD system these functions are implemented using stand-alone National Instrument cards to avoid costly FPGA design.

Not included:

- The PXI-chassis
- The laptop PC
- The optical head. It will comprise a waveguide, a ball lens, a small conventional lens and an enclosure. It is expected to weight 500 grams at most, but more likely ~100 grams.

Based on the information available on the modelled performance and component specifications, projected specifications for the SIPOD breadboard demonstrator and final systems are given in Table 8.5.

8.11 Projected specifications for the SIPOD demonstrator and final systems

<u>No.</u>	<u>Property</u>	<u>Required</u>	<u>Expected</u>	<u>Long Term</u>
1	Operating range	25 ... 250m	20 ... 250m	20m ... 2km
2	Maximum Laser Power	500mW	500mW	500mW
3	Laser Power Control	10-500mW	10-500mW	10-500mW
4	Optical system size	10 litres	~5 litres	~3.5 litres
5	Optical system weight	10 kg	~5kg	<5 kg
7	Beam diameter	~30mm	30mm	30mm
8	Beam divergence	>0.05mrad	0.1mrad	0.1mrad
9	Range Accuracy	30 microns	<30 microns	<5 microns
10	Recovered bandwidth	>10 Hz	20 Hz	>100 Hz
11	Data-logging	Labview files	Labview files	TBD
12	Optical Head volume	<10 litres	1 litres	<<1 litres
13	Signal Processor size	PC based	PC based	PIC board
14	Signal Processor weight	<15 kg	<15 kg	<500 grams
15	Power consumption	<30 W	~39.7 Watt	TBC
16	Power format	AC mains	AC mains	TBD
17	Control Interface	PC front-panel	PC front-panel	TBD
18	Interferometric resolution	<50 nm	<50 nm	<50 nm
19	Operating Temp	5 – 35 deg C	5 – 35 deg C	5 – 35 deg C

Table 8.5. SIPOD projected performance figures.

Notes on Table 8.5:

- Volume figures are based on individual component volumes. The long-term system will require an optimised design and packaging iteration to realise these predictions.
- The power consumption of 39.7 W comprises a large contribution from two National Instruments boards. In future these functions could be integrated onto the FPGA board to reduce the system power consumption by around 8 Watts or more.

8.12 SIPOD design summary

Based on the system analysis discussed in this chapter, and the commercially available components found to be suitable for use in a breadboard demonstrator, the overall SIPOD system will consist of a compact optical system linked to a transmitter head via fibre, as well as a PC based FPGA development system, which simulates the functions eventually to be performed on a single FPGA based processor board. Fig. 8.12 below shows that layout.

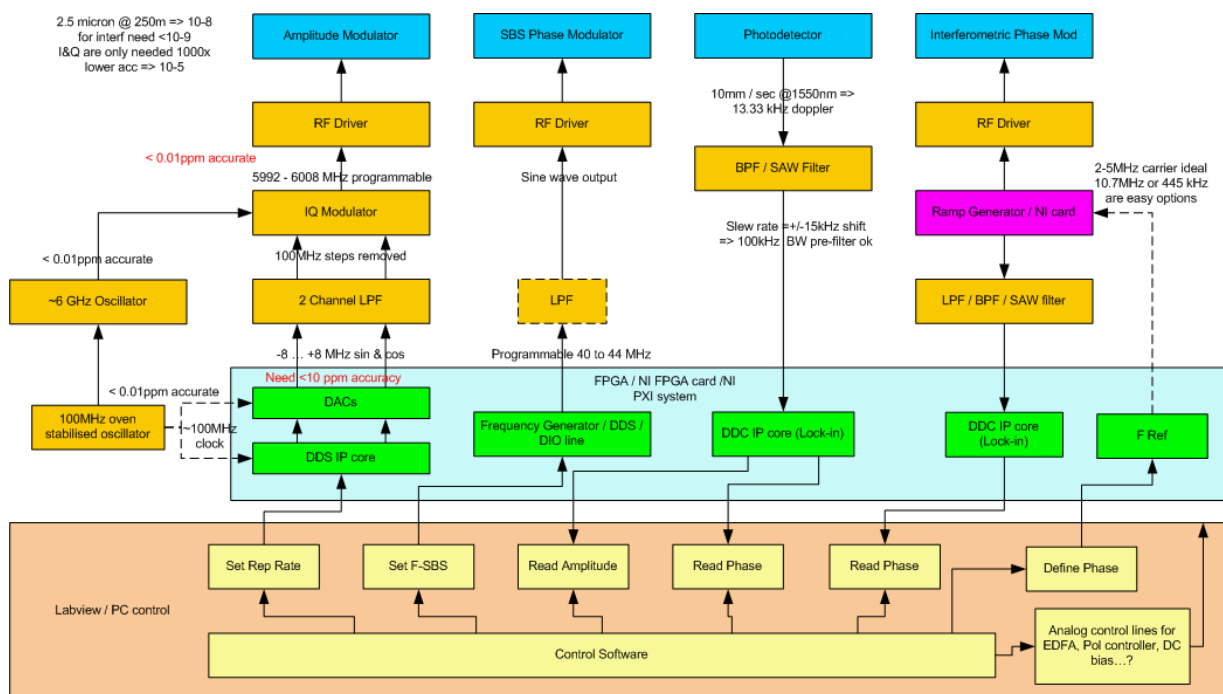


Fig. 8.12. The proposed SIPOD system architecture.

References for Chapter 8

1. Koheras Basik Fibre Laser module. Datasheet retrieved on 20th February 2008 from http://www.koheras.com/Menu/Products/Ultra+Precise+Laser/BASIK%e2%84%a2+Module/KOHERAS+BASIK+Fiber+Laser+Module_portrait.pdf
2. Miteq SDM0307LI1CDQ 3.7 to 6.4 GHz direct satellite I/Q test modulator. Datasheet retrieved on 20th February 2008 from <http://amps.miteq.com/datasheets/MITEQ-SDM0307LI1CDQ.PDF>
3. Harris, M.; Hand, M.; Wright, A, "Lidar for Turbine Control: March 1, 2005 - November 30, 2005." 55 pp.; NREL Report No. TP-500-39154 (2006). Retrieved on 29/02/08 from www.nrel.gov/wind/pdfs/39154.pdf
4. Kersey A.D., Lewin A.C., and Jackson D.A., "Two wide-dynamic range signal-recovery schemes for the fiber-optic gyroscope," Proc. Instr. Elec. Eng, vol. 132, pp. 271-276, Oct. 1985.

9. Optical metrology experimental implementation

This chapter details an experimental de-risking implementation of the scanning interferometric pulse overlap detection (SIPOD) optical metrology system, verifying that system performance meets the European Space Agency requirements for formation flying satellite range accuracies of 30 microns or better. The components employed in this initial demonstration system were selected from existing items procured under previous QinetiQ programmes. This experimental de-risking exercise has confirmed component specification requirements of the final breadboard prototype which will be delivered to the European Space Agency. The experimental work described in this chapter is believed to be the first ever implementation of the SIPOD technique. A second, optimised, breadboard was subsequently constructed and is detailed in Chapter 10.

9.1 Experimental implementation of SIPOD

An experimental test arrangement was established to prove the principle of the SIPOD operation. The compression pulse source was implemented using standard telecommunications fibre, Fig. 9.1, with a CW DFB laser output being phase modulated and intensity modulated, prior to amplification via an IPG Photonics EDFA. The periodic waveform was then launched into 25.2 km of Corning SMF-28 fibre. The intensity modulation is provided by driving an intensity modulator with a single sinusoidal tone from an hp 83711A signal generator.

9. Optical metrology experimental implementation

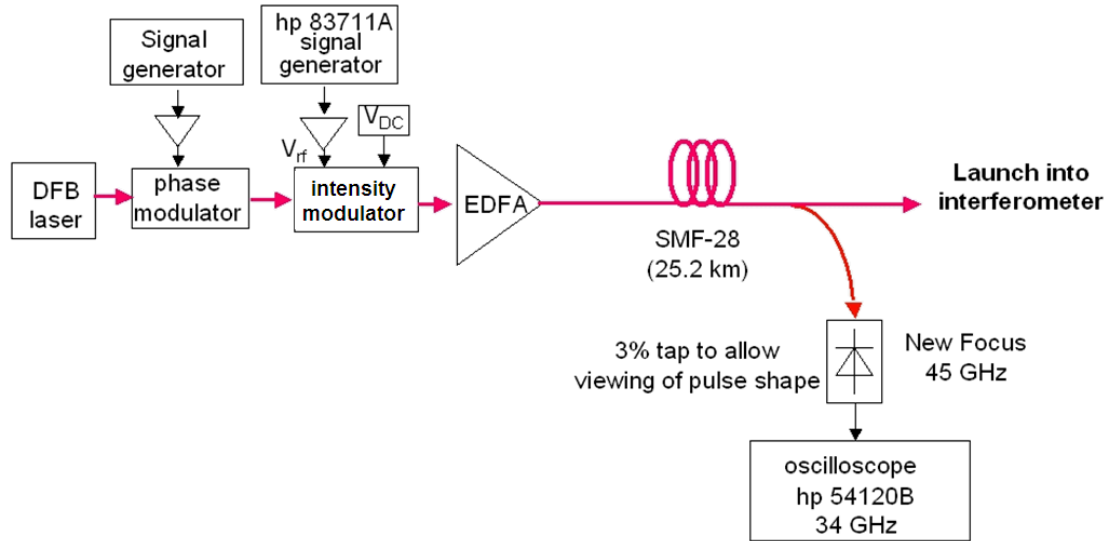


Fig. 9.1. Optical pulse generation system based on SMF-28 compression fibre and an hp 83711A signal generator.

In terms of pulse repetition rate, a major difference between the optical *sampling* and optical *metrology* applications is that the metrology pulse repetition rate does not need to be chosen for its compatibility with an electronic ADC sample rate. For the experimental implementation of the optical sampling discussed in Chapter 7, the pulses were used to perform sampling in conjunction with either an 8-bit 1 GSamples/s or a 14-bit 100 MSamples/s back-end ADC, making it desirable that the optical pulse repetition rate is as low as possible to make pulse picking to the ADC sample rate as convenient as possible. Since the bias-at-null mode of operation produced pulses with a lower percentage of pulse power in the pedestal at repetition rates of ~ 2 GHz, this modulator bias regime was selected for the optical sampling application. The optical pulse repetition rate for the SIPOD system however has been chosen as ~ 6 GHz, which allows for the use of either the biased-at-null or biased-away-from-null modes of operation with minimal pedestals generated. The 6 GHz repetition rate figure was chosen for SIPOD for a number of reasons. Firstly, it provides a coarse synthetic wavelength (pulse-to-pulse spacing) of 5 cm in vacuum which is sufficiently large to avoid ambiguities following hand-over from the RF metrology system. At 6 GHz, a relatively low peak optical power produces highly compressed pulses as will be discussed, and finally 6.684 GHz is an output frequency of rubidium atomic clocks and longer term it may be possible to use this ultra-stable frequency directly. After operation was chosen to be at 6 GHz, the modulator bias method selected for SIPOD was to bias-

away-from-null and drive the modulator transmission to null, since it is highly desirable that every successive pulse is identical and the biased-away-from-null approach is more robust to bias drift.

In order to evaluate the SIPOD principle, the optical pulse stream was launched into an all fibre Mach-Zehnder interferometer, Fig. 9.2. On one arm of the interferometer an electronically generated ramp function drives a phase modulator through 2π at 5 MHz (using a Tektronix 2021 arbitrary waveform generator), with the result that the carrier has 5 MHz sinusoidal phase modulation superimposed on this arm. The other arm comprises a fibre delay line. Several delay lines lengths have been tested, ranging from a few metres up to 200 metres (note the formation flying range requirement of 25-250 metres). The two interferometer arms are recombined before being directed onto a New Focus 1617 balanced detector. The output from the balanced detector is then band-pass filtered and then sent through a rectifying circuit. A digital voltmeter (Agilent 34410A 6½ digit multimeter) capable of performing measurements at up to 10 kHz reads the level output from the rectifier. In this way, the SIPOD system benefits from the resolution and performance of highly compressed, high repetition rate optical pulses, but requires only relatively simple slow-speed electronics in order to perform the measurement and analysis of these pulses.

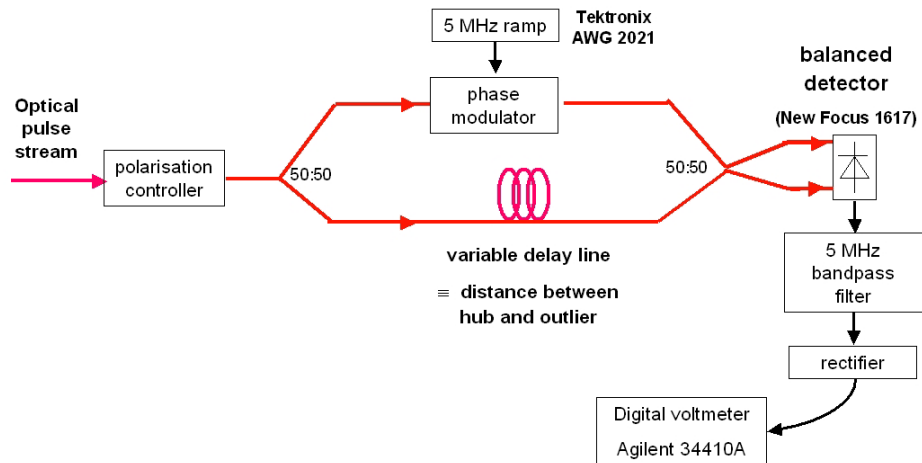


Fig. 9.2. Interferometer arrangement used to simulate the variable distance between the hub and outlying satellite in the PROBA-3 mission. One arm of the interferometer (the hub) experiences a ramped phase modulation, and the other simulates the extended round trip distance to the outlying satellite. A balanced detector arrangement measured the strength of the heterodyne signal, and hence the pulse overlap condition.

9. Optical metrology experimental implementation

As a first iteration of the system, prior to obtaining a function generator capable of generating a high quality 5 MHz ramp signal, an interferometer arrangement was also implemented using a 70 MHz acousto-optic modulator with an accompanying 70 MHz surface acoustic wave (SAW) filter, to provide the heterodyne carrier signal. Although this approach provided a clear set of heterodyne carrier peaks when the optical pulse repetition rate was swept, this arrangement was not taken any further since it does not superimpose an optimum sinusoidal carrier on the signal, unlike the ramp function applied to a Mach-Zehnder modulator. Also, acousto-optic modulators are not considered as robust as waveguide modulators for the space environment, as they comprise free space components.

The level on the voltmeter indicates the level of heterodyne signal detected on the balanced detector. This will be at a maximum when the differential path length between the two arms of the fibre interferometer is such that the two sets of pulses exactly overlap on recombination. As derived in the previous chapter, this occurs for a given pulse repetition rate R when the path difference D satisfies:

$$D = n \frac{c}{R} \quad \text{where } n = 1, 2, 3, \dots \quad (9.1)$$

In turn, by scanning the pulse repetition rate to find two adjacent overlapping frequencies, R_1 and R_2 , which provide separate peaks in the heterodyne signal, it is possible to determine the differential fibre length:

$$D = \frac{c}{R_2 - R_1} \quad (9.2)$$

The absolute frequency of the n th peak, F_n , is given by $F_n = nR_n$. The value of n is obtained from Eq. 9.3, rounded to the nearest integer. An improved estimate for D is then given by Eq. 9.4.

$$n_1 = \frac{R_1}{|R_2 - R_1|} \quad (9.3)$$

$$d = \frac{n_1 c}{R_1} = \frac{n_2 c}{R_2} \quad (9.4)$$

For n to be unambiguously determined, the fractional uncertainty in R must be much less than n^{-1} . For large values of n , it may be necessary to perform an additional scan over an extended frequency range to achieve this precision. This represents an n -fold improvement in range accuracy over that derived using the frequency difference between successive overlapping peaks. In the SIPOD system, a coarse RF metrology system will be an additional aid to finding the overlap order n .

A Labview interface was written to step the frequency output of the hp 83711A signal generator, wait for output frequency to settle, and then read the value measured by the Agilent 34410A digital voltmeter. The 83711A has a specified frequency settle time of 20 ms, giving a maximum scan rate of only ≤ 0.5 Hz if 100 points are used per frequency sweep. In the final SIPOD system, a refresh rate of 10 Hz is required. The frequency settle time of the hp 83711A signal generator is the limiting component on the scan rate update rate in this de-risking arrangement.

A 200 metre delay line was inserted into the interferometer test arrangement and the repetition rate of the pulse was varied. Fig. 9.3 shows the detected optical interference pattern when the two arms of the interferometer are recombined onto an optical detector, captured using an hp 54120B high-speed sampling oscilloscope. For a 2.90 GHz repetition rate the pulses do not overlap and two peaks are clearly visible. As the repetition rate is varied to 2.86 GHz, the pulses begin to overlap and only one coherent pulse is observed (note the axes are identical in both plots).

The 200 metre delay line is approaching the limit of the coherence length of the DFB laser in the pulse source arrangement, since 200 metres requires a linewidth of 1 MHz for coherent operation, which was the specified value of the particular DFB laser used in the pulse compression scheme. Therefore much shorter delay line lengths were used to analyse the system performance over extended timescales, to avoid limited laser coherence confusing the results. In the optimised SIPOD system discussed in Chapter 10, a narrow linewidth (5 kHz) fibre laser is used to provide a coherence length of around 40 km.

9. Optical metrology experimental implementation

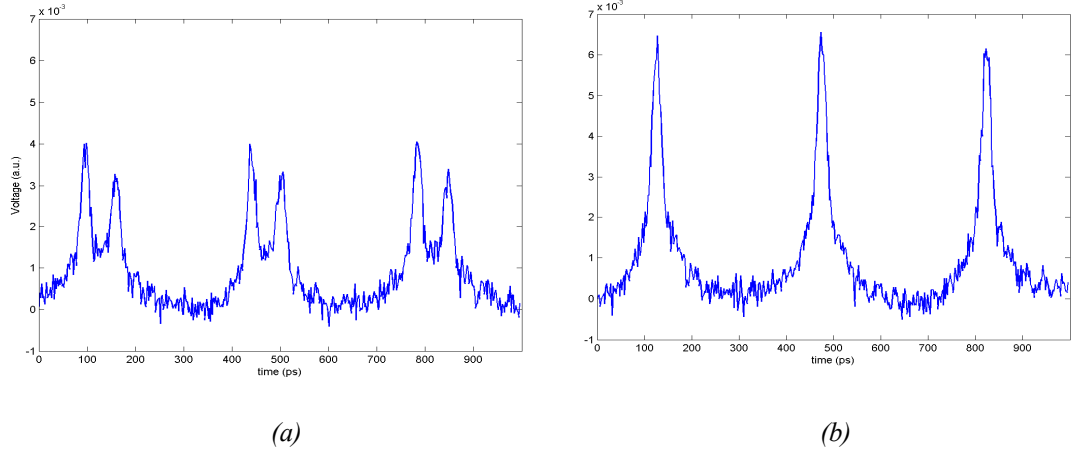


Fig. 9.3. Interferometer output with a 200 metre delay line present in one arm, captured on a high-speed sampling oscilloscope. (a) repetition rate = 2.90 GHz and the pulse trains from the two interferometer arms do not overlap, which would result in negligible interferometric beat signal, and (b), tuning the frequency to 2.86 GHz provide a coherent overlap, which would provide a large interferometric beat signal.

An example frequency scan and measured heterodyne signal is shown in Fig. 9.4, for a path difference of approximately 7.4 metres. Side lobes are clearly evident, confirming the presence of a pedestal on the pulses, as predicted by the modelling. The plot of the heterodyne signal strength as the pulse repetition frequency is scanned is reminiscent of an autocorrelation plot, which is not entirely unexpected given the similarity of the techniques. Whereas an autocorrelator typically scans one pulse through another by mechanically displacing one arm of a Michelson interferometer, the SIPOD system performs the same operation by scanning the pulse repetition rate. The pulse detection method differs, since the autocorrelator typically uses a non-linear crystal to detect the overlap condition instead of the heterodyne detection method used by SIPOD.

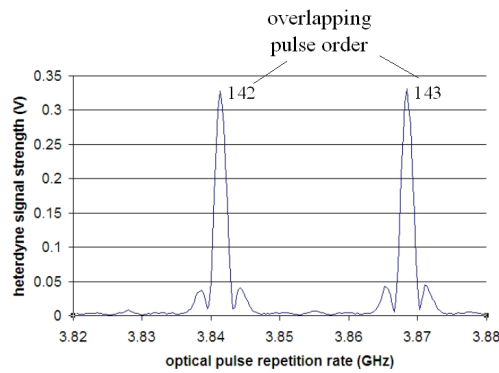


Fig. 9.4. Heterodyne signal as the optical repetition rate is scanned through 60 MHz in 250 frequency steps. The coarse path difference in the interferometer arms is approximately 7.4 metres. The pulse order is derived using Eq. 9.3.

There are several options for determining the exact frequency corresponding to the maximum heterodyne signal (i.e. maximum pulse overlap). For example, fitting a polynomial to the highest value and the surrounding peaks allows interpolation of the peak heterodyne signal and corresponding frequency of the pulse repetition rate. This is relatively trivial to implement in computational terms has been easily be performed on a standard laptop PC at 10 Hz.

For formation flying satellite application, it is anticipated the initial range estimate will be input to the system from an external RF metrology source, in which case an estimate of the range drift rate should also be supplied. However a highly desirable property of the SIPOD system, in terms of satellite instrument redundancy, is that the range estimate can be derived by the SIPOD system itself if required. In order to do this, the system will perform a series of scans over a variety of frequency ranges to ensure that at least two well-defined overlap signals appear in at least one scan, regardless of range. One way to achieve this is to scan a frequency range corresponding to 2.5 overlap intervals at the longest possible range in steps fine enough to resolve the peaks. The next measurement iterations would then be performed with double the frequency step and frequency range for each subsequent scan. The scans should be performed in both directions (i.e. scanning the frequency upwards and downwards) to accommodate range drift during the scans. The direction and magnitude of the rate of drift between satellites will be given by the difference in the heterodyne peak spacing between scans. This information can be used to predict the required frequency scan range for the next set of scans.

As mentioned, peak-finding routines will be used to determine the number and position of maxima in each of the scans. In future, algorithm performance may be improved using a model based on the expected form of the scan. For the SIPOD de-risking arrangement, a simple model is used which assumes only that a peak should have a full width at half maximum value (FWHM) of between 10 and 30 frequency steps and a peak value greater than half way between the maximum and minimum values of all the scans. Currently the precise position of the peak is determined by fitting a quadratic polynomial to 5 points around the peak. If the peak positions differ between scans in opposite directions, the positions should be re-calculated by assuming a linear displacement with time (i.e. constant relative velocity) to estimate the positions at the

same time for all peaks. The finest scan containing at least two identified peaks is used to calculate the range.

An interferometer test arrangement was measured as having a coarse range of somewhere around 7.4 metres, using the extremely crude method of a manual measuring tape. An hp 85107A optical frequency domain reflectometry (OFDR) system indicated that the path difference between the two arms is 7.3932 metres. This same OFDR was used by the author in a separate programme, to construct a set of digitiser delay lines, where it displayed accuracies of the order 100 microns^[1]. The same interferometer delay line arrangement is measured using the SIPOD system, Fig. 9.5, with a nominal pulse repetition rate of around 3.84 GHz, giving a pulse-to-pulse spacing of around 5 cm in fibre. The peak-to-peak spacing of adjacent heterodyne signal peaks is 26.9088 MHz, which rounded to the nearest integer provides orders 142 and 143. By observing the interpolated location of a single heterodyne signal peak for a **known peak order** during an extended duration trial, it is possible to observe the effective path difference between the two interferometer arms, to 10's of micron accuracy, Fig. 9.5.

The detected signal has been shown to be highly stable and highly repeatable throughout a working day. The experimental arrangement has been shown to be so stable that it is possible to autonomously measure the order of the pulse overlap and subsequently derive the path difference of the interferometer arms to much better than 50 microns accuracy, Fig. 9.5. Already it has been observed that the measurement performance is approaching the thermal and acoustic limit of the current laboratory arrangement, since the path difference expands with the daily increase in temperature of the laboratory. Environmental influences such as doors closing and other laboratory users can be seen to affect the measured range, due to acoustic pick-up through the fibre interferometer. A customer visit to the laboratory is clearly visible on Fig. 9.5.

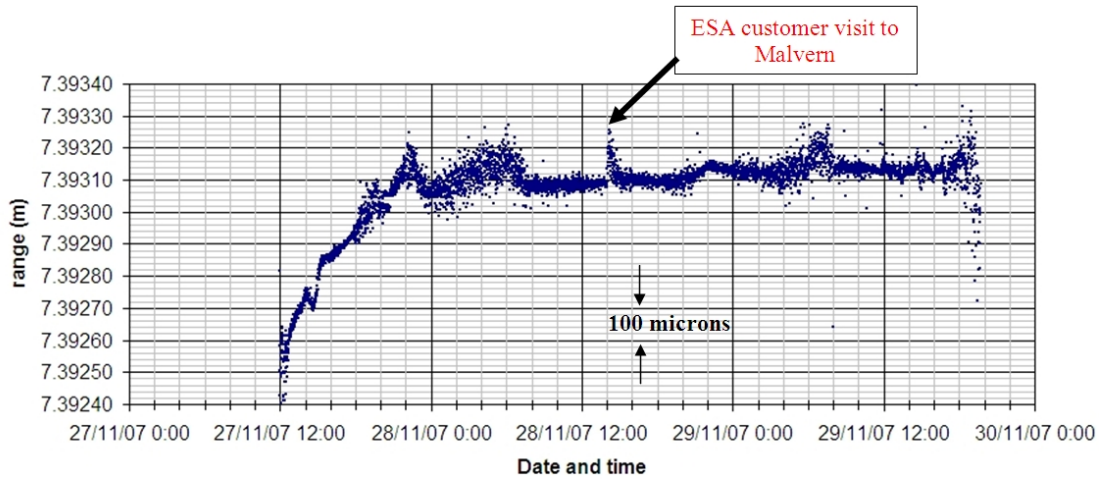


Fig. 9.5. Measured path difference throughout a 3 day measurement period. Note the system settles down to measure the path difference to an accuracy well below the 100 micron grid line spacing. A general upward trend can be observed corresponding to a rise in the laboratory temperature. The system is susceptible to environmental pick-up such as the presence of a large group of people when the customer visited on the 28th of November at 2 pm.

Following initial extended duration trials, several limitations of the first SIPOD experimental demonstrator were identified. The first iteration of the fibre interferometer was implemented using non-polarisation maintaining fibre, with the result that several optical path lengths were possible when recombining the two arms onto a balanced detector. This in turn leads to a variety of different interference profiles. As conditions in the laboratory changed, for example due to temperature changes, vibration effects or movement of the fibre due to air circulation, the relative contributions of the polarisation modes vary. The pulses have been shown to demonstrate low timing and amplitude jitter in Chapter 7, i.e. the optical pulses can be considered to possess a high level of uniformity over the 20 ms it takes for each new pulse repetition frequency output by the hp 83711A signal generator to settle and the heterodyne signal strength to be measured. Therefore, it was initially surprising to see that sometimes there was a dip in the heterodyne signal where there should have been a strong peak, since the autocorrelation of any waveform will provide a peak when both waveforms exactly overlap, irrespective of the waveform shape. It became apparent after fitting a polarisation controller to one arm of the interferometer that it was possible to manually tune the interferometer polarisations to coherently provide the single-peak condition, removing the unwanted multi-peak effects shown in Fig. 9.6. The trough therefore arises due to the correlation between different polarisations, emphasising the

requirement for either polarisation control or the use of only polarisation maintaining components.

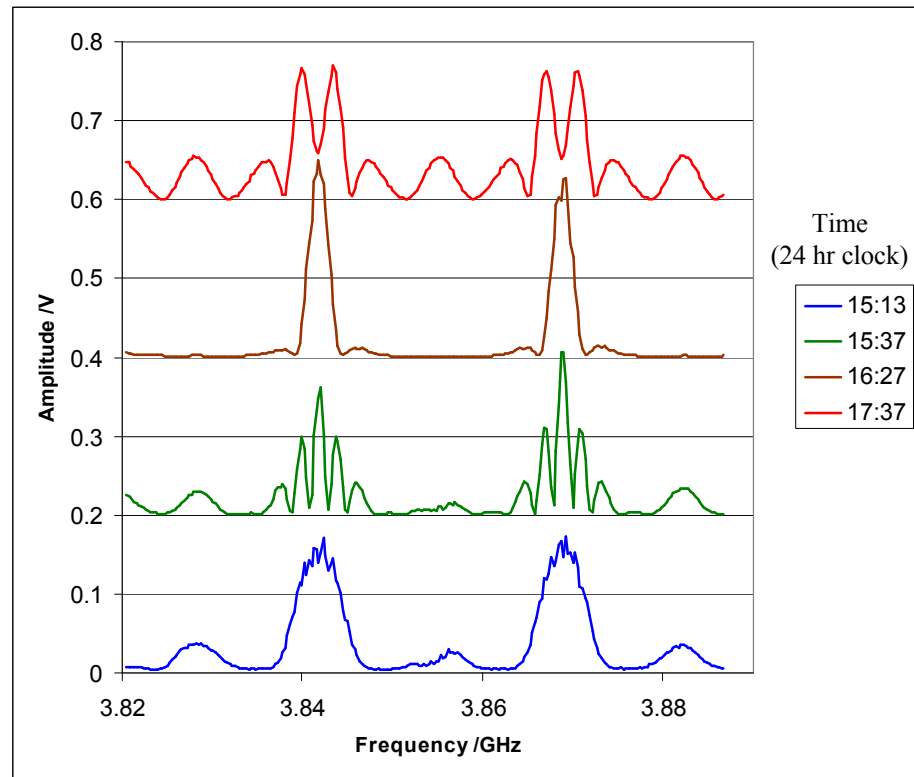


Fig. 9.6. Some of the varied heterodyne signal captures throughout an extended trial period over an afternoon, when using a non-polarisation maintaining interferometer arrangement. Note that dips were observed at 17:37 (red plot) where there was expected to be a peak corresponding to a maxima in the heterodyne signal such as in the 16:27 plot (brown plot). Adding a polarisation control to one arm of the interferometer removes these unwanted polarisation artefacts.

Plotting the set of heterodyne signal captures as a 3D plot to represent all the scans taken during an extended trial, the evolution of the detected signal can be observed, Figs. 9.7 and 9.8. In these diagrams, the bright red spots illustrate the periods when the heterodyne signal was particularly strong, before subsequent polarisation drift reduced carrier strength. Substantial structure is present on some of the 3D plots obtained, and Fig. 9.8 displays bifurcation of the carrier peaks. Fig. 9.9(a) demonstrates what appears to be instantaneous polarisation flips. By implementing the test interferometer wholly in polarisation maintaining components and using a polariser at its input, the problem of multiple path lengths through the test interferometer was removed. However, since the SMF-28 is not polarisation maintaining, this arrangement means that a substantial portion of pulse power may be discarded if the output polarisation from the compression

9. Optical metrology experimental implementation

fibre is not aligned to the input polariser. The de-risking prototype therefore identified that improvements to the system would include the use of polarisation maintaining components throughout the SIPOD system, or alternatively emphasised the need for an active polarisation rotator and control loop to maximise the carrier strength in the chosen polarisation prior to a polariser.

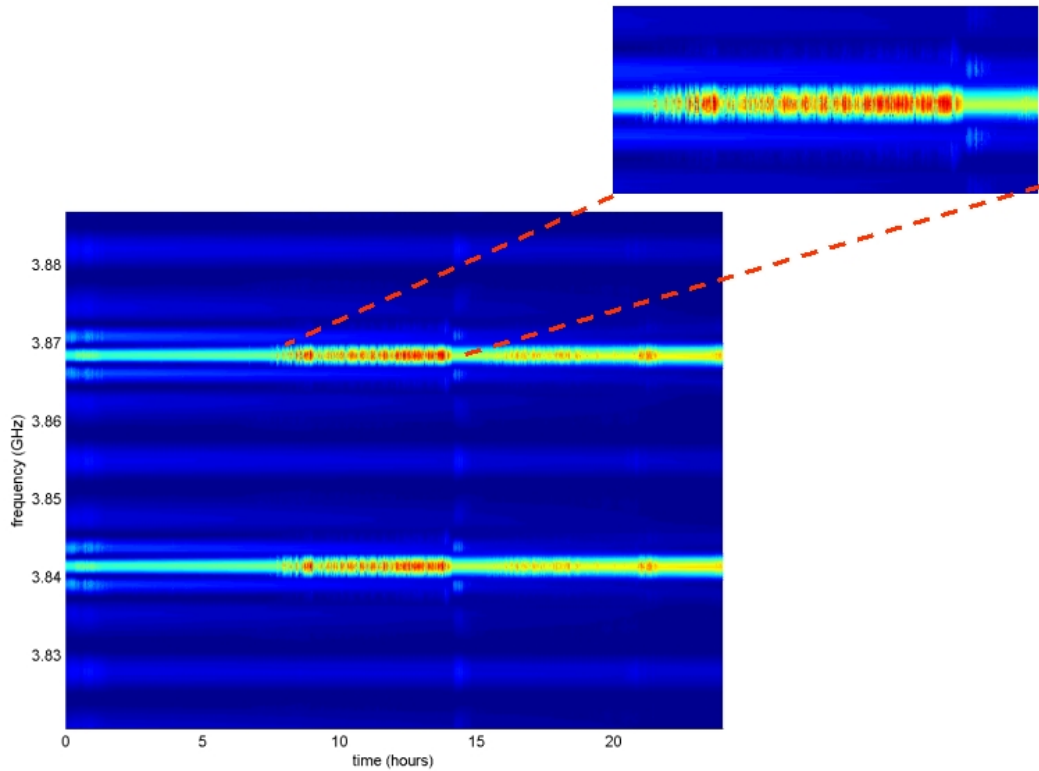


Fig. 9.7. A 3D representation of heterodyne scan measurements made continuously throughout a 24 hour period, measured every couple of seconds. Substantial fine detail is present on the scans indicating polarisation instabilities in the measurement approach.

9. Optical metrology experimental implementation

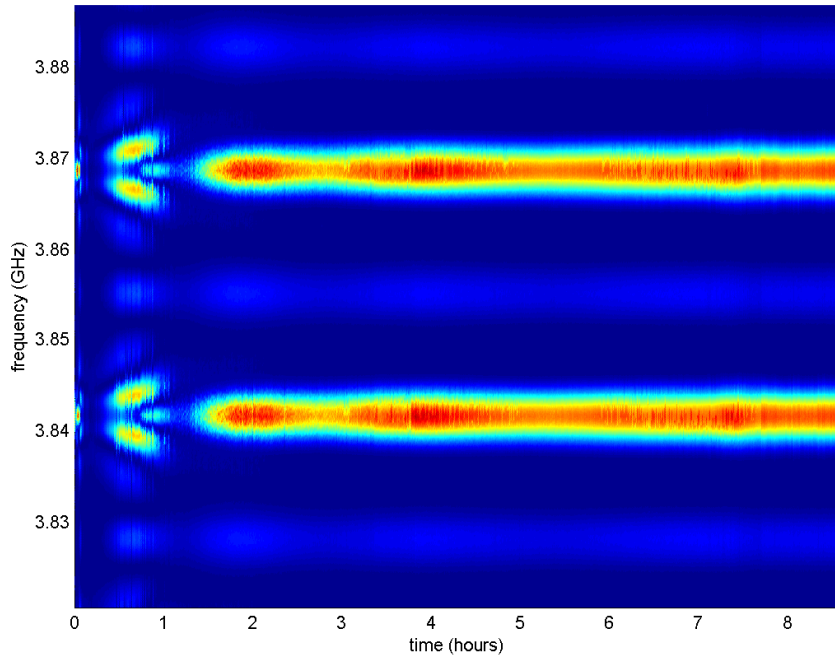


Fig. 9.8. Prior to the use of polarisation maintaining fibre and a polarisor as shown in Fig. 9.2, bifurcation of the heterodyne peak was sometime observed during the measurement evolution. Between 0-1 hours of the measurement capture, double peaks are observed, which evolve to triple peaks, before the system settles down to provide a single peak capture from around 1.5 – 8 hours.

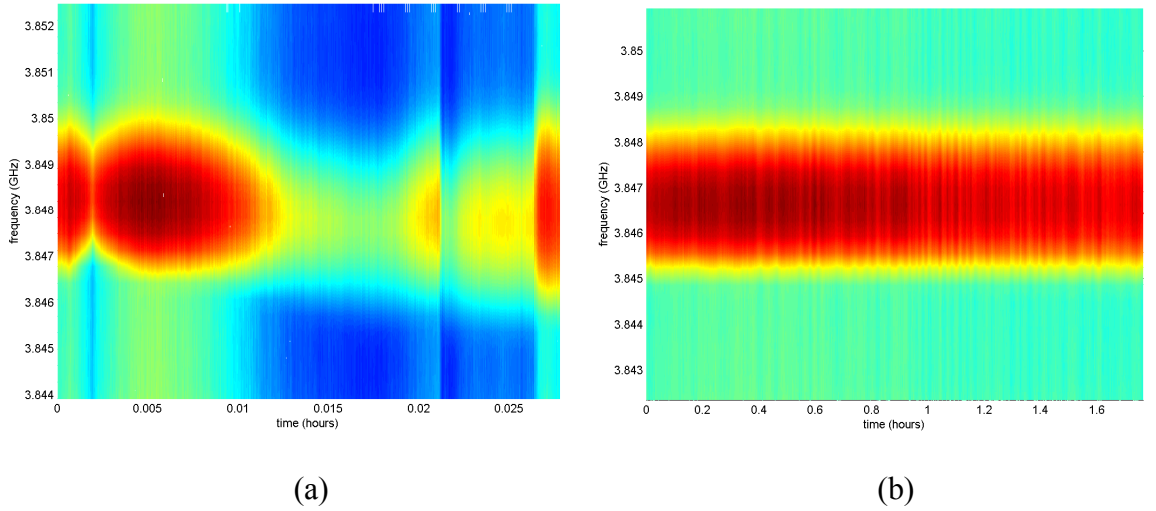


Fig. 9.9. A set of heterodyne signal scans captured over an extended duration capture, represented as a 3D plot, where the interferometer is implemented in polarisation maintaining fibre. (a) When the system is first switched on, polarisation flips and large variations in the peak signal strength are observed, but importantly no multiple peaks have ever been observed over several months of measurement observation. (b) A 2 hour highly stable period of operation during Christmas Day 2007 after the system had reached equilibrium.

9. Optical metrology experimental implementation

In an attempt to isolate the fibre interferometer arrangement shown in Fig. 9.10 from vibration effects, it was mounted on a series of alternating foam and metal plates (i.e. highly decoupled acoustic interfaces). The fibre interferometer was then housed inside a thick polystyrene enclosure placed on top of the vibration mount to try and smooth the effects of external temperature changes on the optical path length through the fibre. Additionally, a 20 kg mass of copper was placed inside the enclosure, with the aim that the combined polystyrene and copper arrangement would provide a more stable temperature environment for the test interferometer. The enclosure was also intended to shield the fibre components from air circulations within the laboratory, reducing polarisation related artefacts.

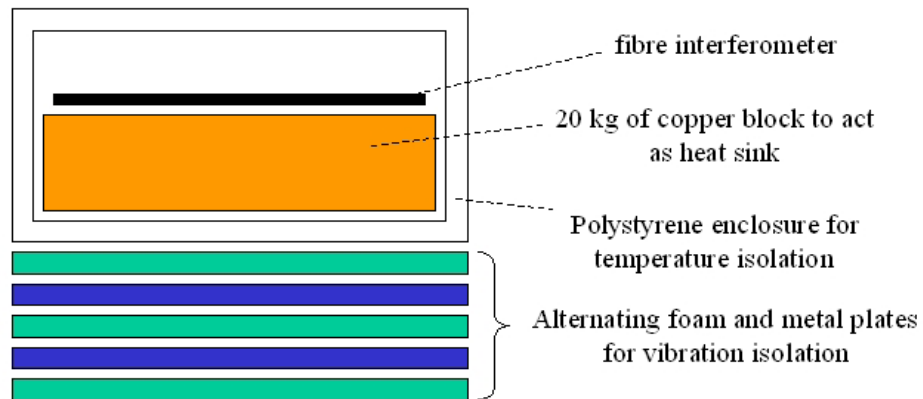


Fig. 9.10. Experimental arrangement used to minimise the temperature, air circulation and vibration effects on the test interferometer. The remaining air space inside the enclosure was filled with polystyrene beads to complete the insulated heat-sink arrangement.

The longest continuous trial of the SIPOD de-risking prototype was performed during a three week period over Christmas 2007. The vibration and temperature isolated interferometer arrangement had not been tampered with for approximately three weeks prior to this extended test, so all fibre components were assumed to have settled to a static position. All test equipment had been running for a minimum of two full days (including the optical pulse compression system) and was considered to have reached its equilibrium state. A scan of 100 points per heterodyne peak was captured, at a rate of approximately 1 Hz. Once the order of the pulse overlap is known, it is not necessary to have two distinct heterodyne peaks present in the capture, and so only the 142nd order was analysed during this extended trial to increase the refresh rate to ~ 1 Hz. Fig. 9.11

shows the measured optical path difference in the interferometer, over a 24 hour period on Christmas Day 2007. This plot shows the laboratory gradually warming up from around 5 am onwards due to the building's heating system coming on, which exhibits itself on Fig. 9.11 as an optical path length increase. The measured path difference remains consistent to less than 50 microns for the 12 hour period from around 8 am through to 8 pm with no erroneous points present on the plot. Zooming in on 1 hour sections of the plot demonstrates that it is possible to consistently measure the path length to better than 30 microns accuracy for every single scan throughout the hour. The Christmas Day measurement data is presented here as the QinetiQ Malvern site was closed to all staff (except security staff) and therefore the internal building vibrations and site vehicular traffic were at their lowest levels. The measurements made from 12 am to 1 am demonstrate an oscillation which visually has periodic structure. The origin of this is currently unknown. Each "oscillation fringe" comprised many points, which suggests they are not noise spikes, so this structure appears to be a real feature of the optical path length and not the SIPOD measurement system. It was considered that these were due to excessive strong wind rattling the laboratory windows during that period, leading to acoustic pick-up.

9. Optical metrology experimental implementation

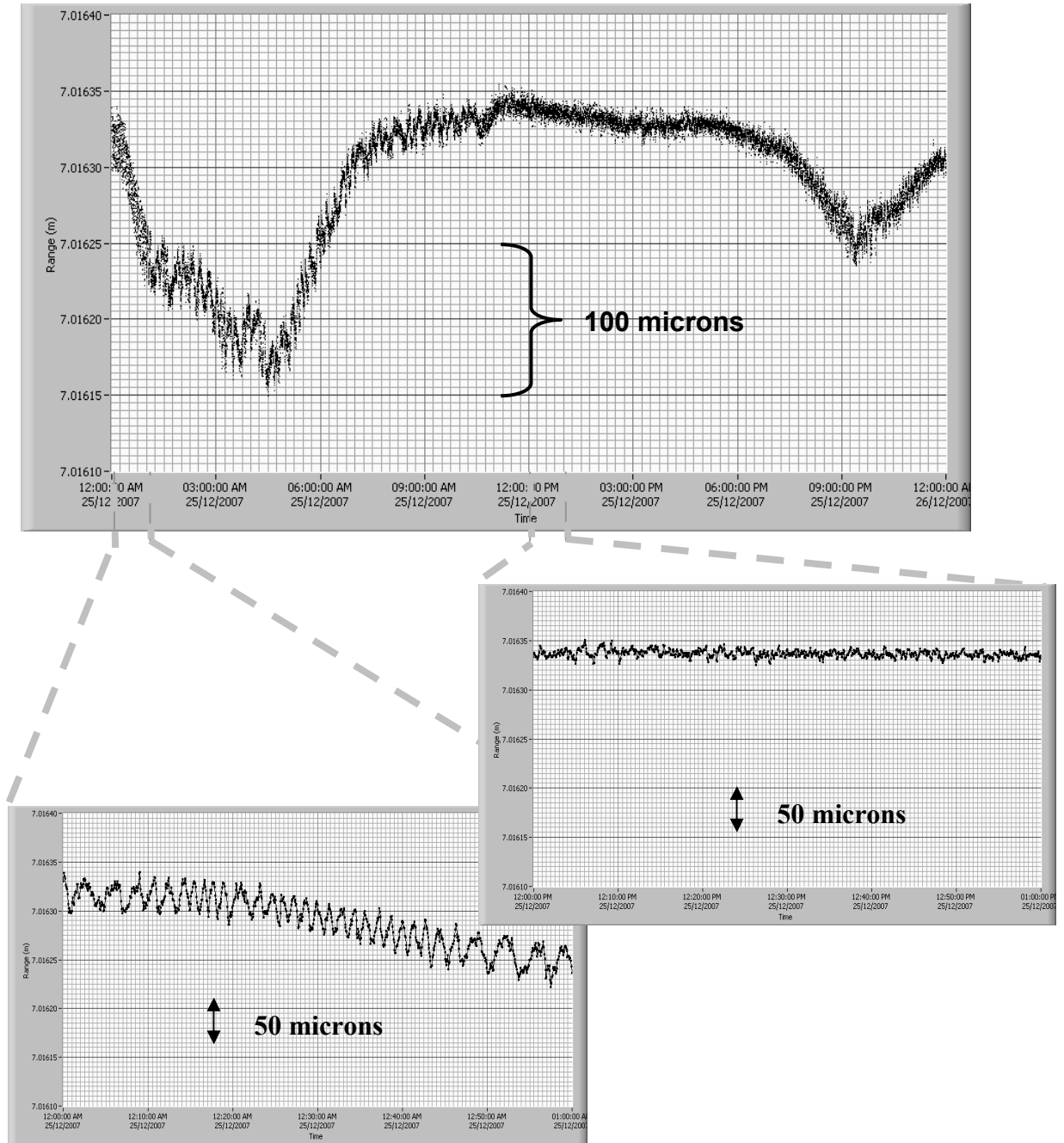


Fig. 9.11. SIPOD scans conducted throughout Christmas Day 2007 (1 Hz scan rate throughout 24 hour measurement period). Note that the measurements for any given hour are significantly within the 100 micron grid spacing. The plot demonstrates the optical path increasing during the day due to the building's heating system warming the laboratory. The zoomed in section depicting 12 am to 1 am (bottom left plot) highlights an oscillation effect, the origin of which is uncertain. The magnified plot of 12 pm to 1 pm (bottom right) shows that the measured path difference was consistent to well under 50 microns through the entire hour (3600 measurements).

9.2 Conclusions on experimental de-risking implementation

It is believed that experimental implementation of the SIPOD discussed in this chapter is the very first time that this method for performing longitudinal metrology has ever been demonstrated. Using existing components available at QinetiQ from other programmes, a SIPOD de-risking prototype system has demonstrated better than 50 microns path length measurement accuracy over many hours of operation. Range measurements have been demonstrated up to 200 metres through a fibre delay line using a DFB laser, and it is expected that the maximum possible range can be extended significantly in future using a fibre laser with a 5 kHz linewidth. The de-risking system prototype has demonstrated the problems associated with testing the SIPOD system, including vibration, temperature and polarisation issues. The next stage of the programme involves procuring optimised components to build a bespoke SIPOD breadboard system, to increase the measurement refresh rate to ≥ 10 Hz, to demonstrate increased absolute range beyond 200 metres, and to increase the range resolution to as far below 30 microns as possible. An optimised breadboard demonstrator is described in the next chapter.

References for Chapter 9

1. McDonald G.J., Olliero J.D., Cooper M.J., Wilson R.A., "A transient waveform digitiser for wideband signal capture", *SPIE Proc. on Advanced Free-Space Optical Communication Techniques/Applications II and Photonic Components/Architectures for Microwave Systems and Displays*, Vol. 6399, 63990N, Oct 2006

10. Build and testing of an optimised SIPOD demonstrator

This chapter describes the completed build and verification procedures for an optimised SIPOD breadboard system, including detailed analysis of its static and dynamic range measurement capabilities. The tests have been devised to verify that the system achieves its design goals and to explore its limitations within the constraints of a laboratory environment. The system build includes an analysis of the key components. The test procedures describe the principal system performance areas, including range resolution, absolute range accuracy, and ability to cope with range drift velocities.

10.1 Introduction to system design and build

This section lists the key components of the SIPOD system and describes the functional tests carried out to ensure that the components meet the overall system requirements. Fig. 10.1 shows a functional block diagram of the system.

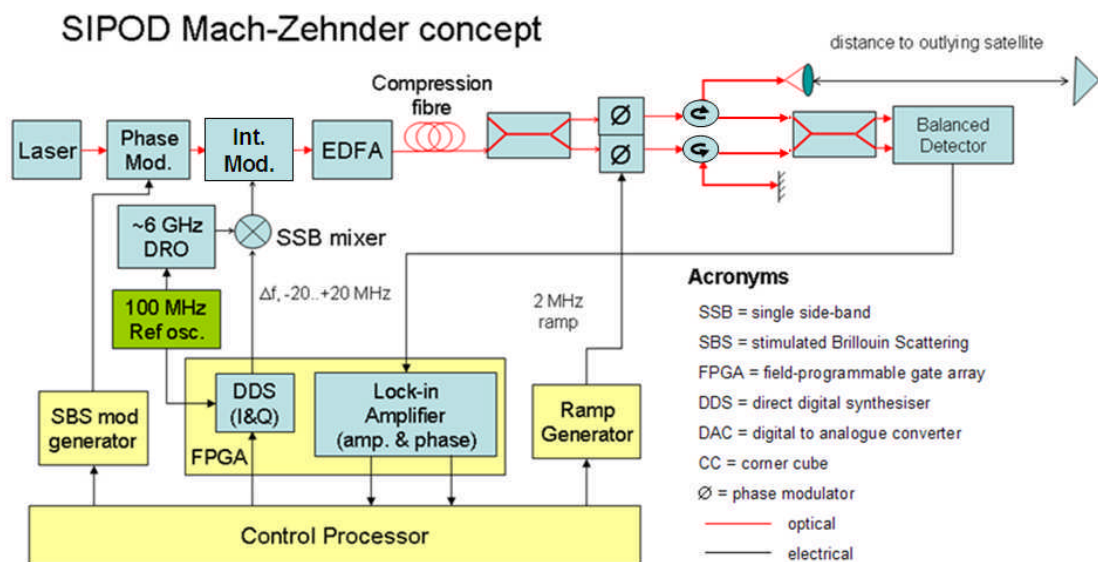


Fig. 10.1. Functional block diagram of the SIPOD system

Goods-in testing (against manufacturer specifications) was successfully performed on all system components.

10. Build and testing of an optimised SIPOD demonstrator

Detailed 3D CAD models of both the optical head and the main optical control unit were commissioned, Fig. 10.2 (bottom middle and bottom right respectively). The optical head unit has been built and populated with components by the author of this thesis, Fig. 10.2 (bottom left). Currently the main optical control unit exists in a compact arrangement on two standard optical plates, which replicates the layout proposed in the design study output, Fig. 10.2 (bottom right).

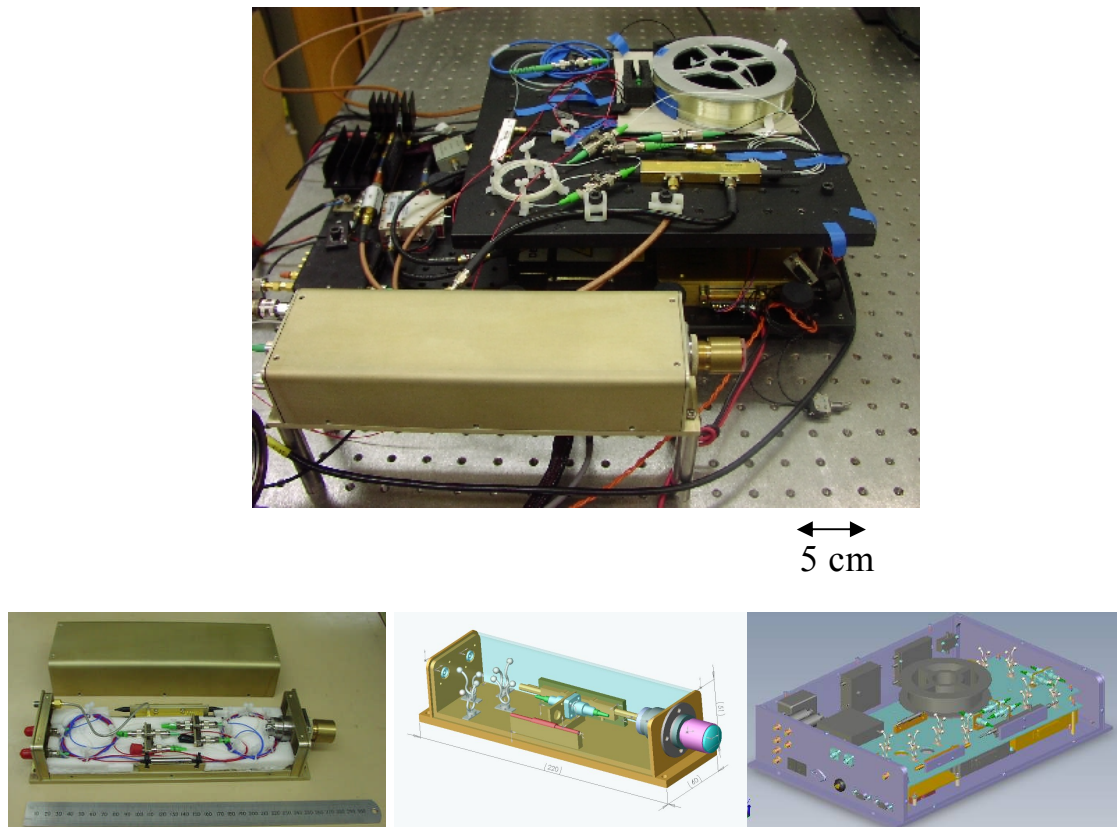


Fig. 10.2. SIPOD breadboard demonstrator system. Top: current optical interferometer head and main optical unit, including bespoke 2.5 km reel of compression fibre. Bottom left: optical head with lid off to display internal fibre winding and component population. Bottom middle: CAD model of optical head. Bottom right: CAD model of main optical unit produced from design study (not fabricated).

10.2 Key SIPOD component tests

This section describes the results of measurements of key SIPOD sub-systems, including the optical pulse source, the interferometer output and the laser coherence

properties. Later sections describe system testing undertaken to analyse the range finding capabilities of the overall SIPOD system.

Pulse generation sub-system

The electronic microwave components have been assembled as a ~ 6 GHz drive train sub-module, Fig. 10.3.

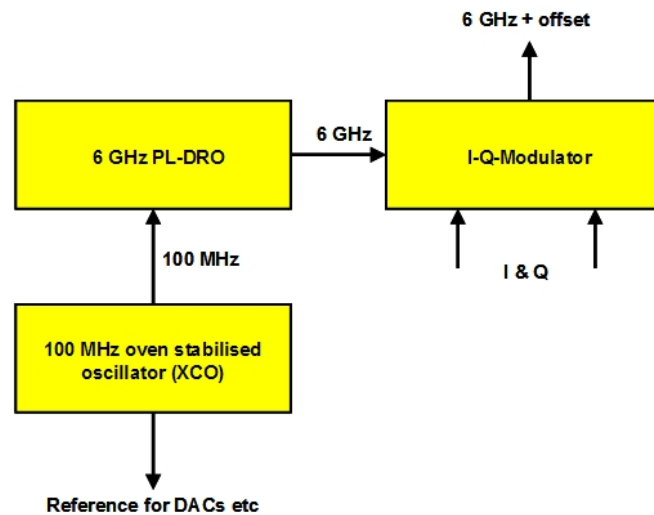


Fig. 10.3. Sub-module providing ~ 6 GHz microwave frequency.

Pulse Generation Sub-assembly

The Pulse Generation Sub-assembly comprises of the following components:

- 1) Long coherence length laser
- 2) Phase modulator (SBS)
- 3) Intensity modulator
- 4) Erbium Doped Fibre Amplifier (EDFA)
- 5) Pulse compression fibre

Laser

The fibre laser “The Rock”, manufactured by NP Photonics, was selected as the SIPOD source due to its 5 kHz linewidth, compact form and relatively high optical output power of ~ 40 mW. As will be discussed in this section, it exhibits a coherence length

and carrier signal which exceed the values required to meet the 500 metre round trip path PROBA-3 specification.

Phase modulation

A Covega phase modulator was successfully driven through $\sim 1/4 V\pi$ in order to eliminate stimulated Brillouin scattering (SBS). Single tone frequencies of the order 80 MHz have been employed for this purpose. The specific frequency used to inhibit SBS is provided by an Acquitek signal generator PCI card and is defined by the system based on the initial range estimate. The system autonomously determines a coarse range, as discussed later in Section 10.4, and then optimises the frequency to ensure the minimal reduction in carrier strength due to the path difference between the two interferometer arms.

Intensity modulator

A Covega Mach-10 intensity modulator has exhibited a stable bias point, and short duration pulses have been experimentally demonstrated using Corning SMF-28 compression fibre. The intensity modulation is behaving as required.

Optical amplifier (EDFA)

The output power from the Keopsys EDFA is fully software controllable (via Labview), the output is polarisation maintaining and linear with input drive current up to 500 mW peak power.

Compression fibre

Pulse compression down to durations of the order 15-20 ps has already been discussed, using a 25 km length of Corning's standard telecommunications SMF-28 fibre. In terms of the laboratory demonstrator, the SIPOD system can operate with the previously demonstrated non-polarisation maintaining SMF-28 fibre. Development of an optimised pulse compression source is discussed in Chapter 11.

Laser coherence

To measure the coherence length of the laser, the free-space section of the interferometer was replaced (or extended) by a series of lengths of optical fibre. The carrier strength was monitored in the absence of pulse modulation and corrected for fibre losses. The variation of the carrier strength with path length difference was used to estimate a lower limit for coherence length. This test is intended merely to demonstrate that the coherence length of the laser significantly exceeds the longest round-trip path length at which the system will be used. Phase noise measurements of the carrier strength are used to provide a more quantitative value, which is particularly relevant to potential fringe tracking capabilities.

The test were repeated with the laser modulation turned on (and the pulse frequency tuned to an overlap peak) to verify that the modulation does not adversely affect the coherence properties of the laser.

Two lasers have been studied: the temperature controlled DFB laser used for the early demonstration of the SIPOD concept in Chapter 9, and the narrow linewidth laser “The Rock” which was purchased specifically for the SIPOD programme. Vastly improved laser stability has been demonstrated by the new laser (NP Photonics fibre laser “The Rock”), which replaces the temperature controlled DFB laser. The coherence properties of both lasers are discussed in this section.

Using the SIPOD optical head as a stable interferometer, different path lengths were employed to evaluate the performance of the two lasers. In addition to a common 12 metre free space delay used in all the measurements, polarisation maintaining fibre was used to provide 200 and 5000 metre round trip path difference delays, Fig. 10.4.

10. Build and testing of an optimised SIPOD demonstrator

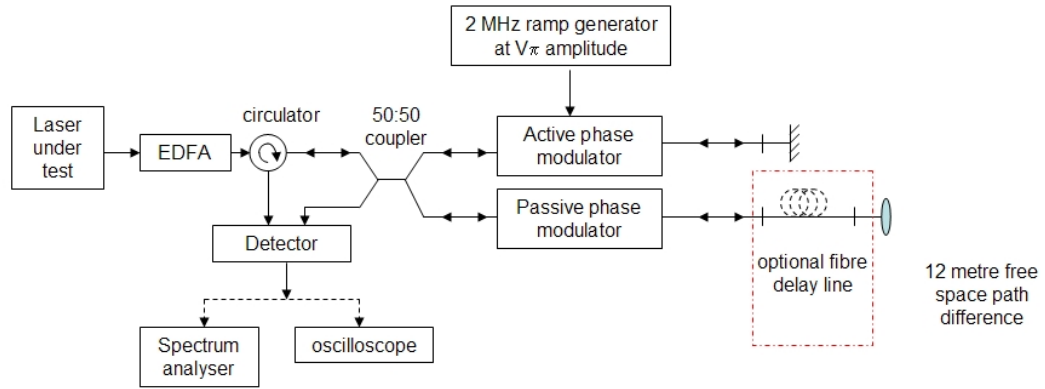


Fig. 10.4. The laser under test is amplified and propagated through a Michelson interferometer arrangement, with one arm experiencing a 2π round trip ramp phase modulation. A 12 metre free space round trip path difference between the arms can be increased to either 200 metres or 5000 metres using polarisation maintaining fibre delay lines.

The 2 MHz carrier was observed on an oscilloscope to qualitatively evaluate the carrier, Figures 10.5-10.7. The Rock fibre laser provides a clearly visible heterodyne signal at 2 MHz over 12 metres, Fig. 10.5, and even for path differences of 5000 metres, Fig. 10.6. The ramp fly-back artefacts can be clearly observed on each cycle; in practice these can be low pass filtered out. The DFB however does not possess sufficient coherence to generate a visually clean signal even over only a 12 metre path difference, Fig. 10.6.

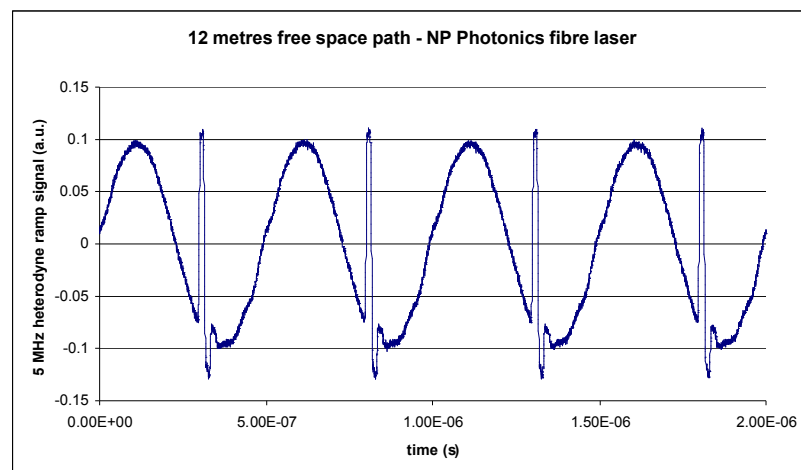


Fig. 10.5. The NP Photonics fibre laser (The Rock) visually provides a well defined 2 MHz carrier signal when viewed on an oscilloscope, through a 12 metre free space path difference. Note the ramp flyback artefacts are clearly visible.

10. Build and testing of an optimised SIPOD demonstrator

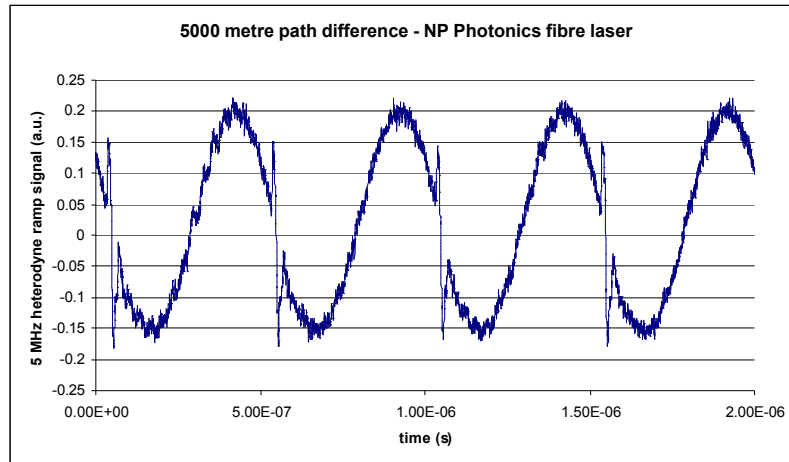


Fig. 10.6. The NP Photonics fibre laser carrier is still clearly visible even after 5000 metres of polarisation maintaining fibre path difference in addition to the 12 metre free space path.

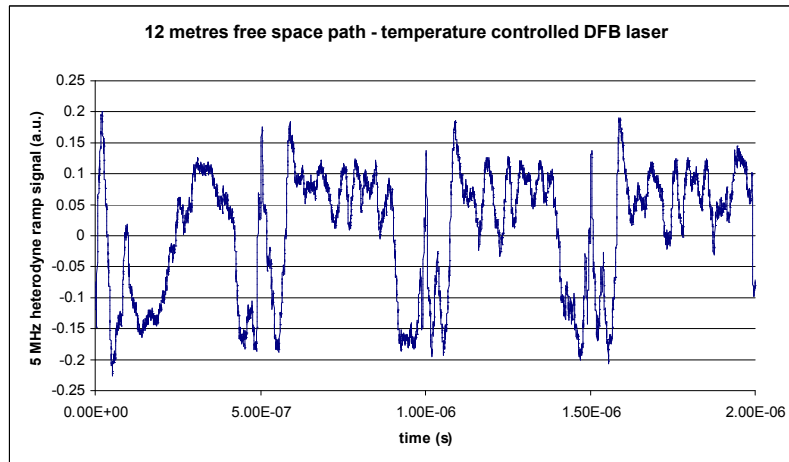


Fig. 10.7. The 2 MHz carrier signal is heavily distorted for the temperature controlled DFB laser through only a 12 metre path difference.

More quantitative performance metrics are obtained from spectrum analyser measurements of the 2 MHz carrier strength and associated laser phase noise. In the following discussion, the analyser resolution and video bandwidths are set as 10 kHz and the span is 1 MHz around the 2 MHz carrier. The analyser resolution bandwidth is representative of the SIPOD operational bandwidth.

The carrier to noise floor ratios were found to be independent of whether the system operates in scanning pulsed mode or CW laser launch.

10. Build and testing of an optimised SIPOD demonstrator

Figs 10.8-10.10 show the carrier to noise floor performance of the DFB and NP Photonics “The Rock” fibre laser for the path differences of 12, 200 and 5000 metres. Both lasers have identical launch powers (governed by the optical amplifier held constant at 84 mW average optical power). The figures in Table 10.1 take into account the additional 13.7 dB and 6.1 dB loss of the 200 and 5000 metre delay line respectively (the 200 metre delay is the more lossy due to additional couplers).

Path difference (m)	The Rock fibre laser, measured (dBc/Hz)	The Rock, corrected for losses (dBc/Hz)
12	71.5	71.5
200	41	47.85
5000	32	35

Table 10.1. Carrier to noise floor ratio for the fibre laser for three different path difference lengths.

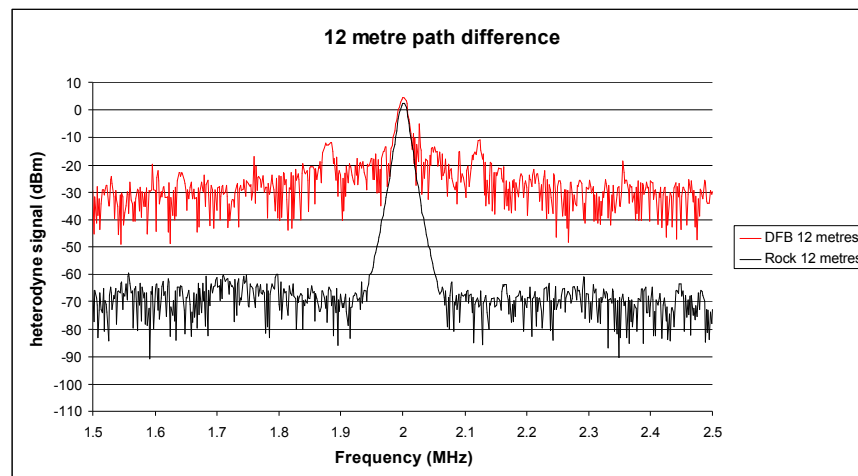


Fig. 10.8. Carrier phase noise performance for both lasers through 12 metre path difference.

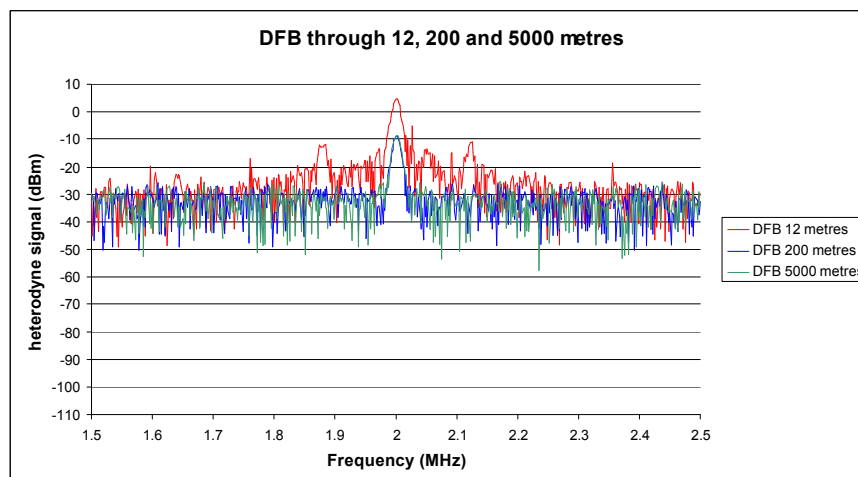


Fig. 10.9. Carrier phase noise performance for the DFB laser through the three different path lengths.

10. Build and testing of an optimised SIPOD demonstrator

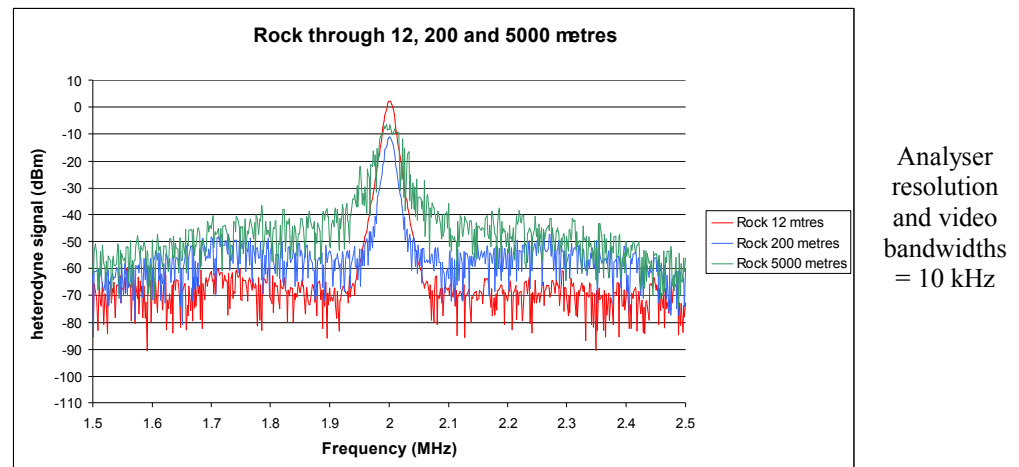


Fig. 10.10. Carrier phase noise performance for the 'The Rock' fibre laser through the three different path lengths.

Fig. 10.11 shows a plot of carrier to noise ratio as a function of interference path length for the two lasers. In an ideal system, the carrier strength should approach the noise floor for long path difference. This is not the case for the lower coherence DFB laser, suggesting that the 'carrier' signal includes some intensity modulation of the signal in the reference arm of the interferometer, either from a small amount of intensity modulation by the phase modulator or from a secondary reflection within the interferometer which gives rise to an additional interference signal. The Rock carrier to noise ratio is still ~15 dB above the ~20 dB limiting contributions from the unwanted interference signals, even after 5000 metres path difference. The unwanted system interference contributions are currently being investigated.

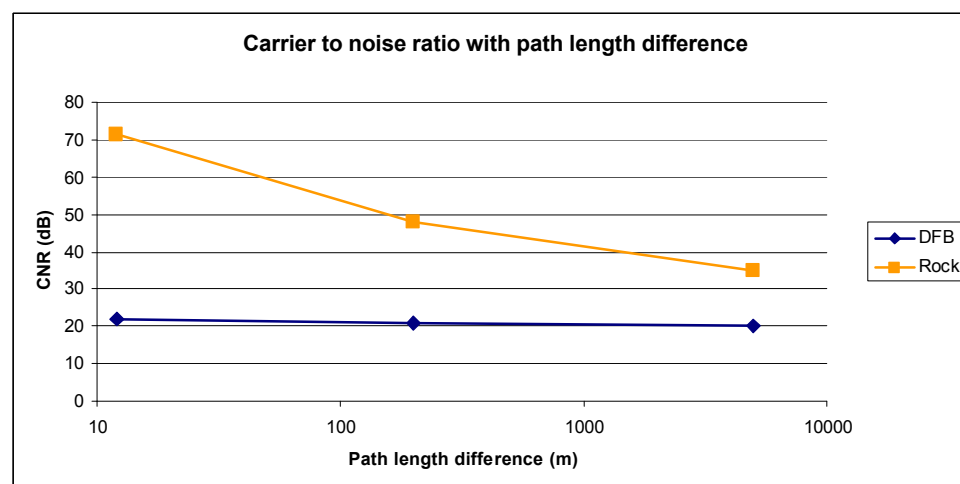


Fig. 10.11. Carrier to noise ratio as a function of path length difference.

10.3 Experimental arrangement for performing range measurements

The SIPOD system will be used to measure the length of a free-space optical path within a laboratory, using a corner cube reflector to mimic the anticipated mode of operation on the PROBA-3 mission. The possibility of using a commercially available optical frequency domain reflectometry (OFDR) system to measure common path lengths allows verification that SIPOD can perform range measurements which are linear with absolute range. Simultaneous observation of the interference fringes can very easily be used to verify system stability, and is thus the prime assessment method to ensure stability of the absolute range.

The retro-reflector is mounted on a translation stage such that the optical path can be varied in a precise manner, allowing the SIPOD system to monitor the changes in the path length. Translations of up to 1000 mm are possible, based on a commercially available translation stage.

Experimental layout

The experimental layout for the system tests is shown in Figs. 10.12 & 10.13. The transceiver head will be mounted at one end of an optical table measuring 2.5 by 1.5 metres. The beam will be directed by a series of mirrors onto a corner cube, which acts as the target for range-finding purposes. The corner cube will be mounted on a translation stage so that the range can be adjusted in precise increments.

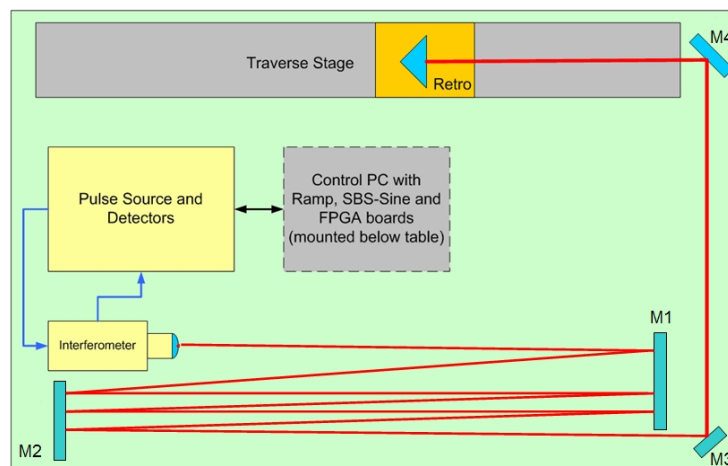


Fig. 10.12. Test layout on optical table.

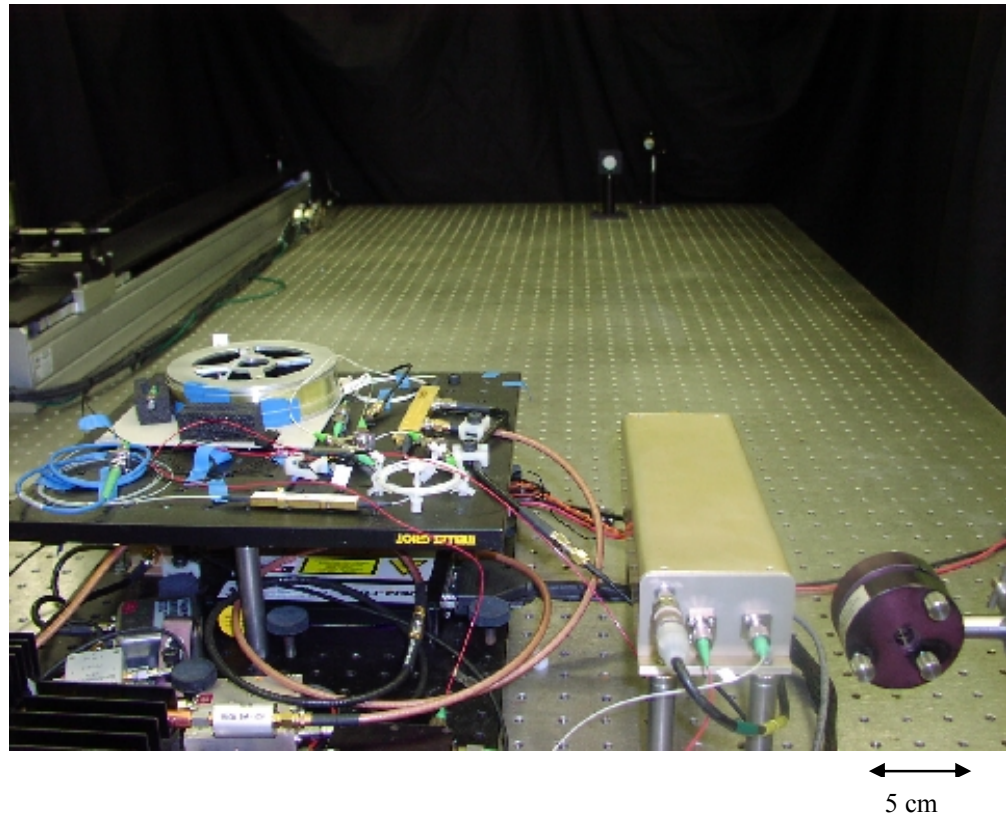


Fig. 10.13. Main optical unit and optical head unit on 2.5 metre optical bench. The translation stage is visible on the far left of the picture. Multiple passes allow SIPOD testing over approximately 12 metres of free space in the arrangement shown. This range was subsequently extended to ~22 metres.

Laboratory environment

Although the laboratory is not air conditioned, observations of the fringe stability for the 12 m test air path have shown that drifts typically do not exceed 1-2 microns per second. This is low enough to allow evaluation of the SIPOD system without concerns about environmental drift swamping the system noise floor. When required, the interferometer can be opened up to allow access to the internal fibre connectors, in order to insert fibre delays to simulate longer paths.

Beam path

The beam path is constructed from multiple transits of the length of the table using a series of plane metallised mirrors. The length of the path from interferometer to the

closest position of the retro on the traverse stage is of order 6 m, providing a 12 m round trip air path. Longer paths can be achieved by the insertion of a fibre optic delay line in the transmit arm of the interferometer. The system performance tests will be carried out both with no delay and with a 100 m fibre delay (equivalent to a 150 m air path).

The traverse stage allowed the range to be varied between ~21.5 and ~22.5 m, with programmable position and velocity, enabling dynamic testing. Alignment of the system was achieved by initially focussing the beam slightly, to achieve sufficient power density to make the spot visible on a phosphor IR card and using this visual indication to trace the beam along its path. The collimation was then optimised by maximising the return signal from a second retro-reflector placed close to the interferometer output. Final fine alignment was verified by adjusting the alignment mirrors to maximise the return signal as the translation stage was moved over its full range.

Translation stage

The translation stage is model ALA10100 manufactured by Aerotech Ltd. The stage has a travel of 1000 mm and can move the corner cube at speeds of up to 200 mms^{-1} , considerably exceeding the 50 mms^{-1} required for testing SIPOD's PROBA-3 performance.

The stage includes a linear encoder to provide position information. The resolution of the encoder is specified as $1 \mu\text{m}$ and the positional uncertainty is one encoder step. According to the manufacturer's specifications, the relative position error between two positions on the stage is proportional to the distance between the positions and may be up to $40 \mu\text{m}$ between the extreme ends of the stage. Furthermore, the encoder scale varies with temperature according to the thermal expansion of substrate onto which it is fixed; the base of the stage is aluminium. The stage has not been further calibrated for the tests described here.

If the resolution performance of SIPOD warrants the investigation of finer range changes, a second translation stage could be mounted on top of the first stage. This would allow precise range increments of a few tens of nanometres over a range of a few millimetres.

Range calibration

The linear encoder on the translation stage will be used to measure the difference between ranges measured with the corner cube at different positions along the stage with a precision of 1 μm . An absolute range measurement was considered using a commercial OFDR, however the reference point of this system will inevitably differ from that of the SIPOD interferometer, resulting in a significant offset. Also, the precision of SIPOD was expected to exceed that of the OFDR.

A weather station was used to monitor the temperature, pressure and humidity in the laboratory. This allows for correction of changes in path length due to ambient conditions if required.

A series of static and dynamic range measurements were designed to assess the SIPOD performance, including:

- constant velocity drift tests
- lateral alignment sensitivity tests
- temperature sensitivity tests
- measurement of an oscillatory target
- sensitivity at reduced signal strength

10.4 SIPOD range detection algorithms

The system has been programmed for three distinct modes of operation. These are designated ‘uncued’, ‘coarse’ and ‘fine’. In the current system, hand-over between the modes is performed manually. However, it is envisaged that in future systems the handover would be automatic based on the results obtained in the various modes. A brief overview of the three algorithm modes is provided below.

The ‘uncued’ mode of operation is designed to allow unambiguous range estimation in the absence of *a priori* range information. The accuracy of the range estimate at this stage is typically a few percent. This is sufficient for hand-over to the ‘coarse’ mode.

The ‘coarse’ mode of operation is designed to refine the range estimate obtained from the ‘uncued’ mode sufficiently to provide unambiguous range determination. The update rate in this mode is approximately one hundred readings per second. The mean frequency interval is used to estimate the range as in the ‘uncued’ mode. The estimated range is then used to determine the order, n , of each of the peaks and thereby derive a refined range estimate for each peak according to the equation:

$$range = nc/2f \quad (10.1)$$

The ‘fine’ mode of operation is the normal mode of operation of the system and provides the most accurate measurements at the fastest rate. In this mode, rapid scans are performed over a narrow range of frequencies corresponding to the location of a peak estimated from the previous measurements. The frequency corresponding to the peak of the scan is determined and the range is calculated as before. The update rate in this mode is approximately 500 readings per second. In this mode the target can be tracked at relative speeds of up to 50 mm/s. At velocities less than 30 mm/s, a range estimate is calculated from the time derivative of the phase of the interference signal.

10.5 SIPOD operational testing

This section describes the key SIPOD range finding performance metrics. Where appropriate, the test objectives are stated prior to the detailed results as an introduction to each set of measurements. Where the actual testing has deviated from the stated objective, the reasoning for this has been provided.

10.5.1 Static range measurement performance

Fig. 10.14 shows the typical variation of readings for a nominally fixed range over a period of 20 seconds. During this time the drift of the actual path length (as indicated by fringes observed on an oscilloscope) was small, hence the graph indicates the repeatability of the SIPOD system itself. The data were obtained with system operating in ‘fine’ mode and the nominal range was 21491 mm. The raw data rate was ~465 readings per second and almost all of the readings lie within a $\pm 30 \mu\text{m}$ band, with

a standard deviation of $9.4\ \mu\text{m}$. The graph also shows a moving average of 46 consecutive readings to indicate the equivalent variation for a 10 Hz data rate. In the latter case the data lie within a $\pm 5\ \mu\text{m}$ band and the standard deviation has fallen to $1.7\ \mu\text{m}$.

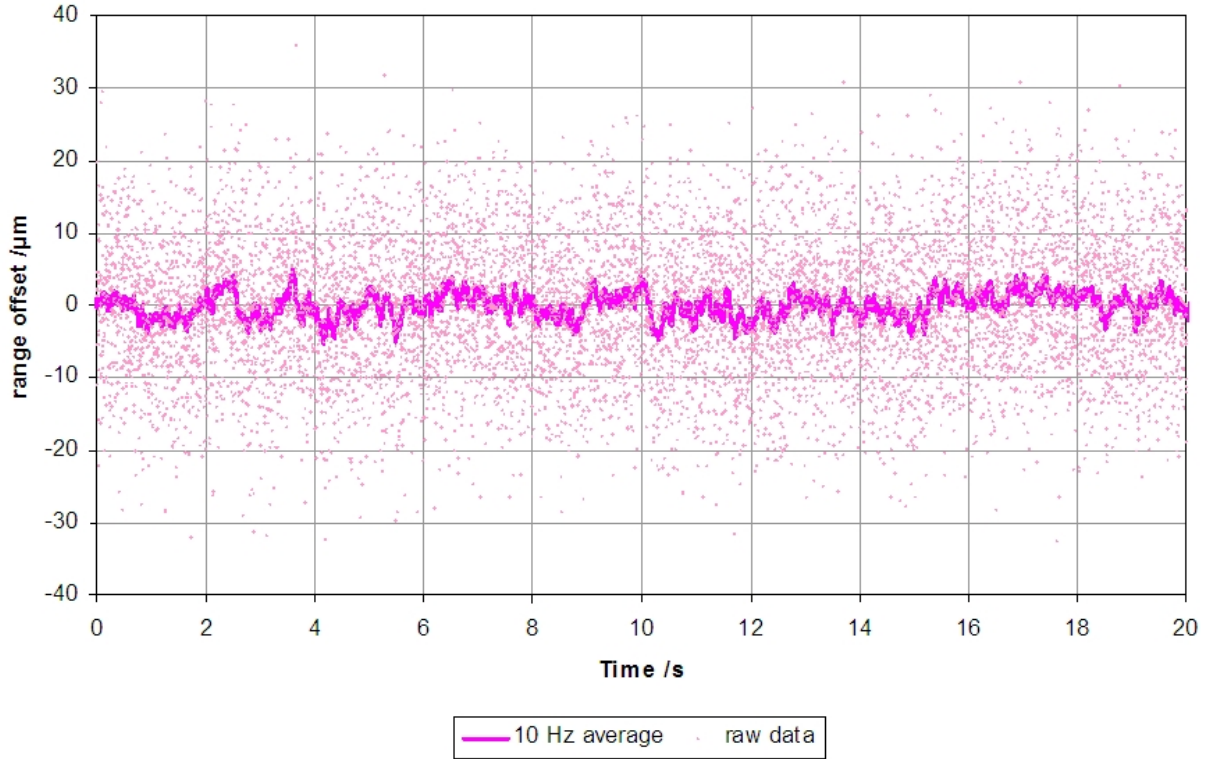


Fig. 10.14. Variation of SIPOD range estimates at fixed range. The single points are individual range measurements made at $\sim 465\ \text{Hz}$, all generally lying within $\pm 30\ \mu\text{m}$ of the nominal range, and the solid trace is a 10 Hz average, showing a variation in range of $\pm 5\ \mu\text{m}$ (with a corresponding standard deviation of $1.7\ \mu\text{m}$).

Over longer timescales, the range varies with the temperature of the laboratory. The portion of the optical path in air is $\sim 17\ \text{m}$ and the optical table was stainless steel. Assuming a thermal expansion coefficient $16\ \text{ppm/K}$, the path length change due to a $1\ \text{K}$ temperature rise is $\sim 270\ \mu\text{m}$. Path length changes as large as $800\ \mu\text{m}$ have been observed during the course of a day as the laboratory temperature changed by a few degrees. However, such changes were slow and did not significantly impact the measurements described in this chapter, which generally were taken over a period of no more than a few minutes each.

10.5.2 Range calibration

A commercial OFDR was used to measure the length of a PM delay line, which was then inserted into the system, and the relative SIPOD range measurements were assessed. This approach does not provide absolute length calibration, but instead measures offsets from a fixed (but unknown) datum. This approach is considered a valid calibration method, since the inter-satellite range will be measured as the *relative difference* between the datum point representing the launch point from the optical head and the outlying satellite.

For these measurements, the SIPOD interferometer head was configured as a Mach-Zehnder interferometer as shown in Fig. 10.15. In this configuration, the delay line can be inserted either at position A or B. When the delay line is added at position A, the system measures a range increase corresponding to a single pass through the delay line. When the delay line is in position B, the system measures a range increase corresponding to a double pass through the delay line. A set of three ranges with identical differences between them could therefore be used to assess the linearity of the SIPOD system over extended ranges.

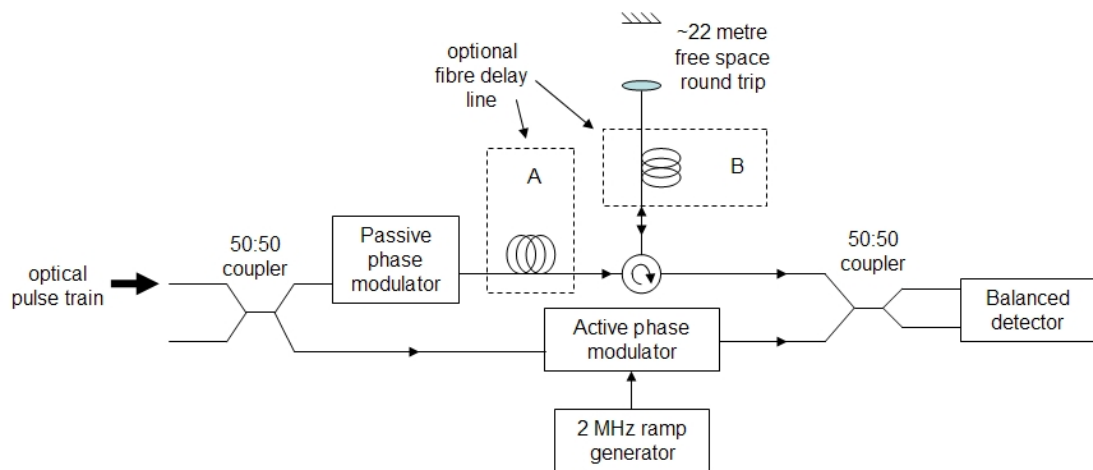


Fig. 10.15. The SIPOD optical head unit arranged in a Mach-Zehnder configuration can have optional fibre delay lines inserted at position A or B. Position A offers a single pass through the delay, and position B provides a double pass.

The OFDR measured an optical delay through a PM fibre delay line of 501.952 ns at 1550 nm, corresponding to a range of 150481.334 mm (based on an average of 5 successive measurements). This delay line was then inserted into *position A* and *position B*. Note that inserting the delay into one of the arms of the SIPOD optical head interferometer results in a length measurement which is half of the actual length. Note also that both the OFDR and SIPOD systems are measuring the time of flight through the optical path. Using the refractive index for air as opposed to 1.455 for fibre, the ~100 metre delay line is actually measured as ~150 metres by both systems.

For the ~100 metre delay line tests, SIPOD determined that the range measurement was ~21.89 m without the extra fibre delay, 97.13 m with the delay in *position A* (single pass) and ~172.37 m with the delay in *position B* (double pass). A range increment of ~75.24 m, consistent with half the 150.48 m OFDR measurement, is observed when inserting the delay in *position A* (compared to the range observed when no fibre delay is present), and then when the delay is subsequently inserted into *position B*. Therefore a multiple increment in the range equivalent to the fibre delay is observed when the delay is in *A* or *B*, demonstrating that the SIPOD system performs absolute range finding linearly with range. This linear range performance is perhaps easier to interpret when presented in tabulated form, as in Table 10.2.

Due to ambient temperature fluctuations between measurements, the measured length of the delay can fluctuate from measurement to measurement, whether using SIPOD or the OFDR. Discrepancies between measurement sets following head layout changes have been as low as 60 microns, as presented in Table 10.2. A variation of between 160 and 370 microns between the SIPOD and OFDR delay line lengths is shown in Table 10.2. Therefore, the length of a ~100 metre PM optical fibre delay line has been consistently verified by both a commercial OFDR system and the SIPOD system, limited by temperature drift within the fibre delay during the manual transfer of the fibre between the two systems (a 10 ppm/°C delay variation over 100 metres = 1 mm/°C length variation).

10. Build and testing of an optimised SIPOD demonstrator

OFDR time delay (ns)	501.952
OFDR range (mm)	150481.334
OFDR range (mm) / 2	75240.667
(1) SIPOD position A - no extra delay (mm)	75241.041
(2) SIPOD position B – position A (mm)	75240.828
SIPOD(1) - OFDR (mm)	0.373
SIPOD(2) - OFDR (mm)	0.161

Table 10.2. Both the OFDR and SIPOD systems were used to measure a 104.14 metre optical delay line (= 150.48 metres before taking the refractive index of 1.445 into account). Both systems were consistent to 160 microns, limited by temperature fluctuations within the delay line between measurements.

10.5.3 Long translation stage scans at extended ranges

Range measurements were performed for each of the three configurations described above (i.e. with no extra delay line and with the delay line in positions A and B) as the position of the translation stage was scanned through 800 mm, Fig. 10.16. The translation stage was initially positioned in the “home position”, the mid-point of the translation stage scan. The ‘uncued’ then ‘coarse’ algorithms were used to determine the range without any external range cues. The ‘fine’ scanning algorithm was then selected and the stage was moved to a position at the extremity of the stage which provides the maximum range measurement. The stage then scanned through 800 mm at 20 mm/s, before pausing and then returning 800 mm to the maximum range location. The scan length (out and back) measured in all three configurations was of the order of 800.25 mm, Table 10.3. This agrees well with the path length of 800.22 mm obtained by multiplying the physical path length difference by the refractive index of air (1.00027). The remaining difference between these two values is within the uncertainty arising from stage calibration errors and temperature fluctuations.

This test demonstrates that SIPOD can determine the range unambiguously from 22 m to 172 m without any a priori information from another system, using the coarse algorithm. The fine tracker has been observed to remain locked to the initial pulse order provided by the coarse algorithm throughout the 800 mm scan.

10. Build and testing of an optimised SIPOD demonstrator

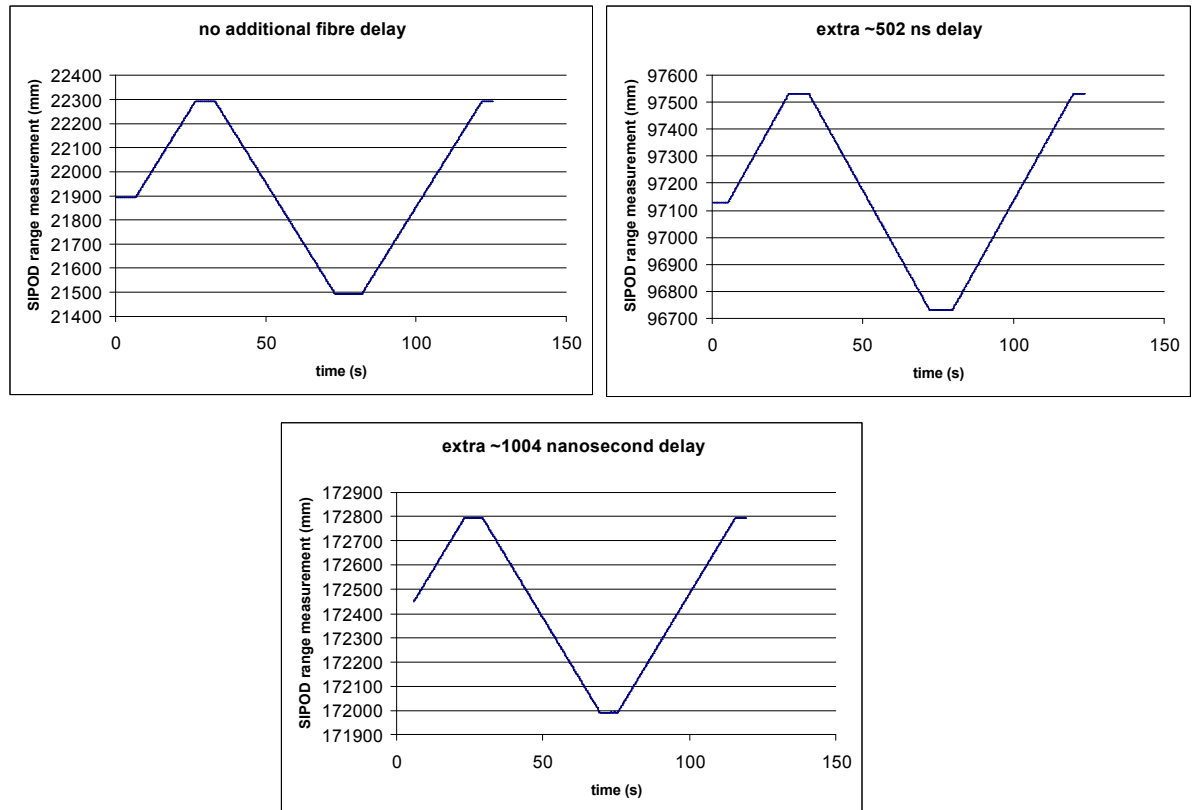


Fig. 10.16. Scanning through 800 mm at 20 mm/s for ranges ~22 m, ~97 m, and ~172 m.

Extra delay	Home	-400 mm to start	800 mm ramp	-800 mm to end	Range out	Range back	Difference
1004 ns	172370.737	172770.872	171970.653	172770.920	800.219	800.267	0.048
502 ns	97130.751	97530.896	96730.643	97530.904	800.253	800.261	0.008
None	21890.832	22290.966	21490.734	22290.978	800.232	800.244	0.012

Table 10.3. Performing an 800 mm translation stage scan for three different ranges. The same ~502 ns delay line is inserted into position A and then position B to allow absolute range finding to be determined, when compared to the arrangement without the delay line. In all three cases, the important result is that the scan length is consistently measured to be ~800.25 mm, irrespective of absolute range. All values are in mm unless otherwise stated.

Position B - Position A (mm)	75239.985
Position A - no delay (mm)	75239.920
Difference (mm)	0.065

Table 10.4. The range for the stage “home” position is an integer multiple of the fibre delay line, demonstrating that absolute range measurements can be made up to at least 172 m. The 65 micron discrepancy may arise from thermally-induced drift in the fibre and free space paths during the extended duration test runs.

10.5.4 Dynamic range measurement - constant velocity drift

Dynamic range tests were designed to assess the performance of SIPOD when the target is moving and to determine the maximum target speed at which the system performance remains acceptable in terms of the PROBA-3 scenario.

The corner cube was positioned at one end of the translation stage and then translated to other end of the stage at a constant speed of 5 mm s^{-1} . During the movement, SIPOD measured the range as a function of time using the ‘fine’ mode. Simultaneously, the position reported by the linear encoder was recorded. The test was then repeated with the movement in the opposite direction. These tests were repeated at increasing speeds of 10, 20, 30, ... mm s^{-1} until SIPOD could no longer track the movement.

SIPOD successfully maintained lock over an 800 mm scan range for the full range of constant drift speeds 5, 10, 20, 30, 40 and 50 mm s^{-1} , Fig. 10.17. The measured displacement for all translation stage velocities varied by only 16 microns around the nominal stage displacement of $\sim 800.26 \text{ mm}$, Table 10.5. Similar results were obtained for translations in both directions.

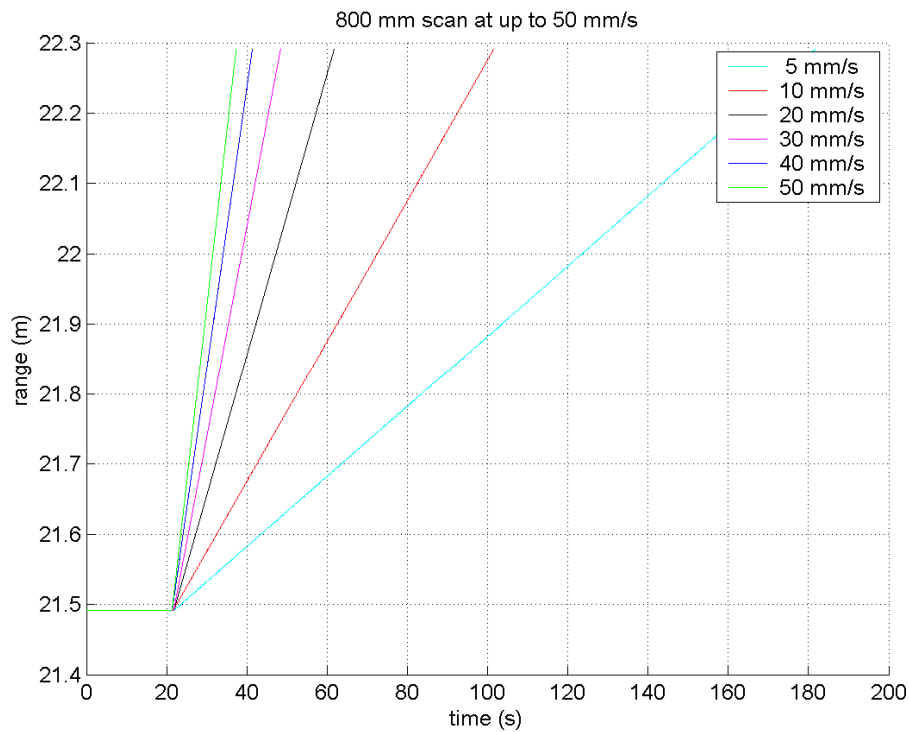


Fig. 10.17. SIPOD maintained lock for all constant translation stage velocities tested, up to and including 50 mm s^{-1} .

10. Build and testing of an optimised SIPOD demonstrator

Velocity (mm/s)	Start point (mm)	End point (mm)	Displacement (mm)
5	21491.105	22291.362	800.257
10	21491.088	22291.346	800.258
20	21491.066	22291.321	800.255
30	21491.049	22291.305	800.256
40	21491.008	22291.276	800.268
50	21491.020	22291.271	800.251

Table 10.5. The total displacement for the different translation speeds only varied by 16 microns, around the nominal displacement of 800.26 mm, demonstrating that the pulse order was consistently maintained throughout all the scans at all stage velocities.

A velocity estimate was also recorded at each range position. The velocity estimate was based on the derivative of the phase of the interference signal during each frequency scan. Phase unwrapping algorithms were used to eliminate phase discontinuities during the scan. However, these algorithms were unable to cope with large phase shifts between successive points in a scan, thereby placing an upper limit on the maximum velocity that could be measured in this way. Fig. 10.18 demonstrates that the ‘fine’ tracking algorithm was able to correctly provide the stage velocity information for speeds up to 30 mm/s, in addition to the range information. The fine tracking algorithm cannot provide this information when the speed is increased to 40 mm/s. In principle, a faster scan would allow measurement of slightly larger velocities at the expense of range accuracy; the minimum time between points in a scan is limited by the round-trip time of the measurement beam.

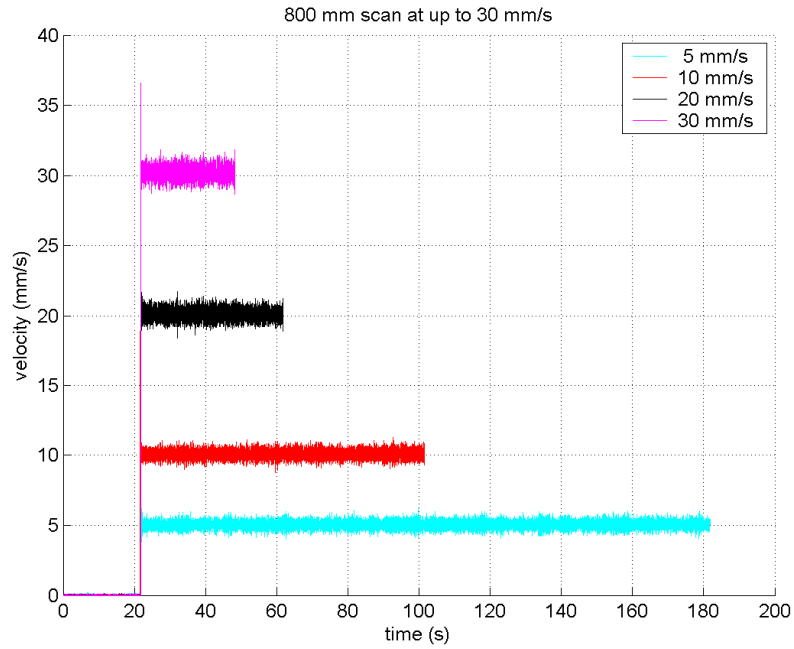


Fig. 10.18. Velocity measurements in fine mode were successfully achieved up to 30 mm/s.

10.5.5 Lateral alignment sensitivity

This test is designed to evaluate the angular pointing tolerance required for successful operation of SIPOD. The PROBA-3 requirement for this test is that the range measurement is substantially unaffected for lateral offsets corresponding to an angular misalignment of $50 \mu\text{rad}$.

The longitudinal position of the corner cube on the translation stage was held as constant as possible while the lateral position was varied manually. The SIPOD control software was set to coarse then fine mode to allow pulse order tracking. The strength of the pulse order peak provided by the SIPOD software was noted for each lateral offset.

Importantly, the fine peak tracking algorithm was able to maintain lock as the corner cube was scanned through 1.5 cm of lateral displacement, Fig. 10.19. At the maximum lateral offsets which still allow a range measurement to be made, i.e. $\pm 0.75 \text{ cm}$, the noise on the range measurement increases but the mean value remains unchanged. The small underlying range measurement variation in Fig. 10.20 is assumed to arise from flexing of the corner cube mount as it is manually scanned laterally.

10. Build and testing of an optimised SIPOD demonstrator

A suggested maximum “safe” operating lateral displacement range is ± 50 mm, corresponding to an angular misalignment of $200 \mu\text{rad}$ at the 250 m maximum operating range, thus exceeding the $50 \mu\text{rad}$ target specification.

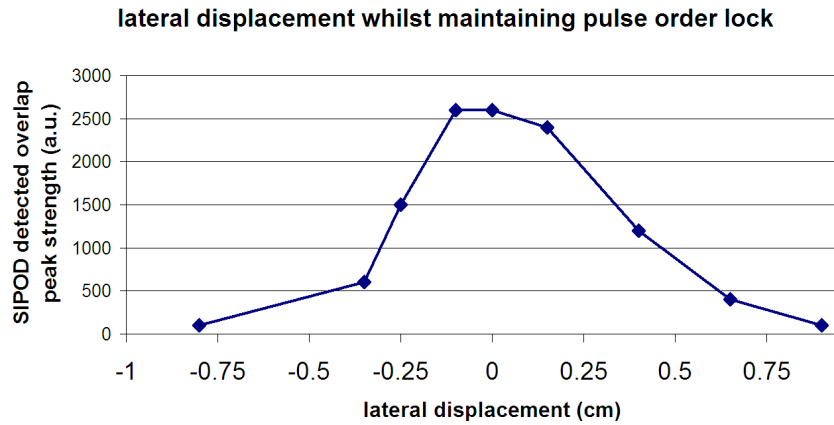


Fig. 10.19. The SIPOD system can accommodate up to ± 0.75 cm of lateral corner cube displacement and still maintain lock on the same optical pulse using the fine tracking algorithm (range was ~ 22 m). However a realistic lateral operating range is suggested to be around ± 0.5 cm.

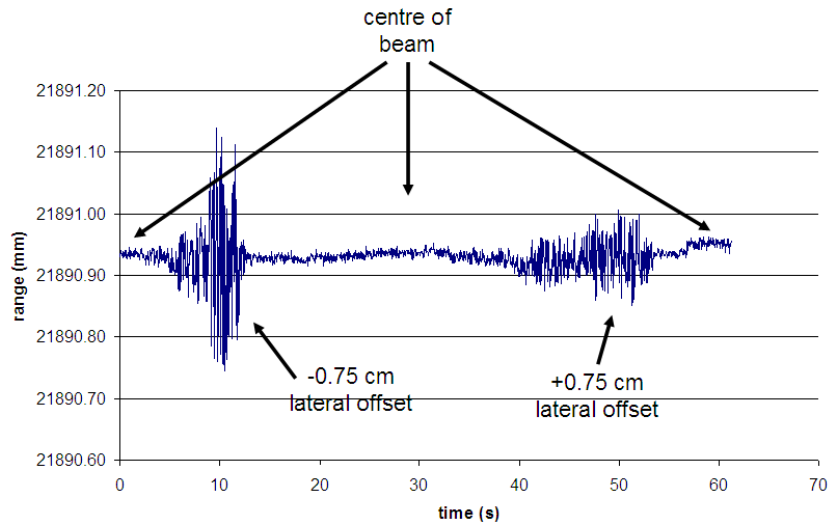


Fig. 10.20. SIPOD's longitudinal range measurement performance as the corner cube is manually scanned from centre (start of plot), through to -0.75 cm (10 s) then back through centre to $+0.75$ cm (45 s) before returning to the centre point (60 s). Note that the mean range of ~ 21890.93 mm is maintained throughout.

10.5.6 Temperature sensitivity

The temperature of the SIPOD interferometer head was varied whilst measuring a constant optical path difference. This was achieved by wrapping a heater coil around the

10. Build and testing of an optimised SIPOD demonstrator

head and using it to control the temperature of a single thermocouple connected to the head.

The temperature was actively increased through 10°C (27°C to 37°C) and then allowed to passively cool through 9°C , Fig. 10.21. The thermocouple was measuring the temperature of the optical head metal case throughout this process, and not the optical fibres within the case. It is likely that the optical fibre components within the case continued to experience some heating after the active temperature control was removed, hence the general trend of increasing range throughout the 37 minute trial. The maximum range variation throughout the entire heating and cooling test was 152 microns, which is consistent with a $10\text{ ppm}/^{\circ}\text{C}$ propagation constant for typical 1550 nm optical fibre ($\sim 2\text{ metre path difference through }10^{\circ}\text{C at }10\text{ ppm} = 200\text{ microns}$).

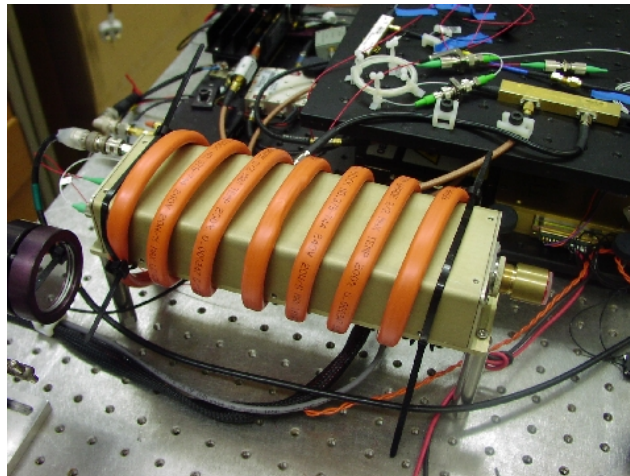


Fig. 10.21. Simple heating arrangement to assess range limitations of optical head.

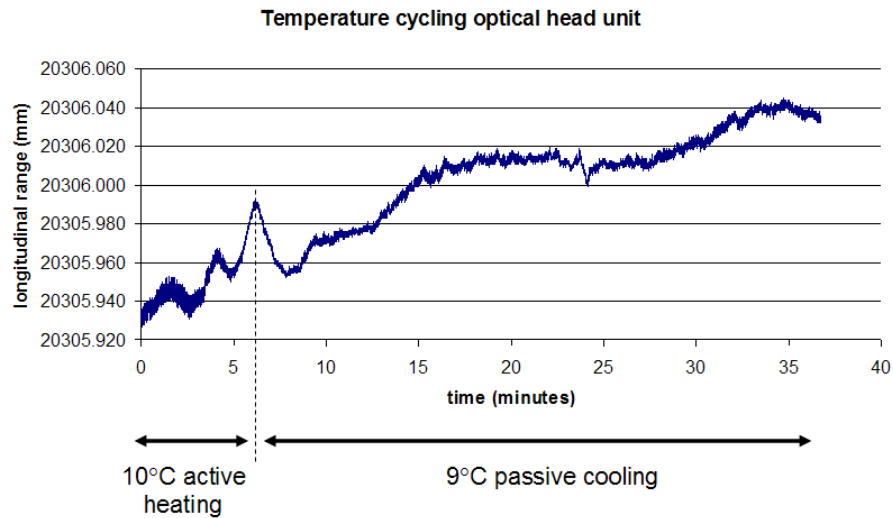


Fig. 10.22. SIPOD measured a 152 micron maximum range variation as the optical head is heated through 10°C from 27°C to 37°C.

10.5.7 Measurement of an oscillatory target

This test was designed to assess the performance of SIPOD to measure ranges to a target which has a low amplitude oscillatory motion such as might arise from vibrations of the satellite.

For this test, the corner cube was moved in a periodic fashion whilst the average range remained constant. The range of possible motions was limited by the performance of the translation stage. It was noted that the corner cube was in continuous motion whenever the stage was active. This was a consequence of the operating principle of the stage, whereby the stage was free to move when not active and the position of the stage when active was defined by the encoder reading. Since the encoder had a finite resolution, the position of the stage was continuously corrected whenever the reading changed by one encoder step. The resulting vibration was observed by monitoring the interference signal on an oscilloscope; however there was no discernible impact on the performance of SIPOD.

Fig. 10.23 shows a measurement of a 10 μm amplitude square wave displacement. Data were taken at 465 readings per second. A 46 point moving average was then applied to

the data, resulting in an effective sampling rate of 10 Hz. This demonstrates the resolution of the system.

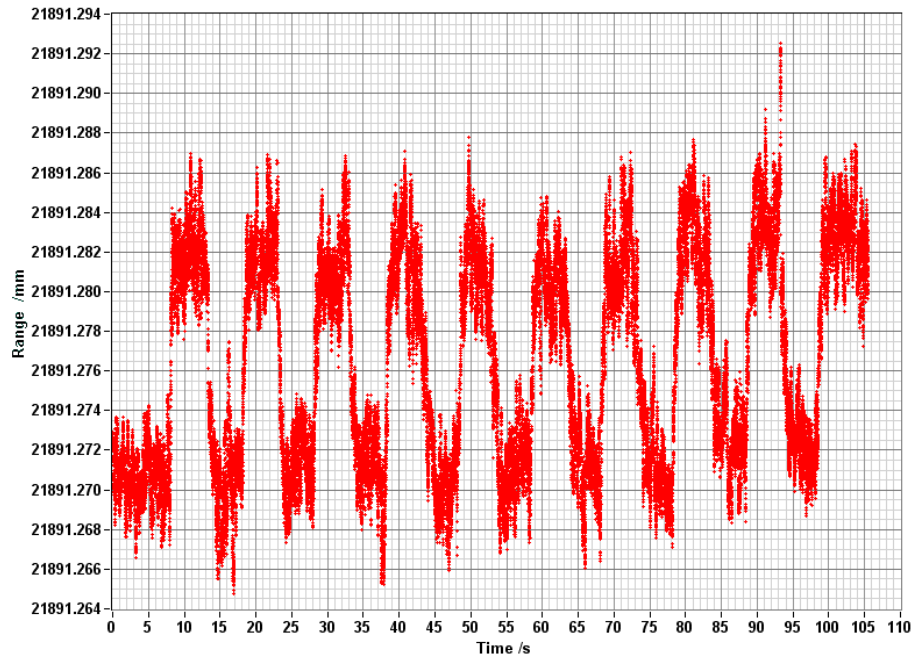


Fig. 10.23. Measurement of nominal 10 μ m amplitude square wave. Successive readings have been averaged to produce a 10 Hz equivalent sampling rate.

The translation stage was able to produce oscillations at up to ~ 10 Hz. Fig. 10.24 shows data taken as the corner cube was moved in an oscillatory fashion at the maximum possible frequency. The plot also shows the encoder readings taken at the same time. The time difference between the two sets of readings has been adjusted to maximise the overlap between them for comparison purposes. However, it should be noted that, since SIPOD returns measurements at 465 Hz and each measurement result is calculated prior to the start of the subsequent measurement, there may be a delay of up to ~ 2.2 ms between the measurement of a position and the report of that position. The nominal range at which these measurements were taken was ~ 97 m.

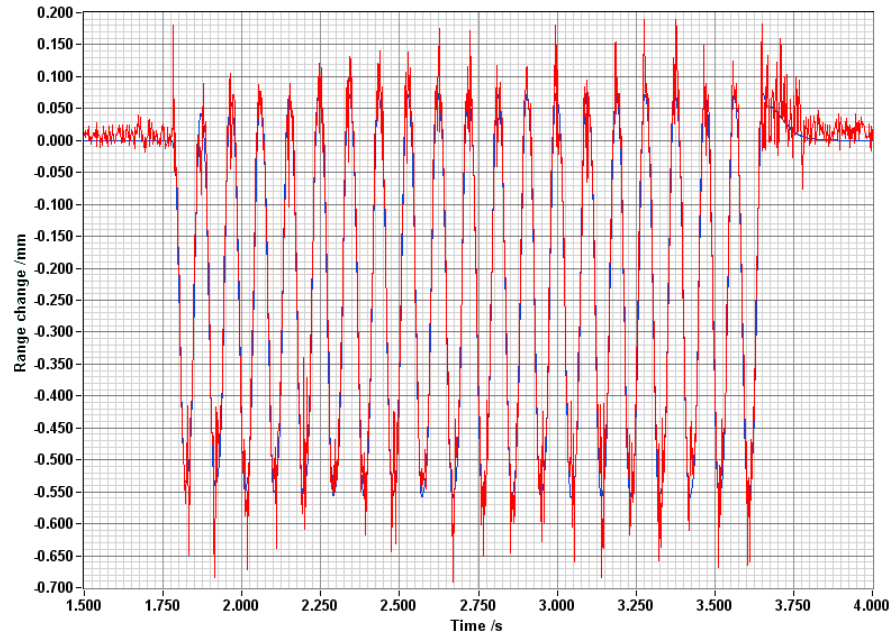


Fig. 10.24. Measurement of an oscillatory target at 97 metres. Red curve: SIPOD range readings. Blue curve: encoder position.

At these frequencies, the full data rate from SIPOD is required to resolve the motion and hence the uncertainty of each point increases since no averaging can be done. It is apparent from Fig. 10.24 that the motion is fully resolved, although some individual readings may vary by as much as 100 μm . At lower data rates, the SIPOD readings average to the mean displacement. This suggests that the system will not be susceptible to errors due to small vibrations at higher frequencies when the motion can not be resolved.

10.5.8 Sensitivity at reduced signal strength

The performance of the system at maximum range will be limited by the coherence length of the laser and the strength of the return signal from the retro-reflector. Tests described previously in this chapter have indicated that the coherence of the laser is sufficient to provide sufficient carrier to noise performance at the maximum envisaged range. The sensitivity of the system to attenuation of the return signal will be assessed over a shorter range by monitoring the changes in system performance as a series of attenuators is introduced into the beam path.

Although it would be desirable to test the system using a free-space path of 250 m, the stability of the optical path in air would be strongly affected by atmospheric effects and so the value of such a test would be limited. Should future funding allow, tests could be carried out at facilities with a long vacuum path.

A series of neutral density (ND) filters were placed in the beam path, for a static corner cube position. The SIPOD system was operated in fine tracking mode and was able to remain consistently locked to the same pulse order throughout the addition of 3 different ND filters to the system, which provided a total attenuation of approximately 2.8 ND of the beam following a double pass, Figure 3.18. Pulse order lock was lost when a 3.0 ND filter was inserted in place of the previous 3 lower attenuation plates. Interestingly, the range measurement increases in Fig. 10.26 by ~ 0.75 mm for each ND filter, corresponding to the increased refractive index of the glass relative to the air path.

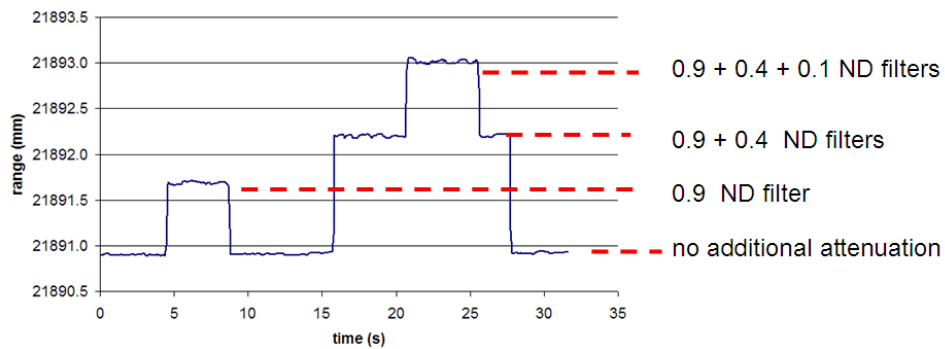


Fig. 10.26. The SIPOD system consistently remained locked to the same pulse order using the fine tracking mode, as three separate ND filters were placed in the beam path (attenuating the beam by a factor of 1000 after a double pass). Note the increase in measured range due to the different refractive index of the filters compared to the air path.

10.6. Conclusions of SIPOD range finding performance testing

The SIPOD system meets the following goals:

Unambiguous range determination: The system has been shown to determine the range to a target without recourse to *a priori* range information at simulated ranges up to ~170 m by using a variety of different scan modes. Switching between these modes is currently done manually but could be readily automated.

Range tracking: The system can track a moving corner cube at speeds of up to 50 mms^{-1} in fine mode and somewhat faster in coarse mode. At speeds below 30 mms^{-1} , the system returns the velocity independently of the range estimate.

Range linearity: The system is linear for (optical fibre simulated) ranges up to 170 m. The measurement of a length of optical fibre in single and double pass configurations differed by less than one part in 10^6 . At shorter ranges, linearity has been demonstrated over a continuous interval of 800 mm.

Range repeatability: Successive measurements of a constant range at ~465 Hz had a standard deviation of $9.4 \text{ }\mu\text{m}$. Averaging successive measurements reduces the error to $1.7 \text{ }\mu\text{m}$ at 10 Hz.

Range accuracy: A commercial OFDR system has been used to verify that SIPOD's absolute accuracy is at least a few parts in 10^6 . A discrepancy of ~30 μm over 800 mm has been noted between lengths measured by the translation stage encoder and those measured by SIPOD. However, this is within the stated accuracy of the stage and corresponds to a temperature difference of only a few degrees Celsius between the (unknown) temperature at which the stage was calibrated and the ambient temperature within the laboratory.

The SIPOD measurement system described in this chapter meets or exceeds the technical goals defined at the start of the ESA programme. In addition, the system measures absolute range without *a priori* range information and measures target velocity independently of the range. The system therefore remains a promising candidate metrology solution for PROBA-3 and subsequent missions and it is recommended that the system should be developed further to meet this requirement.

11. Design of an optimised SIPOD compression fibre

Various commercially available highly non-linear fibres were modelled, with the aim of determining a compression arrangement which substantially reduces either the output pulse durations or the required fibre length in comparison to the pulses already demonstrated through 25 km of standard telecommunications fibre (Corning's SMF 28). The SIPOD application in particular requires the minimum possible system volume and weight for use on micro-satellite platforms. Modelling suggests at least two different manufacturers (Sumitomo and Furukawa) supply fibres which can generate <2 picosecond pulses after propagation through a length of fibre an order of magnitude shorter than the 25 km of SMF-28 implemented in the previous chapters. Compressed pulses of the order of 10 picoseconds duration were experimentally demonstrated using 2.5 km of a reduced core diameter fibre from a third manufacturer, Fibercore, a company which has previously supplied ESA with radiation tolerant fibres for gyroscope applications. Fibercore also offer a broad range of polarisation maintaining fibres. A custom draw was subsequently specified, combining three desirable properties from Fibercore's existing fibre portfolio to create a new fibre; these parameters are polarisation maintaining, radiation tolerant composition, and reduced core diameter to achieve a higher non-linear coefficient to increase pulse compression per unit length.

11.1 Introduction to fibre modelling

Pulse propagation has been modelled through a variety of different fibre types, including commercially available fibres and idealised fibres which could feasibly be commissioned if modelling suggests exceptionally improved performance would be achieved. The aim of this work was to identify a fibre which provides much higher performance than the default Corning SMF-28 option initially used to implement the compression source, both in terms of pulse duration and fibre weight/volume. In addition, the peak launch power should be as low as possible to minimise system power requirements. Several commercially available speciality fibres exist which exhibit much higher non-linear coefficients than SMF-28 fibre. This is not surprising since long haul telecommunications system designers specifically wish to avoid non-linear effects such as four wave mixing, and so SMF-28 fibre is purposely designed to have a low non-

linear coefficient. The remainder of this chapter explains that modelling and experimental investigations confirm that certain speciality fibres can indeed generate usefully compressed pulses for vastly reduced fibre lengths and/or launch powers.

As discussed in Chapter 4 and Ref. [1], the most important fibre parameters in terms of pulse compression performance are the non-linear coefficient γ ($[\text{W.km}]^{-1}$), the fibre attenuation α (dB/km), and the dispersion parameter D (ps/nm/km), which must be positive (i.e. anomalous). Commercially available highly non-linear fibres modelled include those offered by OFS (Furukawa), Sumitomo, Fibercore and photonic crystal fibre manufacturer Crystal Fibre. Fibre parameters for these manufacturers are given in Table 11.1. In addition, it is considered highly desirable for the fibre to be polarisation maintaining (PM) to eliminate polarisation control issues when launching into the interferometer head, particularly for space borne missions where autonomous system stability is essential. The overall weight of the compression fibre is also vitally important for ESA's micro-satellite applications; a standard 25 km reel SMF-28 weighs an unacceptable 2 kg. A straightforward weight reduction method is simply to use a fibre with an 80 μm reduced outer cladding diameter (SMF-28 has a 125 μm outer diameter), providing an immediate $\sim 60\%$ weight saving per unit length.

	Attenuation (dB/km)	Non-linear coeff. (W.km) ⁻¹	Dispersion (ps/nm/km)	Polarisation maintaining	Potentially radiation robust
Corning SMF-28	0.21	1.3	15.5	No	No
OFS highly non-linear fibre	<0.9	11.5	-2.5 to 3.0	No	No
Sumitomo highly non-linear fibre	<0.9	26	3.0	No	No
Fibercore 1500 (5.3/80)	0.5	7.0	19	No	No
Fibercore 1500 (4.2/80)	1.6	11.2	19	No	No
Fibercore 1500HBG-RT	0.89	3.2	19	Yes	Yes
Crystal Fibre NL-1550-POS-1	<9.0	11.0	<1.5	No	Yes
Crystal Fibre PM-NL-3.0-850	44	58	127	Yes	Yes

Table 11.1. Summary of selected commercially available compression fibre options and their specifications.

The main driver for shorter pulse durations and also substantially reduced weight/volume was the SIPOD system's goal of flying on the micro-satellite PROBA-3,

however both reduced pulse duration and system weight are also of importance in the optical sampling application for military applications.

Input pulses at 6 GHz (the nominal SIPOD pulse repetition rate) were modelled through lengths of fibre up to 5 km (in 1 metres step sizes, 32678 points per pulse window), with a maximum optical peak power of 1 Watt considered in 25 mW steps. For each step through the fibre and for every input launch power, the pulses were evaluated to determine modelled pulse width. The following Figs. 11.1-11.7 show interesting trend lines for the peak launch powers which provide <20 ps, <10 ps, <5 ps, <2 ps, <1 ps and <500 fs pulses at the stated fibre length. For most fibres modelled, the upper plot shows the performance over the ranges 0-5 km and 0-1 Watts. Where shown, the lower plot provides a zoomed in version of the most relevant plot region for the SIPOD application. *In Figs. 11.1-11.7 the modelled pulse repetition rate is 6 GHz.*

The traces generally exhibit break points towards the low power and longer fibre lengths of the plot, since for these combinations of launch parameters the peak powers are too low for the pulses to experience significant enough non-linear effects for strong compression to occur. Conversely, for very short lengths of fibre, even peak launch powers of 1 Watt are not high enough for the pulses to experience significant non-linearities for them to compress sufficiently.

Fig. 11.1 demonstrates the modelled performance through SMF-28. A peak optical launch power of ~430 mW into 4 km of fibre is predicted to produce <20 ps pulses. For 4 km, the launch power would have to be increased to ~600 mW peak optical power to reduce the pulse duration to <10 ps. This increases to ~750 mW for < 5 ps. This launch power becomes unattractive due to electrical power consumption, stimulated Brillouin scattering (SBS) problems and the fact that the pulses are not particularly short.

11. Design of an optimised SIPOD compression fibre

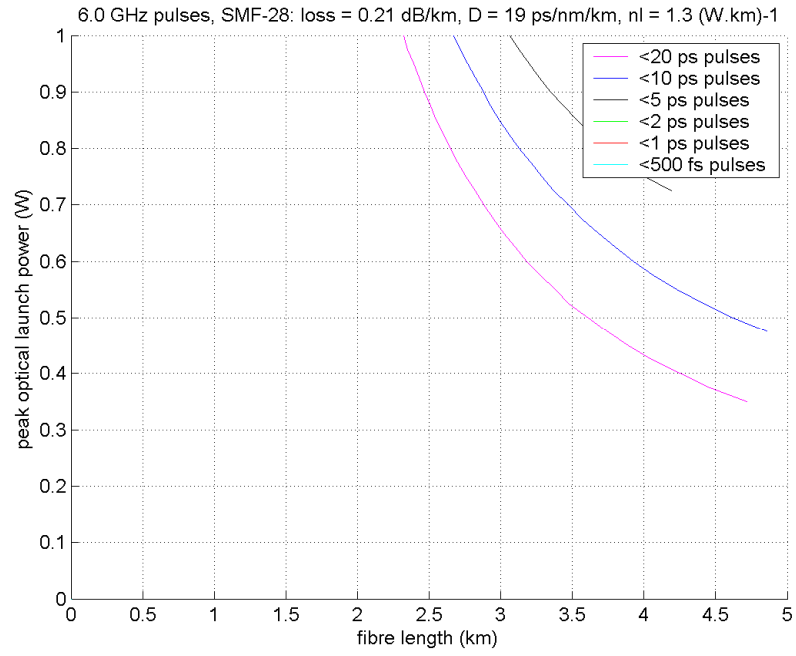


Fig. 11.1. Pulse propagation through SMF-28 for 6 GHz repetition rate pulses. Pulses as short as <5 ps are predicted but they require unacceptably high peak launch powers.

11.2 Modelling commercially available highly non-linear compression fibres

OFS Furukawa highly non-linear fibre

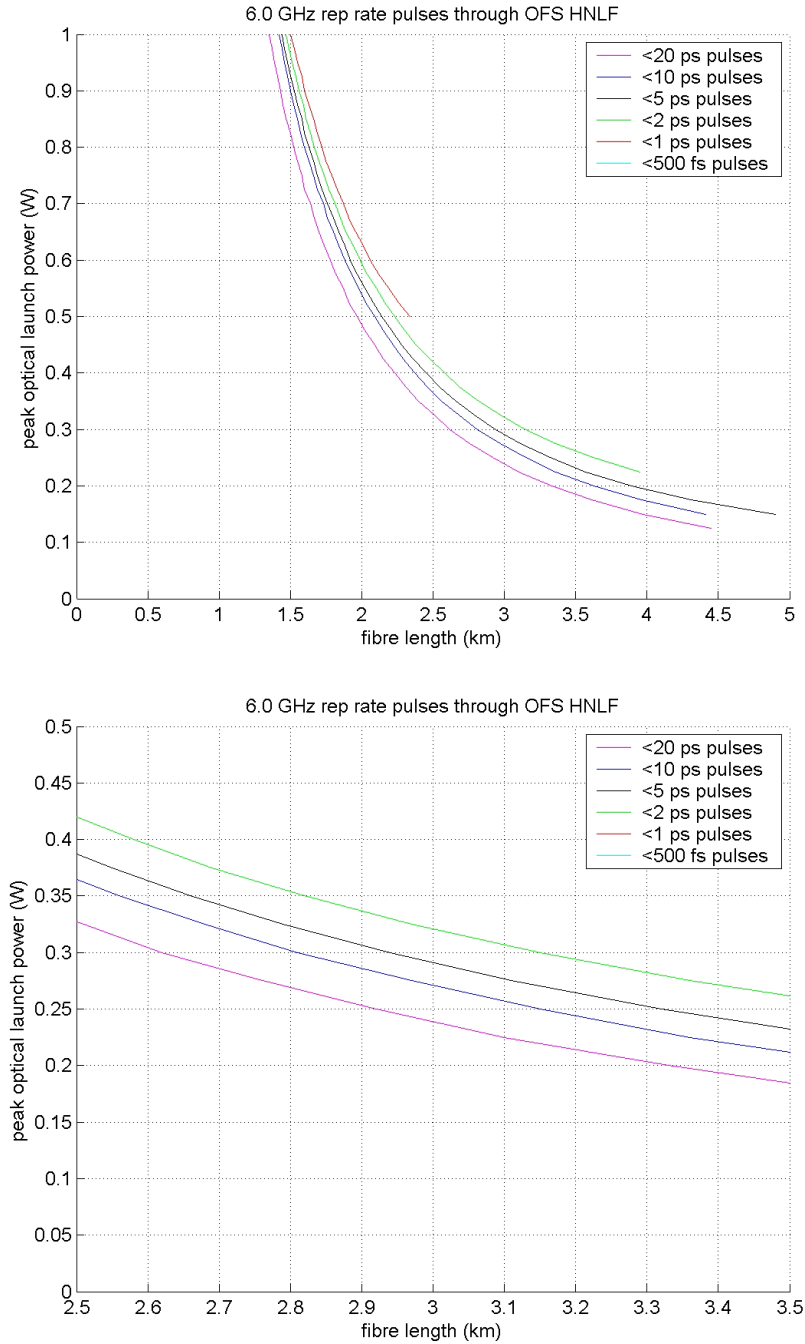


Fig. 11.2. OFS Furukawa highly non-linear fibre modelled performance. Upper plot shows pulse performance over the range 0-1 Watts and 0-5 km. The lower plot shows the region of optimum pulse performance for the SIPOD application.

OFS Furukawa highly non-linear fibre HNLF modelling summary:

- 3 km and ~330 mW peak launch power are predicted to provide <2 ps pulses.
- This fibre can be supplied on a compact 200x200x20 mm reel.

Sumitomo highly non-linear fibre

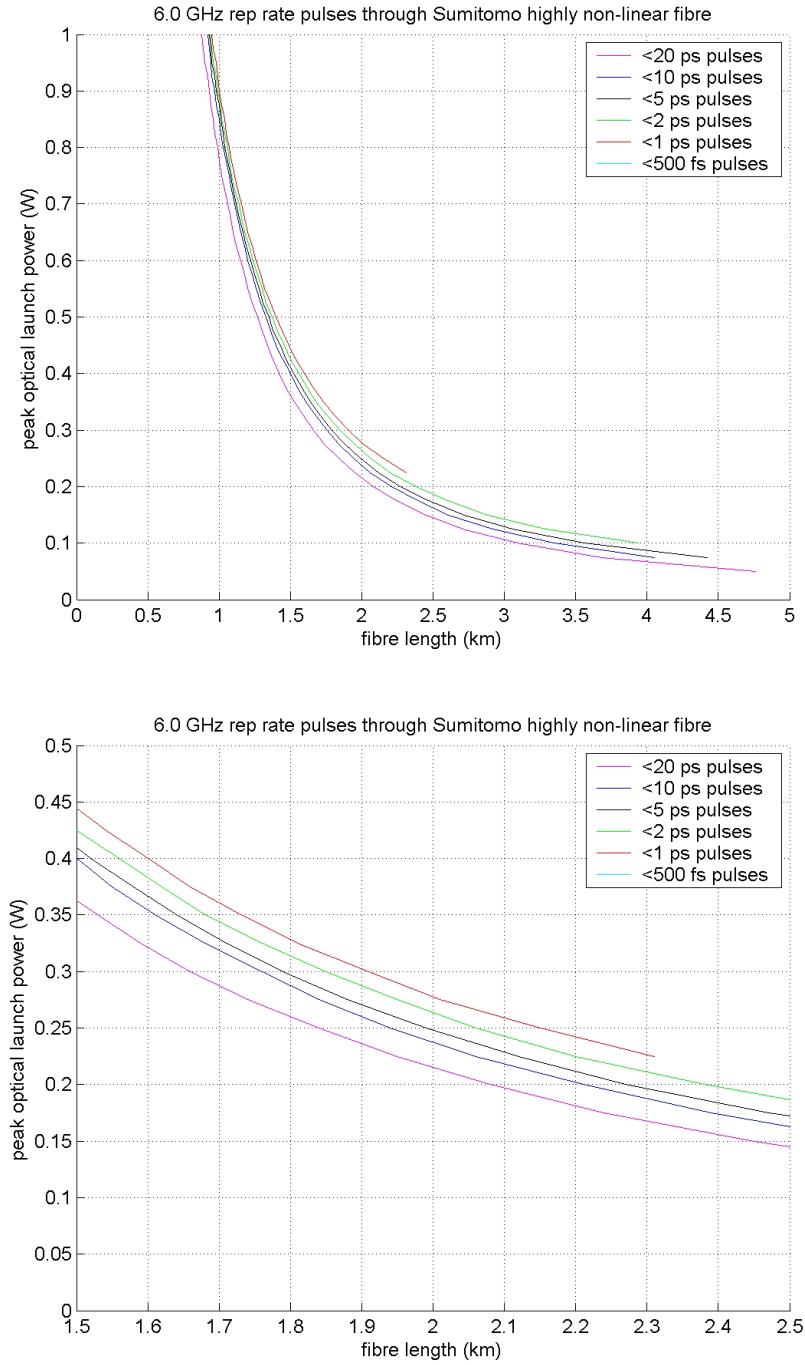


Fig. 11.3. Sumitomo highly non-linear fibre modelled performance. Upper shows the pulse performance over the range 0-1 Watts and 0-5 km. The lower plot shows the region of optimum pulse performance for the SIPOD application.

Sumitomo highly non-linear fibre HNLF-B modelling summary:

- 2 km and ~270 mW peak launch power are predicted to provide <1 ps pulses.
- The fibre can be supplied on a compact reel of 170x170x20 mm.

Fibercore speciality fibres

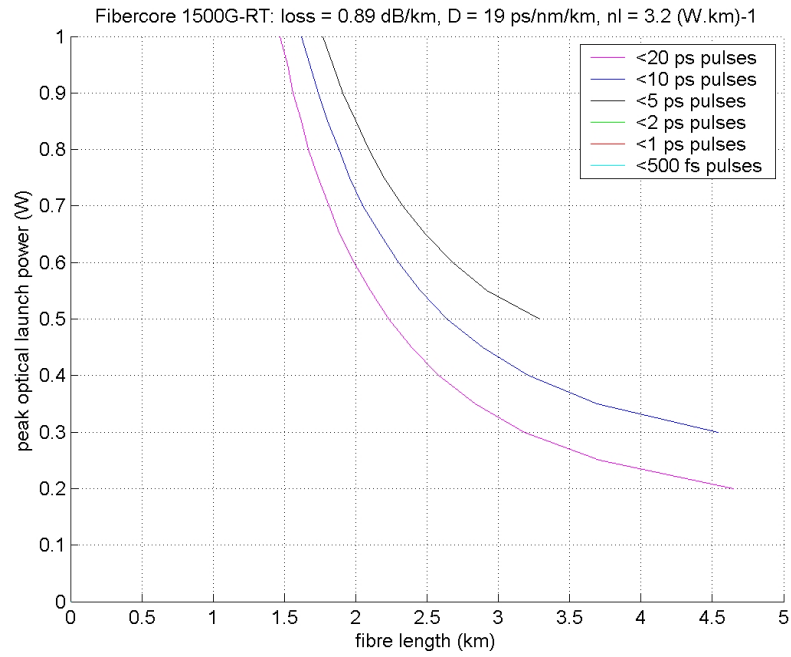


Fig. 11.4. Modelled performance for Fibercore's radiation tested, polarisation maintaining fibre.

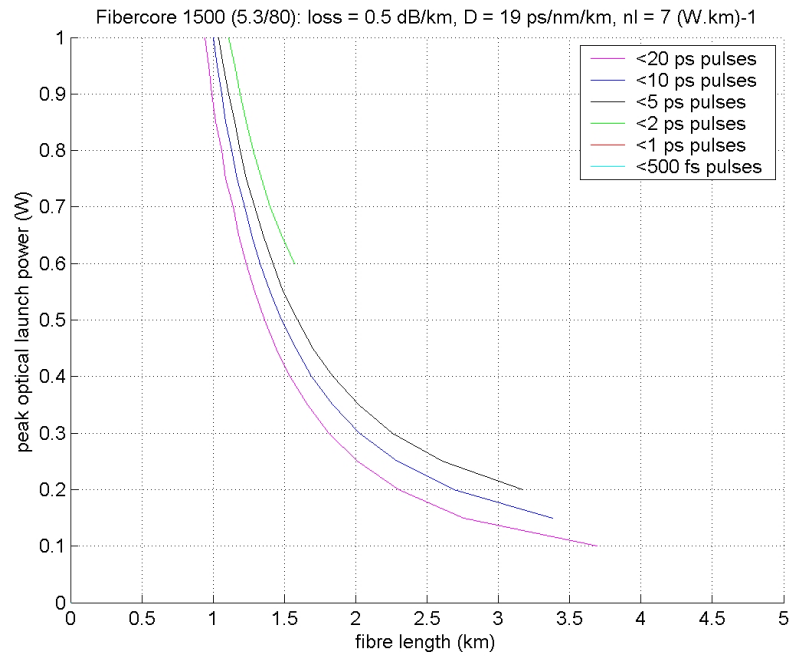


Fig. 11.5. Modelled performance for Fibercore's 1500 (5.3/80) reduced core ($5.3 \mu\text{m}$) and cladding ($80 \mu\text{m}$) fibre.

11. Design of an optimised SIPOD compression fibre

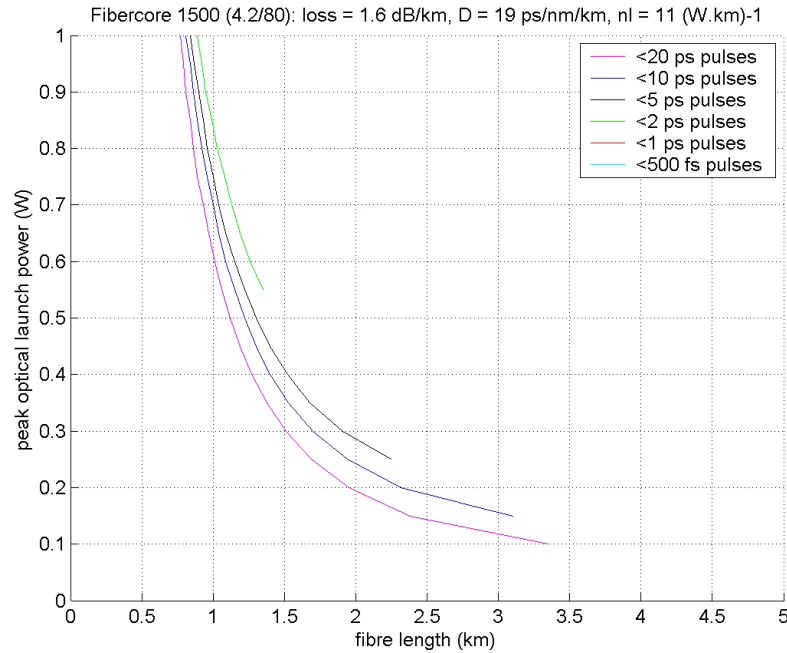


Fig. 11.6. Modelled performance for Fibercore's 1500 (4.2/80) reduced core (4.2 μm) and cladding (80 μm) fibre.

Fibercore HB1500G-RT modelling summary:

- Attractive fibre properties include polarisation maintaining and radiation tested.
- Pulses do not compress particularly well due to low non-linear coefficient of only 3.2 W.km^{-1} .
- 2.5 km and 430 mW peak powers achieve <20 ps pulses.

Fibercore 1500 (5.3/80) summary:

- 2.5 km and 270 mW peak power are predicted to provide <5 ps pulses
- Reduced cladding of 80 microns reduces reel weight.
- Low loss of 0.5 dB/km compensates for modest non-linear coefficient of 7 W.km^{-1} .
- Not polarisation maintaining and not radiation tolerant composition.

Fibercore 1500 (4.2/80) summary:

- 2.5 km and 200 mW peak power are predicted to provide <10 ps pulses.
- Reduced cladding of 80 microns reduces reel weight.
- Higher non-linear coefficient of 11 W.km^{-1} and relatively low loss of 1.6 dB/km provides compression at modest lengths and peak powers; 2.5 km and 200 mW peak powers provide <10 ps pulses.
- Not polarisation maintaining and not radiation tolerant composition.

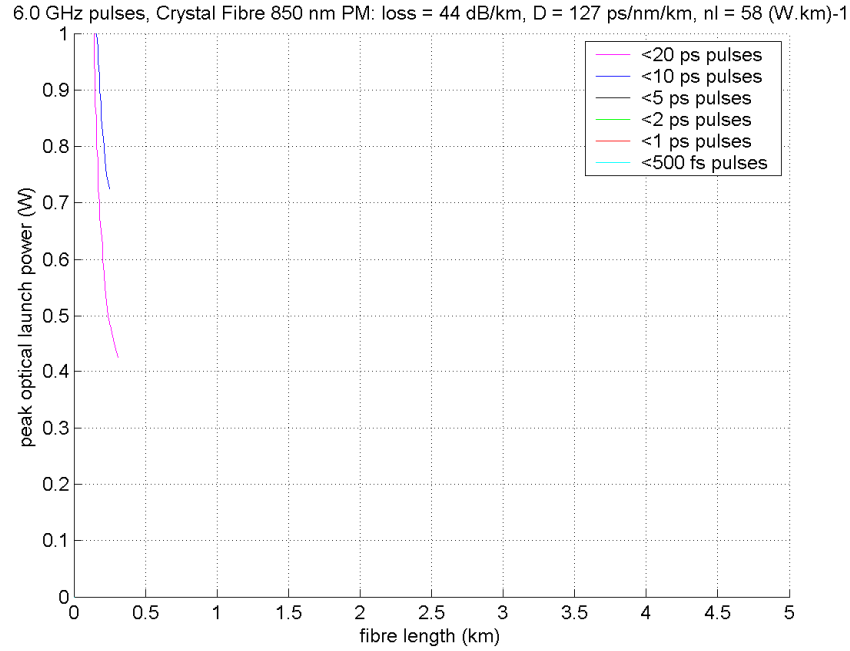
Crystal Fibre highly non-linear photonic fibre

Fig. 11.7. Crystal Fibre's photonic crystal fibre is optimised for use at 850 nm, although the manufacturer provides fibre specifications for use at 1550 nm.

Crystal Fibre's commercially available standard products do not currently meet the aims of the SIPOD system. Their 1550 nm fibre, NL-1550-POS-1, is polarisation maintaining and possesses a fairly high non-linear coefficient of 11 W.km^{-1} , however the high loss of 9 dB/km means that it does not provide any satisfactory pulse compression. A second polarisation maintaining fibre is designed for use at 850 nm, although parameters for use at 1550 nm are provided; the loss (44 dB/km), dispersion (127 ps/nm/km) and non-linear coefficient (58 W.km^{-1}) are all extremely high at 1550 nm, however <20 ps pulses are predicted from only ~300 metres of fibre, for a peak launch power of ~430 mW.

11. Design of an optimised SIPOD compression fibre

Table 11.2 provides a summary of commercially available highly non-linear fibre options with the predicted minimum pulse widths and corresponding fibre lengths required.

Fibre manufacturer & brand/model	Attenuation (dB/km)	Non-linear coeff. (W.km) ⁻¹	Dispersion parameter (ps/nm/km)	Approx. length required	Approx. weight	Lead time & approx. cost	Min. pulse width & required peak power
Corning SMF-28 (arrangement 1)	0.21	1.3	15.5	25 km	>2 kg	4 weeks ~£1k	~10-15 ps 120 mW
Corning SMF-28 (arrangement 2)	0.21	1.3	15.5	4 km	300 grams	4 weeks <£1k	<20 ps 430 mW
OFS highly non-linear fibre HNLF	<0.9	11.5	-2.5 to 3.0	3 km	250 grams	4-5 weeks £8.7k	<2 ps 330 mW
Sumitomo highly non-linear fibre HNLF-B	<0.9	~26	3.0	2 km	200 grams	4-5 weeks £8.5k	<1 ps 270 mW
Fibrecore radiation tolerant PM fibre	0.9	3.2	19	4 km	300 grams	2-4 weeks £8k	<20 ps 450 mW
Fibercore 1500 (5.3/80)	0.5	7.0	19	2.5 km	200 grams	2-4 weeks £4.5k	<5 ps 280 mW
Fibercore 1500 (4.2/80)	1.6	11.2	19	2.5 km	200 grams	2-4 weeks £4.5k	<10 ps 200 mW
Crystal Fibre NL-1550-POS-1	<9.0	11.0	<1.5	n/a	-	-	no compression
Crystal Fibre PM-NL-3.0-850 (PM)	44	58	127	300 m	<100 grams	-	<20 ps 430 mW
Crystal Fibre PM-NL-3.0-1550 (PM)	TBC	TBC	TBC	100's m	<100 grams	R&D programme	TBC

Table 11.2. Summary of commercially available compression fibre options.

11.3 Modelling custom manufactured fibres

One of the strong attractions of using a photonic crystal fibre is that at least the core, and often the whole fibre, is fabricated entirely from silica (SiO_2) and does not comprise any doping. Therefore it is considered to be inherently radiation immune^[2].

This section investigates the ideal parameters for a custom photonic crystal fibre draw. The three main fibre parameters of non-linear coefficient, fibre attenuation and the dispersion parameter were each varied in turn while the other two were held constant. In each case, the parameters which generated pulses as short as $<5\text{ps}$ and $<2\text{ps}$ were plotted.

Non-linear coefficients greater than the Sumitomo HNLF fibre non-linear coefficient were investigated in Fig.11.6, with γ set as 40, 60 and 80 W.km^{-1} . For low loss and a low dispersion parameter (1 dB/km and 4 ps/nm/km respectively), pulses with durations $<2\text{ ps}$ can be generated for peak launch powers as low as $\sim 100\text{ mW}$, for fibre lengths between 2 km and 3 km, Fig. 11.8.

11. Design of an optimised SIPOD compression fibre

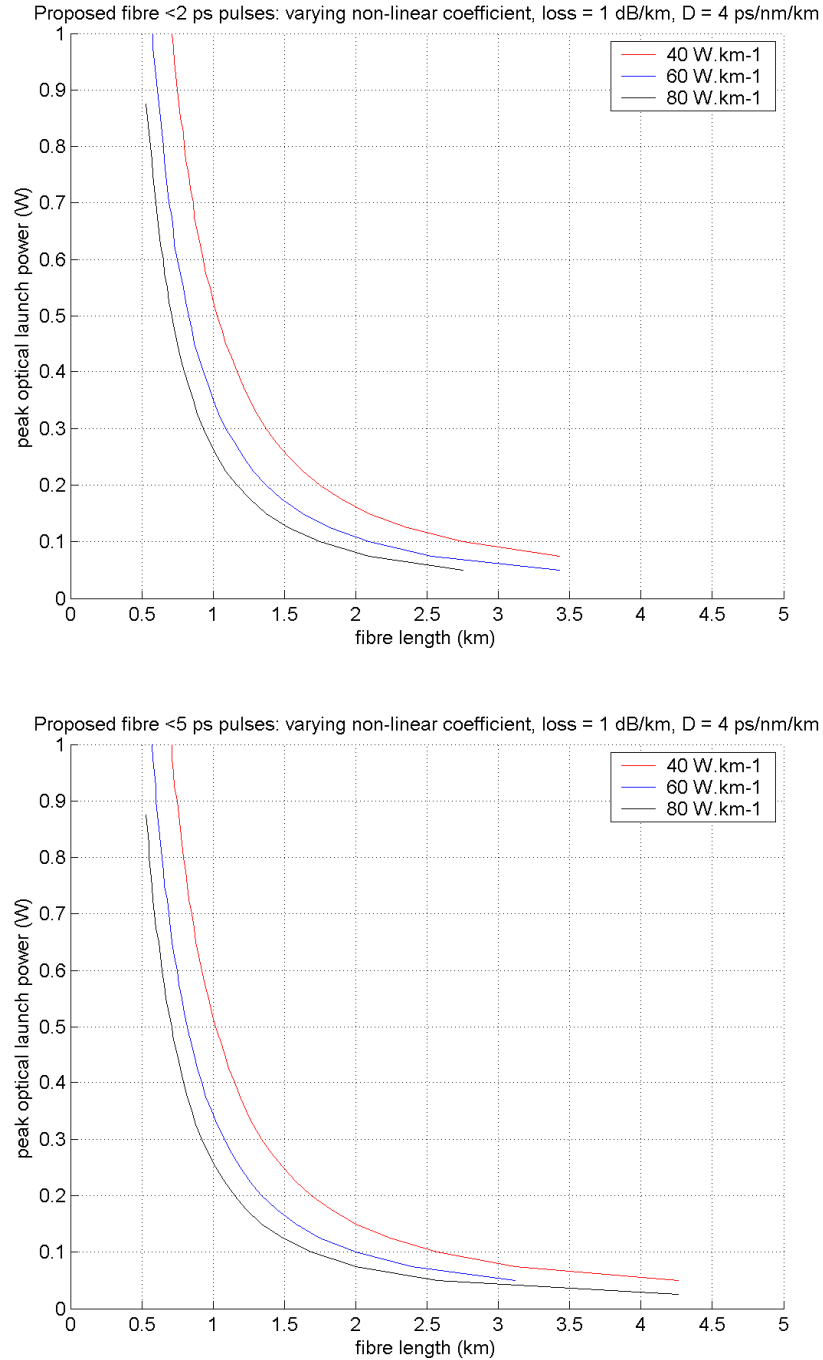


Fig. 11.8. Varying the non-linear coefficient, while keeping the loss and dispersion constant at relatively low values of 1 dB/km and 4 ps/nm/km respectively. The upper plot shows the peak power and fibre lengths which provide <2 ps pulse durations for the 3 values of non-linear coefficient, and the bottom plot shows the parameters which provide <5 ps pulses.

The fibre attenuation is varied in Fig. 11.9, for values 1, 3, 6.5 and 10 dB/km, while the non-linear coefficient and dispersion parameter remain constant at 40 W.km⁻¹ and

11. Design of an optimised SIPOD compression fibre

4 ps/nm/km respectively. It is apparent that increasing the fibre attenuation is highly detrimental in terms of the peak launch power required to generate short pulses. For 10 dB/km loss the required peak powers are unacceptably high at ~900 mW.

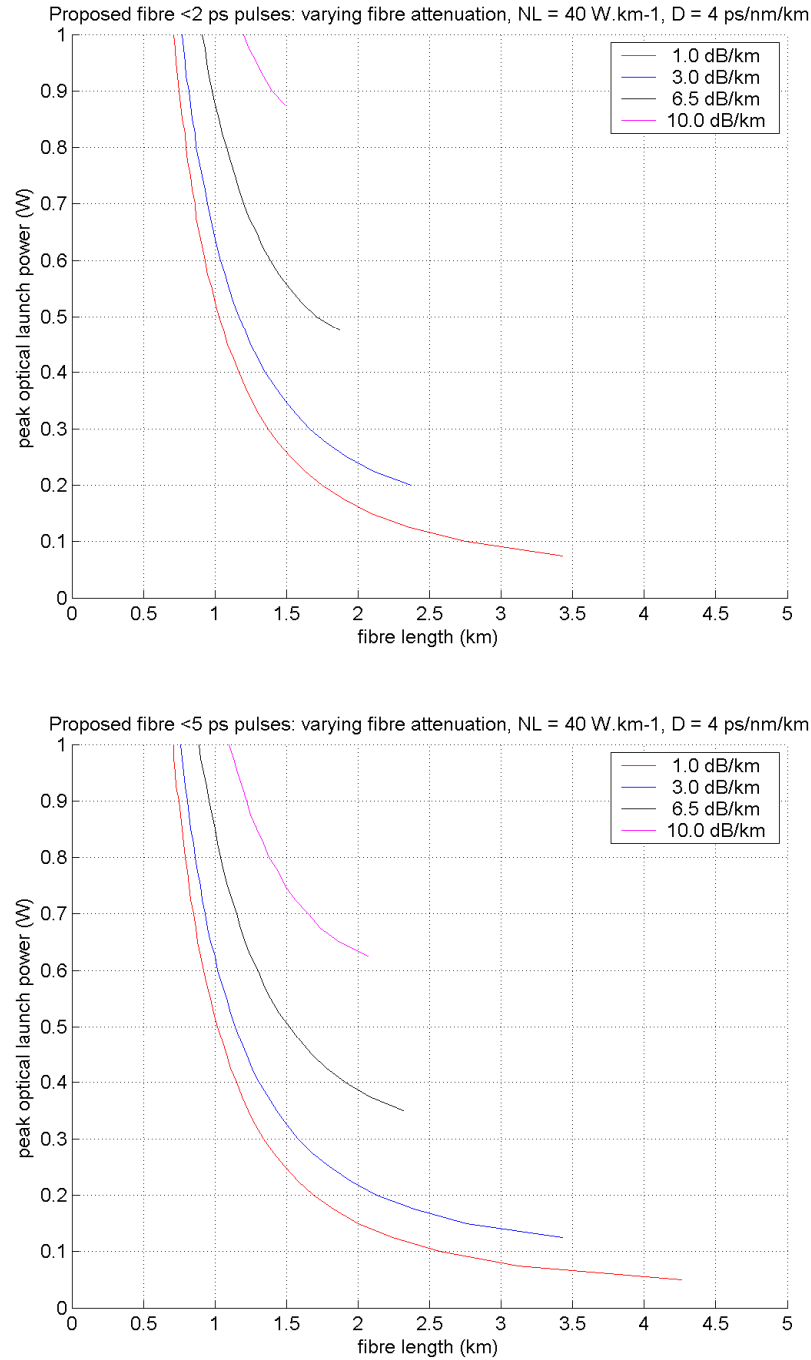


Fig. 11.9. Varying the fibre attenuation, while keeping the loss and dispersion parameter constant at 1 dB/km and 40 W.km⁻¹ respectively. The upper plot shows the peak power and fibre lengths which provide <2 ps pulse durations for the 3 values of fibre attenuation, and the bottom plot shows the parameters which are predicted to provide <5 ps pulses.

11. Design of an optimised SIPOD compression fibre

The dispersion parameter is varied in Fig. 11.10, with D set to 5, 15 and 25 ps/nm/km, while the loss and non-linear coefficients were held constant at 1 dB/km and 40 W.km⁻¹ respectively.

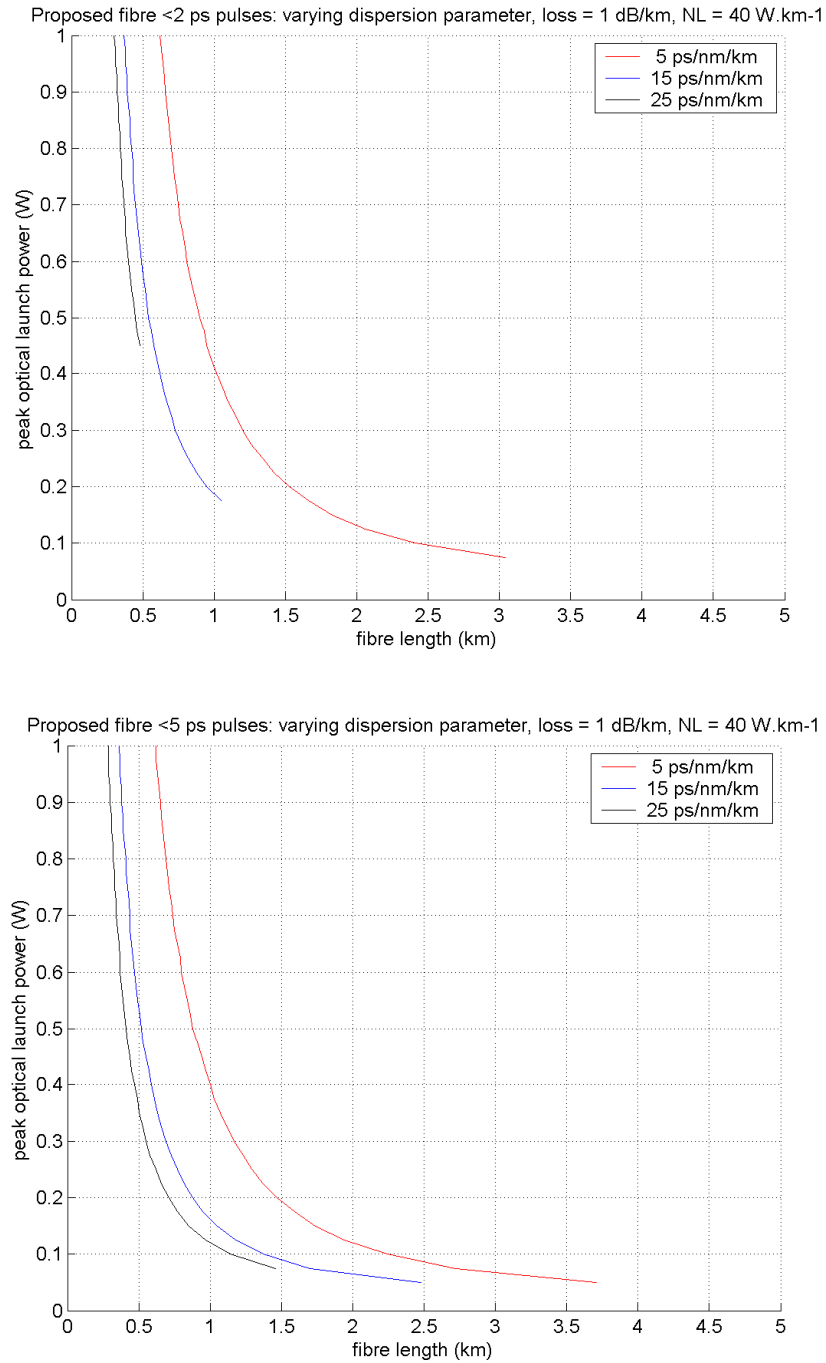


Fig. 11.10. Varying the dispersion parameter, while keeping the loss and non-linear coefficient, constant at 1 dB/km and 40 W.km⁻¹ respectively. The upper plot shows the peak power and fibre lengths which provide <2 ps pulse durations for the 3 values of dispersion parameter, and the bottom plot shows the parameters which are predicted to provide <5 ps pulses.

Increasing the dispersion parameter D reduces the fibre length required to realise <5 ps pulses (lower plot in Fig. 11.10), but it does also increase the power required to generate <2 ps pulses (upper plot in Fig. 11.10). Therefore, a trade-off exists between whether lower power or lower weight/volume is preferable for the pulse source application. The weight of 1 km of bareunjacketed fibre is only of the order 100 grams, so a saving of 1 km fibre length is generally fairly negligible in terms of weight reduction, making launch power the seemingly more critical parameter.

If the peak power requirement can be reduced enough, then in the ideal case it would remove the need for optical amplification (the EDFA), thus substantial cost, power and weight savings may be realised. If a narrow linewidth single-mode laser could be sourced which could provide ~ 125 mW output power, and an intensity and phase modulator with a total insertion loss of 4 dB provided SBS suppression and a periodic input waveform, then the resulting peak launch power into the compression fibre would be ~ 50 mW, meeting the peak power predictions required in Fig. 11.8 to generate <5 ps pulses. There would therefore be no requirement to use an EDFA to provide amplification. Low insertion loss modulators exist (e.g. Eospace Inc. manufacture <2 dB insertion loss LiNbO_3 modulators^[3]), and highly stable single-mode lasers exist at 1550 nm which can provide of the order 125 mW optical power^[4]. Therefore if a custom fibre could be manufactured with a non-linear coefficient $\geq 40 \text{ W.km}^{-1}$, an attenuation coefficient of $\leq 1 \text{ dB/km}$ and a dispersion parameter of the order 5-15 ps/nm/km, then <5 ps pulses could be achieved without the need for an EDFA to provide optical amplification prior to launch into the compression fibre. Similarly, Fig. 11.3 predicts that the Sumitomo highly non-linear fibre can provide <20 ps for 4.5 km of fibre, without the need for an EDFA in the pulse generation arrangement, assuming a 125 mW output power laser and 4 dB total insertion loss phase and intensity modulators.

11.4 Summary of highly non-linear fibre modelling

Corning's SMF-28 has already been shown to generate compressed pulses of duration 10-15 ps through 25 km. Over the modelling range of 0-1 Watts and 0-5 km, the optimum peak launch power and fibre length arrangement predicted by the modelling

for SMF-28 is 4 km and 430 mW to achieve <20 ps pulses at a 6 GHz repetition rate. In this case, the total fibre weight would be 300 grams or less (compared to ~ 2 kg at present).

The commercially available photonic crystal fibres made by Crystal Fibre suffer from very high losses. Many photonic crystal fibres were investigated, although the results were not detailed in this chapter as they predicted unsatisfactory pulse performance. Crystal Fibre's commercially available highly non-linear fibre designed for 1550 nm proved to be unsuitable as the pulses do not compress satisfactorily before the high attenuation of 9 dB/km dominates, at which point non-linear effects are negligible. The second Crystal Fibre product modelled (PM-NL-3.0-850) is primarily designed for use at 850 nm, although this fibre is still usable at 1550 nm, albeit with exceptionally high losses of 44 dB/km. The non-linear coefficient and dispersion parameters are also particularly high for a fibre, at 58 (W.km)^{-1} and 127 ps/nm/km respectively. However, for short lengths (less than 100 metres) and high peak launch powers of 2 Watts, the high non-linear coefficient is predicted to generate pulses of <2 ps duration. This launch power is unacceptably high given a rule-of-thumb electrical-to-optical conversion efficiency of 10% from an EDFA (corresponding to 20 Watts electrical consumption).

In terms of short pulse durations, the most promising fibres investigated to date are the OFS (Furukawa) HNLF (highly non-linear fibre) and Sumitomo's HNLF-B. A combination of 3 km of the OFS (Furukawa) fibre and 300 mW optical peak launch power are predicted to achieve <2 ps pulses at 6 GHz. Better still is the Sumitomo HNLF-B fibre which is predicted to provide sub-picosecond pulses for 2.5 km of fibre and peak launch powers of 270 mW. Either of these fibres offers significant pulse compression and weight reduction when compared to SMF-28. Both fibres can be supplied on compact reels by the manufacturer. Neither of these fibres are polarisation maintaining which means active polarisation control is required prior to launch into the optical interferometer head.

A custom photonic crystal fibre draw would be highly attractive since it would be inherently radiation immune due to the core being wholly fabricated of silica, and it can also be made to be polarisation maintaining. A non-linear coefficient greater than 40 W.km^{-1} , with a dispersion parameter around 5 ps/nm/km and as low fibre attenuation

as possible, certainly <5 dB/km, would provide usefully compressed pulses with low launch peak power requirements of <200 mW. Optimum fibre parameters of $\gamma > 40$ W.km⁻¹, $\alpha \leq 1$ dB/km and $D \sim 10$ ps/nm/km could eventually remove the need for optical amplification prior to launch into the compression fibre, with the benefits of reduced system weight and potentially much lower jitter due to the removal of the optical amplifier ASE and potential Gordon-Haus jitter problems.

The final decision for compression fibre selection for the ESA programme was based on several mission factors. Firstly, to avoid the requirement to perform active control of the polarisation launched into the optical interferometer head throughout the 2 year mission cycle, it was considered essential that the compression fibre was polarisation maintaining. All other SIPOD system components are polarisation maintaining and it significantly de-risks the system if the compression fibre is also PM to remove the possibility that the active polarisation control fails for some reason. Therefore, the Sumitomo and Furukawa highly non-linear fibres were discounted, as those manufacturers do not appear to have heritage of drawing long lengths of radiation tolerant PM speciality fibre. Although the commercial offerings supplied by Fibercore possess lower non-linear coefficients than the Sumitomo and Furukawa fibres, the company specialise in polarisation maintaining fibre and have already supplied ESA with radiation tolerant fibres for space-based gyroscopes. Fibercore are also a UK based company, a fact which was anticipated to make interactions regarding custom fibre draws easier. Therefore, due to Fibercore's experience regarding radiation hardening fibre and their polarisation maintaining fibre pedigree, they were selected as the supplier to provide a custom polarisation maintaining compression fibre for the SIPOD system. Given the complexity involved in manufacturing PM fibres, particularly involving unusual radiation tolerant fibre material mixtures (i.e. with no phosphorous to aid the molten glass flow), the fibres may possess higher attenuation than planned due to leakage from the boron stress rods which provide the PM properties. Since the SIPOD system has already demonstrated range resolution measurements in excess of its target specifications using 10-15 ps pulses, a target of 10-20 ps pulse durations after 2.5 km of radiation tolerant PM fibre was agreed. Such a fibre would allow SIPOD to demonstrate sub-10 micron range resolution and would impose the most feasible specifications for a

successful draw of a custom, polarisation maintaining, highly non-linear fibre which is robust to radiation effects.

11.5 Experimentally verifying model with Fibercore's reduced core fibres

Prior to ordering a custom fibre draw for a radiation robust, PM compression fibre, a de-risking exercise was undertaken to verify the pulse modelling, by experimentally testing two different non-PM fibres with small cores (5.3 and 4.2 microns) manufactured by Fibercore.

In order to insert the reduced cladding fibre into the pulse compression system, it was necessary to splice 9 micron core diameter pigtails onto the compression fibre reel, using a Vytran splicer at QinetiQ. This was achieved with an input splice loss of 1.5 dB for the 5.3 micron core diameter fibre and 3.8 dB input loss for the 4.2 micron core diameter fibre, Fig. 11.11. Comparable output splice losses were observed, with the lowest loss splice being selected as the input. A couple of iterations may initially be required to determine the correct splice settings, Fig. 11.12.

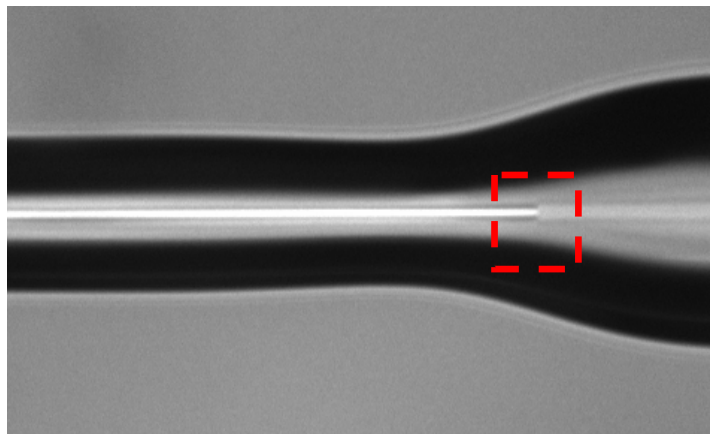


Fig.11.11. Example of successfully splicing a 9 micron core pigtail onto a reduced core compression fibre. Losses of the order 1.5 dB were observed for the 5.3 micron core fibre and 3.8 dB for the 4.2 micron fibre. The mis-matched core diameter interface can be seen inside the red dashed box. There is also clearly a cladding mis-match (125 μm and 80 μm).

11. Design of an optimised SIPOD compression fibre

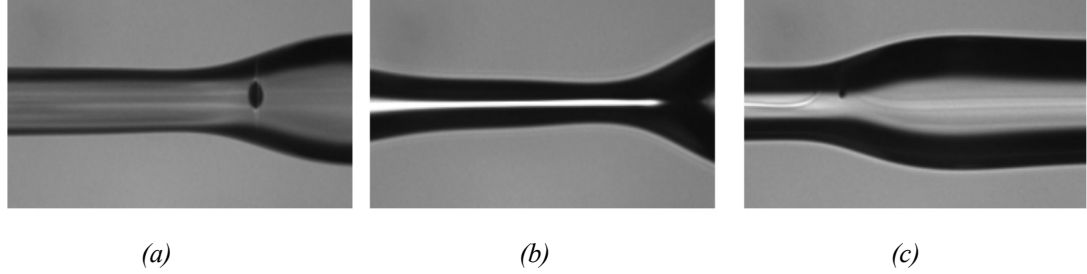


Fig. 11.12. Example of three different failed splice attempts; (a) air bubble present, (b) too hot a burn and (c) corrupted core.

The nonlinear coefficients of the two Fibercore fibres are increased relative to the 1.3 W.km^{-1} of Corning's SMF-28, due to the reduced core size (and hence reduced A_{eff}) and also increased germanium doping leading to an increase in n_2 by a factor of around 1.4. The non-linear coefficient, γ , is given by

$$\gamma = \left(\frac{n_2(\omega_0)\omega_0}{cA_{\text{eff}}} \right) \quad \begin{array}{l} A_{\text{eff}} = \text{effective area} \\ n_2 = \text{nonlinear index coefficient} \\ \omega_0 = 2\pi c/\lambda \end{array} \quad (11.1)$$

Figs. 11.14-11.17 show the compression of the optical pulses, at the 6 GHz nominal SIPOD repetition rate, through 4 different fibres:

- 25 km of Corning's SMF-28
- 2.5 km of Fibercore's RT-1500G radiation tested polarisation maintaining fibre
- 2.5 km of Fibercore's 1500 (5.3/80) reduced core (non-PM)
- 2.5 km of Fibercore's 1500 (4.2/80) reduced core (non-PM)

The highest bandwidth sampling oscilloscope available to the project was an hp 54120B with a 34 GHz sampling head. Typically this only allows pulse widths to be resolved to the order of 20-25 ps. Therefore the SIPOD system itself was used to measure pulse compressions for the reduced core fibres, acting in effect as an autocorrelator.

The propagation of 6 GHz pulses was investigated through 25 km of SMF-28. Single peak pulses were observed on the hp 54120B oscilloscope for peak launch powers of the order 120 mW, and double peaks were observed as the peak launch power was increased to around 310 mW, Fig. 11.13. These values match modelled predictions.

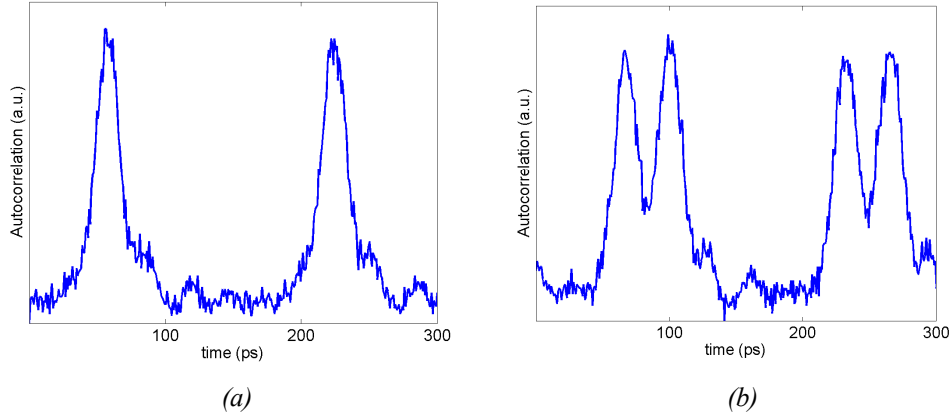


Fig. 11.13. High-speed sampling oscilloscope traces demonstrating that as the input launch power is increased, the 6 GHz pulses become multi-peaked through 25 km of SMF-28. The oscilloscope sampling head has a bandwidth of 34 GHz. Peak launch powers (a) 120 mW and (b) 310 mW.

The SIPOD system was used to obtain “autocorrelation” scans of the pulses generated at a nominal 6 GHz repetition rate through 25 km of SMF-28, Fig. 11.14. Each peak-to-peak spacing represents a 6 GHz time slot, i.e. 167 ps, allowing an estimation of the pulse width. As with any autocorrelation method, calculating the actual pulse width relies on knowing the pulse shape, however a scaling factor of 1.54 was assumed for these pulses since the mathematical solution for optimum pulse compression using soliton-effect compression is a soliton, i.e. a sech waveform. By increasing the launch power, the pulse compression is visible apparent on the SIPOD scans, and sidelobes representing double-peaked pulses appear at the launch powers predicted by the modelling and observed using the high-speed sampling oscilloscope. Note that a glitch is visible on Figs. 11.14-11.17, at approximately 270 ps. SIPOD generates these “autocorrelation” plots by scanning the pulse repetition rate through a range of frequencies around the nominal 6 GHz master frequency. The glitch occurs when the scan frequency passes through the nominal 6 GHz master frequency.

11. Design of an optimised SIPOD compression fibre

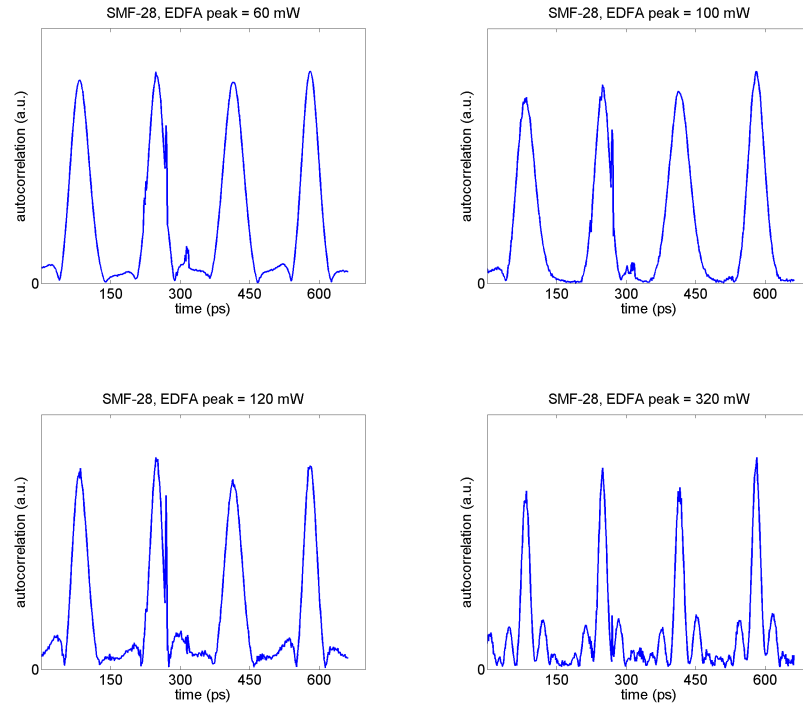


Fig. 11.14. Corning's SMF-28. "Autocorrelation" traces captured using the SIPOD system, for varying peak input powers. The peak-to-peak spacing is 167 ps (corresponding to the 6 GHz repetition rate). The pulses are optimum at a peak launch power of around 110-120 mW. The sidelobes for 320 mW indicate that the pulses have become double-peaked.

Replacing the SMF-28 with 2.5 km of Fibercore's radiation tested polarisation maintaining fibre RT-1500G, Fig. 11.15, it is evident that very little compression occurs, even when launching a peak power as high as 450 mW. The previous modelling, Fig. 11.4, suggested that pulses as short as ~20 ps should be possible with around 430 mW and 2.5 km, however this was not observed. It may be that the pigtail splicing losses for this reel was underestimated in the model or simply that the model used the wrong fibre parameters. The fact that no significant compression occurred, even for high peak powers of 450 mW, indicates that a non-linear coefficient of 3 W.km^{-1} is not suitable for this application when using short fibre lengths.

11. Design of an optimised SIPOD compression fibre

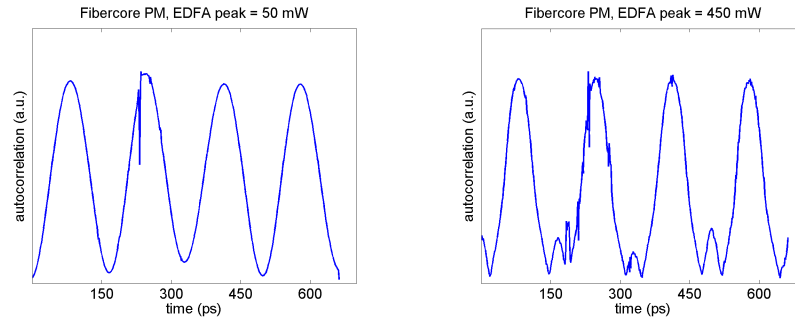


Fig. 11.15. Fibercore 1500G-RT. “Autocorrelation” traces captured using the SIPOD system for varying peak input powers. The peak-to-peak spacing is 167 ps (corresponding to the 6 GHz repetition rate). Visually, minimal compression is observed, even for 450 mW peak powers. Fibre length = 2.5 km.

The next fibre tested was a 2.5 km reel of reduced core diameter (5.3 microns) non-PM fibre manufactured by Fibercore. In this case, significant pulse compression can be observed, Fig. 11.16, with optimum compression found for peak launch powers of around 340 mW. This compares reasonably favourably with the ~280 mW peak predicted by the modelling.

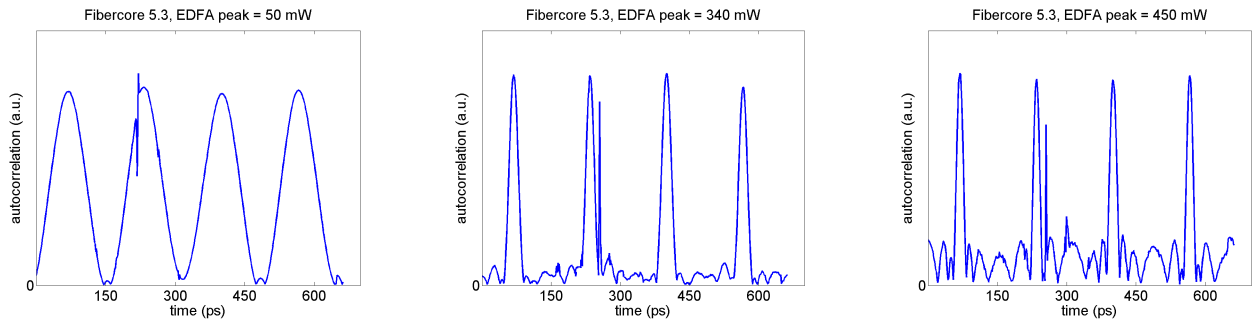


Fig. 11.16. Fibercore 1500 (5.3/80). “Autocorrelation” traces captured using the SIPOD system for varying peak input powers. The peak-to-peak spacing is 167 ps (corresponding to the 6 GHz repetition rate). The pulses are optimum at ~340 mW peak power, with multi-peak artefacts present at 450 mW peak launch power. Fibre length = 2.5 km.

The final fibre which was experimentally tested was a second 2.5 km reel of reduced core diameter non-PM fibre manufactured by Fibercore. This reel has a 4.2 micron core diameter (smaller than the 5.3 micron core employed in Fig. 11.16). Again significant pulse compression can be observed, Fig. 11.17, with optimum compression found for peak launch powers of around 250 mW. As with the 5.3 micron diameter core fibre, the required peak power is slightly higher than the ~200 mW peak predicted by the modelling. The increased powers required may be due to the fact that the model

11. Design of an optimised SIPOD compression fibre

assumes a perfect idealised cylindrical waveguide and does not accommodate non-uniform fibre geometry and composition along the 2.5 km lengths, nor does the model include the fact that parasitic SBS detrimentally interferes with the pulse evolution with the effect that a few percent of the launch power is backscattered Fig. 11.20, slightly lowering the peak power in the fibre in comparison to the launched peak power and hence reducing the compression effects. Alternatively, the small discrepancy in the power levels may arise from incorrect biasing of the experimental input periodic waveform in comparison to the ideal mathematical waveform used in the model.

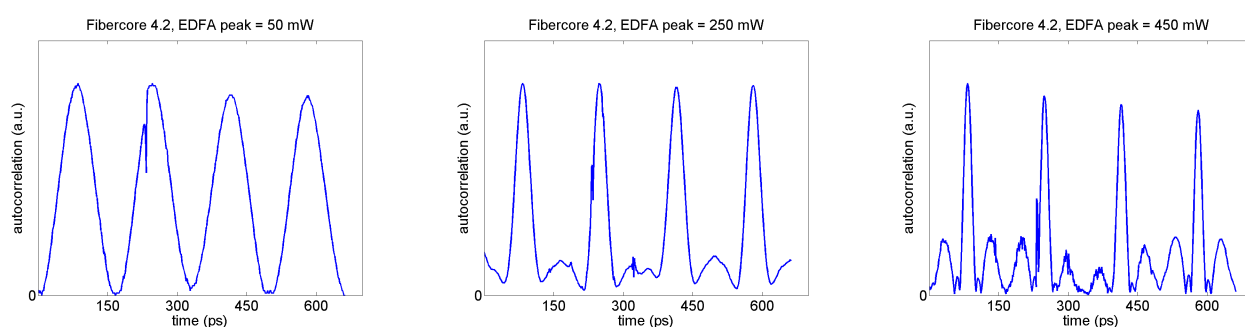


Fig. 11.17. Fibercore 1500 (4.2/80). “Autocorrelation” traces captured using the SIPOD system for varying peak input powers. The peak-to-peak spacing is 167 ps (corresponding to the 6 GHz repetition rate). The pulses are optimal for a peak power around 250 mW. When the power is increased further to 450 mW peak power, multi-peak artefacts are present. Fibre length = 2.5 km.

Fibre	Radiation robust	Polarisation maintaining	Length (km)	Peak power (mW)		Pulse FWHM (ps)		
				Modelled	Experimental	Modelled	SIPOD (raw)	SIPOD (corrected)
Corning SMF-28	No	No	25.2	120	~120	<20	29.7	19.3
Fibercore RT-1500G	Yes	Yes	2.5	450	~450	<20	64.0	41.8
Fibercore (5.3/80) 1500	No	No	2.5	280	~340	<5	19.5	12.7
Fibercore (4.2 /80) 1500	No	No	2.5	200	~250	<10	33.8	21.9

Table 11.3. Summary of de-risking experimental work, prior to custom compression fibre procurement, detailing experimental and modelled performance for Fibercore’s reduced core diameter fibres, Fibercore’s radiation tested PM fibre and Corning’s SMF-28. Note that the raw SIPOD “autocorrelation” is corrected by a factor of 1.54 to accommodate sech pulse shape.

11.6 SBS implications of smaller core fibres

Ref [1] derives the SBS pump threshold, P_{th} , as

$$P_{th} \approx \frac{21A_{eff}}{g_B L_{eff}} \quad (11.2)$$

where g_B is the peak value of the Brillouin gain (typically $\sim 5 \times 10^{-11}$ m/W for telecommunications fibre) and L_{eff} and A_{eff} are the effective lengths and areas respectively. When reducing the core diameter from 10 microns to 4.2 microns, the effective area A_{eff} and hence the SBS threshold P_{th} is lowered by a factor of around 6. However, the proposed lengths of the higher non-linearity fibres have reduced significantly by a factor of 10 (25 km down to 2.5 km), and so the net effect of the new reduced core compression fibre arrangements on the SBS threshold should be a favourable increase by a factor of around 1.5, compared to SMF-28, if the Brillouin gain g_B does not vary significantly due to different fibre composition.

Fig. 11.18 shows an experimental arrangement for measuring the backscattered light due to SBS, with the measured results expressed in both absolute power and as a percentage of the average launch power, for 6 GHz repetition rate pulses launched into 2.5 km of Fibercore's 4.2 micron reduced core fibre, Fig. 11.20. The average launch power is used as opposed to the peak launch in order to compare the ratio of launch to the backscattered light; the average launch power is approximately 35% of the peak launch power for the biased modulator waveform, Fig. 11.19.

11. Design of an optimised SIPOD compression fibre

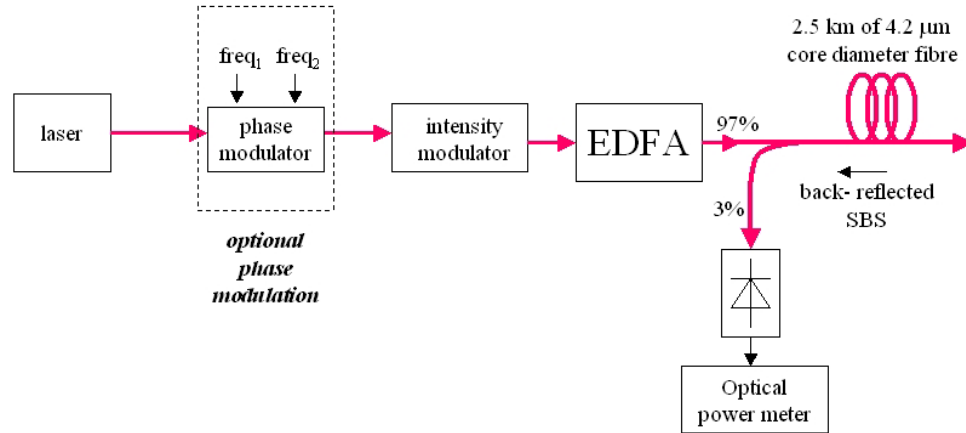


Fig. 11.18. Experimental arrangement to measure SBS for a given EDFA launch power, for 6 GHz pulses launched into 2.5 km of Fibercore's 4.2 micron core diameter fibre.

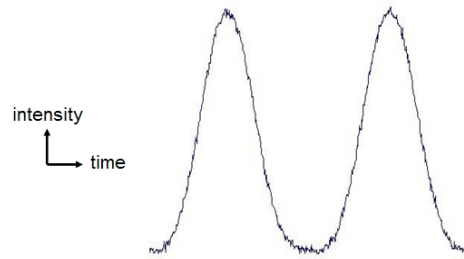


Fig. 11.19. Generic diagram showing a generic oscilloscope capture of launch waveform. The average power is $\sim 35\%$ of the peak launch power into the compression fibre for the biased modulator input waveform, driven by a sinusoid.

Fig. 11.20 shows that significant SBS occurs when no phase modulation suppression is applied to the 6 GHz pulse train, with 30 mW average optical power leading to around 8% on average of the launch power being back-scattered, increasing to over 20% backscattering of the input light as the average launch power increases beyond around 90 mW average launch power. The application of a single frequency phase modulation reduces the SBS significantly for average powers of less than around 160 mW, however beyond this power the backscattered SBS rises to around 10% of the launch power. Using the 35% ratio in Fig. 11.19, an average power of 160 mW corresponds to a peak power of around 450 mW for the intensity modulation regime employed. Therefore the peak launch power should be kept below this threshold value if only one SBS suppression frequency is applied. The application of two asynchronous phase modulation frequencies reduces the SBS level to $<2\%$ of the launch power, even for high average powers of 350 mW (i.e. a peak power of ~ 1 Watt). In practice it is an

undesirable system overhead to have to generate two separate frequencies, particularly when they must be dynamically adjusted to accommodate a specific longitudinal range in the case of the SIPOD system. Therefore it appears that the peak launch powers should be kept lower than around 450 mW, in order that a single frequency phase modulation can be used to satisfactorily suppress SBS. As discussed, the 2.5 km reduced core diameter fibres of 4.2 and 5.3 microns required an optimum peak power below this threshold.

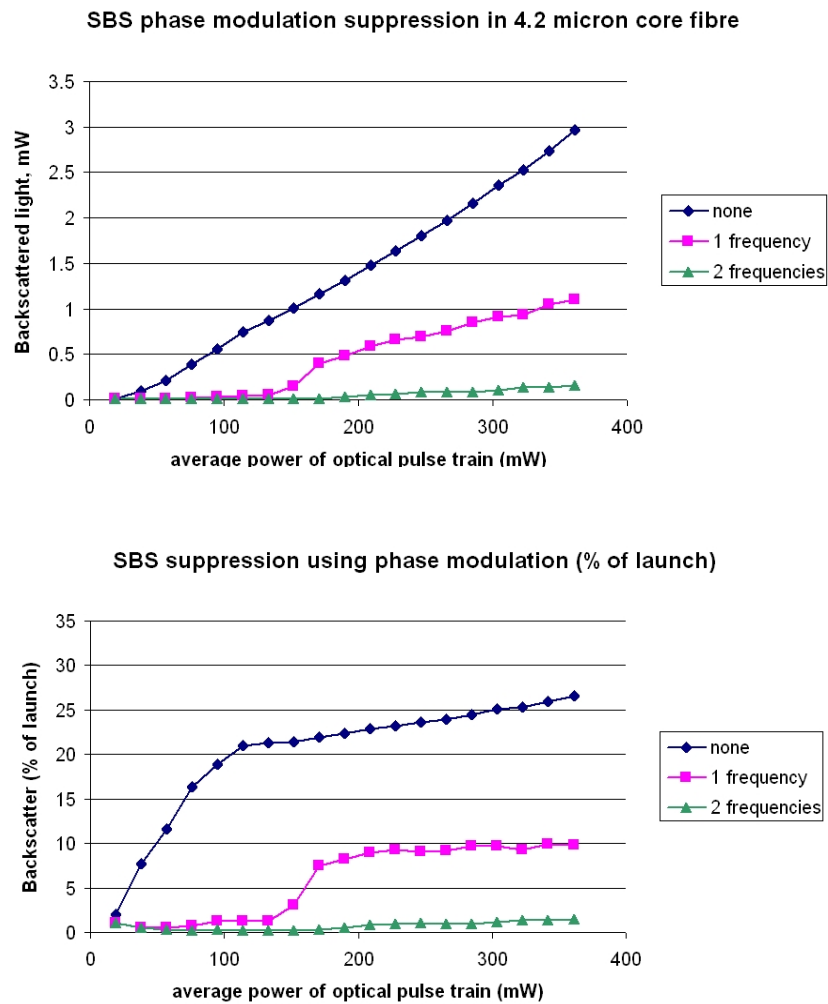


Fig. 11.20. Experimentally observed SBS backscattering, using no phase modulation, a single phase modulation frequency and two different phase modulation frequencies for 4.2 micron reduced core fibre. All plots are for 6 GHz optical pulses through 2.5 km of fibre. Top plot: actual SBS power backscattered. Bottom plot: SBS backscattered as a % of average launch power.

11.7 Summary of compression fibre modelling and experimental de-risking

Speciality fibre manufacturer Fibercore produce commercially available polarisation maintaining fibre, including a radiation robust variant. Previously they have supplied ESA with radiation tolerant fibres for use in gyroscope applications. Fibercore also manufacture reduced core diameter fibres, which provide an increased non-linear coefficient and therefore better pulse compression performance. Two different specification reduced core diameter fibres were obtained on loan from Fibercore for testing in the SIPOD system, neither of which were polarisation maintaining. A 2.5 km length of 5.3 micron core diameter fibre generated 10 ps duration pulses, as measured using SIPOD, a pulse width which has been shown to provide range resolution to better than 5 microns. This fibre has provided the shortest pulses ever generated with the SIPOD pulse compression scheme. The peak launch power in this case was around 340 mW, requiring a modest average optical launch power of around 120 mW. SBS at these power levels can be suppressed using single frequency phase modulation. Based on the experimental performance of this fibre, and similar performance from a higher loss 4.2 micron core diameter fibre, Fibercore were approached to perform a custom draw, which will aim to replicate the reduce core fibre geometries in a new fibre fabricated using the same material composition as Fibercore's radiation tolerant fibres. The output from this custom draw should be a compression fibre which offers weight savings through a ten-fold reduction in length and 60% reduced fibre cross-sectional area (via reduced cladding) compared to the current Corning SMF-28 compression fibre, as well as reduced pulse duration and hence improved range accuracy; all in a fibre which is both polarisation maintaining and radiation robust.

References for Chapter 11

1. G. P. Agrawal, "Nonlinear Fibre Optics", 2nd edition, Academic Press (1995)
2. Girard S., Yahya A., Boukenter A., Ouerdane Y., Meunier J.P., Kristiansen R.E., Vienne G., "Gamma-radiation-induced attenuation in photonic crystal fibre", *Electron. Lett.*, 38(20), pp. 1169-1171, 2002
3. EOSPACE Inc., 8711 148th Avenue NE, Redmond, WA 98052; www.eospace.com
4. NP Photonics Scorpio fibre laser datasheet, retrieved on 10/10/2008 from NP Photonics website: http://www.npphotonics.com/files/products/Laser_Module.pdf

12. Experimental characterisation of a bespoke compression fibre

This chapter discusses the experimental characterisation of a bespoke compression fibre which was designed for the SIPOD system, prior to being custom manufactured by specialist fibre experts Fibercore. The fibre was specified to be phosphorous free to increase radiation tolerance^[1], possess a reduced core size to increase the non-linear coefficient, and to have reduced cladding to reduce the overall weight. It is also polarisation maintaining. The experimental performance of the bespoke compression fibre performance correlates well with modelled predictions. Notably, the fibre has experimentally compressed a 6 GHz pulse train to the order of 10 picoseconds, using peak launch powers of the order of 300 mW, which allows SIPOD range measurements to be made to better than 10 microns resolution.

12.1 Fibre specifications on delivery

Custom fibre specifications, as per Certificate of Conformance supplied by Fibercore:

Fibre type	Fibercore 1500-RT-HI
Attenuation	1.07 dB/km
Mode-field diameter	5.6 microns
Numerical aperture	0.24
Length	3000 metres

Fibercore fusion spliced PM pigtails onto the custom reel prior to shipping. Fibercore measured the splice losses as 1.1 dB and 1.2 dB during this process. The reel + fibre weighed a total of 420 grams. The fibre length was measured as 3020.5 metres using an hp 85107A network analyser at QinetiQ.

12.2 Experimental pulse compression performance

The SIPOD system was used to obtain “autocorrelation” scans of the pulses generated at a nominal 6 GHz repetition rate through the 3 km of Fibercore 1500-RT-HI, Fig. 12.1. Each peak-to-peak spacing represents a 6 GHz time slot, i.e. 167 ps, allowing an

estimation of the pulse width. As with any autocorrelation method, calculating the actual pulse width relies on knowing the pulse shape, however a scaling factor of 1.54 was assumed for these pulses since the mathematical solution for optimum pulse compression using soliton-effect compression is a soliton, i.e. a hyperbolic secant waveform. By increasing the launch power, pulse compression can be observed on the SIPOD scans. Sidelobes representing pulse pedestals appear as the launch powers increase, which is predicted by the modelling, as discussed in Chapter 5. Note that systematic glitches are visible on each of the plots Fig. 12.1; SIPOD generates these “autocorrelation” plots by scanning the pulse repetition rate through a range of frequencies around the nominal 6 GHz master frequency. The glitches occur when the scan frequency passes through the nominal 6 GHz master frequency and at ± 2 MHz offsets corresponding to the heterodyne signal.

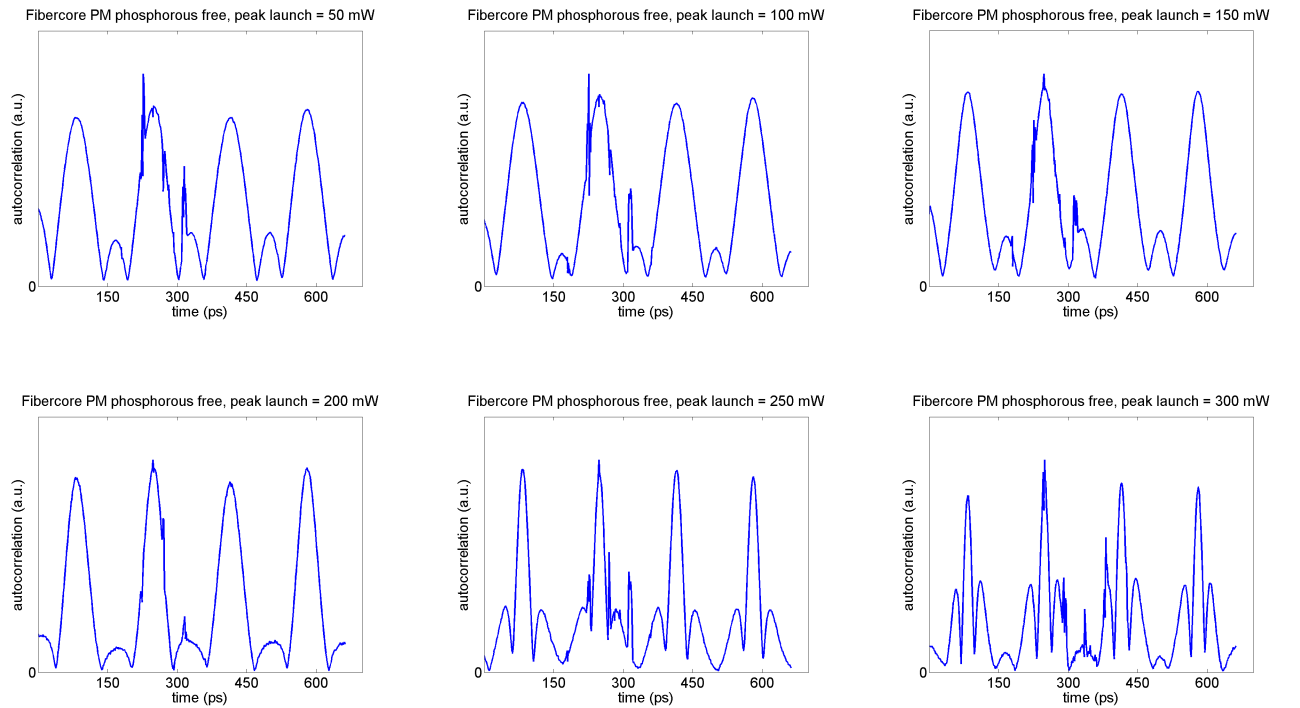


Figure 12.1. “Autocorrelation” plots obtained by scanning the SIPOD pulse repetition rate. Note that significant compression occurs for peak launch powers of around 250 mW and greater.

The pulse full width half maximum (FWHM) values are provided in Table 12.1, for the modelled pulse performance and the experimentally measured pulse performance. Both the raw autocorrelation and the corrected experimental values are given (using the 1.54 correction factor when assuming a sech pulse). Fig. 12.2 shows the excellent correlation between the modelled and corrected experimental pulse widths. The 1.54 correction

12. Experimental characterisation of a bespoke compression fibre

factor does indeed appear to be appropriate as the pulse width with no compression (i.e. low power of <5 mW) matches the pulse width measured using a high-speed sampling oscilloscope (hp 54120B with 34 GHz sampling head). Compressed pulse cannot be measured with the sampling oscilloscope due to its bandwidth limitations.

Launch power (mW)	FWHM (ps)		
	Experimental (raw autocorrelation)	Experimental (corrected for 1.54 sech factor)	Modelled
<5	77.6	55.0	55
53	74.2	48.2	49
96	74.2	48.2	41
143	58.6	38.1	32
197	46.9	30.5	23
259	22.1	14.4	14
299	15.6	10.1	9

Table 12.1. Modelled and experimentally measured pulse widths after 3 km of Fibercore 1500-RT-HI. The experimental values are provided both as raw values obtained from the actual SIPOD scans, and corrected values assuming a sech pulse shape and using a correction factor of 1.54.

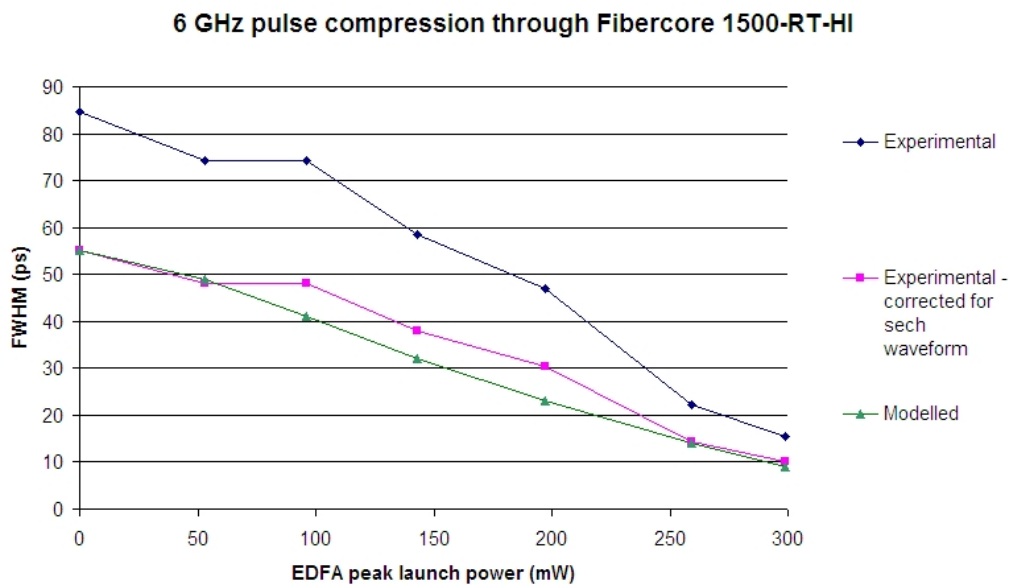


Fig. 12.2. Plotting the FWHM values in Table 12.1, shows a high correlation between the modelled pulse compression and the corrected experimental pulse widths obtained using the SIPOD “autocorrelation” scans.

Conclusions on experimental pulses. The experimental pulses have been demonstrated to be as short as 10 ps for 300 mW peak launch powers into the fibre. The experimental pulse widths show a very good match to the modelled pulse performance. This implies that the model accurately predicts fibre performance for the SIPOD application and is a useful tool for specifying further custom fibre draws.

12.3 Range finding performance using the bespoke compression fibre

The new custom compression fibre has been successfully implemented into the SIPOD system and has allowed range finding measurements to be performed to the order of 10 microns resolution or better, Fig. 12.3.

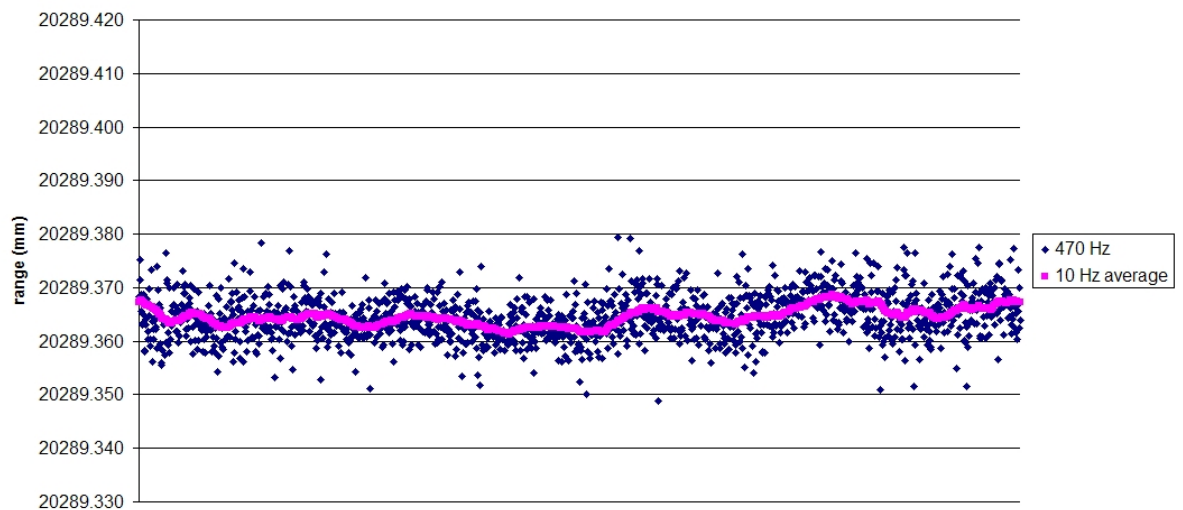


Fig. 12.3. The new custom phosphorous-free PM compression fibre provides sufficient pulse compression for modest launch powers of a few hundred mW to allow range measurements to be performed to resolutions of the order ± 10 microns at 470 Hz, and finer still at 10 Hz measurement update rates.

12.4 SBS implications for bespoke compression fibre

Fig. 12.4 confirms that the single frequency phase modulation approach effectively reduces the SBS effects to negligible levels for the new custom fibre Fibercore 1500-RT-HI. For peak launch powers of the order 250 mW, the backscattered light is reduced from the order of 25% to under 1% of the launch power by driving a phase modulator with a single frequency generated by the SIPOD system.

Section 11.6 demonstrated that for higher launch powers than shown in Fig. 12.4, typically 450 mW peak launch powers (~150 mW average powers for the launch waveform employed), two frequencies are required to adequately suppress the SBS as the single frequency approach ceases to provide sufficient suppression. It appears on Fig. 12.4 that the single frequency approach is just about to begin to fail as at 300 mW peak launch the backscatter plot (blue line) shows an upward trend. The upper power limit of the PM EDFA used here prevented further investigation of this effect. However, since a peak power of 250-300 mW has provided suitable pulse compression, only single frequency phase modulation SBS suppression is required for 6 GHz repetition rate pulses through the custom compression fibre.

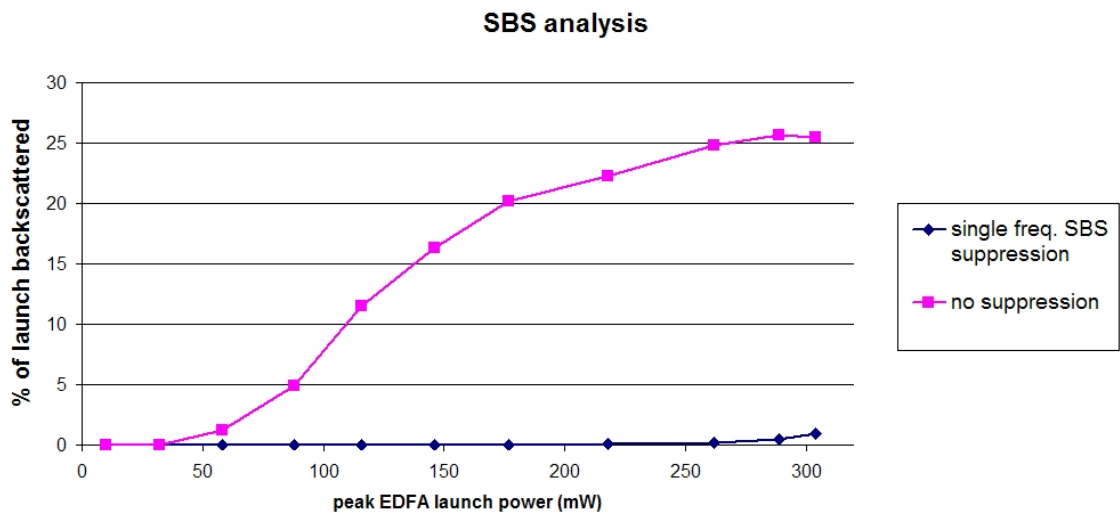


Fig. 12.4. Driving a phase modulator with a single frequency (> 40 MHz) generated by the SIPOD system is sufficient to reduce SBS backscatter to negligible levels through the custom PM radiation tolerant fibre.

Conclusions on SBS suppression. A single frequency phase modulation of the carrier sufficiently suppresses the SBS through the new custom PM fibre for the SIPOD application.

12.5 Polarisation maintaining performance

Low attenuation per unit length (1.07 dB/km) was achieved by imposing a relatively large spacing between the core and the boron stress rods, at the expense of reduced polarisation extinction. A substantial reduction in the output polarisation extinction ratio

12. Experimental characterisation of a bespoke compression fibre

is observed, resulting in a correspondingly high level of power being present in the unwanted polarisation at the fibre output. A polarising beam splitter should therefore be used following the compression fibre to prevent the unwanted polarisation being launched into the optical head.

The “worst case” polarisation extinction ratio values were obtained by manually twisting the launch fibre to maximise the power in the unwanted beam-splitter output. Table 12.2 compares the worst case extinction ratios output:

- Directly from the EDFA
- From 2.5 km of the commercially available PM fibre 1500-RT manufactured by Fibercore
- From 3 km of the custom phosphorous free fibre with increased non-linearity (Fibercore 1500-RT-HI fibre)

Source	Worst case polarisation extinction ratio
Keopsys PM EDFA	150:1 (22 dB)
Fibercore 1500-RT	20:1 (13 dB)
Fibercore 1500-RT-HI	5:1 (7 dB)

Table 12.2. Reduction in the polarisation extinction ratio output from the two PM compression fibres and the EDFA. The “worst case” values were obtained by manually twisting the launch fibre to maximise the power in the unwanted polarising beam-splitter output.

The reduced extinction ratio observed from both compression fibres detailed in Table 12.2 means that a passive polarising beam splitter should be used after the compression fibre to discard the unwanted polarisation; this adds a negligible system overhead in terms of weight, volume, power requirements or system ruggedness. Discussions with Fibercore suggest that the sub-optimal fibre pigtail selection may be responsible for some of this extinction ratio reduction, and this area could be investigated under further custom fibre development in any follow-on SIPOD programme. The SIPOD system can accommodate a reduction in return power of at least 1000-fold, as discussed in Section 10.5.8. Since the new custom compression fibre allows SIPOD to achieve range resolutions of the order of ± 10 microns at 470 Hz and

significantly better at 10 Hz data output rates, Fig. 12.3, the reduced extinction ratio due to the compression fibre does not impact on SIPOD's ability to exceed the PROBA-3 range resolution requirements.

The custom reel was wound simply onto a standard reel, with standard pigtails fused to each end. Many more sophisticated winding approaches exist (for gyroscope applications for example). Fibercore advise that a mixture of better packaging and improved fibre iterations could increase the polarisation extinction ratio considerably.

It should also be noted that the light present in the “unwanted” polarisation may in fact be of use for other system functions other than longitudinal metrology, for example for a coarse *lateral* sensor (SIPOD currently only measures longitudinal range).

Longer term, the non-optimal extinction ratio may limit the system's ability to perform range measurements to sub-wavelength accuracy. As the pulses propagate through the compression fibre the extinction ratio reduces from the launch value of $\sim 150:1$ to the order of $5:1$; therefore each launched pulse “sees” two different path lengths as it propagates through the compression fibre, placing an uncertainty on the time it takes each pulse to propagate through the entire system to the back-end detector. Another potential concern is that there may be an interaction between the high peak power pulses if they oscillate between different polarisations along the fibre, leading to potential non-linear effects such as four wave mixing and hence some pulse corruption and sub-optimal pulse compression. This polarisation related time delay is not insignificant, since typically fibres possess a polarisation dispersion mode coefficient of the order of $0.1 \text{ ps}/\sqrt{\text{km}}$, leading to a couple of hundred femtoseconds of polarisation related timing variation for the 3 km of compression fibre used here, equivalent to a few tens of microns range uncertainty. If light oscillates between the launch and the unwanted polarisation before being launched into the optical head in the desired polarisation, then it may possess a significant fraction of the maximum polarisation mode dispersion of 10 's of microns delay.

Conclusions on polarisation extinction ratio. A fairly substantial reduction in the polarisation extinction ratio from the compression fibre, compared to the launch ratio,

could be expected given the relatively long fibre length of a couple of kilometres and the fact that the fibre pigtails are of different fibre geometry from the compression fibre (in order to mate with the standard EDFA and optical head components). Experimentally the extinction ratio reduces from 150:1 to 5:1 after 3 km; however this does not prevent SIPOD from making measurements to better than ± 10 microns, Fig. 12.3. It may be that the “unwanted” polarisation can be constructively used, i.e. for a fine lateral sensor. In future the current extinction ratio may be a limiting factor in preventing the range resolution being improved to sub-wavelength.

12.6 Predicted pulse width performance from future improved draw iterations

The current NA aperture provides a mode-field diameter of 5.6 microns, as measured by Fibercore, which leads to a non-linear coefficient of around 5 W.km^{-1} . Fibercore advise that they are confident of being able to fabricate a PM phosphorous free fibre with a reduced core size, following the success of the fibre delivered under the SIPOD programme. They advise that the fibre loss should not be significantly affected. As the non-linear coefficient varies with $1/r^2$, reducing the core diameter rapidly increases the non-linear coefficient, leading to improved pulse compression per unit length. Pulse propagation was modelled for the following core diameters, Fig. 12.5:

- 4.0 micron ($\gamma = 9.8 \text{ W.km}^{-1}$),
- 4.5 micron ($\gamma = 7.7 \text{ W.km}^{-1}$)
- 5.0 micron ($\gamma = 6.3 \text{ W.km}^{-1}$)

The benefit of the reduced core diameter and hence increased non-linear coefficient is that the same level of pulse compression can be achieved for either reduced fibre length or reduced peak launch power. Given that the undesirable effects of radiation induced darkening and polarisation extinction ratio reduction are related to fibre length, it is advisable to reduce the fibre length if the system power budget allows. Fig. 12.6 indicates the potential fibre length savings for a given peak launch power. Note that other combinations of powers and lengths can also provide 10 ps pulses for these modelled fibres, however the values in Fig. 12.6 are indicative of the fibre length reductions possible with reduced core diameters for the given peak power of 300 mW.

12. Experimental characterisation of a bespoke compression fibre

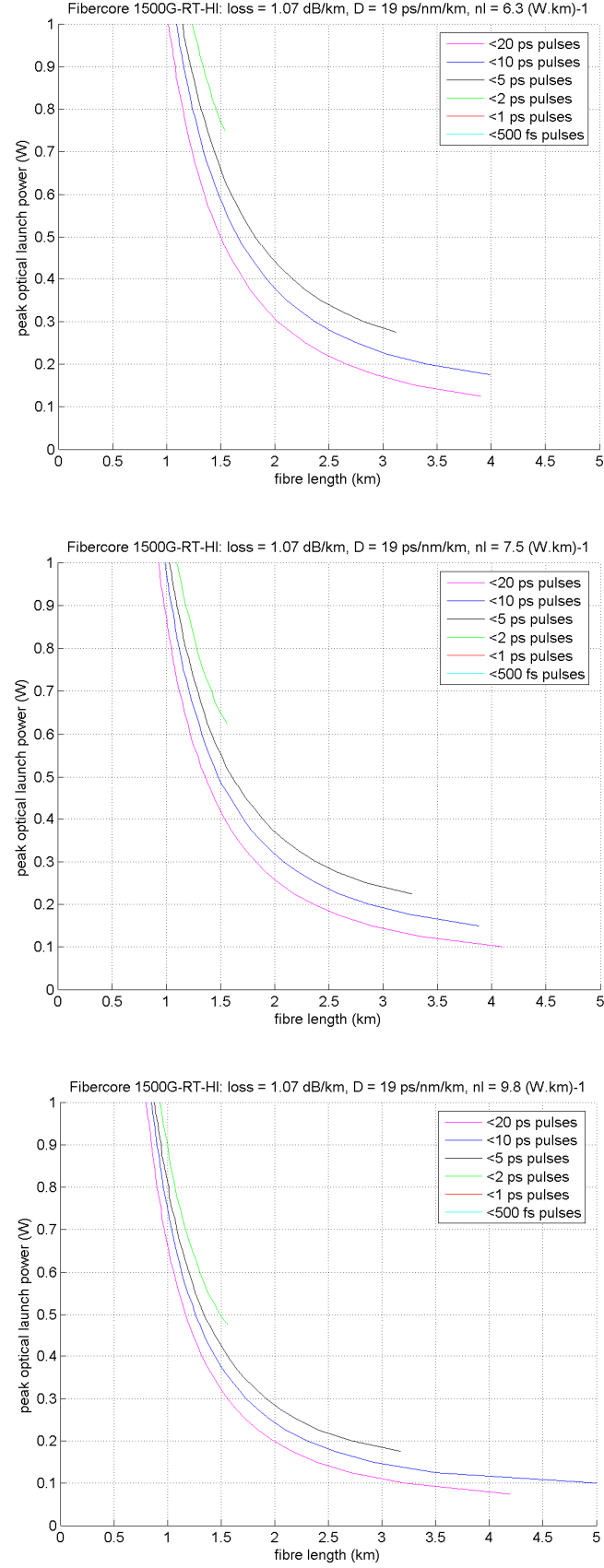


Fig. 12.5. Modelled pulse compression for reduced core diameters 5.0 μm (top), 4.5 μm (middle) and 4.0 μm (bottom) [reduced from the current 5.6 microns]. Note pulse repetition rate is 6 GHz.

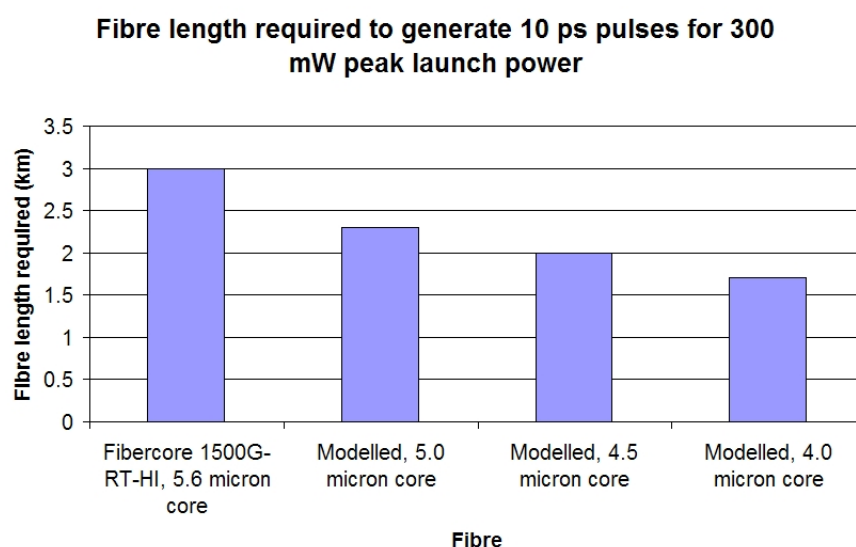


Fig. 12.6. Compression fibre length required to realise 10 ps pulses for 300 mW peak power launch pulses

12.7 Conclusions on experimental performance of custom compression fibre

Fibercore have delivered a phosphorous free, polarisation maintaining fibre on a compact reel. The total weight of the fibre and the standard reel is currently 420 grams, which could be further reduced with a bespoke reel design. The fact that the fibre contains no phosphorous is expected to significantly increase its radiation tolerance through the removal of this particularly radiation susceptible dopant^[1].

The custom fibre meets all of its specified physical parameters in terms of mode-field diameter (inferred from the high correlation between modelled and experimental compression), attenuation, length, reduced cladding and the fact that it is polarisation maintaining (PM). The PM aspect of the fibre removes the requirement for active polarisation control, which both simplifies and ruggedises the SIPOD system.

Stimulated Brillouin scattering through the PM compression fibre has been satisfactorily suppressed by broadening the optical carrier, achieved by applying a sinusoidal phase modulation generated within the SIPOD system.

In order to achieve low attenuation through the fibre, the polarisation stress rods were purposely separated by a relatively large spacing compared to standard PM fibres. This

leads to a polarisation extinction ratio of the order 5:1 at the output of the 3 km compression fibre. Currently the relatively high level of unwanted polarisation power can simply be rejected through the use of a polarising beam splitter.

The new custom fibre has enabled the generation of the shortest pulses observed to date using the SIPOD system, providing pulses of the order of 10 ps for peak launch powers of the order 300 mW. These pulse parameters are a very close match to model predictions. SIPOD has demonstrated better than 10 micron resolution using the new radiation tolerant PM fibre.

12.8 Future compression fibre development

The bespoke compression fibre does not contain phosphorous dopants in order to make it robust to excessive radiation induced attenuation (RIA) during the mission. It is recommended that several hundred metres of excess custom compression fibre should be radiation tested, to confirm the radiation tolerance of the custom fibre.

In future, a second iteration of the custom compression fibre draw could aim to reduce the core size to increase the non-linear performance of the fibre, thus reducing either the required launch power or the required fibre length. It is also desirable to increase the polarisation control through the fibre by narrowing the separation of the stress rods. It is likely that reduced fibre length is more desirable than reduced launch power since this would reduce radiation induced darkening effects and also increase the output polarisation extinction ratio due to a shorter interaction length.

References for Chapter 12

1. Regnier E., Flammer I., Girard S., Gooijer F., Achten F., and Kuyt G., “Low-Dose Radiation-Induced Attenuation at InfraRed Wavelengths for P-Doped, Ge-Doped and Pure Silica-Core Optical Fibres”, IEEE Trans. Nucl. Sci., Vol. 54, No. 4, pp. 1115-1119, Aug. 2007

13. Conclusions on compression source and applications

13.1 Introduction

This thesis is believed to present three novel areas of research: the first detailed jitter characterisation of a soliton-effect compression source, the first optical sampling using such a compression source, and a novel optical metrology range finding system, known as SIPOD (Scanning Interferometric Pulse Overlap and Detection), which utilises the tuneable repetition rate and highly stable nature of the compression source pulses.

Due to the high resolution range finding performance of the SIPOD system, coupled with the attractive system parameters of low size, weight and power, SIPOD is due to fly on the European Space Agency's PROBA-3 formation flying satellite mission in 2012.

Throughout this thesis, the emphasis of the discussions has focussed on the engineering issues which were overcome to physically realise the optical pulse source, such as the optimal removal of stimulated Brillouin scattering. Where appropriate the underlying physical properties have been investigated and modelled. The design and engineering considerations of the SIPOD system, for which the pulse source with its tuneable and highly stable pulses is the key enabling component, forms another major section of the engineering analysis which is a common theme throughout this thesis. Again, where appropriate, analysis of the underlying physical mechanisms has been included for completeness.

13.1 Summary and conclusions of the compression source development

A UK Ministry of Defence photonic analogue-to-digital converter (ADC) programme was the original driver behind the development of a soliton-effect compression source for optical sampling. A survey had identified that this type of optical pulse source did not appear to have been used for this application before, and it was hoped that it would provide a rugged source of very short duration, highly stable optical pulses at a repetition rate which was compatible with the very fastest electronic ADC chips. In

comparison to the most stable gain switched lasers, which achieve their pulse stability via extended cavities to reduce spontaneous turn-on events via pulse seeding, the soliton-effect compression source is a seemingly more rugged all-fibre design. Unlike mode-locked lasers, the compression source does not require the use of techniques to overcome susceptibility to thermal variations which affect the laser cavity round-trip time and hence the pulse repetition rate. Instead, the main environmental requirement for the compression source pulse stability is that the microwave oscillator frequency remains stable over time-windows of interest, i.e. ≤ 100 milliseconds for frequency analysis purposes for high-bandwidth ADC sampling applications; this condition is readily achievable using commercially available ovened quartz oscillators.

In terms of timing jitter values, the compression source value of 257 fs for a 3 GHz pulse train, measured over the offset range of 100Hz-10MHz, is comparable to the lowest gain-switched and Q-switched laser values published in the literature (over the same frequency offset range), but two orders of magnitude higher than the lowest mode-locked laser figures (full details in Table A.4 in Appendix A). The compression source therefore has the potential to fill a niche in optical sampling, offering comparable sampling performance to the very best gain-switched lasers, but in a far more rugged arrangement. Therefore the compression source may be attractive for many military platforms, where extreme temperature and vibration may be encountered. However, when the ultimate in pulse resolution is required, mode-locked lasers must be employed. A 30 fs timing jitter mode-locked laser would facilitate 9-bit resolution optical sampling of a 10 GHz input bandwidth signal, where as the 257 fs compression source will only support around 6-bits.

The compression source possesses one important pulse parameter not obviously available to conventional short pulse sources, and that is rapid and highly accurate pulse repetition rate tuneability. Mode-locked lasers and gain- and Q-switched lasers have a repetition rate governed by the cavity round-trip time, hence to vary the pulse rate the cavity length must be physically scanned in some way. Even if this were possible at high modulation rates, it is far from trivial to determine the instantaneous pulse repetition rate accurately to the order of 1 part in 10^6 . In contrast, the compression source repetition rate has been experimentally demonstrated to have an electronically

programmable output rate which can be set to Hertz resolution around a nominal frequency of 6 GHz, as discussed in Chapter 10 of this thesis.

It was this pulse tuneability which led to the compression source becoming the key enabling component in the development of a novel approach to optical metrology for longitudinal range finding, known as the Scanning Interferometric Pulse Overlap Detection (SIPOD) system. This system has exhibited unambiguous range finding performance with better than 30 microns range resolution, over ranges of up to ~200 metres, at update rates of the order of 500 Hertz. At 10 Hz update rates, the standard deviation of the range measurements is only 1.7 microns. This combination of range-finding performance does not appear to have been achieved before. Whereas conventional interferometer techniques can indicate range variations to sub-wavelength accuracy, i.e. 10's of nanometres, they cannot resolve the absolute range since there is always an ambiguity as to the number of fringes spanning the measurement arm. SIPOD's performance is now approaching the stage at which it can make unambiguous range measurements to sub-wavelength accuracy. Component upgrades may allow accuracies of better than half a wavelength to be achieved (i.e. <0.8 microns), in which case the SIPOD system would be able to determine unambiguously the fringe *order* to the target, at which point it could hand-over to a conventional interferometer system. In this way, the system could then resolve the range to interferometric accuracy over measurement lengths limited by the stability of the clock, the coherence length of the laser and the wavelength stability. Since SIPOD can operate either in pulsed mode or in cw mode, simply by turning the optical intensity modulation on or off, it can offer both the SIPOD scanning mode of operation and the conventional interferometer approach to metrology, in the one system. In this way, it is anticipated that SIPOD may be able to resolve longitudinal range to 10's of nanometres over many hundreds or even thousands of metres. The system has aroused great interest at the European Space Agency and has been short-listed as the key enabling technology for ESA's formation flying satellite ambitions. SIPOD is due to fly on the PROBA-3 mission which is scheduled to launch in 2012.

As an aside, one unintended bonus of the SIPOD system is that because it can electronically perform a frequency sweep of the pulses at several hundred Hertz, it provides a "real-time" method of visualising the pulse shape which does not require

either a high level of averaging on a sampling oscilloscope nor a mechanical sweep of an interferometer arm as in a conventional autocorrelator. Therefore it more quickly detects dynamic pulse shape variations which are free from time-delayed averaging effects or long time-delays. SIPOD is therefore a useful tool for observing effects such as polarisation drift and modulator bias drift. The major limitation of the SIPOD system for use as an autocorrelator is that it can only measure pulses for sources which have electronically tuneable repetition rates, discounting it from measuring the pulse shapes of conventional fixed-cavity lasers.

The compression pulses generated to date using either 25 km of Corning's SMF-28 fibre or 2.5 km of Fibercore's reduced core diameter fibres [1500 (5.3/80) and 1500-RT-HI], have demonstrated pulse widths of the order 10-15 picoseconds, measured using both a traditional autocorrelator and the SIPOD metrology system. As with the timing jitter parameters, these pulse durations are broadly comparable with the 10-20 ps pulses typical for gain switched lasers, but are several orders of magnitude longer than optimised low-jitter mode-locked laser pulses of around 10 fs or less. Therefore the compression source and the best gain-switched lasers currently exhibit comparable performance in terms of pulse duration. As with the timing jitter parameter, the ultimate in short pulses is provided by mode-locked lasers.

13.2 Future work

The compression source repetition rate has been rapidly scanned over ± 20 MHz around a nominal 6 GHz frequency, with each new frequency electronically programmable at the FPGA clock rate, i.e. at MHz update rates. In future it would be attractive to extend the pulse repetition rate tuneability to cover a multi-gigahertz tuning range. The lowest repetition rate which produces ~ 10 ps pulses is of the order of 1.5 GHz; therefore the compression source could be adapted to provide repetition rate tuneability over a frequency range from say 2 to 40 GHz. In order to realise comparable pulse shapes at widely different repetition rates, it would be necessary to dynamically vary the peak optical launch power for each new pulse repetition rate; this could be achieved using a calibrated look-up-table. The maximum pulse repetition rate refresh rate would most likely be limited by the time taken to vary the EDFA drive current and allow the

waveform launched into the compression fibre to settle into a stable state. Tuning steps of multi-gigahertz should be possible at rates of at least tens of Hz, with fine tuning around each nominal frequency possible at MHz rates (assuming the appropriate IQ modulator can be developed to cover the total tuning range).

Currently the compression source pulse durations and timing jitter are comparable to the best published values for gain switched and Q-switched lasers. Modelling suggests that the use of a highly non-linear fibre, as manufactured by both Sumitomo and Furukawa, would generate pulses of ~ 1 picosecond duration, an order of magnitude shorter than the 10-15 picosecond pulses generated to date and shorter than gain-switched laser pulses. For the ~ 2 km lengths required, these specialist fibres would cost around £10k. Currently there is no programme scheduled at QinetiQ to fund this specialist fibre work to investigate the possibility of compressing pulses down to the femtosecond regime.

The European Space Agency has funded a custom draw of a polarisation maintaining radiation tolerant fibre, for use on the 2012 PROBA-3 mission. Since the current 10-15 picosecond pulses have proved to be sufficiently short to enable high-accuracy range finding, improved pulse compression was not the main aim of this fibre procurement. Instead, the custom draw included a polarisation maintaining design to remove the need for polarisation control in the SIPOD system, and it also addressed the important issue of radiation tolerance which aims to avoid fibre darkening and hence sub-optimal pulse compression during the latter stages of the mission. Radiation tolerance is achieved through the correct choice of dopants; for example Fibercore advise that phosphorous dopants lead to excessive colour centres which are particularly radiation susceptible. A further iteration of this fibre would aim to shorten the required fibre length from 3 km to ~ 1.5 km, along with improving the polarisation extinction ratio from 6 dB to perhaps 20 dB.

Future work on the SIPOD system concerns space ruggedisation in preparation for the 2012 mission. In particular, the compression fibre and EDFA were considered high risk components in this regard and work is currently on-going investigating ruggedisation options for these components, and for all other system components. Much longer term, if SIPOD is adopted as the European Space Agency's principal metrology solution, it

may be necessary to develop a SIPOD variant which can interrogate multiple platforms simultaneously. This may be achieved by using a multi-wavelength compression source and demultiplexing components.

The removal of the requirement to use an optical amplifier (EDFA) would be attractive for reasons including system cost and radiation susceptibility. More importantly for optical sampling applications, the removal of the EDFA would substantially reduce the optical pulse timing jitter. The modelling in Chapter 11 suggests that it is possible to generate compressed pulses of the order of 10-20 picoseconds duration without the need for an EDFA, through the use of a high power laser source (125 mW) and low insertion loss modulators (2 dB each), coupled to an appropriate highly non-linear fibre. It is anticipated that this approach would offer the potential for reduced timing jitter, since the EDFA inherently introduces parasitic ASE around the optical carrier which cannot be filtered out, even by the narrowest available band-pass filters. The removal of the EDFA would also reduce the possibility of random wavelength fluctuations leading to dispersion related timing jitter (Gordon-Haus jitter). In this way, the compression source may offer improved timing jitter values compared to gain switched lasers if the EDFA can be omitted from the system; this would require the development of a high power (>125 mW) single frequency laser source.

Fig. 13.1(a) demonstrates that the EDFA introduces around a 20 dB increase in the SSB phase noise at frequency offsets greater than 10 kHz on the 6 GHz SIPOD pulse arrangement. Fig. 13.1(b) shows the timing jitter values calculated from these SSB phase noise plots, with the EDFA noise substantially increasing the timing jitter from 390 fs to 3.5 ps for this arrangement, over the frequency offset range 100 Hz to the Nyquist frequency of 3 GHz. In future, by using a microwave oscillator with 10 dB lower close-in phase noise at frequency offsets <10 kHz, the timing jitter reduces to ~400 fs and ~350 fs respectively over the frequency ranges 10 Hz and 100 Hz to the Nyquist frequency (assuming the far out noise floor remains at -135 dBc/Hz). These timing jitter values would still be an order of magnitude higher than the ~30 fs reported for the best mode-locked laser systems but would improve the compression source performance by an order of magnitude compared to the best gain- and Q-switched lasers. When comparing the compression source performance to the best reported figures in the literature, it should be noted that the SIPOD system has been operated in a

13. Conclusions on compression source and applications

free-running state for over 2 months with no human intervention or calibration, with no reduction in timing stability; it would be interesting to perform a similarly long duration test on the mode-locked lasers to compare long-term stability and ruggedness.

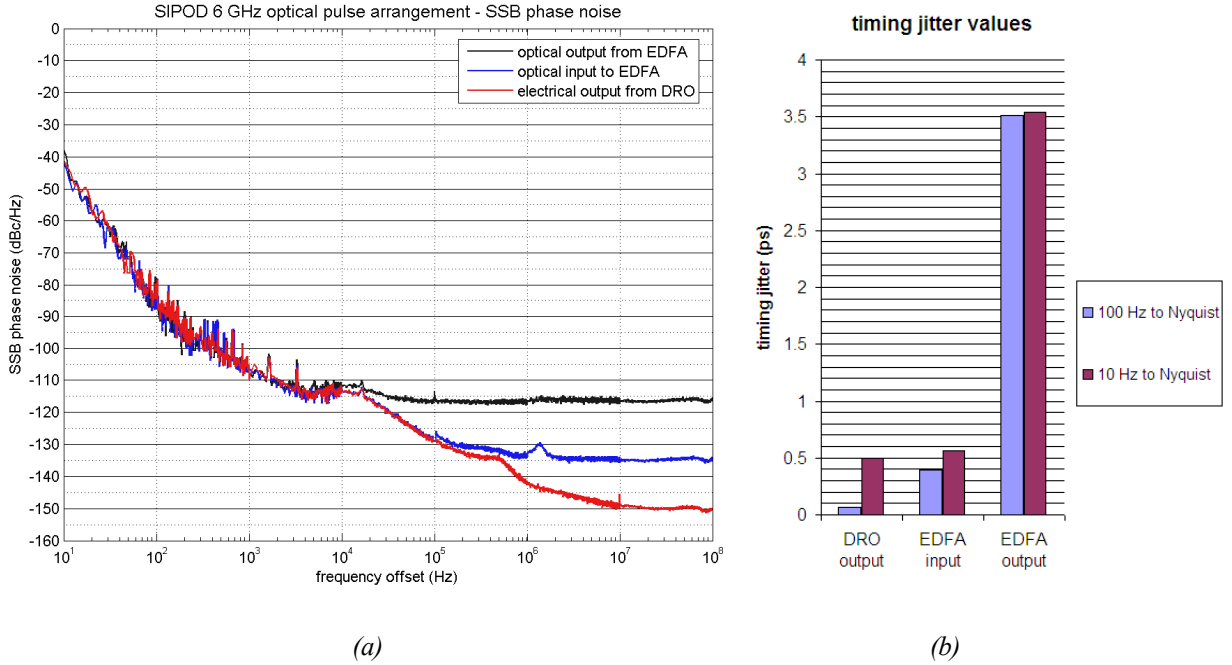


Fig. 13.1. Measurements performed on the 6 GHz SIPOD optical pulse source arrangement.

(a) SSB phase noise measurements of the electrical input to the optical intensity modulator (from the DRO), the optical input to the EDFA and the optical output from the EDFA (spikes removed from all 3 plots).

(b) Timing jitter calculations over the stated frequency offset ranges based on the SSB phase noise results in (a).

Note the substantial contribution to the timing jitter added by the EDFA.

Finally, a full characterisation of the current SIPOD breadboard measurement resolution has been limited by the fact that it is difficult to distinguish between system artefacts and external environmental conditions. Calculated temperature and vibration effects are significant enough to vary the optical path length by several microns in the current laboratory arrangement, a variation which is comparable to the standard deviation of 1.7 microns observed in the range measurements made over short timescales of a minute or less. Therefore to characterise the SIPOD system range measurement performance fully and remove uncertainties due to the measurement arrangement, the system could be trialled in a long temperature controlled vacuum chamber such as the 3 km Virgo gravitational wave detector in Pisa, Italy. This option has been discussed with the ESA customer and will require additional funding.

13.3 Summary

In summary, an optical pulse compression source based on soliton-effect compression was modelled and experimentally implemented after a survey of available pulsed laser options identified that this approach had not been implemented for low gigahertz repetition rates before. Additionally, the detailed characterisation of the timing jitter of the compression source undertaken in this thesis does not appear to have been reported previously in the literature. Pulse characterisation identified that the compression source generates pulses which are comparable in duration and stability to the best gain-switched lasers, but at least two orders of magnitude lower quality than the best mode-locked lasers. Therefore the compression source is not the optimum pulsed laser option for high-resolution optical sampling; instead mode-locked lasers should be used for this application when the highest bit-depth is required at multi-gigahertz sampling rates. However, where the ultimate in source ruggedness is required, the all-fibre compression source is a very attractive option due to its inherent temperature robustness.

The compression source possesses one distinguishing feature which does not appear to be available from conventional laser sources, and that is rapid and highly accurate pulse repetition rate tuneability. Exploiting this feature, the pulse source was tailored for use in a novel approach to optical metrology known as SIPOD. Due to the high resolution range finding performance of the SIPOD system, coupled with the attractive system parameters of low size, weight and power, SIPOD is due to fly on the European Space Agency's PROBA-3 mission in 2012. Over the next 18 months the system is expected to undergo rapid space engineering, testing and qualification in preparation for this two year mission.

A. Options for ultra-short, ultra-stable optical pulse generation

The generation of ultra-short (sub nanosecond) optical pulses has been an active area of research for several decades, and the existence of such pulses has opened up a range of applications in addition to photonic analogue to digital conversion. Arguably the most notable application of short optical pulses to date has been in ultra-high bit-rate optical telecommunications systems, although ultra-short pulse sources are also of great importance to various physical science research areas including observing processes occurring in semiconductors, as well as being used in time resolved spectroscopy, through to medical applications such as non-invasive tissue ablation. There are various optical pulse parameters of interest depending on the system application such as pulse repetition rate, peak/average pulse power, optical wavelength, and total power consumption. All applications, but particularly those outside of the research laboratory, benefit from compact, robust, economic sources which do not require complex power-hungry drive electronics.

This Appendix section provides an overview of the main techniques used to obtain ultra-short pulsed laser sources, with examples given of specific commercial and research implementations which address the requirements of the photonic ADC pulse sources. As discussed in the main body of this report, timing jitter is of paramount importance for photonic ADC technology in particular, and ideally the system will have the potential to be compact, lightweight and rugged in order to make the system suitable for use on various military and satellite platforms (such as ESA's PROBA-3 mission). It is also a distinct advantage if the pulse source operates in the 1550 nm waveband in order to utilise components emerging from the telecommunications industry, such as time or wavelength demultiplexers which can be used downstream of the pulse source.

The main options for generating ultra-fast low jitter optical pulse trains are gain switched (or loss switched) lasers, Q-switched lasers, mode-locked lasers and soliton-effect compression of repetitive input waveforms. The following sections in Appendix A assume familiarity with these techniques, however of an overview of each technique is given as an introduction to each section.

For each pulse source type, the lowest published timing jitter value is stated along with the measurement technique used to calculate it. A very common approach for the timing jitter measurements, particularly for the gigahertz repetition rate mode-locked laser approaches, appears to be the integration of the SSB phase noise over the frequency offset range 10 Hz to 10 MHz. Therefore, where possible, the SSB phase noise timing jitter measurements over 10 Hz to 10 MHz offsets have been collated for this report to try and objectively compare each source. Where this “benchmark” range has not been explicitly stated, it has been interpolated for this report from the published SSB phase noise plot (if given).

A.1 Gain switched lasers

A semiconductor laser diode can be made to generate a train of optical pulses by periodically varying the drive current, so that during each repetitive drive cycle a large population inversion is generated, which is then pumped hard to enable rapid gain depletion, with the result being that all excited atoms contribute to a large short pulse, Fig. A.1. Pulse shortening occurs due to the fact that the trailing edge of the pulse suffers power loss (or sees no gain) since the population inversion is depleted and hence gain saturation occurs. Typically pulses of duration of the order of 10 to 20 ps can be generated by this method, known as gain switching.

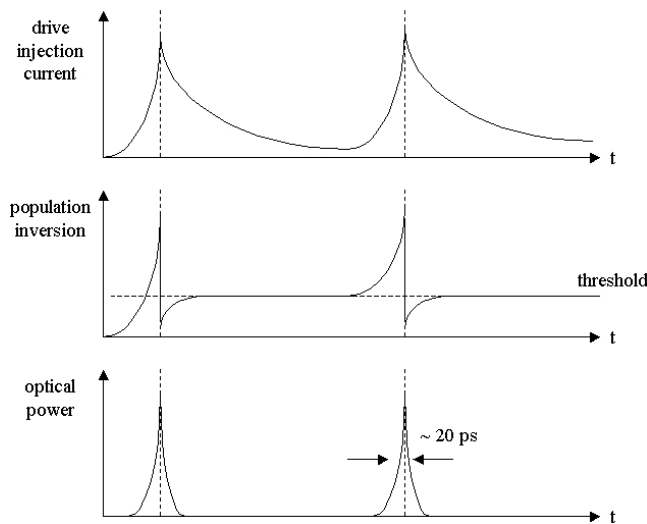


Fig. A.1. During gain switching, a periodic input drive current leads to a large population inversion well above threshold which is then rapidly depleted to the point of gain saturation, resulting in a train of short pulses.

Gain switched pulses can be a very convenient method for generating an optical clock since the repetition rate is tuneable and laser diodes can be used as compact sources. Analysis of the jitter from basic gain switched diode lasers with no timing jitter reduction method employed has generally been found to be of the order of ~ 1 ps^[1], which primarily consists of spontaneous emission noise during the population inversion build-up phase^[2,3].

In order to reduce the uncorrelated component of the jitter from both Fabry Perot (FP) and distributed feedback (DFB) gain switched diode lasers, some groups have investigated self-seeding, where some of the output pulse is reflected back into the laser cavity, although a disadvantage with this approach is that the cavity length must be adjusted to match the repetition rate, leading to a loss of dynamic tunability of the source and also a much less rugged system since it becomes susceptible to thermal effects^[2,4]. The total jitter relies on the quality of the electrical modulation, the mechanical and thermal stability of the cavity, and the reliance of the pulse generation on spontaneous emission.

A feedback variation which is independent of the repetition rate is the use of CW light injection which was shown by Gunning et al.^[2] to be capable of generating 2.5 GHz pulses with 0.6 ps of uncorrelated timing jitter, derived using Leep and Holm's jitter calculation method. When the CW injection was removed the uncorrelated timing jitter rose to 3.6 ps. The drawback to the CW light injection was that the pulses were both broadened and a pedestal was introduced^[5], although this was experimentally demonstrated to be removable with an electro-absorption modulator^[2].

Huhse et al.^[6] argue that the presence of a constant high CW background light being reflected into the output pulse train can cause problems for optical sampling systems. They proposed solving the problem of seeding the gain switched laser without adding a CW background by seeding a FP laser diode with a gain-switched DFB laser diode, both of which are driven by the same tuneable electronic source, with appropriate time delays and settings throughout to ensure that the DFB gain switched seed pulse arrives just as the FP laser reaches its threshold value. Using the single sideband phase noise timing jitter measurement, they obtain timing jitter values of 0.86 ps and 1.45 ps with and without seeding pulses, over the frequency offset range 10 Hz to 311 MHz, for

311 MHz repetition rate pulses. Reading values from their published SSB plot, interpolating and integrating, yields a timing jitter of ~ 300 fs over the frequency range 10 Hz to 10 MHz.

Schell et al.^[7] developed a model for the timing jitter behaviour of self-seeded diode lasers, stemming from the fluctuations induced by spontaneous emission. Their analysis showed a timing jitter lower limit of 425 fs in multimode free running operation, reducing to 210 fs in single-mode self-seeded operation, calculated from the harmonic spectra. They also discovered that due to different photon statistics for multimode FP lasers, the gain switched DFB laser will always have significantly larger timing jitter than a gain switched FP diode laser. An attractive property of self-seeding is that it potentially allows fast wavelength switching since a stable gain switching state is achieved in only around 5-10 cavity round trips which is over an order of magnitude faster than with passively mode-locked laser^[7], which typically require 170 cavity round trips to become stable.

One of lowest reported timing jitters for a gain switched laser was described by Nogiwa et al.^[3], with a measured timing jitter from a gain switched laser with CW seeding of 165 fs. However, this was for the frequency offset integration range 10 kHz to 40 MHz. They used three different methods of timing jitter analysis including spectral analysis, optical sampling and single sideband (SSB) phase noise analysis and they state all three methods agreed. Their SSB phase noise spectra clearly show the noise improvements when using the CW seeding. However, it should be noted that they state that they only integrated the SSB-phase-noise spectra over the range 10 kHz – 40 MHz to ensure the close agreement for the three methods. Reading the values from their published SSB phase noise plot, interpolating and integrating, yields a timing jitter of approximately 320 fs over 10 Hz to 10 MHz (the same method yields $\sigma_\tau \sim 160$ fs over 10 kHz to 40 MHz as they state).

The lowest published timing jitter for gain switched lasers would therefore appear to be of the order of two to three hundred femtoseconds for SSB phase noise integrated over 10 Hz to 10 MHz, for pulse trains seeded either with CW light or a pulse train with the same repetition rate as the gain switched pulses.

A.2 Q-switched lasers

Q-switched lasers differ from gain switched lasers in that the pump is kept constant and it is the quality factor of the laser cavity which is periodically varied in order to generate a train of ultra-short pulses. The quality factor, or Q , of the laser cavity can be varied so that for appropriately high levels of pumping, a large population inversion can be established during the period when the cavity has a large loss, when stimulated emission is suppressed. If the cavity Q is then very quickly switched to a high value then the huge population inversion rapidly depletes to such an extent that the population inversion falls to a level below laser threshold. In this way all the atoms in an excited state contribute to one very large pulse as opposed to operating in a constant output mode.

Q-switching is considered attractive for generating high power pulses, with the peak power derivable from the laser rate equations:

$$\frac{dN_2}{dt} = R - \frac{N_2}{\tau_{sp}} - \left(N_2 - \frac{g_2}{g_1} N_1 \right) B_{21} \rho(\nu) \quad (\text{A.1})$$

$$\frac{d\phi}{dt} = \left(N_2 - \frac{g_2}{g_1} N_1 \right) B_{21} \rho(\nu) - \frac{\phi}{\tau_c} \quad (\text{A.2})$$

where N_1 and N_2 are the populations of the upper and lower lasing levels, ϕ is the photon density, B_{21} is the Einstein coefficient, $\rho(\nu)$ is the energy density and R is the pump rate.

Re-writing the rate equations, where N is the population inversion and N_{th} is the inversion required to reach threshold:

$$\frac{d\phi}{dt} = \left(\frac{N}{N_{th}} - 1 \right) \left(\frac{\phi}{\tau_c} \right) \quad (\text{A.3})$$

The rate equation for population inversion N , if there is no pumping when the cavity quality Q is restored and spontaneous emission is negligible compared to stimulated emission is given by (τ_c is the decay rate of the Q-switched pulse):

$$\frac{dN}{dt} = -2 \frac{N}{N_{th}} \left(\frac{\phi}{\tau_c} \right) \quad (\text{A.4})$$

For an initial inversion of N_0 this gives a maximum peak pulse of

$$P_{\max} \approx \frac{h\nu}{2\tau_c} N_0 \quad (\text{A.5})$$

since the maximum number of photons in the cavity is $\phi_{\max} \approx N_0/2$.

The cavity quality factor can be either actively or passively switched from low to high Q. Active Q-switch implementations include mechanical switching, for example by a rotating chopper, or by a vibrating mirror mount which mis-aligns the cavity. Electro-optic switching using a Pockell's cell is also possible via fast electro-optic switching in materials such as KDP, although a major drawback with this approach is that it requires voltage pulses in the 1-10kV range. An alternative switching approach is the use of an acousto-optic modulator to generate a standing compression wave in optical material, which behaves as a refractive index grating so that the laser periodically experiences Bragg scattering. However these active Q-switching techniques mentioned so far have two drawbacks: the inability to generate truly short pulses (sub 100 ps), and unacceptably large jitter values^[8] for photonic ADC applications. These drawbacks can be overcome however using multi-contact diode laser devices or Mach-Zehnder switching. The multi-section diode laser approach will be discussed shortly.

Passive Q-switching can achieve short pulses through adding a saturable absorber to the cavity, so that at the start of the cycle all the spontaneous emission is absorbed by the saturable absorber and the cavity has a low-Q. Eventually the absorber becomes saturated and since there is a large inversion (for the appropriate level of pumping) the gain is large and therefore quickly depleted, leading to a short high power pulse. However, this method is not suited to the photonic ADC application since the random nature of the spontaneous emission required for saturating the absorber for each pulse leads to large pulse-to-pulse jitter. In addition, the pulse is self-starting and is therefore not able to be locked to an electronic clock, which is not ideal for the photonic ADC application.

The multi-contact actively Q-switched semiconductor laser diode method benefits from both electronic tunability and also lower timing jitter than the passive Q-switch saturable absorber approach. In this set-up, most of the active region is a gain region driven by a constant current, and a second much smaller section of the active region acts as an absorber, which is modulated to achieve the Q-switching operation. This is a very attractive approach to short pulse generation since, unlike with gain switching, only a very small part of the active region requires to be driven with a modulated current, making the drive electronics more practical to implement, Fig. A.2(a). Various multi-contact architectures have been designed to minimise facet damage and improve performance, such as the flared design, Fig. A.2(b).

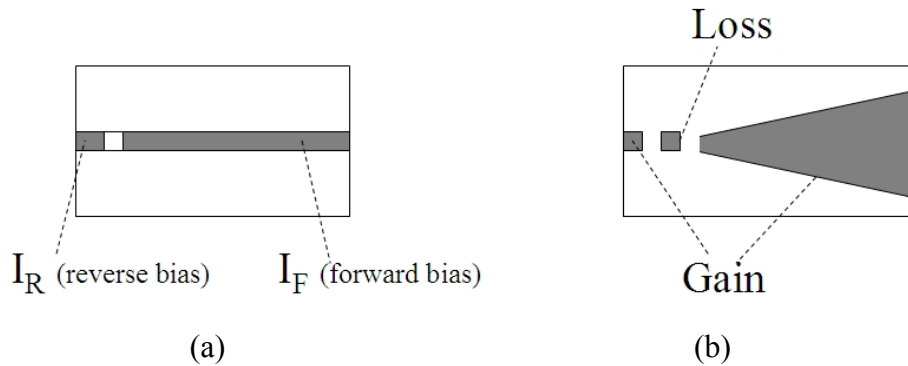


Fig A.2. (a) The simplest multi-contact Q-switched diode device, consisting of a large gain section forward biased and a much smaller reverse biased active region which switches the cavity Q, and (b) One of the many variations, incorporating a “flared” design and multi-gain sections to minimise diode damage during high power pulses.

Often the main reason cited for using the Q-switching technique is that it produces larger pulse energies when compared with mode-locking^[9]. In order to increase the output power various setups have been proposed, including the use of bow-tie diode arrays, which comprise 5 flared gain sections which taper linearly towards the facets (similar to Fig. A.2(b)). Peak powers of over 20 Watts have been achieved with pulse durations <20 ps. In these cases, timing jitter has not been the main priority and it was crudely quoted as < 2 ps, measured simply using a sampling oscilloscope.

More detailed analysis by Shen et al.^[10] compared the jitter performance of a two-section InGaAs Fabry Perot Q-switched laser with that of an InGaAsP gain switched

DFB laser. Both gave pulses of around 30 ps duration, with Leep and Holm's jitter analysis (see Appendix B) method yielding jitter values which decreased with increasing modulation frequency over the range 2-5 GHz. An important finding was that the two-section Q-switched lasers had lower jitter than the gain switched version for all modulation frequencies, with a measurement limited timing jitter of around 250 fs (± 100 fs) for 5 GHz modulation. The lower jitter of the Q-switched laser was considered to be due to the fact that the high saturation intensity of the absorbing (reversed biased) section suggests a short recovery time of the absorption, which favours fast laser switching and short turn-on delay leading to low timing jitter.

Analysis performed on multi-contact Q-switched lasers at St Andrews University by Sibbett et al.^[1] again found that Fabry-Perot diode lasers have much lower timing jitter than DFB lasers of the same material (InGaAsP), in this case for repetition rates of 650 MHz, 1.3 GHz and 1.9 GHz. The best performance was achieved with high DC bias on the gain sections, with timing jitters of ~ 6 ps measured with both SSB phase noise and Leep and Holm's method for the DFB Q-switched devices. The Fabry Perot devices had lower timing jitters of 1.9 ps for 650 MHz repetition rates, 1.4 ps for 1.3 GHz rates and 900 fs timing jitter for 1.9 GHz rates. The group investigated the use of electrical feedback from the gain section to drive the absorber sections, with a successful reduction in timing jitter from 6 ps to 2.5 ps for the DFB version, and 1.3 to 1.0 ps for the Fabry-Perot device. The group then investigated the benefits of using a similar resonant feedback electrical loop on a gain switched single contact device. Here they fed back the voltage fluctuations across the diode via a variable length delay line with a 20 MHz filter centred at the repetition rate of 1.015 GHz. This reduced the timing jitter of the gain switched DFB from 6 ps to 0.8 ps, and from 1.3 ps to 0.8 ps for the Fabry-Perot set-up. The fact that the jitter is now the same for both the DFB and FP lasers suggests that a more fundamental laser material limit is being reached rather than just a laser geometry issue. The St Andrews group conclude their paper by discussing an optical feedback scheme which was shown to reduce the timing jitter from a single contact gain switched device to around 1 ps, showing no improvement on the multi-contact Q-switched device performance.

In summary, several groups have used optoelectronic and electronic feedback schemes to realise timing jitters as low as of the order of 200 fs for gain and Q-switched diode lasers. For basic schemes, Fabry-Perot diode lasers have lower timing jitter than DFB equivalents, but with care both diode types can be optimised through multi-contact set-ups and/or optical feedback schemes to have very similar low timing jitter performance. The lower limit quoted for timing jitter for both gain and Q-switched semiconductor diode lasers is around 200 fs, for repetition rates around the GHz region. These sources are therefore an attractive option for many of the photonic ADC implementations.

A.3 Mode-locking

The technique of mode-locking has produced the lowest pulsed laser timing jitter values to date, at over an order of magnitude lower than gain or Q-switch techniques. Commercially available mode-locked lasers exist with repetition rates of the order of gigahertz, pulse widths as short as sub-picosecond and timing jitters of <100 fs ^[11,12]. Mode-locked lasers in the research lab however have quoted even lower timing jitters, with values of under 10 fs published for repetition rates around 10 GHz.

Mode-locking is performed by modulating the gain or path length of the cavity, so that all the longitudinal modes above threshold can be adjusted to be in phase. The effect of the modulation is to transfer some of the longitudinal mode energy into the sidebands, which for the case of modulation at the round-trip frequency, corresponds to the adjacent longitudinal mode. In this way energy is exchanged between adjacent longitudinal modes and all of their phases are kept “in-step”. It should be noted that mode-locking does not encourage longitudinal modes below threshold to lase.

Each mode has the field:

$$E_n(t) = E_0 e^{i(\omega_n t + \phi)} \quad (\text{A.7})$$

So for N longitudinal modes

$$E(t) = E_0 \sum_{n=0}^{N-1} e^{i(\omega_n t + \phi_n)} \quad (\text{A.8})$$

Usually all these modes vary incoherently in time in which case the intensity is:

$$I(t) = |E(t)|^2 = E_0^2 N \quad (\text{A.9})$$

However, if the phases of all the modes are locked together so that $\phi_n = \phi_0$ for all n :

$$E(t) = E_0 \sum_{n=0}^{N-1} e^{i(\omega_n t + \phi_n)} = E_0 e^{i\phi_0} \sum_{n=0}^{N-1} e^{i\omega_n t} \quad (\text{A.10})$$

where $\omega_{n+1} - \omega_n = \Delta\omega$, i.e. $\omega_n = \omega_{N-1} - n\Delta\omega$

The intensity of the now mode locked (or phase locked) longitudinal modes becomes:

$$I(t) = |E(t)|^2 = E_0^2 \frac{\sin^2\left(\frac{N\Delta\omega t}{2}\right)}{\sin^2\left(\frac{\Delta\omega t}{2}\right)} \quad (\text{A.11})$$

So as $\Delta\omega \rightarrow 0$,

$$I(t) \rightarrow E_0^2 N^2 \quad (\text{A.12})$$

Therefore the result of fundamental mode-locking of a laser is a series of pulses with pulse widths equal to the cavity round trip time divided by N number of mode-locked modes.

Much of the early mode-locking work was based on solid state lasers, with the first mode-locked paper published in 1966, only 6 years after the invention of the laser^[13]. However, the mode-locked pulse energies generated varied rapidly within longer Q-switched macropulses and this continued to be a problem until the early 1990's^[14], see Fig. A.3. Some highlights of mode-locked solid state lasers include 5 fs pulses produced directly from a Kerr lens mode-locked Ti:sapphire laser^[15], 60 Watts of average power produced from a Yb:YAG laser in the form of fs pulses (1.9 MW peak

powers)^[16], and a picosecond pulse stream at 160 GHz from a passively mode-locked diode pumped Nd:YVO₄ crystal^[17].

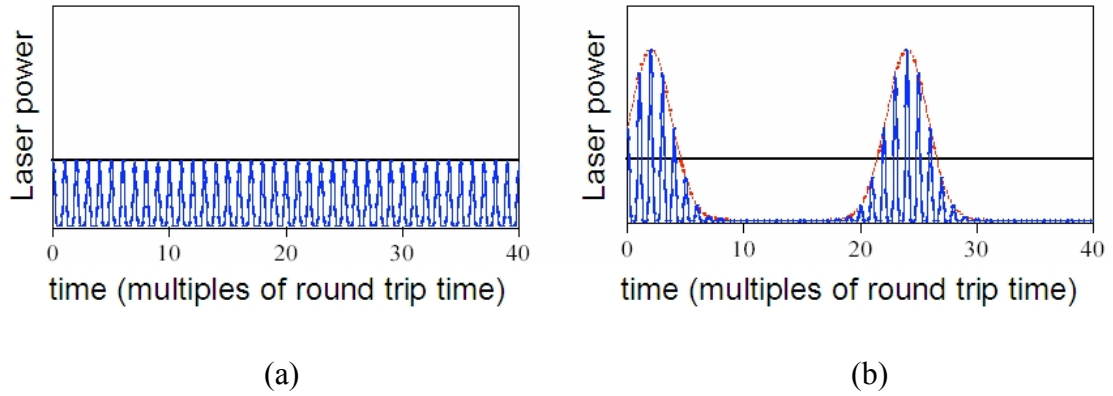


Fig. A.3. (a) The ideal mode-locked situation where every pulse is of uniform height, and (b) where the mode-locked pulses are present within a lower repetition rate Q-switch pulse (Q-switched mode-locking).

While crystal-based lasers have produced pulses as short as a few femtoseconds, they often have the practical drawback of extended cavity configurations and very high pump powers. For example, the Yb:YAG mode-locked laser quoted above which produces 60 Watts average power has 18 cavity components and requires a pump power of 370 Watts, Fig. A.4. Typically, the solid-state crystal systems involve geometries that require at least several discrete optical components to form the cavity. The crystals also tend to be low gain, requiring long lengths of active medium for higher pulse powers. Also, many crystals are not compatible with 1550 nm telecommunication components, although Cr⁴⁺:YAG crystals do have tuneable emission around this region and pulses as short as 115 fs for repetition rates of 2.6 GHz have been demonstrated^[18]. The primary goal for much of the mode-locked solid-state laser development appears to be ultra-short pulse duration (<10's of fs) with as high peak pulse power and wall plug efficiency as possible. A few papers do quote timing jitter for mode-locked crystal lasers, i.e. 53 fs (integrated SSB phase noise over 1 kHz – 40 MHz) for a 100 MHz repetition rate Ti:sapphire ($\lambda=600\text{-}1200\text{nm}$) laser^[19], and 20 fs for a Cr:LiSAf over the frequency range 25 mHz – 10 kHz^[20].

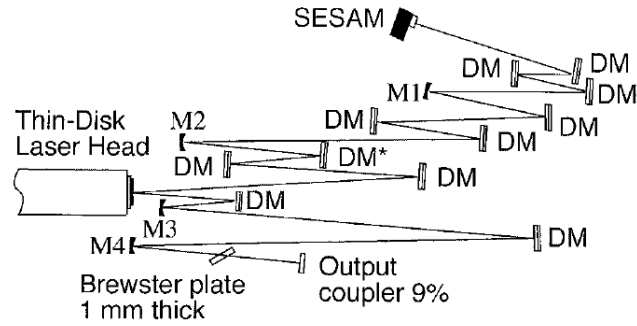


Fig. A.A. Yb:YAG extended cavity with 18 intra-cavity components (taken from *Optics Letters*, 28(5), 2003, Ref. [16]). DM = dispersive mirror.

Krainer et al.^[21] have reported a Nd:GdVO₄ mode-locked laser system with a repetition rate of 10 GHz and a footprint of only 13 cm by 3 cm, a compact device. They also analysed the timing jitter from the pulses, using the single sideband phase noise method, and found it to be measurement limited to 146 fs over the integration range 10 Hz – 10 MHz. Since this is a passive device, they used a phase locked loop to lock the cavity length to a clock signal^[20]. The only practical drawback to this system is that the wavelength is 1063 nm and not 1550 nm. There do not appear to be any similar timing jitter figures published for Cr⁴⁺:YAG mode-locked lasers operating in the 1550 nm region.

Since this study is concerned with pulses applicable to the ADC application, i.e. pulses sources with GHz repetition rates around 1550 nm with as low timing jitter as possible, only mode-locked lasers meeting these criteria will be discussed in any detail for the remainder of this section, in particular mode-locked semiconductor diode lasers and mode-locked fibre lasers.

A.3.1 Diode laser mode-locking

The simplest diode laser mode-locking technique is the direct modulation of a single contact device's gain section, with a frequency equal to the repetition frequency of the cavity. Alternatively, the electro-absorption section of a multi-contact device can also be modulated at the cavity repetition frequency to achieve mode-locking (c.f. Q-switching discussed in Section A.2). Since internal cavity diode lasers can typically have very short cavity lengths of the order ~250μm, repetition rates can be 100's of

GHz, which is not feasible to drive electronically. Therefore an external cavity can be used or alternatively the diode can be driven with a sub-harmonic frequency, as implemented at 50 GHz^[22].

Many of the techniques employed to reduce the mode-locked diode laser timing jitter are similar to those described previously for gain and Q-switched diode timing jitter reduction, such as optical pulse train injection. Passive mode-locking can be achieved in a multi-contact diode laser by having one section reverse biased^[23]. Generally, passively mode-locked diode lasers have a higher timing jitter since there is no stable frequency reference, hence the spontaneous emission fluctuates the phases of the optical pulses within the laser cavity and therefore the mode-locked frequency fluctuates giving timing jitter^[24]. Actively mode-locked diode lasers with external electronic drive frequencies do not have this problem. Passively mode-locked lasers can be stabilised by the injection of optical pulse trains into the cavity, which need only be a sub-harmonic of the mode-locked frequency, a convenient technique for realising very high repetition rate passively mode-locked diode lasers (>100 GHz). However, optical feedback methods only give a minimum timing jitter of around 200 fs^[24] for 10 GHz sources, around the same value possible with gain and Q-switching of a diode laser.

As early as 1990, results were being published detailing sub-100fs timing jitters for actively mode-locked semiconductor diode lasers^[25]. The physical set-up used in Ref. [25] appears fairly robust, consisting of only the diode laser and two anti-reflection coated grin lenses within an extended cavity. The laser in this instance was a single contact device, modulated with a drive current at 5 GHz. The output pulse train had pulse widths of 600 fs and 30 mW peak powers, and an absolute timing jitter of 170 fs (calculated by analysis of the harmonics on a spectrum analyser) and a residual timing jitter of 50 fs calculated over the frequency offset range of 150 Hz to 50 MHz (using the SSB phase noise approach). The residual phase noise is obtained by mixing at quadrature the optical pulse train output from a detector with a split portion of the signal from the microwave synthesiser used to mode-lock the laser. The synthesiser noise is therefore cancelled out, leaving only the noise from the laser. It was not possible from their published SSB phase noise spectra to interpolate over the range 10 Hz – 10 MHz.

Work by Delfyett et al.^[26,27], demonstrated that there is a fundamental relationship between the residual phase noise spectra (and hence timing jitter) and the line-width of the optical longitudinal modes in mode-locked lasers. In a later paper^[28], the same group reported in detail simulated and experimental results which demonstrate the different phase noise spectra for fundamental and harmonically mode-locked lasers. Here they demonstrate that a “corner frequency” is observed for both fundamental and harmonic mode-locking, the frequency at which the relatively uniform phase noise sharply decreases, see schematic Fig. A.5. This corner frequency is a useful figure of merit for describing mode-locked laser timing jitter performance. An important discovery is that the corner frequency occurs at a higher frequency for fundamentally mode-locked lasers than the harmonically mode-locked variation. In the example given, the authors compare a fundamentally mode-locked 10 GHz pulse train with a laser harmonically mode-locked to the 10th harmonic which also has an output repetition rate of 10 GHz. The corner frequencies are 44.6 MHz and 5.4 MHz respectively, showing the superior timing jitter of the harmonically mode-locked laser (both versions had a SSB phase noise of approx -100 dBc/Hz out to the corner frequency), and it would appear that the corner frequency is directly linked to the linewidth. For frequency offsets beyond the corner frequency they observe a roll-off of approximately 25 dB/decade in the SSB phase noise for both setups.

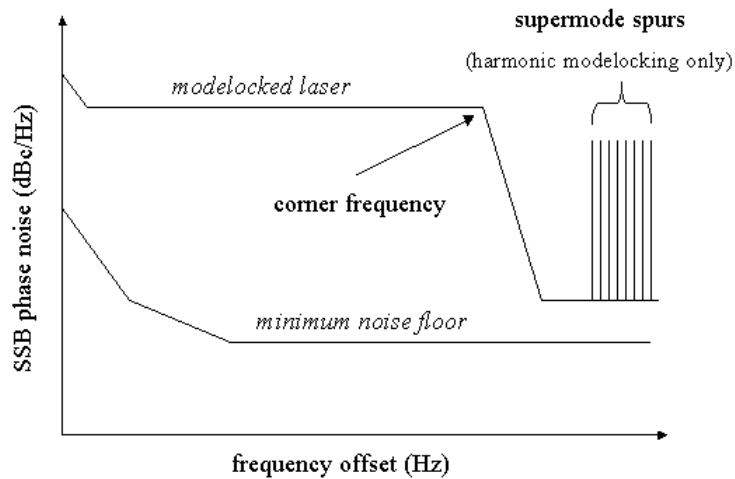


Fig. A.5. Generic plot demonstrating the flat SSB phase noise, out to a corner frequency, after which the phase noise falls off at approximately 25 dB/decade. Harmonically mode-locked lasers exhibit supermode spurs at higher frequencies – these are not present for fundamentally mode-locked lasers.

The attraction of harmonic mode-locking is that, in conjunction with long cavity lengths, it generates narrow longitudinal mode linewidths with a close-in corner frequency (compared to fundamental mode-locking) and hence low timing jitter. A less desirable property is that harmonic mode-locking also generates super-mode beat noise, which appears as noise spurs at cavity harmonics at frequencies beyond the corner frequency, Fig. A.5. These are not present for fundamental mode-locking. These noise spurs can however be completely removed through the use of an intra-cavity high finesse etalon, chosen to have a free spectral range which matches the mode-locking frequency^[27]. Using the SSB phase noise approach, in 2001 the same group published figures of 670 fs timing jitter for fundamental mode-locking and 240 fs for harmonically mode-locked diode lasers, over the offset range 10 Hz up to the Nyquist frequency of 5 GHz (not 10 MHz!)^[29]. To summarise the work of Delfyett et al., by harmonically mode-locking a semiconductor diode laser with an extended cavity and an intra-cavity etalon, they have realised timing jitters as low as 18 fs, by integrating the SSB phase noise over the range 10 Hz – 10 MHz^[27]. It should be noted that the setup in Ref. [27] is a complex structure and does not appear to be very robust. However, the next section of this report will detail a much more rugged waveguide version of this laser developed by the same group, with very similar timing jitter properties.

Even better figures have been reported by Jones et al.^[30], with a mode-locked semiconductor diode laser locked via a feedback loop to an external atomic clock signal. Again this is a complex and apparently delicate set-up, with the mode-locked diode laser locked to a Ti:sapphire optical comb which in turn is locked to an atomic iodine transition at 532 nm. The SSB phase noise for this set-up yields a timing jitter of 22 fs, integrated from 1 Hz to 100 MHz (not 10 Hz – 10 MHz). Due to the complexity and cost of this system, it is unlikely to be of use to a deployable, practical ADC system. However, for fixed location applications requiring a highly accurate optical clock pulse, this system appears to a very attractive option.

A.3.2 Mode-locked fibre lasers

Single-mode, rare-earth-doped fibres are widely used for lasers and amplifiers in telecommunications and other applications requiring compact, rugged optical sources with high beam quality. Attractive properties of fibre sources include low-threshold

operation and high electrical-to-optical efficiency (up to 39% for Yb-doped fibre amplifiers^[31], although efficiencies around 15% are more typical for commercial Er-doped units^[32]). The glass host broadens the optical transitions in the rare-earth ion dopants, yielding continuous tunability of ~100 nm around the centre frequency, with erbium doped fibre lasers (EDFLs) and amplifiers centred on the 1550 nm region. EDFLs can be diode pumped and offer low heat dissipation and easy heat removal since they have high surface area to volume ratios. A significant advantage of using an EDFL is its obvious compatibility with other fibre-optic components, removing the alignment and ruggedness difficulties associated with bulk optics components.

Fig. A.6 shows the generic set-up for an actively mode-locked EDFL. An electro-optic modulator is driven by an external microwave source with a frequency corresponding to a high harmonic of the cavity's fundamental round trip time. For a 190 metre cavity length, operating at 10 GHz, there are over 10,000 pulses travelling within the cavity^[33]. A drawback with all mode-locked EDFLs is their susceptibility to temperature variations and mechanical disturbances, which can cause the cavity length to fluctuate. When this happens, the microwave source is detuned from the harmonic frequency of the cavity resonance and the pulse train becomes unstable (with higher timing jitter). To counteract this a regenerative feedback technique can be employed^[34], where a portion of the output pulse train is detected and fed back to the modulator in the ring cavity via an appropriate phase delay in the regenerative feedback loop to ensure that the phase of the optical pulses compensates for any change in cavity length. The regenerative technique therefore continually adjusts the RF drive frequency of the modulator using a frequency derived from the mode-locked laser itself.

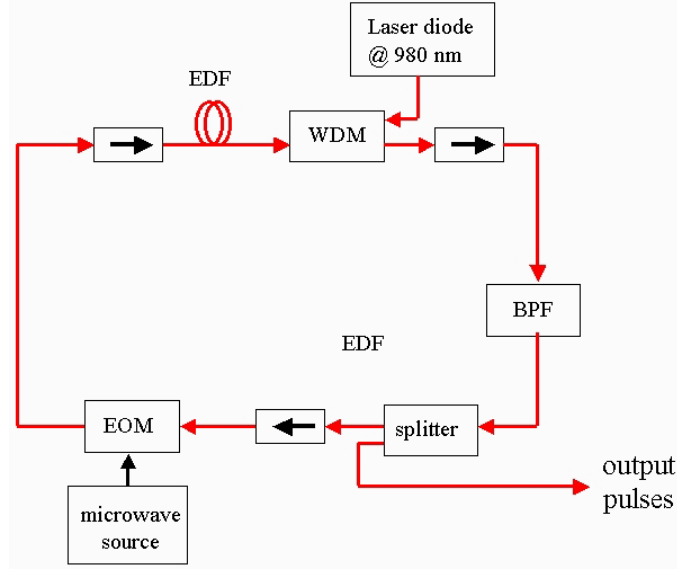


Fig. A.6. Schematic of an actively mode-locked fibre ring laser set-up. The diode pump is added to the ring via a wavelength selective coupler (WDM), a band pass filter (BPF) selects the desired output wavelength and a microwave source drives an electro-optic modulator (EOM) to mode-lock the EDFL. Isolators ensure that pulses travel around the ring in one direction only.

In the photonic ADC literature, some of the lowest fibre laser timing jitter results published are those from the much cited work by the HRL/Pritel group (Ng et al.), the Naval Research Laboratory group (NRL) (Duling et al.) and the MIT group (Grein, Ippen, Haus et al.), see Table A.1. All groups actively mode-lock a fibre laser to obtain pulses very close to 10 GHz repetition rates. The HRL group in particular detail extensively in their papers their timing jitter measurement techniques. In a recent paper^[35], they discuss SSB-phase noise measurements over several ranges, measurements via the harmonic approach and they also use the pulses in an ADC sampling system to assess the pulse performance. Ippen's MIT group believe that the performance of these mode-locked EDFL is now approaching the fundamental limit of timing jitter imposed by amplified spontaneous emission within the laser cavity^[36]. They have developed a model on the theory of timing jitter and for the SSB phase noise integration range 10 Hz – 10 MHz they obtain 37 fs timing jitter experimentally compared to 19.3 fs in theory^[36]. The discrepancy is mainly due to the inclusion of erroneous noise spurs from the measurement system. Here the cavity length fluctuations are controlled by a phase-lock loop with a fibre-wound piezoelectric cylinder and a control circuit. Finally, Clark's group have published a timing jitter of 9.9 fs, integrated over the range 100 Hz – 1 MHz^[33]. They add dispersion compensating fibre to the

cavity to obtain a net anomalous dispersion which they believe is important for controlling the ASE contribution to timing jitter.

Frequency range	Timing jitter in fs		
	MIT [Haus, Grein, Ippen et al.]	HRL [Ng et al.]	NRL [Clark, Curruthers, Duling et al.]
10 Hz – 1 MHz	-	-	<153 (151)
100 Hz – 1 MHz	-	10.3	<9.9 (8.9)
1 k Hz – 1 MHz	-	-	<5.1 (2.1)
10 Hz – 10 MHz	37	30.58	-
100 Hz – 40 MHz	-	14.9	-

Table A.1. Selected published EDFL mode-locked ring set-up timing jitters. Values in brackets are the synthesiser noise for that range. Note that the MIT group use the same microwave source to drive the laser and act as the local oscillator (LO) in the phase noise measurements, where as NRL and HRL use a different source for the LO.

To compare the results from these three mode-locked EDFL set-ups over the same frequency offset range, values were taken from the NRL's published SSB phase noise plots and interpolated for this report to provide a "normalised" offset range of 10 Hz to 10 MHz. The MIT and HRL groups already quote over this range. The values then become: 153 fs (NRL), 37 fs (MIT) and 30 fs (for the HRL group), as shown in Table A.2. The MIT group split the microwave source signal which drives the mode-locked laser and use that signal as the local oscillator for the SSB phase noise measurements. The other two groups use a second independent source for their measurements. Inexplicably the NRL group have a factor of 2 in their timing jitter equation, and so when interpolating their timing jitter values, an answer equal to half of their published values is obtained, whereas interpolating the HRL values yields the same timing jitters as those published to within a few fs. It is not possible to interpolate the MIT results as the format of the published plots is not suitable.

Fig. A.7 and Table A.3 show that due to the very low SSB phase noise at frequency offsets greater than 10 MHz, the contribution of the SSB phase noise at offsets from 10 MHz to Nyquist or to the full repetition rate roughly doubles the timing jitter. This

interpolation assumes that there are no significant phase noise artefacts present at large frequency offsets.

Frequency range	Timing jitter in fs		
	MIT [Haus, Grein, Ippen et al.]	HRL [Ng et al.]	NRL [Clark, Curruthers, Duling et al.]
10 Hz – 10 MHz	37	31	78

Table A.2. Comparison of timing jitter over “normalised” offset range of 10 Hz – 10 MHz. The MIT and HRL values are published figures and the NRL value is interpolated from published SSB phase noise plots.

Frequency range	Timing jitter in fs	
	HRL [Ng et al.]	NRL [Clark, Curruthers, Duling et al.]
10 Hz - 10 MHz	31	78
10 Hz – Nyquist	45	92
10 Hz – repetition rate	54	110

Table A.3. Interpolating the SSB phase noise timing jitter figures for offsets from 10 Hz up to the Nyquist frequency and beyond. Note, interpolated value of 31 fs over 10 Hz to 10 MHz matches published value.

[NRL^[33] repetition rate = 11.4 GHz (i.e. Nyquist = 5.7 GHz)

HRL^[35] repetition rate = 10.24 GHz (i.e. Nyquist = 5.12 GHz)]

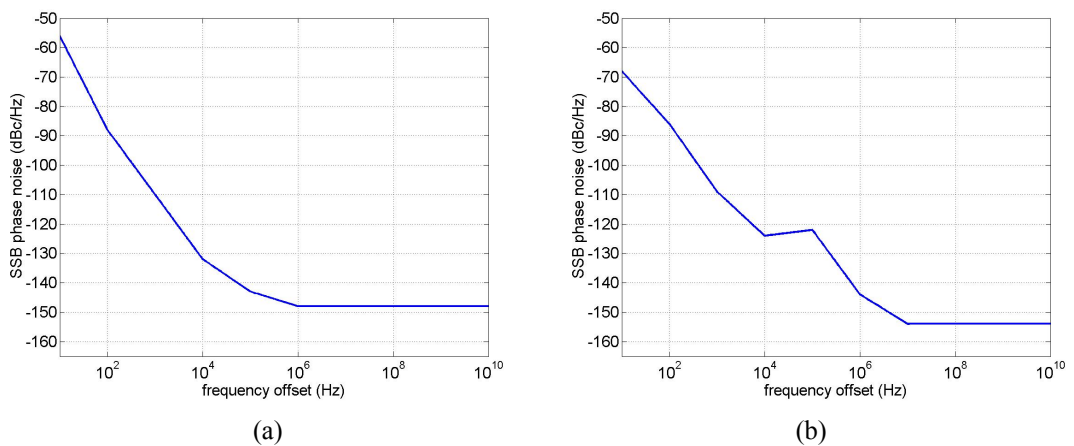


Fig. A.7. The interpolated SSB phase noise plots of (a) Clark et al.^[33] and (b) Ng. et al.^[35].

A.3.3 Mode-locked waveguide lasers

This chapter now concludes the review of low timing jitter laser implementation options by considering one final approach based on mode-locked erbium doped waveguide lasers (EDWL), as opposed to erbium doped fibre. The advantage of using a waveguide is that it can be doped with a much higher concentration than the fibre equivalent, so that the high dopant concentration and low cavity loss allow for compact mode-locking set-ups. Delfyett et al.^[37] harmonically mode-locked a cavity at 10 GHz (using the 469th harmonic) and used a Fabry Perot etalon to suppress the supermodes as discussed previously. A residual timing jitter of 21 fs was measured using the residual SSB phase noise over the range 10 Hz – 100 MHz, where the reference frequency of the phase noise kit was supplied by the same microwave source which was used to mode-lock the laser. Whilst this set-up has not yet been ruggedised, it is potentially a compact and environmentally stable set-up, see Fig. A.7, attractive for airborne ADC applications.

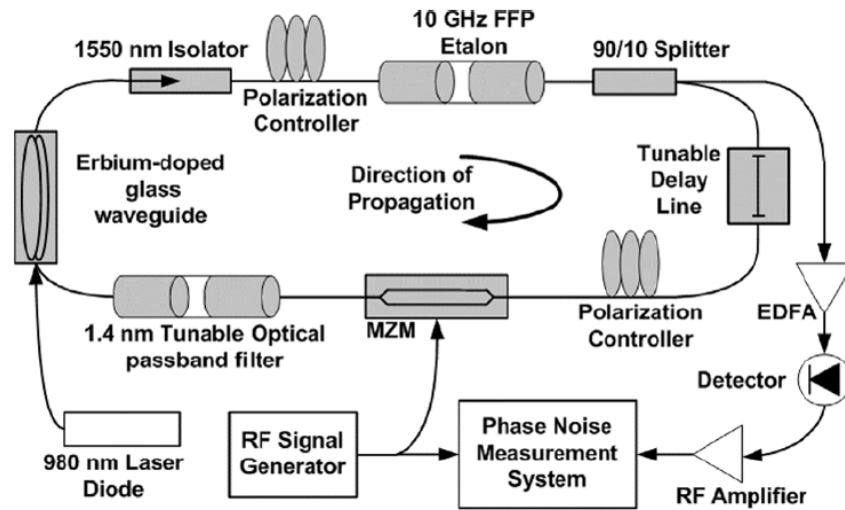


Fig. A.7. Potentially compact EDWL ring structure which could be ruggedised if required (image taken from IEEE Phot Tech Lett 2005, Ref. [37]).

A.4 Conclusions on options for low jitter, high repetition rate pulse sources

By investigating the timing jitter of gain switched, Q-switched and mode-locked lasers, it has become apparent that there is a difficulty in direct comparison of published timing jitter figures since different groups use different measurement techniques. Where

harmonic analysis of the timing jitter (Leep and Holm's approach) is compared to the SSB phase noise approach in the same paper, the SSB frequency range often appears to be chosen selectively to ensure that the two sets of figures match^[3].

Table A.4 is an attempt to solve this variation in measurement techniques, as it gives some of the lowest published timing jitter for each laser type, and also a second column which contains an estimated timing jitter measured from the published SSB phase noise spectra which is then interpolated and integrated to give a "normalised" range of 10 Hz to 10 MHz for this report. Some groups such as Delfyett et al. state that the SSB phase noise should be integrated up to the Nyquist frequency (5 GHz for the 10 GHz sources), however this has simply not been possible for many groups given their measurement equipment. Ng et al.^[35] state that the lower frequency offset limit is set to 100 Hz by the long-term period of stability of interest to their application in ADC sampling (set by $\Delta T \sim 1/\sqrt{[2\pi\Delta f_L]}$).

Another complication in making direct comparisons of published timing jitter using integrated SSB phase noise is that some groups measure the residual phase noise and others the absolute phase noise (residual measurements use the same microwave source, hence eliminating the source's phase noise, whereas the absolute measurements use a second source). While residual measurements are of interest in isolating the laser performance, for practical ADC systems where the input signal to be quantised is not related to the microwave source generating the sampling pulses, the absolute timing jitter is the limiting factor for the sampling system. Therefore, for practical implementations of the pulse source, such as the ADC application, the timing jitter derived from the absolute SSB phase noise is the important parameter.

Laser type	Ref.	Repetition rate (GHz)	Published timing jitter (fs) [and measurement method]	‘Normalised’ timing jitter (fs) [SSB phase noise $\Delta f = 10\text{ Hz to } 10\text{ MHz}$]
Gain switched				
DFB seeded FP diode laser	6	311 MHz	860 fs over $\Delta f = 10\text{ Hz to } 311\text{ MHz}$	~300 fs*
Self-seeded FP diode laser	7	500 MHz	210 fs via harmonic analysis	N/a
CW seeded DFB	3	100 MHz	160 fs over $\Delta f = 10\text{ kHz to } 40\text{ MHz}$	~320 fs*
Q-switched				
2-section FP diode laser	10	5 GHz	250 fs via harmonic analysis	N/a
Mode-locked				
Nd:GdVO ₃ solid state system at 1063 nm	17	10 GHz	146 fs over $\Delta f = 10\text{ Hz to } 10\text{ MHz}$	146 fs
Actively mode-locked diode laser	25	5 GHz	170 fs absolute and 50 fs residual over $\Delta f = 150\text{ Hz to } 50\text{ MHz}$	N/a
Harmonically mode-locked diode lasers	27	10 GHz	240 fs over $\Delta f = 10\text{ Hz to } 5\text{ GHz}$, and 18 fs over $\Delta f = 10\text{ Hz to } 10\text{ MHz}$	18 fs
Mode-locked diode laser locked to Ti:sapphire comb and iodine atomic transition	30	5.98 GHz	22 fs over $\Delta f = 1\text{ Hz to } 100\text{ MHz}$	<<22 fs*
EDFL	36	10 GHz	37 fs over $\Delta f = 10\text{ Hz to } 10\text{ MHz}$	37 fs (R)
EDFL	33	10 GHz	153 fs over $\Delta f = 10\text{ Hz to } 1\text{ MHz}$	~78 fs*
EDFL	35	~10 GHz	30.58 fs $\Delta f = 10\text{ Hz to } 10\text{ MHz}$	30.58 fs
EDFW	37	10 GHz	21 fs $\Delta f = 10\text{ Hz to } 100\text{ MHz}$	<21 fs*(R)

Table A.4. Table of some of the lowest published timing jitter figures for each laser type. Emission wavelength is around 1550 nm unless otherwise stated. The right-hand column is an attempt to allow direct comparison by normalising over the SSB integration range 10 Hz – 10 MHz.

Key: *indicates this figure has been interpolated from published SSB spectra, (R) indicates that this is the residual phase noise and not the absolute value

Table A.4 summarises that gain switched and Q-switched lasers can have timing jitters as low as 200-300 fs. The best published timing jitter performances for the gain switching technique has been where seeding is used to stabilise the pulse operation. Low Q-switching timing jitter values have been obtained where a multi-contact laser diode has been driven by an external microwave source. These low jitter diode based devices are attractive as they offer acceptably low jitter performance for many mid-range ADC applications, leading to ~ 9 effective bits of resolution at 1 GHz sampling rates (5.7 bits at 10 GHz sampling rates). They are relatively cheap and compact, being based on diode lasers and as long as the feedback mechanism of the gain switched version can be implemented in fibre, both options could be ruggedised and compact in nature.

At least an order of magnitude improvement in timing jitter is observed for the mode-locking technique, with diode laser mode-locking offering telecommunications waveband pulse trains with timing jitters as low as around the order of 20 fs. This timing jitter allows ~ 10 bits of resolution at 10 GSa/s and ~ 13 bits at 1 GSa/s. Harmonic mode-locking has demonstrated the lowest jitter for laser diode mode-locking (lower than fundamental mode-locking), and requires a Fabry Perot etalon to remove supermode noise spurs. The mode-locked diode laser publications claiming the best timing jitter values have all involved extended cavity set-ups with multiple cavity elements in addition to the laser diode, making ruggedisation more difficult but not impossible. A much more elegant solution in terms of low timing jitter coupled with a potentially rugged set-up is employed through the use of a fibre ring laser, with either a laser diode pumped erbium doped fibre or waveguide providing the intra-cavity gain, and a modulator providing the mode-locking frequency. An additional complexity with the fibre ring approach is that cavity length fluctuations due to environmental effects must be compensated for, typically by the use of phase locked loops or piezo-electric stressing of the fibre.

If the ultimate goal is the lowest possible timing jitter at 1550 nm wavelength operation, then mode-locking a diode laser to a solid state laser comb, which in turn is locked to an atomic transition, would appear to provide by far the best timing jitter of $\ll 22$ fs, however this is not an economic or robust approach, and would seemingly have to be confined to a fixed, environmentally stable location.

A.5 Comparison with state-of-the-art crystal oscillators

For completeness, the SSB phase noise performance of two different crystal materials, quartz and sapphire, are mentioned to provide a comparison with the laser jitter performance. Ref. [19] compares the SSB phase noise of a 100 MHz Ti:sapphire mode-locked laser with a leading 100 MHz quartz crystal, made by Wenzel^[38]. State-of-the-art performance at ~ 10 GHz is demonstrated by Poseidon's sapphire crystal technology^[39]. The SSB phase noise of both crystals is plotted on Fig. A.8, with values taken from a paper comparing the performance of both crystal materials^[40].

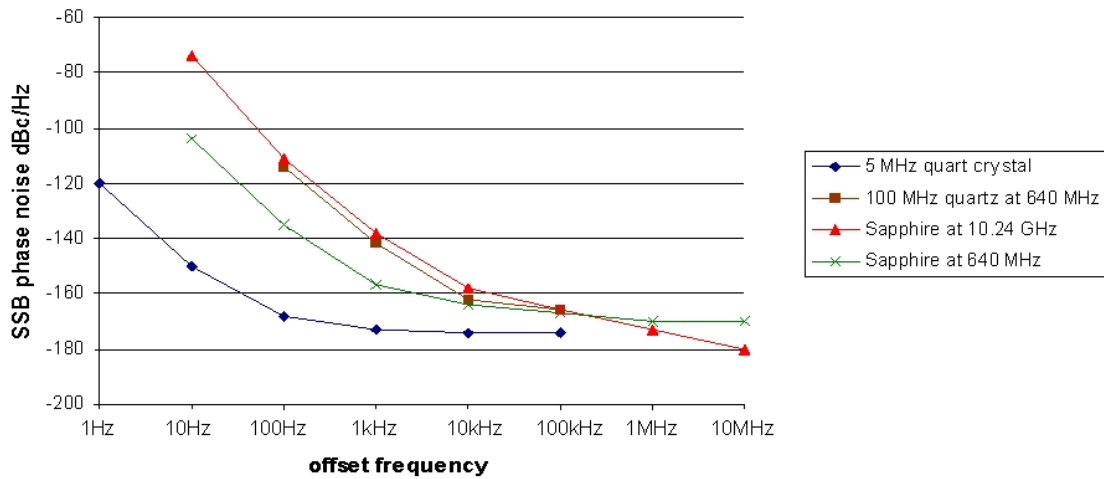


Fig. A.8. Phase noise plots generated from Wenzel and Poseidon published figures.

Integrating these SSB phase noise values yields timing jitters of ~ 5 fs over 10 Hz to 10 MHz for the sapphire crystal at either 640 MHz or 10 GHz (note that timing jitter $\propto 1/f_R$, see Eq. 3.1 on page 18), values that are less than an order of magnitude lower than the best published mode-locked laser timing jitter values, indicating just how stable the laser pulse sources are.

References for Appendix A

Gain switched

1. Williams K.A., White I.H., Burns D., Sibbett W., "Jitter reduction through feedback for picosecond pulsed InGaAsP lasers", IEEE J. Quantum. Elec., 32(11), pp. 1988-1994, 1996
2. Gunning P., Lucek J.K., Moodie D.G., Smith K., Davey R.P., Chernikov S.V., Guy M.J., Taylor J.R., Siddiqui A.S., "Gain switched DFB laser diode pulse source using continuous wave light

injection for jitter suppression and an electroabsorption modulator for pedestal suppression,”
Electron. Lett., 32(11), pp. 1010–1011, 1996

3. Nogiwa S., Kawaguchi Y., Ohta H., Endo Y., “Generation of gain-switched optical pulses with very low timing jitter by using external CW-light injection seeding”, Electron. Lett., 36(3), pp. 235-236, 2000
4. Huhse D., Schell M., Kaessner J., Bimberg D., Tarasov I.S., Gorbachov A.V., Garbuzov D.Z., “Generation of electrically wavelength tunable ($\Delta\lambda=40$ nm) singlemode laser pulses from a 1.3 μm Fabry-Perot laser by self-seeding in a fibre-optic configuration”, Electron. Lett., 30(2), pp. 157-158, 1994
5. Seo D-S, Kim D.Y., Liu H-F, "Timing jitter reduction of gain-switched DFB laser by external injection-seeding", Electron. Lett., 32(1), pp. 44-45, 1996
6. Reimann O., Huhse D., Bottcher E.H., Bimberg D., Stahlmann H.D., "Low jitter dual semiconductor laser system using electrical phase shift for fast temporal scanning in time-resolved pump and probe experiments", Conf. on Lasers and Electro-Optics (LEOS), Vol. 2, pp. 203 - 204, 1999
7. Schell M., Huhse D., Utz W., Kaessner J., Bimberg D., Tarasov I.S., “Jitter and dynamics of self-seeded Fabry-Perot laser diodes”, IEEE J. Quantum. Elec., 1(2), pp. 528-534, 1995

Q-switched

8. Vasil’ev P.P., White I.H., Burns D., Sibbett W., “High power, low jitter encoded picosecond pulse generation using an RF-locked self-Q-switched multicontact GaAs/GaAlAs diode laser”, Electron. Lett., 29(18), pp. 1593-1594, 1993
9. Khrushchev I.Y., Kitcher D.J., Williams K.A., White I.H., Laughton F.R., Pentty R.V., “Picosecond Q-switched bow-tie laser diode array”, Electron. Lett., 33(5), 1997
10. Shen A., Bouchoule S., Crozat P., Matorasing D., Lourtioz J.M., Kazmierski C., “Low timing jitter of gain- and Q-switched laser diodes for high bit rate OTDM applications,” Electron. Lett., 33(22), pp. 1875–1877, 1997

Mode-locked

11. GigaTera Product Group, CH-8005 Zurich, Switzerland; www.gigatera.com

12. PriTel Inc., Naperville, Illinois 60567-4025, USA; www.pritel.biz
13. DeMaria A.J., Stetser D.A., Heynau H., "Self mode-locking of lasers with saturable absorbers", *Appl. Phys. Lett.*, 8(7), pp. 174-176, 1996
14. Keller U., Miller D.A.B., Boyd G.D., Chiu T.H., Ferguson J.F., Asom M.T., "Solid-state low-loss intracavity saturable absorber for Nd:YLF lasers: an antiresonant semiconductor Fabry-Perot saturable absorber," *Opt. Lett.*, 17(7), pp. 505-507, 1992
15. Ell R., Morgner U., Krtner F.X., Fujimoto J.G., Ippen E.P., Scheuer V., Angelow G., Tschudi T., Lederer M.J., Boiko A., Luther-Davies B., "Generation of 5-fs pulses and octave-spanning spectra directly from a Ti:sapphire laser", *Opt. Lett.*, 26(6), pp. 373-375, 2001
16. Innerhofer E., Südmeyer T., Brunner F., Häring R., Aschwanden A., Paschotta R., Hönninger C., Kumkar M., Keller U., "60-W average power in 810-fs pulses from a thin-disk Yb:YAG laser", *Opt. Lett.*, 28(5), pp. 367-369, 2003
17. Krainer, L., Paschotta, R., Lecomte, S., Moser, M., Weingarten, K.J., Keller, U., "Compact Nd:YVO₄ lasers with pulse repetition rates up to 160 GHz", *IEEE J. of Quantum. Elect.*, 38(10), 2002
18. Tomaru T., "Two-element-cavity femtosecond Cr⁴⁺:YAG laser operating at a 2.6-GHz repetition rate", *Opt. Lett.*, 26(18), pp. 1439-1441, 2001
19. Scott, R.P., Langrock, C., Kolner, B.H., "Ultralow phase noise Ti:sapphire laser rivals 100 MHz crystal oscillator", *Conf. Lasers and Electro-Optics Society, LEOS*, Vol. 2, pp. 904 - 905, 2001
20. Tsuchida H., "Pulse timing stabilization of a mode-locked CrLiSAF laser", *Opt. Lett.*, 24(22), pp. 1641-1643, 1999
21. Krainer L., Nodop, D., Spühler, Lecomte S., Golling M. Paschotta R., Ebling D., Ohgoh T., Hayakawa T., Weingarten K.J., Keller U., "Compact 10-GHz Nd:GdVO₄ laser with a 0.5-W average output power and low timing jitter", *Opt. Lett.*, 29(22), pp. 2629-2631, 2004
22. Sato K., Kotaka I., Kondo Y., Yamamoto M., "Active mode locking at 50 GHz repetition frequency by half-frequency modulation of monolithic semiconductor lasers integrated with electroabsorption modulators", *Appl. Phys. Lett.*, 69(18), pp. 2626-2628, 1996

23. Derickson D.J., Morton P.A., Bowers J.E., Thornton R.L., "Comparison of timing jitter in external and monolithic cavity mode-locked semiconductor lasers", *Appl. Phys. Lett.* 59(26), pp. 3372-3374, 1991
24. Arahira S., Kutsuzawa S., Ogawa Y., "Extreme timing jitter reduction of a passively mode-locked laser diode by optical pulse injection", *IEEE J. Quantum Elect.*, 35(12), pp. 1805-1811, 1999
25. Derickson D.J., Mar A., Bowers J.E., "Residual and absolute timing jitter in actively mode-locked semiconductor lasers", *Electron. Lett.*, 26(24), pp. 2026-2028, 1990
26. Delfyett P.J., DePriest C., Yilmaz T., "Signal processing at the speed of light. Mode-locked semiconductor optical clocks for photonic sampling applications", *IEEE Circuit Device*, pp. 28-35, Sept. 2002
27. DePriest C.M., Yilmaz T., Delfyett P.J., Etemad S., Braun A., Abeles J., "Ultralow noise and supermode suppression in an actively mode-locked external-cavity semiconductor diode ring laser", *Opt. Lett.*, 27(9), pp. 719-721, 2002
28. Yilmaz T., DePriest C. M., Braun A., Abeles J.H., Delfyett P.J., "Noise in fundamental and harmonic mode-locked semiconductor lasers: experiments and simulations", *IEEE J. Quantum Elect.*, 39(7), pp. 838-849, 2003
29. Yilmaz T., DePriest C.M., Delfyett P.J., "Complete noise characterization of external cavity semiconductor laser hybridly mode-locked at 10 GHz", *Electron. Lett.*, 37(22), pp. 1338-1339, 2001
30. Jones D.J., Holman K.W., Notcutt M., Ye J., Chandalia J., Jiang L.A., Ippen E.P., Yokoyama H., "Ultralow-jitter, 1550-nm mode-locked semiconductor laser synchronized to a visible optical frequency standard", *Opt. Lett.*, 28(10), pp. 813-815, 2003

Mode-locked fibre lasers

31. Goldberg L., Koplow R.P., Kliner D.A.V., "Highly efficient 4-W Yb-doped fiber amplifier pumped by a broad-stripe laser diode", *Opt. Lett.*, 24(10), pp. 673-675, 1999
32. IPG Photonics Corporation, Oxford, MA 01540, USA; www.ipgphotonics.com
33. Clark T.R., Carruthers T.F., Mathews P.J., Duling I.N., "Phase noise measurements of ultrastable 10 GHz harmonically mode-locked fibre laser", *Electron. Lett.*, 35(9), pp. 720-721, 1999

- 34. Nakazaw M., Yoshida E., Kimura Y., “Ultrastable harmonically and regeneratively mode-locked polarisation maintaining erbium fibre ring laser”, *Electron. Lett.*, 30(19), pp. 1603-1605, 1994
- 35. Ng W., So M.Y., Stephens R., Persechini D., “Characterization of the jitter in a mode-locked Er-fiber laser and its application in photonic sampling for analog-to-digital conversion at 10 GSa/s”, *J Lightwave Technol.*, 22(8), pp 1953-1961, 2004
- 36. Grein M.E., Jiang L.A., Haus H.A., Ippen E.P., McNeilage C., Searls J.H., Windeler R.S., “Observation of quantum-limited timing jitter in an active, harmonically mode-locked fiber laser”, *Opt. Lett.*, 27(11), pp. 957-959, 2002
- 37. Malowicki J.E., Fanto M.L., Hayduk M.J., Delfyett P.J., “Harmonically mode-locked glass waveguide laser with 21-fs timing jitter”, *IEEE Photon. Tech. L.*, 17(1), 2005

Crystal references

- 38. Wenzel Associates, Texas 78758, USA; www.wenzel.com
- 39. Poseidon Scientific Instruments Pty Ltd, Fremantle WA 6160, Australia; www.psi.com.au
- 40. Mossammaparast M., McNeilage C., Stockwell A., Searls J.H., Suddaby M.E., "Low phase noise division from X-band to 640 MHz", *IEEE Frequency Control Symposium and PDA Exhibition*, pp. 685-689, 2002

B. Jitter measurement techniques

B.1 Introduction

In the literature describing pulsed laser sources, there are three main methods employed to determine the amplitude and timing jitter. By far the crudest of these is the use of a sampling oscilloscope with a long persistence display time so that many successive pulses are overlapped and the amplitude or timing jitter is simply the width of the resulting trace. This method may be acceptable for large jitter values, such as 10% amplitude jitter^[1], however, it is not accurate enough to determine sub-picosecond timing jitter, even with the fastest available oscilloscopes.

Instead, two accurate jitter measurement techniques widely used involve either integrating the relative harmonic powers captured on a spectrum analyser or alternatively integrating the single-sideband phase noise of the pulse train using a phase noise measurement set-up. For the remainder of Appendix B, these two techniques are referred to as RIHP (relative integrated harmonic power) and SSB (single-sideband) phase noise for convenience.

In order to increase confidence in the timing jitter results obtained using the RIHP method, it is desirable to be able to measure many harmonics, but this is not possible for high repetition rate pulse trains of several 10's of GHz, since commercially available detectors and spectrum analysers are typically limited to ~50 GHz. Therefore the approach using the SSB phase-noise measurement is the most reliable technique for pulse trains with repetition rates of 10's of GHz, since only frequency offsets around the repetition rate of the pulses needs to be analysed.

Another approach is to use a photonic ADC to sample a known input sinusoidal waveform to determine the accuracy of the sampling pulse train. The phase encoded method employed by the MIT group^[2] has the benefit that it inherently performs a high level of amplitude modulation suppression, therefore allowing isolation and measurement of the timing jitter only. This was verified by intentionally amplitude modulating the input sampling pulse train and observing that the phase encoded set-up

suppressed the added amplitude jitter by 48 dB. Using this technique they experimentally measured an upper bound of 55 fs for the modelocked fibre laser used to perform the optical sampling.

B.2 Phase noise approach to jitter measurement

The carrier frequency instability is commonly measured by noting the average carrier frequency and power and then measuring the signal power at various offsets from the carrier frequency in a defined bandwidth, expressed as a logarithmic ratio compared to the total carrier power^[3]. Typically this is normalised to be the equivalent signal power that would be present if the measurement bandwidth were 1 Hz.

The most basic approach to making phase noise measurements involves using a spectrum analyser to measure the RF signal power in a specific bandwidth. In fact most modern analysers include software functions which convert a measured signal level from its absolute value to the equivalent noise signal in a 1 Hz bandwidth. Often this software will allow for the different equivalent noise bandwidths of the analyser's filters. In addition the software needs to correct for the fact that analysers typically use logarithmic detectors rather than true RMS devices. In practice however this approach is limited by the poor noise figure of most spectrum analyser's front end and the fact that they often offer very limited offset ranges.

The *quadrature technique* is a much more accurate approach involving the use of two oscillators at identical frequencies, one being the source under test and the other a reference source, (ideally) with a phase noise performance known to be better than that of the test source. The oscillator outputs are combined in a mixer and the resulting output signal is filtered and amplified by a low noise amplifier. The output is then measured by a fast Fourier transform (FFT) analyser or a spectrum analyser. The phase of the two oscillators must be set so that they are at quadrature at the mixer input, so that it behaves as a phase detector. One difficulty with this set-up can be ensuring that the source phases remain at quadrature, via the use of a phase locked loop, which requires calibration to ensure that the relatively high level of low phase noise does not overload the mixer, making it behave in a nonlinear manner and hence invalidating the measurement. It is therefore necessary to recalibrate the system before every

measurement since the sensitivity of the measurement is dependent on the insertion loss and drive level used for the mixer.

Once the phase noise spectrum has been measured, it is then possible to calculate the total jitter by integrating the single sideband phase noise measured relative to the carrier, $L(\phi)$, over the required bandwidth. Therefore the rms phase jitter is given by

$$\sigma_{\tau} = \sqrt{2.L(\phi)} \approx \frac{1}{2\pi f_R} \sqrt{\int_{f_{\min}}^{f_{\max}} 2.L(f)df} \quad (\text{B.1})$$

where f_{\max} and f_{\min} represent the upper and lower boundaries of the frequency range and f_R is the pulse repetition rate. Curiously the NRL group^[4] have an additional factor of 2 in their equivalent version of Eq. B.1, in contrast to others such as the Pritel/HRL group^[5].

For pulsed lasers driven by an electronic microwave source, the absolute SSB phase noise is obtained when the reference frequency is from a second independent microwave source. This allows calculation of the absolute timing jitter of the pulsed laser system as a whole. The contribution of the optical set-up to the timing jitter can be isolated by calculating the residual timing jitter measured from the residual SSB phase noise, where the microwave source is split and used as both the laser drive and the reference source.

One major difficulty in comparing the performance of sources using the SSB phase noise approach is that different authors quote different frequency ranges, so care must be taken to ensure that a seemingly low jitter source has not been measured over a very narrow frequency range.

In a review of methods for obtaining picosecond pulses from InGaAsP diode lasers^[6], a group at St Andrews University discuss the important integration ranges for accurate timing jitter calculation. They argue that for pulses generated using an electronic microwave source, the source has frequency variations which correlate to the nominal modulation frequency. Therefore, after several modulation periods, the jitter builds-up cumulatively, leading to higher long-term correlated jitter. In the frequency domain, this

corresponds to higher levels of phase noise close to the nominal modulation frequency, which decreases for frequencies further offset from the modulation frequency. Any laser pulse train driven from such a microwave oscillator will have phase noise directly corresponding to the oscillator's phase noise. Additional phase noise contributions will come from the laser noise processes such as spontaneous emission noise and pulse turn-on dynamics. However laser noise is a broadband jitter source which is generally uncorrelated to the electrical drive, manifesting itself as pulse-to-pulse jitter, and can be measured from a lower limit of a few megahertz across the complete spectrum. Papers have shown that the long-term correlated timing jitter added by the laser is negligible, for gain-switching^[7], Q-switching^[8] and mode-locking^[9] pulse generation techniques.

Where the pulses are to be used for optical sampling however, it is important that the SSB phase noise is integrated up to offset frequencies equal to the Nyquist frequency (Nyquist frequency = half the pulse repetition rate). It may be that the contributions to the timing jitter due to the SSB at large offsets are relatively negligible but for completeness integration up to the Nyquist frequency should be performed. The lower frequency offset for high sample rate ADC applications is governed by the time window over which information is to be extracted, for example from FFT windowing. For ADC systems operating at in the GSample/s regime, 0.1 seconds provides a significant amount of data for a subsequent FFT windowing process, and so a lower offset of 10 Hz would seem to be acceptable^[4,5].

One of the highest specification commercially available phase noise measurement systems is the Agilent E5505A, which can measure over the frequency offset range of 0.01 Hz to 100 MHz, with a phase noise sensitivity of -180 dBc/Hz. This limited upper frequency limit eliminates the possibility of integrating the phase noise from \sim DC up to the Nyquist frequency of a gigahertz pulse train, hence either discrete manual SSB phase noise measurements of high frequency offsets must be performed or assumptions made about the high frequency SSB phase noise behaviour.

B.3 Measuring jitter from the power spectrum

Both Von der Linde^[10] and Leep and Holm^[11] are widely quoted for their work detailing the method of using a spectrum analyser to determine both the timing and amplitude jitter from harmonic analysis of a train of optical pulses. Von der Linde detailed how different types of noise present in mode-locked dye and argon ion lasers can be recognised in a quantitative manner, even when they occur simultaneously, such as fluctuations of the pulse energy, pulse repetition rate and pulse duration. Leep and Holm's analysis gives detailed description of how information present in the spectrum can be used to directly calculate both the amplitude and timing jitter. Leep and Holm assume that the pulse train jitter is from an uncorrelated jitter source, which in their case was a gain-switched semiconductor laser with incoherent jitter artefacts introduced by turn-on transients. However they state that their derived equations are so similar to those used to interpret spectra exhibiting mixed correlated and uncorrelated noise that both types of noise are accommodated by their approach.

Fig. B.1 illustrates a schematic of the first 4 harmonics of a pulse train captured on a spectrum analyser, with the higher harmonics gradually decreasing in magnitude while the noise floor simultaneously increases for the higher frequencies. Mathematically, for every k 'th harmonic, the integrated relative power B_k is the power of the continuous part of the envelope of discrete lines, $M(\omega)$, relative to the power in each harmonic ω_k .

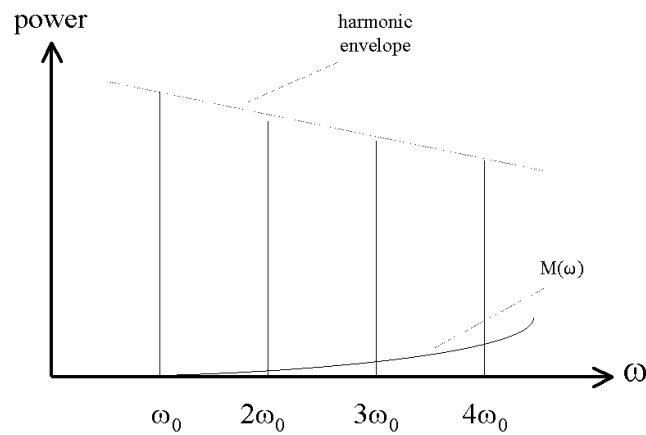


Fig. B.1. Schematic of spectrum of a pulse train displaying uncorrelated jitter. Note the decreasing intensity of the harmonic envelope and increasing noise floor $M(\omega)$ as ω increases.

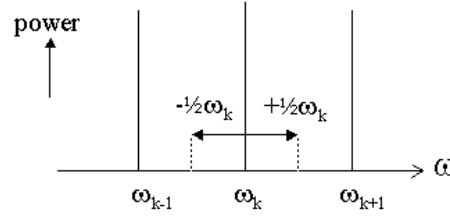


Fig. B.2. The integrated relative power, B_k , is the integral of the continuous part of the power spectral density $M(\omega)$ of every k 'th harmonic, integrated over the range $\omega_k \pm \frac{1}{2}\omega_0$, relative to the power in the k 'th harmonic

Leep and Holm derive the following relationship between the relative integrated harmonic power and the amplitude and timing jitter:

$$B_k = \sigma_r^2 + (k^2 + \frac{1}{12})\omega_0^2 \sigma_t^2 \quad (\text{B.2})$$

where σ_r^2 = relative variance of the intensities x_n

σ_t^2 = timing jitter variance

k = harmonic number

$\omega_0 = \frac{2\pi}{T}$ = pulse repetition frequency

$$\text{and } \sigma_r^2 = \frac{\sigma_x^2}{\langle x \rangle^2} \quad \text{where } \sigma_x^2 = \langle x^2 \rangle - \langle x \rangle^2$$

By simultaneous equations, both the amplitude and timing jitter can be found independently from two successive relative integrated harmonic values:

$$\sigma_r^2 = B_k - \frac{(k^2 + \frac{1}{12})(B_{k+1} - B_k)}{2k + 1} \quad (\text{B.3})$$

$$\sigma_t^2 = \frac{B_{k+1} - B_k}{(2k + 1)\omega^2} \quad (\text{B.4})$$

It is therefore possible to measure both the amplitude and timing jitter from information obtained from only the first two successive harmonics, although in practice it is desirable to compare the jitter values from multiple harmonics to confirm consistency. It can be seen from Eqs. B.3 & B.4 that only the amplitude jitter is independent of ω .

It is possible to solve for the more general case where any two relative integrated harmonic powers (the i 'th and j 'th harmonics) are used to derive the jitter:

$$\sigma_t^2 = \frac{B_j - B_i}{(j^2 - i^2)\omega_0^2} \quad (\text{B.5})$$

$$\sigma_r^2 = \frac{B_i(j^2 + 1/12) - B_j(i^2 + 1/12)}{(j^2 - i^2)} \quad (\text{B.6})$$

B.4 Summary of jitter measurement approaches

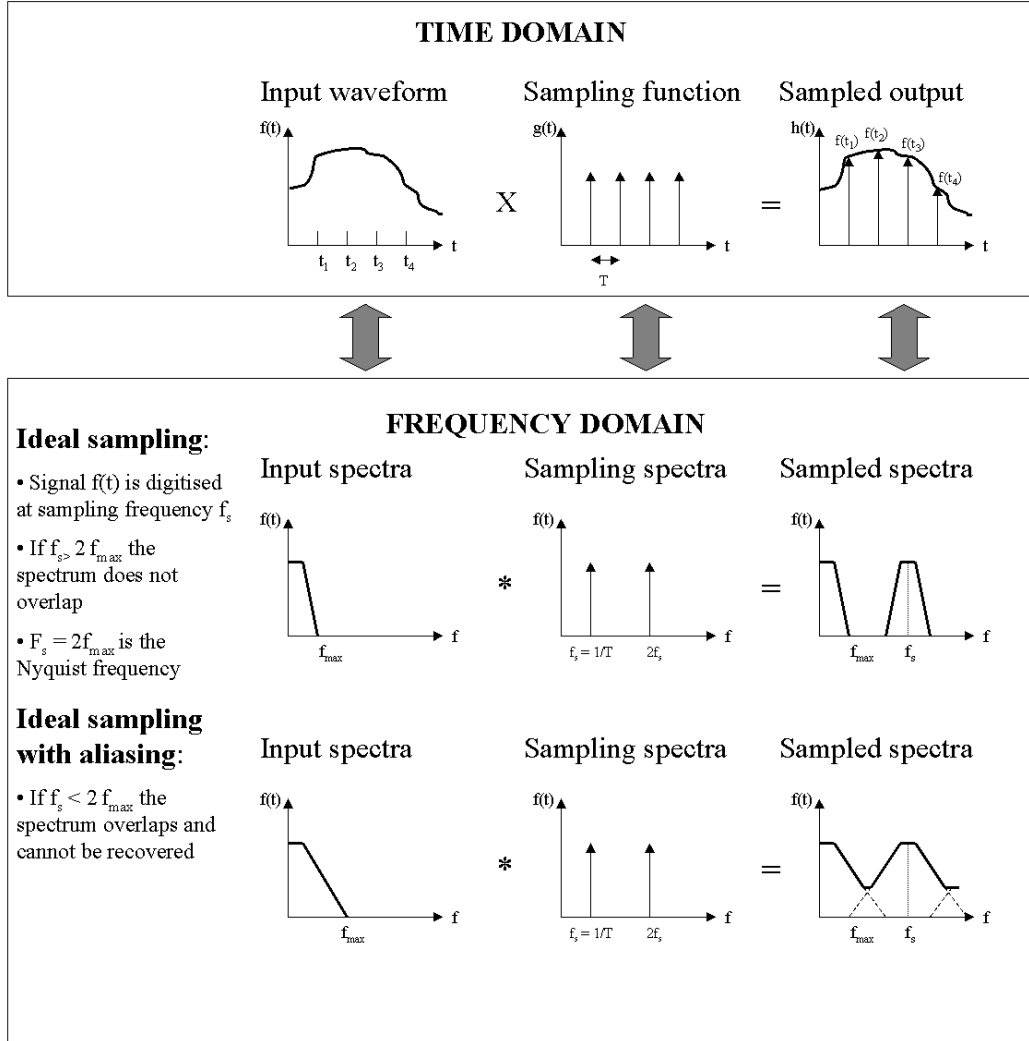
Two practical options exist for the experimental measurement of the jitter of optical pulse trains, following capture on a suitably fast detector: single sideband phase noise can be integrated to give the timing jitter, or Leep and Holm's method can be applied to spectrum analyser measurements to give the timing and amplitude jitter calculated using the relative integrated harmonic powers.

In practice, the noise floor of the measurement set-up may ultimately limit either method from an absolute measurement of the optical jitter and instead only an upper bound may be all that can be obtained experimentally.

References for Appendix B

1. Khrushchev I.Y., Kitcher D.J., Williams K.A., White I.H., Laughton F.R., Penty R.V., "Picosecond Q-switched bow-tie laser diode array", *Elect. Lett.*, 33(5), pp. 426 – 428, 1997
2. Juodawlkis P.W., Twichell J.C., Wasserman J.L., Williamson R.C., "Measurement of mode-locked laser timing jitter using phase-encoded optical sampling", *Conf. on Lasers and Electro-Optics*, 2000. (CLEO 2000), pp. 78 – 79, May 2000
3. Owen D., "Good practice guide to phase noise measurement", National Physical Laboratory publication, May 2004, ISSN 1368-6550
4. Clark T.R., Carruthers T.F., Matthews P.J., Duling I.N., "Phase noise measurements of ultrastable 10 GHz harmonically modelocked fibre laser"; *Electron. Lett.*, 35(9), pp. 720-721, 1999
5. Ng W., Stephens R., Persechini D., Reddy K.V., "Ultra-low jitter modelocking of Er-fibre laser at 10 GHz and its application in photonic sampling for analogue-to-digital conversion"; *Elect. Lett.*, 37(2), pp.113-115, 2001
6. Williams K.A., White I.H., Burns D., Sibbett W., "Jitter reduction through feedback for picosecond pulsed InGaAsP lasers", *IEEE J. of Quant. Elect.*, 32(11), pp.1988-1994, 1996
7. Jinno M., "Correlated and uncorrelated timing jitter in gain-switched laser diodes", *IEEE Photon. Tech. Lett.*, 5(10), pp. 1140-1143, 1993
8. Williams K.A., Burns D., White I.H., Sibbett W., Fice M.J., "Picosecond pulse generation with ultralow timing jitter in 1.5 μm multicontact MQW lasers using Q-switching", *IEEE Photon. Technol. Lett.*, 5(8), pp. 867-869, 1993
9. Burns D., Finch A., Sleat W., Sibbett W., "Noise characterization of a mode-locked InGaAsP semiconductor diode laser", *IEEE J. Quantum Electron.*, 26(11), pp. 1860-1863, 1990
10. Von der Linde D., "Characterization of the noise in continuously operating mode-locked lasers", *Appl. Phys. B* 39, pp. 201-217, 1986
11. Leep D.A. and Holm D.A., "Spectral measurement of timing jitter in gain-switched semiconductor lasers", *Leep and Holm, Appl. Phys. Lett.*, **60** (20), pp 24512 – 2453, 1992

C. Sampling issues



D. Timing Jitter and number of bits resolution

The maximum timing jitter which generates no more than 1-bit digitisation error is given by Equation D.1.

$$t = \frac{2^{-n} V_f}{dV/dt} \quad (D.1)$$

If we consider sampling a sinusoidal input waveform then the ideally sampled output will be:

$$x(t) = A \sin(2\pi f_x t) \quad (D.2)$$

However, due to timing jitter the aperture uncertainty error is given by:

$$\partial x = x(t + \partial t) - x(t) = A \sin(2\pi f_x(t + \partial t)) - A \sin(2\pi f_x t) \quad (D.3)$$

Assuming that the timing jitter is relatively small compared to the input waveform period, $\delta t \ll \pi$:

$$\partial x = x(t + \partial t) - x(t) \approx 2\pi f_x \partial t \cos(2\pi f_x t) \quad (D.4)$$

If the timing jitter is assumed to be uncorrelated then we can take the standard deviation, τ_{jitter} , leading to an upper bound for the effective number of bits of resolution obtained with this level of sampling jitter:

$$b_{eff} = \frac{1}{2\pi f_s \tau_{jitter}} \quad (D.5)$$

Where $f_s = f_x/2$, the sampling frequency of the ADC operating at Nyquist on the input signal frequency f_x for the worst case performance.

E. Electric field generated by modulator biased at null

From the wave equation derived from Maxwell's equations, for a wave propagating in the z-direction, with electric field E specified in the x-direction and magnetic field H in the y-direction:

$$\left. \begin{aligned} \frac{\partial^2 E_x}{\partial z^2} &= \mu\epsilon \frac{\partial^2 E_x}{\partial t^2} \\ \frac{\partial^2 H_y}{\partial z^2} &= \mu\epsilon \frac{\partial^2 H_y}{\partial t^2} \\ \mu_0\epsilon_0 &= \frac{1}{c^2} \end{aligned} \right\} \quad (E.1)$$

If the energy in a wave is assumed to travel in the direction of propagation, then the energy flow per unit area is given by:

$$S = c^2 \epsilon_0 E \times B \quad (E.2)$$

An average value for S can be measured over a finite period of time to give the irradiance I:

$$I \equiv \langle S \rangle = \varepsilon_0 c n \langle E^2 \rangle = \varepsilon_0 c n \frac{E_0^2}{2} \quad (\text{E.3})$$

where: $n \approx 1.45$, the refractive index of optical fibre

$$\varepsilon_0 = 8.8542 \times 10^{-12} \text{ F/m}$$

$$c = 2.998 \times 10^8 \text{ m/s}$$

The optical power for the irradiance within a cylindrical optical fibre is given by:

$$P = \iint I dA = \pi r^2 I \quad (\text{E.4})$$

For a modulator biased at null the output field is:

$$E_{out} = \frac{1}{2} E_{in} (1 + e^{i\Delta\phi}) \text{ where } \Delta\phi \text{ is the phase change} \quad (\text{E.5})$$

$$I_{out} = \frac{1}{2} \varepsilon_0 c n E_{out} E_{out}^* = \frac{1}{8} \varepsilon_0 c n E_{in} (1 + e^{i\Delta\phi}) E_{in} (1 + e^{-i\Delta\phi}) \quad (\text{E.6})$$

$$= \frac{1}{8} \varepsilon_0 c n E_{in}^2 (2 + e^{i\Delta\phi} + e^{-i\Delta\phi})$$

$$= \frac{1}{8} \varepsilon_0 c n E_{in}^2 (2 + 2 \cos(\Delta\phi)) \quad \text{since } \cos \alpha = \frac{e^{i\alpha} + e^{-i\alpha}}{2} \quad (\text{E.7})$$

$$= \frac{1}{8} \varepsilon_0 c n E_{in}^2 \left(1 + \cos^2\left(\frac{\Delta\phi}{2}\right)\right) \quad \text{since } 1 + 2\cos(2\alpha) = \cos^2(\alpha)$$

$$P_{out} = \pi r^2 \frac{1}{8} \varepsilon_0 c n E_{in}^2 \left(1 + \cos^2\left(\frac{\Delta\phi}{2}\right)\right) \quad (\text{E.8})$$

$$\text{Here } \Delta\phi = \frac{\pi V}{V_\pi} \quad \text{and} \quad V = V_o \sin(2\pi f_c t)$$

$$\text{Setting } V_o = V_\pi \text{ gives } P_{out} = \pi r^2 \frac{1}{8} \varepsilon_0 c n E_{in}^2 [1 + \cos^2(\frac{\pi}{2} \sin(2\pi f_c t))] \quad (\text{E.9})$$

$$= \frac{1}{4} P_{in} [1 + \cos^2(\frac{\pi}{2} \sin(2\pi f_c t))] \quad (\text{E.10})$$

$$\text{Alternatively, (E.7) gives } I_{out} = \frac{1}{4} I_{in} (2 + 2 \cos(\Delta\phi)) \quad (\text{E.11})$$

$$= \frac{1}{2} I_{in} [1 + \cos(\phi_{\max} \sin(2\pi f_c t))] \quad (\text{E.12})$$

Using the relationship relating trigonometric functions to the Bessel function J:

$$\cos[\delta \sin(\omega t)] = J_0(\delta) + 2 \sum_{n=1}^{\infty} J_{2n}(\delta) \cos(2n\omega t) \quad (\text{E.13})$$

(E.12) becomes:

$$I_{out} = \frac{1}{2} I_{in} \left[1 + J_0(\phi_{\max}) + 2 \sum_{n=1}^{\infty} J_{2n}(\phi_{\max}) \cos(2n\pi f_c t) \right] \quad (\text{E.14})$$

$$= I_{in} \left[\frac{1 + J_0(\phi_{\max})}{2} + \sum_{n=1}^{\infty} J_{2n}(\phi_{\max}) \cos(2n\pi f_c t) \right] \quad (\text{E.15})$$

where $\phi_{\max} = V_0/V_\pi$

So using $E_{out} = \frac{1}{2} E_{in} (1 + e^{i\Delta\phi})$ where $\Delta\phi = \pi \sin(2\pi f_c t)$ as the time domain input for the modelling is analogous to the formula in the report “Sampling Pulse Generators for Optical Analogue to Digital Converters”, prepared by Alwyn Seeds Technical Services under contract CU016 11154 (March 2002)

F. Relating dispersion parameter D to group velocity dispersion β_2

$$D = \frac{d\beta_1}{d\lambda} = -\frac{2\pi c}{\lambda^2} \beta_2 \quad (F.1)$$

\swarrow $\text{ps.nm}^{-1}\text{km}^{-1}$ \searrow $\text{ps}^2\text{km}^{-1}$

Typical values at 1550 nm are $D = 18 \text{ ps.nm}^{-1}.\text{km}^{-1}$, $\beta_2 = -20 \text{ ps}^2\text{km}^{-1}$

$$\begin{aligned} \beta_2 &= -20 \text{ ps}^2.\text{km}^{-1} \\ &= -20 \times (10^{-12})^2 \times 10^{-3} \text{ s.m}^{-1} \\ &= -20 \times 10^{-27} \text{ s.m}^{-1} \end{aligned}$$

$$\begin{aligned} D &= -\frac{2\pi c}{\lambda^2} \beta_2 \\ &= -\frac{2 \times \pi \times 3 \times 10^8}{(1550 \times 10^{-9})^2} \cdot -20 \times 10^{-27} \\ &\approx 17 \times 10^{-6} \text{ s.m}^{-2} \\ &= 17 \text{ ps.nm}^{-1} \text{ km}^{-1} \end{aligned}$$

Therefore, in order to convert between D in $\text{ps.nm}^{-1}\text{km}^{-1}$ and β_2 in $\text{ps}^2\text{km}^{-1}$ using Eq. F.1, above, a scaling factor of 10^6 is required to convert the units from s.m^{-1} to $\text{ps.nm}^{-1}\text{km}^{-1}$

G. Publications arising from the work presented in this thesis

Patents

1. McDonald G.J., “Low jitter optical pulse source for sampling applications”, GB Patent 0618021.0, 11th Sept. 2006

Patent summary:

The frequency of phase modulation used to overcome stimulated Brillouin scattering when generating soliton-effect compression pulses should be exactly half the pulse repetition rate of the output optical pulse train. In this way, the phase modulation artefacts occur exactly at the Nyquist frequency of the optical sampling system, ensuring that the phase modulation does not contribute to the single-sideband phase noise range of interest for the sampling application, and hence does not contribute to timing jitter in the sampling system. In addition, a multi-wavelength compression source is discussed and its application to wavelength demultiplexed ADC architectures.

2. Lewin A.C., McDonald G.J., and Orchard D.A., “Range-Finding Method and Apparatus”, GB patent number 0715368.7, filed 7th August 2007

Patent summary:

An optical metrology system for longitudinal range finding is detailed, based on rapidly scanning the pulse repetition rate of an optical pulse compression scheme (GB Patent 0618021.0) and measuring the output from an interferometer arrangement using a heterodyne detection system. By finding the exact pulse repetition rates which provide two adjacent maxima in the heterodyne signal, it is possible to unambiguously determine the path length difference between the two interferometer arms; the measured path length difference between the reference and measurement arms unambiguously determines the longitudinal range between the source and a remote retro-reflector.

Conference proceedings and presentations

McDonald G.J., Lewin A.C., Orchard D.A., "A Novel, Rugged and Robust Longitudinal Range Finding Method for Formation Flying Missions", 3rd International Symposium on Formation Flying, Missions and Technologies, SP-654, ISBN 978-92-9221-128-6, ESA/ESTEC Noordwijk, The Netherlands, 23 - 25 April 2008

McDonald G.J., Seeds A.J., "A novel pulse source for low-jitter optical sampling: a rugged alternative to mode-locked lasers", SPIE Proc. on Advanced Free-Space Optical Communication Techniques/Applications II and Photonic Components/Architectures for Microwave Systems and Displays, Vol. 6399, 63990J, October 2006

Olliero J.D., Kane M.J., McDonald G.J., "Undersampling photonic ADC using a low jitter soliton compression type pulse source", European Workshop on Photonic Signal Processing for Defence Applications, Rome, March 2005

McDonald G.J., Kane M.J., Seeds A.J., "Ultra-low jitter optical pulse source using soliton-effect compression", IEEE International Topical Meeting on Microwave Photonics (MWP' 04), pp. 123 - 126, October 2004

Magazine article

McDonald G.J., Seeds A.J., "A rugged optical pulse source for low-timing-jitter applications", retrieved from SPIE Newsroom in January 2007

website: <http://newsroom.spie.org/x5388.xml>, DOI: 10.1117/2.1200611.0532

Photonic digitiser proceedings, a related technology to photonic ADCs

McDonald G.J., Olliero J.D., Cooper M.J., Wilson R.A., "A transient waveform digitiser for wideband signal capture", SPIE Proc. on Advanced Free-Space Optical Communication Techniques/Applications II and Photonic Components/Architectures for Microwave Systems and Displays, Vol. 6399, 63990N, October 2006